Universidade de Aveiro Departamento de Engenharia de Materiais e Cerâmica
Ano 2014

Eddy Michael Pedro Domingues

Organossílicas com Mesoporosidade para Aplicação em Pilhas de Combustível

Mesoporous Organosilicas for Application in Fuel Cells

Universidade de Aveiro Departamento de Engenharia de Materiais e Cerâmica
Ano 2014

Eddy Michael Pedro Domingues

Organossílicas com Mesoporosidade para Aplicação em Pilhas de Combustível

Mesoporous Organosilicas for Application in Fuel Cells

Tese apresentada à Universidade de Aveiro para cumprimento dos requisitos necessários à obtenção do grau de Doutor em Ciência e Engenharia de Materiais, realizada sob a orientação científica do Doutor Filipe Miguel Henriques Lebre Ramos Figueiredo, Investigador Principal do Centro de Investigação em Materiais Cerâmicos e Compósitos da Universidade de Aveiro, e da Doutora Paula Celeste da Silva Ferreira, Investigadora Principal do Centro de Investigação em Materiais Cerâmicos e Compósitos da Universidade de Aveiro.

Trabalho realizado com o apoio financeiro dos projectos PTDC/CTM–CER/109843/2009, PTDC/QUI–QUI/113678/2009 e Pest-C/CTM/LA0011/2013.

Trabalho realizado com o apoio da FCT sob a forma de bolsa individual de doutoramento com a referência SFRH/BD/48043/2008.

Para ti Pedro

o júri

presidente

Prof. Doutor João Manuel Nunes Torrão
professor catedrático da Universidade de Aveiro

Prof.ª Doutora Verónica Cortés Zea Bermudez
professora catedrática da Universidade de Trás-os-Montes e Alto Douro

Prof. Doutor Jorge Ribeiro Frade
professor catedrático da Universidade de Aveiro

Doutora Carmen Mireya Rangel Archila
investigadora coordenadora do Laboratório Nacional de Energia e Geologia

Prof.ª Doutora Alexandra Rodrigues Pinto
professora associada da Faculdade de Engenharia da Universidade do Porto

Doutor Filipe Miguel Henriques Lebre Ramos Figueiredo
investigador principal da Universidade de Aveiro

Prof.ª Doutora Maria de Deus Corceiro de Carvalho
professora auxiliar da Faculdade de Ciências da Universidade de Lisboa

Doutora Paula Celeste da Silva Ferreira
investigadora principal da Universidade de Aveiro

agradecimentos

Em primeiro lugar quero agradecer à FCT pelo financiamento desta grande viagem de aprendizagem e crescimento, sem o qual não estaria a escrever estas palavras.
À Universidade de Aveiro e ao CICECO, pela cedência dos espaços, instalações e aparelhos para o desenvolvimento do meu trabalho.
Ao meu orientador Filipe, com quem comecei a trabalhar com uma BIC em 2007, sempre disponível para esclarecer (e duvidar também), ensinar e persistir, nunca deixando na mão e sempre com espírito de equipa. Obrigado por acreditar!
À minha orientadora Paula, pelo apoio e esclarecimento, pelas conversas e discussões, de trabalho ou não, e pelos valiosos ensinamentos.
Ao LACCO (Universidade de Poitiers) e em especial ao Nicolas Bion pela cedência do espaço e equipamento e pela excelente colaboração.
Ao meu pessoal do CICECO, aos que estão e aos que já estiveram, pelo apoio e colaboração, pelo companheirismo, os risos e as conversas parvas (nem sempre!) na cantina ou de volta de um café. A descontracção e alegria que proporcionam aliviam as tensões do dia-a-dia e ajudaram a aligeirar todo este processo.
Ao meu pessoal da FCUL, já se passaram alguns anos desde que deixamos os cadernos na sala do aquário e as cartas da sueca na esplanada do C5, mas formou-se um núcleo duro cujas ligações persistem e espero contar convosco até ser velhinho!
Ao pessoal de Pombal e em particular ao pessoal e "entourage" da nossa famigerada banda punk rock/psicadélico de putos revoltosos, existem amizades de base que o tempo nunca poderá apagar! Rock on!
À nossa "família emprestada" que migrou também para Aveiro, Andreia, Vítor (e a Ritinha claro) e o Flávio, pelo carinho e apoio e pela sua reconfortante presença.
Às duas pessoas que me fizeram pessoa, que sempre me proporcionaram a educação, a atenção, o incondicional Amor e carinho e tudo o que sempre precisei para estar aqui hoje, olhando-me sempre orgulhosamente.
Obrigado Mãe! Obrigado Pai!
À minha vó Maria, minha mãe duas vezes, por ser quem ela é!
Ao Lopes, pela amizade, apoio e disponibilidade para ajudar.
Ao meu mano Heitor, tás a ficar velho pá! Não preciso descrever a importância que tens para mim! À Sónia, minha mana por afiliação, e à minha linda sobrinha e afilhada Maria só vos digo… que saudades!
À minha linda esposa e companheira, namorada e amiga, co-arquitecta do nosso projecto-família, pelo caminho que temos percorrido e quero percorrer, quero-te sempre ao meu lado! AMO-TE profundamente!
Pedro, meu pequeno homenzinho, minha mini-pessoa mais linda do mundo, dedico-te esta tese. Tens e terás sempre um lugar cativo, na primeiríssima fila, no âmago do meu ser. Tu és luz na nossa vida, um raio de alegria e maravilhamento. Espero que um dia leias estas palavras e que te façam sorrir! ADORO-TE!

palavras-chave Mesoporoso, Organossílica, Condutividade Protónica, Nafion®, Compósito

resumo

O objectivo desta dissertação é o de avaliar o potencial de organossílicas mesoporosas periódicas (Ph-PMO) como aditivos para membranas poliméricas de pilhas de combustível, visando um melhor desempenho a baixa humidade relativa (h.r. < 50%) e/ou temperaturas altas (T > 120 ºC). A estrutura dos Ph-PMO mimetiza a do Nafion®, apresentando semelhante tamanho de poro (3 nm) e distância entre grupos ácido (0.8 nm), mas com uma estrutura estável e rígida que reduz o efeito de confinamento protónico à superfície do poro, que ocorre no Nafion®. Este efeito pode potencialmente traduzir-se num aumento da condutividade protónica em condições anidras, para além de melhorar o comportamento visco-elástico. Foram sintetizados Ph-PMO com grupos ácido sulfónico (S-Ph-PMO) e ácido fosfónico (P-Ph-PMO), com características estruturais e microestruturais distintas. A condutividade dos dois tipos de Ph-PMO aumenta com o aumento da área superficial específica e da h.r., confirmando o papel central da superfície e da água de hidratação no transporte protónico. A maior acidez dos S-Ph-PMO resulta em valores de condutividade superiores, da ordem de 0.1 $S \cdot cm^{-1}$ a 94 ºC e 98% de h.r. Os resultados obtidos com uma série de S-Ph-PMO com diferentes concentrações de grupos funcionais, área superficial específica e ordem estrutural, preparados por reacção hidrotermal em micro-ondas, mostram que a condutividade aumenta com o aumento da concentração de grupos ácidos, não sendo, no entanto, correlacionável com a ordem estrutural. Foram seleccionadas várias amostras de S-Ph-PMO para preparar membranas compósitas à base de Nafion®, avaliando as suas propriedades visco-elásticas e de transporte protónico. Para a membrana com cerca de 36 vol.% de aditivos, o efeito de volume dos aditivos é evidenciado por um módulo de armazenamento (*E*') até 10 vezes superior ao do Nafion® puro. O efeito dos aditivos faz-se também sentir na diminuição da dilatação das membranas por absorção de água até 30%, devido à dilatação virtualmente nula dos aditivos. O aumento do *E*' e diminuição da dilatação podem vir a ser cruciais para a melhoria da estabilidade termo-mecânica das membranas e da interface eléctrodo/electrólito. A condutividade das membranas compósitas é menos dependente da h.r. e da T, podendo ser até 1 ordem de grandeza superior à condutividade do Nafion® puro a 40 ºC e 20% de h.r. As diferenças são menos significativas a alta h.r., atingindo o valor máximo de 0.2 $S \cdot cm^{-1}$ a 94 ºC e 98 % h.r. No entanto, contrariamente ao efeito de volume no *E*' e na dilatação, a condutividade máxima foi atingida numa membrana com 20 vol.% de aditivos. Verifica-se que a condutividade das membranas tende a aumentar ligeiramente com o aumento da área superficial e da concentração de grupos ácido dos aditivos, sendo o efeito da ordem estrutural muito pouco visível. O aumento da condutividade das membranas compósitas, a baixa h.r., pode ser interpretado considerando a redução do confinamento protónico e, à medida que a h.r. aumenta, assumindo um efeito de superfície, no qual a presença dos aditivos provoca a ruptura de uma estrutura rígida que se forma à superfície da membrana de Nafion®, libertando a pressão interna e facilitando o acesso da água ao interior da membrana e desse modo aumentando a condutividade.

keywords Mesoporous, Organosilica, Proton Conductivity, Nafion®, Composite

abstract

The objective of this thesis is to assess the potential of acid-functionalized periodic mesoporous organosilicas (Ph-PMO) as fillers for the polymer membrane in polymer electrolyte fuel cells, aiming at improved performance under low relative humidity (r.h.<50%) and/or high temperature (T >120 °C) operation conditions. Ph-PMOs mimic the structure of Nafion®, presenting a similar acid load distributed on pores with similar width (3 nm) and with similar distance between acid sites (0.8 nm), but on a stable, rigid structure preventing the proton confinement to the pore surface that occurs in Nafion®. This offers potentially high protonic conductivity under dry conditions, in addition to improved visco-elastic behaviour. Two protogenic groups based on sulfonic (S-Ph-PMO) and phosphonic (P-Ph-PMO) acids were used to functionalize Ph-PMOs with variable structural and microstructural features. The conductivity of both types of Ph-PMOs increases with increasing specific surface area and r.h., confirming the surface nature of the protonic transport and the key role of the hydration water on the protonic transport. The strongest acid character of S-Ph-PMOs leads to a much higher conductivity, attaining values of up to ~0.1 $S \cdot cm^{-1}$ at 94 °C and 98% r.h. Results obtained for a series of S-Ph-PMO samples with variable acid loadings, surface area and structural order, prepared by a microwave hydrothermal reaction, show that the conductivity increases with increasing acid loading, whereas no clear correlation can be established with structural order parameters. S-Ph-PMOs were selected for the preparation of composite Nafion® membranes and their transport and visco-elastic properties evaluated. The bulk effect of the fillers is demonstrated by a 10 fold increase of the storage modulus (*E*') at 140 °C of composite membranes with up to 36 vol.% S-Ph-PMO, in comparison with pure Nafion®. The effect of fillers on the bulk properties is also apparent on the swelling under saturated conditions, which is reduced by 30% with addition of ~36 vol.% of fillers, indicating virtually zero swelling of the fillers. These improvements may be crucial to increase the thermo-mechanical stability of the membrane and of the electrode/electrolyte interface. The conductivity of the composite membranes is less dependent on r.h. and temperature, and can be up to 1 order of magnitude higher than for pure Nafion®, at 20% r.h. and 40 °C. Differences are smaller at high r.h., with the highest conductivity of 0.2 $S \cdot cm^{-1}$ achieved at 94 °C and 98% r.h. However, and as opposed to the bulk effects on *E*' and swelling, a conductivity maximum is observed for the membranes with 20 vol.% of fillers. The use of different fillers in a series of 20 vol.% composite membranes showed that there is a slight increase of the membrane conductivity with increasing acid load and surface area of the fillers, however no direct correlation could be drawn for the structural properties. The increased conductivity at low r.h. can be interpreted considering a reduction of the proton confinement in the rigid pores of the fillers and, as the r.h. increases, by assuming a surface effect, where the presence of the mesoporous fillers disrupts the “skin-like” structure that forms at the surface of Nafion®, releasing the internal pressure and hence facilitating the access of the hydration water to the bulk of the membrane.

LIST OF FIGURES

LIST OF SCHEMES

LIST OF TABLES

ABBREVIATIONS AND ACRONYMS

AC	alternate current
AFC	alkaline fuel cell
ASC	area-specific conductance
BET	Brunauer, Emmett and Teller method for the calculation of specific surface area
BJH	Barret, Joyner and Halenda method for to calculate pore size distribution and pore volume
BTEB	1,4-bis(triethoxysilyl)-benzene
C12	dodecyl trimethylammonium bromide
C14	tetradecyl trimethylammonium bromide
C16	cetyl trimethylammonium bromide

C18	octadecyl trimethylammonium bromide
CHP	combined heat and power generation
CL	catalyst layer
CP	cross-polarization
CPE	constant phase element
DLS	dynamic light scattering
DMA	dynamic mechanical analysis
DMAc	N,N-dimethylacetamide
DMFC	direct methanol fuel cell
DOE	U.S. department of energy
DPTS	diethyl-phosphatoethyl-trimethoxysilane
DQ	double quantum
DSC	differential scanning calorimetry
EDS	energy dispersive X-ray spectroscopy
EIS	electrochemical impedance spectroscopy
Et	ethyl group
EW	equivalent weight
FCH-JU	fuel cell and hydrogen joint undertaking
FTIR	Fourier transform infrared spectroscopy
GDL	gas diffusion layer
HPA	heteropoly acid $H_5GeW_{11}VO_{40}$
HPDEC	high-power decoupling technique
HPW	heteropoly acid $H_3PW_{12}O_{40}$·nH2O
HR-TEM	high resolution transmission electron microscopy
IP	in-plane
IR	infrared spectroscopy
IUPAC	international union of pure and applied chemistry
KJS	Kruk, Jarionec and Sayari method for the calculation of pore size distribution and pore volume based on BJH, specifically for mesoporous materials
MAS	magic angle spinning
MCFC	molten carbonate fuel cell
MD	molecular dynamics
Me	methyl group
MEA	membrane electrode assembly
MPTMS	3-mercaptopropyl-trimethoxysilane
MW	microwave

NMR	nuclear magnetic resonance
P123	poly(ethylene glycol)-block-poly(propylene glycol)-block-poly(ethylene glycol) $EO_{20}PO_{70}EO_{20}$
PBI	polybenzimidazole
PBI	poly (benzimidazole)
PEK	poly (ether ketone)
PEM	proton exchange membranes
PEMFC	proton exchange membrane fuel cells
PES	poly (ether sulfone)
PFSA	perfluorocarbon-sulfonic acid
PIL	protic ionic liquid
PMO	periodic mesoporous organosilicas
PMS	periodic mesoporous silica
PSiP	diethyl 4-(trimethoxysilyl)-benzylphosphosphonate
PTFE	polytetrafluoroethylene
QENS	quasi-elastic neutron scattering
r.h.	relative humidity
SANS	small-angle neutron scattering
SAXS	small-angle X-ray scattering
SDA	structure directing agent
SEM	scanning electron microscopy
SHS	n-hexadecylsulfuric acid sodium salt
SOFC	solid-oxide fuel cell
SQ	single quantum
SSC	short-side-chain
TEM	transmission electron microscopy
TEOS	tetraethoxysilane
TGA	thermogravimetric analysis
TOF	turn over frequency
TP	through -plane
WAXD	wide-angle X-ray diffraction
XRD	X-ray diffraction

SYMBOLS

A	area of the electrode or the cross-section area of the membrane in the IP configuration
a	angle shift between the centre of the semi-circle and the real axis in the complex plane
a_0	lattice constant
b	universal constant depending on the dimensions of the system
c	volume fraction of the aqueous phase
c_0	percolation threshold
C	capacitor/capacitance
C_{eq}	equivalent capacitance
C_s	stray capacitance
D	diffusion coefficient
d	inter-planar distance (XRD)
d_p	diameter of the particles (DLS)
E''	loss modulus
E'	storage modulus
E_a	activation energy
f	frequency
g	total number of solvating water molecules
h	number of water molecules associated to the sulfonate ion
$[H^+]$	acid load
$I_{(001)}$	XRD intensity of the molecular scale periodicity reflection
$I_{(100)}$	XRD intensity of the pore order reflection
j	number of water molecules associated to the proton
$i(t)$	alternate current resulting from the applied sinusoidal signal (EIS)
k	Boltzmann's constant
$K^{solv}_{(T)}$	solvation constant
l	distance between the SO_3^- sites (Eikerling model)
L	Nafion® pore diameter (Eikerling model)
L_{el}	distance between electrodes (thickness of powder pellets)
m_p	mass of the powder pellet used for EIS
$M H_2O$	molar mass of water
n	integral multiple of the wavelength
pH_2O	water vapour partial pressure

q	SANS scattering vector
R	electrical resistance
R_p	spherical particle radius
S_{BET}	specific surface area calculated from the Brunauer, Emmett and Teller method
T_g	glass transition temperature
V_{KOH}	volume of KOH solution added to reach the equivalence point
V_L	molar volume of the liquid condensate (Kelvin's eq.)
V_m	amplitude of the sinusoidal signal (EIS)
$v(t)$	sinusoidal signal (EIS)
v_s	terminal velocity (Stoke's law)
W	water uptake capacity
W_d	dry weight
W_w	wet weight
Y_0	admittance
Z	impedance
Z'	real part of the impedance
Z''	imaginary part of the impedance

GREEK SYMBOLS

χ	order factor (ratio $I_{(100)}/I_{(001)}$)
α	long-range motion of both the main and the sulfonic acid functionalised side chains (visco-elastic transition in DMA)
β	segmental motions of the main-chain of the physically cross-linked perfluorocarbon phase (visco-elastic transition in DMA)
δ	chemical shift
ΔH_{solv}	solvation enthalpy
ΔS_{solv}	solvation entropy
ε	relative permittivity
ε_0	vacuum permittivity
ϕ	contact angle between the pore surface and the water molecules
γ	short-range motions of the polytetrafluoroethylene-like backbone (visco-elastic transition in DMA)
η	viscosity of the media

φ	DMA phase shift angle
ϑ	phase angle between the applied voltage and the resulting current (EIS)
λ	hydration level
λ_{Cu}	wavelength of the XRD Cu Kα radiation
μ	dynamic viscosity (Stoke's law)
θ	incident angle (XRD)
ρ_f	density of the fluid (Stoke's law)
ρ_p	density of the spherical particle (Stoke's law)
σ	protonic conductivity
σ_0	pre-factor related to the molecular interactions
τ	angle between the centre of the semi-circle and the real axis in the complex plane
ω	radial frequency (EIS)
ω_0	relaxation frequency (EIS)
ψ	surface tension

INDEX

1 INTRODUCTION

1.1 Motivation and Objective

The energy demand is increasing across the globe, putting pressure on the governments in order to guarantee to their citizens a secure supply, which is still satisfied, to a large extent, at the cost of the planet's concealed carbonaceous resources. In 2007, the European Council adopted climate and energy related objectives aiming to reduce the emissions of greenhouse gases in at least 20% with respect to 1990, to increase at least 20% the share of renewable sources in the energy mix, to improve in 20% the energy efficiency and to have at least 10% of the energy consumed in the transportation sector from renewable sources, by the year of 2020.[1] The latest statistics (2011-2012) show that about one third of the total final energy is consumed by the transport sector, to which is responsible by one fifth of the total greenhouse gases emissions. Moreover, less than 4% of the total energy consumption in the sector is generated from renewable sources.[2] In this energy panorama, hydrogen, as the energy carrier, and fuel cell technologies, as chemical energy converter, represent a huge opportunity for the reduction of greenhouse gases and fossil fuel dependence of the transportation sector. They also allow the delocalized production of electricity, thus greatly contributing to a more flexible and efficient distribution grid for stationary applications, offering in addition the possibility for co-

generation of heat. Additionally, hydrogen production and fuel cell/electrolysers technologies can be coupled to renewable energy sources, such as wind or solar, coping with its characteristic intermittence towards a virtually zero-emission goal for the energy mix.

Hydrogen and fuel cells have been at the centre of large research programs across the world. In Europe there is the Fuel Cell and Hydrogen Joint Undertaking (FCH-JU), a public/private partnership joining the European Commission, the fuel cell and hydrogen industries represented by the NEW Industry Grouping and the research community represented by the Research Grouping N.ERGHY. The FCH-JU funds research, technological support and the rising of public awareness towards hydrogen and fuel cells in Europe. By 2020, it expects 500 000 fuel cell vehicles in Europe, powered by hydrogen that should be generated in 50% from renewable energy sources, 1000 fuelling stations and 50 000 households equipped with fuel cells for power generation and/or combined heat and power generation (CHP).[3] The funded investigations are mainly focused on the reduction of the cost of Membrane Electrode Assembly (MEA), the synthesis of new and improved materials for increased working temperatures (above 100 °C) and/or reduced relative humidity (r.h.) and the improvement of cell/stack design for greater lifetime.[4]

The United States Department of Energy (DOE) also has ambitious goals concerning fuel cells and hydrogen. Regarding transportation, which represents 28% of the total energy consumption in the U.S., the DOE is focusing its efforts on the development of proton exchange membrane fuel cell (PEMFC).[5] The DOE has set a series of ambitious targets for the near future (2017) in order to obtain proton exchange membranes (PEM) suitable to run at 120 °C under 25 - 50% r.h. and deliver protonic conductivity of 0.1 $S \cdot cm^{-1}$. The full system should be able to work in environmental conditions for at least 5 000 hours, at an efficiency of at least 60% and the total cost should not exceed $\$30 \cdot kW^{-1}$ (less than $\$8 \cdot kW^{-1}$ for the PEM alone).[6]

The emerging paradigm of hydrogen and fuel cells is the driving force for this PhD thesis in Materials Science and Engineering, focused on the evaluation of the potential of periodic mesoporous organosilicas (PMO) hybrid materials, with sulfonic or

phosphonic acid functional groups, as fillers for polymeric PEM, with enhanced performance under high temperature or low humidity operating conditions. The major scientific objective is to identify the correlations between the microstructural features of the PMOs (acid loading, specific surface area, porosity, structural order, and pore volume) and their protonic conductivity, and how these can impact the properties of the respective composite membranes.

1.2 Fuel Cells

Fuel cells are electrochemical devices that directly convert the chemical energy of a fuel, hydrogen for example, into electricity. Unlike other fuel-based energy conversion systems such as the internal combustion engine, the fuel cell is a device that does not have any mechanical moving parts.

This section starts with a brief review of the history of fuel cell science and technology, placing emphasis on the functional materials used in the polymer electrolyte fuel cells.

1.2.1 Brief History

History is not clear on how to give credit for the finding of the fuel cell principle. In 1839, Christian Friedrich found that a current could be measured between two Pt plates immersed in sulphuric acid (electrolyte) while H_2 and O_2 were separately fed to the electrodes.[7,8] William Grove also made the same observation while experimenting on the reversibility of water electrolysis.[8,9] In 1843 the later published an article describing the "gaseous voltaic cell" which is often considered the first fuel cell stack (Fig. 1.1).[8,10]

Almost 90 years after, in 1932, Francis Bacon took the principle developed by Grove and substituted the expensive Pt electrode with Ni gauzes and the acid electrolyte with an alkaline KOH solution, resulting in the first alkaline fuel cell (AFC).[8,11]

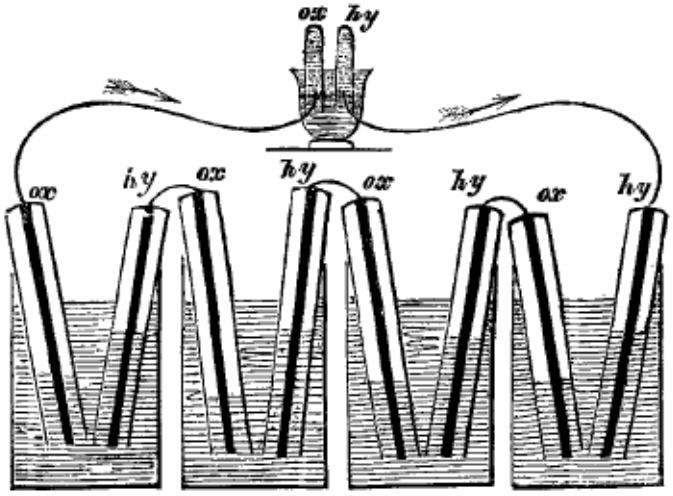

Figure 1.1. Schematic representation of Grove's gaseous voltaic battery (reproduced from[10]).

In 1937, Baur and Preis used a Zr-based material, studied previously by Nernst in 1899, as a solid oxide electrolyte in a fuel cell (SOFC).[8,11,12] The "Nernst-mass" (85% ZrO_2 and 15% Y_2O_3) was found to be the best performing material at operating temperatures up to 1100 ºC. Davtyan later developed, in 1946, a Molten Carbonate Fuel Cell (MCFC) that operated in temperature range 650-750 ºC, with a cell performance of 0.79 V at 20 $mA \cdot cm^{-2}$.[8] Starting in 1965, the NASA Gemini program used fuel cells on-board, developed at General Electric Company by Grubb and Niedrach.[8] These innovative fuel cells had an electrolyte that was in fact an ion-exchange membrane, built from cross-linked polystyrene loaded with sulfonic acid. A new perfluorosulfonated ion-exchange resin branded as Nafion® was developed by the E.I. DuPont Company in the late 1960's.[8] This solid-acid polymer membrane, with a polytetrafluoroethylene backbone, could resist more efficiently the harsh chemical environments in the cell, the high temperatures (up to 200 ºC) and showed better electrical resistance and mechanical strength, resulting in longer lifetime.[8] Some years after, a Canadian company named Ballard made a strong effort to cut-down the cost of PEMFCs. They developed a Nafion® based fuel cell with less expensive materials and techniques which could deliver 0.7 V at 0.54 $A \cdot cm^{-2}$, using H_2 as fuel. These PEMFCs have been installed in submarines, cars, busses, portable and stationary energy generators, etc. Due to its high current density, low working temperature and fuel flexibility (H_2, methanol, hydrocarbons), the PEMFC is the preferred type of fuel cell for portable applications, and is particularly suitable for the

on-board production of electricity for the second generation of electrical vehicles.[8, 11] Nafion® is still the state-of-the-art membrane material, although it suffers from several drawbacks.[13,14] These shall be discussed in sub-section 1.3.1.

1.2.2 PEMFC fundamentals and components

Figure 1.2A shows a schematic representation of various types of fuel cells depending on the type of electrolyte, which ultimately determines the operation temperature and the type of ionic charge carrier. Oxide-ion ceramic conductors such as yttria-doped zirconia are used above 700 °C. Molten carbonates are considered intermediate temperature electrolytes (600-700 °C) displaying high levels of carbonate ion conductivity. Fuel cells operating at lower temperatures are mostly based on proton conducting electrolytes. Phosphoric acid is an excellent protonic conductor and is typically used in the molten state in fuel cells operating up to 220 ºC. The polymer electrolytes in PEMFC can transport protons from room temperature up to nearly 180 °C, and they are also compatible with the direct use of methanol as fuel, in the so-called Direct Methanol Fuel Cells (DMFC). Also designed for low temperature (<100 °C) operation are the alkaline fuel cells using an aqueous alkaline solution as electrolyte (e.g. KOH) with high hydroxyl conductivity, or more recently, using solid polymer electrolytes similar to those used in PEMFCs but in the alkaline form.[11]
The PEMFCs are the technology of interest for this work. The heart of the PEMFC is the PEM, which is sandwiched between an anode and a cathode, forming the Membrane Electrode Assembly (MEA). The electrodes are normally composed of a porous gas diffusion layer (GDL) that is in direct contact with the fuel (at the anode side) and the oxidant (at the cathode side), and with a catalyst layer (CL) at the electrolyte/electrode interfaces (Fig. 1.2C). Several MEAs are stacked and interconnected with bipolar conducting plates, which ensure gas separation and feeding to the electrodes. The number of MEAs determines the stack voltage and the current depends on the electrode surface area (Fig. 1.2B). The other components ensure the thermal and water management, the fuel and oxidant flow and power conditioning.

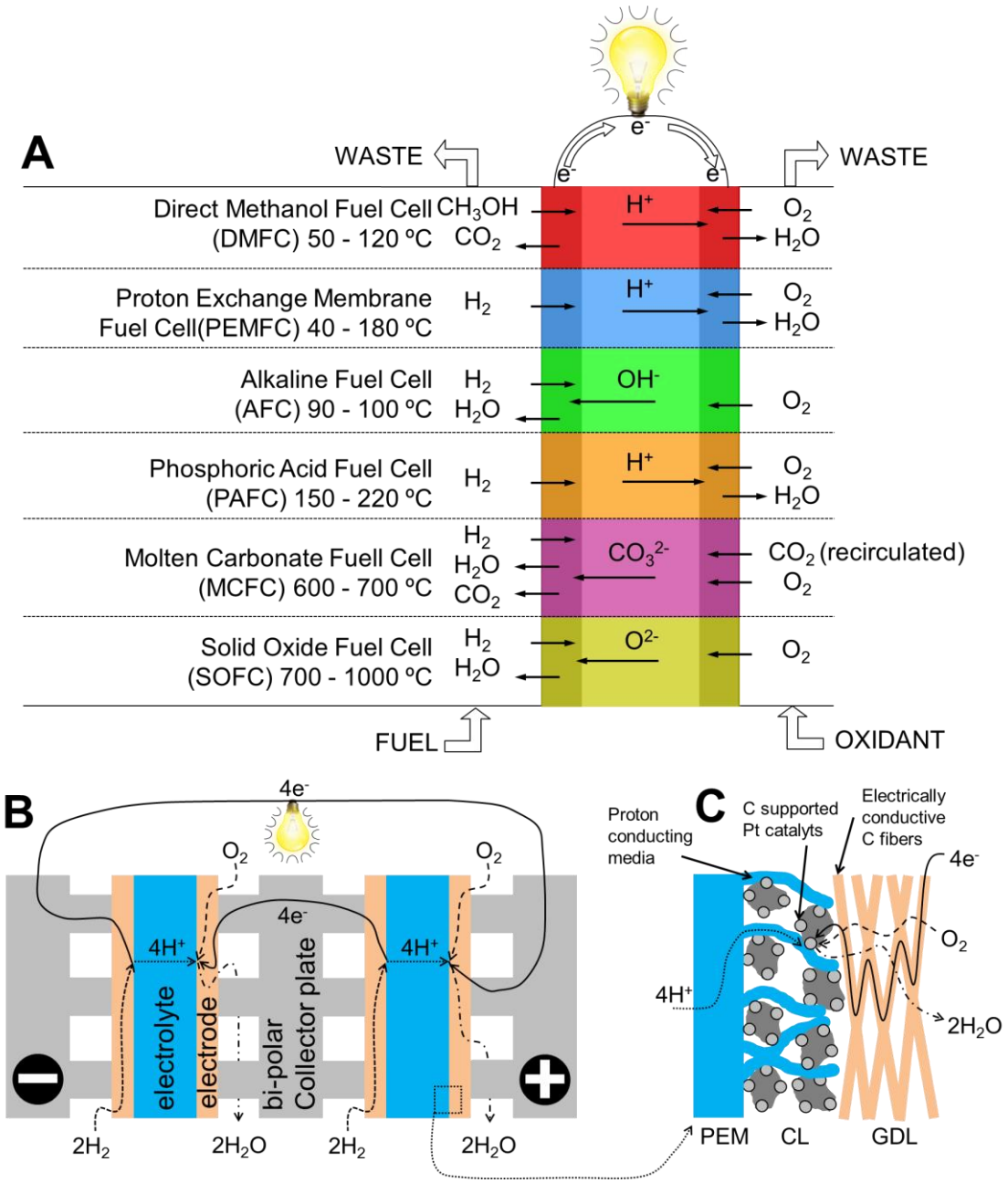

Figure 1.2. A) Types of Fuel Cells and specific electrode reactions. B) Schematic representation of a fuel cell stack. Adapted from[11]. C) Schematic representation of one side of a membrane electrode assembly. Adapted from[15].

At the anode side of the bipolar plates, a continuous flow of fuel (H_2, methanol or hydrocarbons) is supplied, where it is oxidised originating protons and electrons at the CL. In the case of hydrogen, the anodic reaction can be written as

$$H_2 \rightarrow 2H^+ + 2e^- \qquad \text{eq. 1.1}$$

The protons travel through the PEM while the electrons are carried across the bipolar plate to the cathode of the adjacent MEA. In the cathode side, the protons react with the oxygen of the air supplied and electrons to form water.

$$½O_2 + 2H^+ + 2e^- \rightarrow H_2O \qquad \text{eq. 1.2}$$

The total cell reaction is exothermic (producing Q heat) and can be written as:

$$H_2 + ½O_2 \rightarrow H_2O + Q \qquad \text{eq. 1.3}$$

The water formed at the cathode is subsequently removed by an excess flow of O_2 or air. At the end of the stack, the electrons travel through the terminal current collectors to an external circuit where they perform useful work on the load (Fig. 1.2 B).[11,16]
The DMFC is closely related to the PEMFC, using methanol as fuel instead of H_2, where the overall reaction is:

$$CH_3OH + {}^3/_2O_2 \rightarrow 2H_2O + CO_2 \qquad \text{eq. 1.4}$$

In a PEMFC stack, the bipolar plates are normally made of electric and thermal conductive materials such as graphite/thermoplastic composites or metal covered with a layer of non-corrosive conductive material such as carbon (in graphite or diamond-like form), precious metal or conductive polymers. These are normally bulky and stiff components of the PEMFC because the materials are also chosen to provide structural support to the fuel cell stack.

In direct contact with the bipolar plate is the GDL. It has to be sufficiently porous to allow gas and water flow and it also has to be electrical and thermally conductive, to act as an electron collector and diffuse the heat released from the electrochemical reaction. Additionally, it has to be rigid enough to maintain structural stability of the MEA but flexible enough to ensure the electrical contact. Typical GDLs are made from carbon-based materials in the form of paper, cloth or non-woven pressed carbon

fibres. To avoid water from accumulating inside the pores of the GDL, the region close to the catalyst layer also contains some amount of a highly hydrophobic material such as polytetrafluoroethylene (PTFE) in order to promote water removal from the reaction sites.[16,17]

The CL is the layer between the GDL and the PEM. The CL layer should easily allow the diffusion of the reactants, possess high ionic and electrical conductivities, show a reasonable amount of hydrophobicity to avoid water clogging and enough resilience to the harsh conditions resulting from the electrochemical reactions, which occur at the triple point void/catalyst/electrolyte.[15] The intimate contact between the CL and PEM is of crucial importance to ensure that the reaction is effectively occurring on the entire membrane surface. The CL is normally composed of a Pt catalyst supported by porous carbon black, which provides bulk electronic conductivity, all bonded with some amount of polymer of the same (or similar) composition of the electrolyte. This is important for the creation of a proton conduction pathway from the CL to the PEM and also to ensure the adhesion of the CL to the membrane.[16] To minimize the catalyst load and to increase the reaction rate, Pt nano-particles (< 4 nm) have been used, whereas the carbon support is mesoporous with specific surface area (S_{BET}) higher than 75 $m^2 \cdot g^{-1}$, to facilitate the access of the reactant gases to the reaction sites.[17] Efforts to lower the high cost of the Pt/C catalyst include the use of Pt-based alloys with transition metals (e.g. Ru, Ir, V, Rh, Cr, Co, Ni, Fe, Mn, Pd or Mo),[16, 17] or alternative Pt deposition methods, which seem to be able to lower the catalyst load from the usual 0.4 $mg \cdot cm^{-2}$ down to 0.014 $mg \cdot cm^{-2}$.[15]

The PEM is the central component of the MEA and the major focus of this thesis, and are thus reviewed separately in the following section.

1.3 Proton Exchange Membranes (PEM)

The main property of the membrane is the high protonic conductivity, without which the cell efficiency is obviously small. Conversely, the electronic conductivity must be minimal to avoid short-circuit. In addition, it must present adequate mechanical, chemical and electrochemical stability under working conditions and for long

lifetimes, whereas water cross-over and fuel permeability should be minimal. Last but not least, the dimension stability of membrane upon heating/cooling cycles and water absorption/desorption (swelling) should be controlled in order to ensure the long term mechanical integrity of the MEA constrained by the bipolar plates. Of course, the membrane should desirably be recyclable and affordable. Unfortunately, the available membranes fail to fulfil all these requirements.[13,18] The state-of-the-art membranes are since the 1970's based on perfluorocarbon-sulfonic acid (PFSA) ionomers, with the most widely used material being know by the commercial designation of Nafion®, developed by DuPont in the 1960's.[11]

1.3.1 Nafion®

Figure 1.3 depicts the structure of Nafion® constituted by a hydrophobic PTFE backbone, which confers the mechanical stability, and a pending solvated perfluoroether chain with hydrophilic sulfonic acid functional group at the tip, which is responsible for the ionomers characteristic.[13,19]

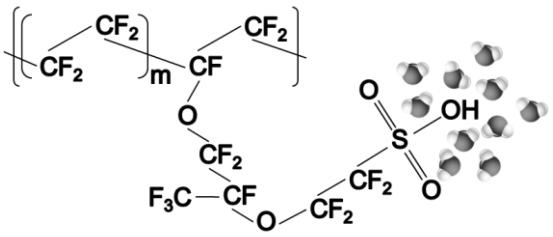

Figure 1.3. Scheme of the chemical structure of Nafion® with the sulfonic acid tip solvated by water.

The equivalent weight (EW) of Nafion® is an average measure of the mass of dry polymer per mole of SO_3H group. The average number of PTFE blocks that are repeated before the perfluoroether side-chain is anchored (m in Fig. 1.3) is related to EW by:

$$EW = 100m + 446 \qquad \text{eq. 1.5}$$

Several extruded Nafion® membranes are available in the market, showing the EW and thickness in its nomenclature. For example the Nafion® membrane N117 has an EW of 1100 g·mol^{-1} (first two digits multiplied by 100) and a thickness of 0.007 inches (last digit divided by 1000).[20]

Another important feature of Nafion® (and ultimately all PFSA membranes) is the hydration level (λ), which expresses the number of water molecules per SO_3H group:

$$\lambda = \frac{n\ H_2O}{n\ SO_3H} \qquad \text{eq. 1.6}$$

The λ value is highly dependent on the physical state of the water used to humidify the membrane. Nevertheless, water adsorption studies in boiling water seem to put the limit of λ = 22, whereas λ = 14 for a membrane equilibrated in a saturated atmosphere.[11] The reason for this difference will be discussed in section 1.3.1.1.

The sulfonic acid group is extremely hydrophilic, conferring to the polymer excellent protonic conductivity of about 0.1 S·cm^{-1}, but only at low temperatures (< 90 ºC) and high humidity conditions.[13,20] The proton transport mechanism in Nafion® occurs by a molecular diffusion of hydronium ions (H_3O^+) (also known as vehicle mechanism), and by the structural diffusion (also referred to as the Grotthus mechanism) of H^+ between solvated SO_3H pending groups and/or between adjacent water molecules adsorbed in the structure.[11,13] In both cases, the dissociation and transport of the proton from the protogenic group is highly dependent on the presence of liquid water, limiting the working temperatures to T < 100 °C, at atmospheric pressure.[11,13,17,18] This limit is also imposed by the relatively low glass transition temperature (T_g) of hydrated Nafion® (80 - 120 °C)[21] above which pinholes start to appear due to a visco-elastic flow, eventually leading to mechanical failure.[21,22]

The consequence of working at such low temperature translates in the use of a fairly large Pt catalyst load to ensure reasonable electrode performance. Unfortunately, the risk of CO-poisoning of the catalyst is very high, if using low-purity H_2 fuel. At 80 °C the CO tolerance of Pt catalysts is as low as 20 ppm.

Another drawback found in Nafion® is that the water generated at the cathode (eq. 1.2) can diffuse in the direction of the anode due to water concentration gradient. In the case of DMFC, the permeation and diffusion of methanol fuel from the anode to the cathode is also observable, which can severely reduce the efficiency of the fuel cell. Interestingly, various reports state that the incorporation of fillers in composite Nafion® can reduce drastically the methanol crossover.[14]

Water molecules can also be transported from the anode to the cathode dragged by the protons, (the so called "electro-osmotic drag"). All these water molecules moving inside the membrane frequently lead to the drying of some areas of the anode or the overflow of the cathode, both occurrences that can lead to cell failure. The water and temperature management are thus key points for PEMFC operation. From the view point of system design and hardware, significant benefits can thus arise if the cell is operated without the presence of liquid water or in non-saturated conditions (above 100 °C and below 50% r.h.).[11,13] In addition, the kinetics at the electrode may be improved and the tolerance to CO is also higher (up to 1000 ppm at 130 ˚C), enabling the use of less pure, less expensive H_2 as fuel.[13,18]

1.3.1.1 Morphology and structure

To understand the transport mechanism of water and proton inside PFSA membranes, it is important to understand its morphology. It is widely known that Nafion® shows a nanoscale separation derived from the presence of hydrophobic and hydrophilic counterparts. The distribution of these two phases, within the matrix of the membrane, has been the subject for many debates. Furthermore, the hydration (and resulting morphological changes due to swelling), the processing conditions (whether if the membrane was extruded from melt or casted from a dispersion), the thermal and water sorption history, the random chemical structure of the copolymer and the low degree of crystallinity make the task of describing the Nafion® morphology very difficult. Some of the most relevant models are briefly presented hereafter.

Gierke and Hsu proposed the first attempt to correlate structural information with transport properties, depicted in Fig. 1.4.[23] After analysing small-angle X-ray

scattering (SAXS) and wide-angle X-ray diffraction (WAXD) data, obtained at different hydration and temperature conditions, they proposed a "cluster-network model" that describes the polymer as an inverted-micelle structure where spherical clusters made of the hydrophilic part of the membrane are separated from the hydrophobic backbone.

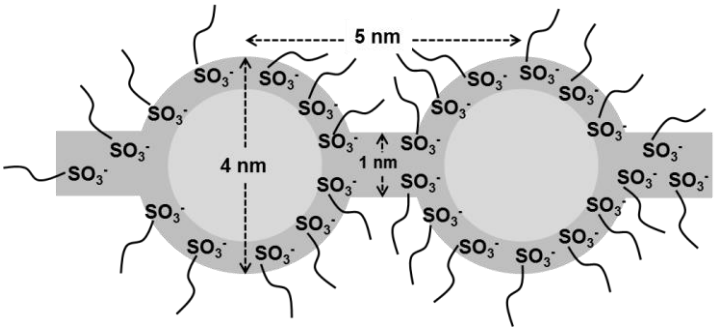

Figure 1.4. Schematic representation of the cluster-network model for Nafion® in the hydrated state. Adapted from[20].

These clusters are connected by short and narrow channels and tend to increase in size with increasing water content (4 nm cluster connected by 1 nm thick channel), containing up to 70 SO_3H groups and, thus, approximately 1000 water molecules per cluster.[18,20,23] These authors also proposed a percolation theory to explain the increase of conductivity with increasing water content. This theory states that there is a critical amount of water below which the protonic conductivity is abruptly diminished. This minimum water content, or percolation threshold, ensures the presence of an extended water layer where protons may flow. Near to the threshold value, the conductivity (σ) of the membrane can be expressed by a typical percolation equation:

$$\sigma = \sigma_0(c - c_0)^b \qquad \text{eq. 1.7}$$

where "σ_0" is a pre-factor related to molecular interactions, "c" is the volume fraction of the aqueous phase, "c_0" is the percolation threshold and "b" is a universal constant depending on the dimensions of the system. Further work on the percolation theory performed by Okada *et al.*[24] showed that half of the water inside the membrane is bounded to SO_3H groups, forming the first hydration layer, while the rest of it experiences some degree of freedom inside the pore, forming several other hydration layers.

Although the cluster-network model was widely accepted, it was regarded as too basic since it assumed a periodic distribution of the clusters. Several structures with various geometrical and spatial assumptions as how the clusters are distributed have been proposed since. For example, a lamellar model was proposed by Litt,[25] where hydrophobic sheets are separated by the hydrophilic domains. A similar model based on a sandwich-like structure was suggested by Haubold *et al.*[26] These models are only focused on the basic structure of Nafion®, lacking a description of the extended structure. Studies by SAXS and small-angle neutron scattering (SANS) have provided the basis for morphological models that cover the length scale up to 1 μm. For example, a study proposed that the microstructure of Nafion® is composed by elongated structures of polymer aggregates with 4 nm diameter and up to 100 nm in length, packed into oriented bundles, randomly dispersed in the mesoscale range.[27]

A widely accepted representation of the microstructure of Nafion® was given by Kreuer *et al.*[28], as shown in Fig. 1.5. According to this model, the covalent bonds between the hydrophilic sulfonic acid groups and the hydrophobic backbone lead to the creation of hydrophilic/hydrophobic aggregates with a nano-separation of ~0.8 nm in average. The hydrophilic domains are well connected, even at low humidity levels, which ensures the absence of pockets or dead-ends and a very good percolation. The existence of side-chains in Nafion® represents another transition region between the aqueous domain and the hydrophobic backbone. SAXS studies by Haubold *et al.*[26] suggest that this region swells at the expense of the purely aqueous regions as the λ increases. The thickness of the water channels or pores inside Nafion® is highly affected by the quantity of water inside the membrane (swelling).

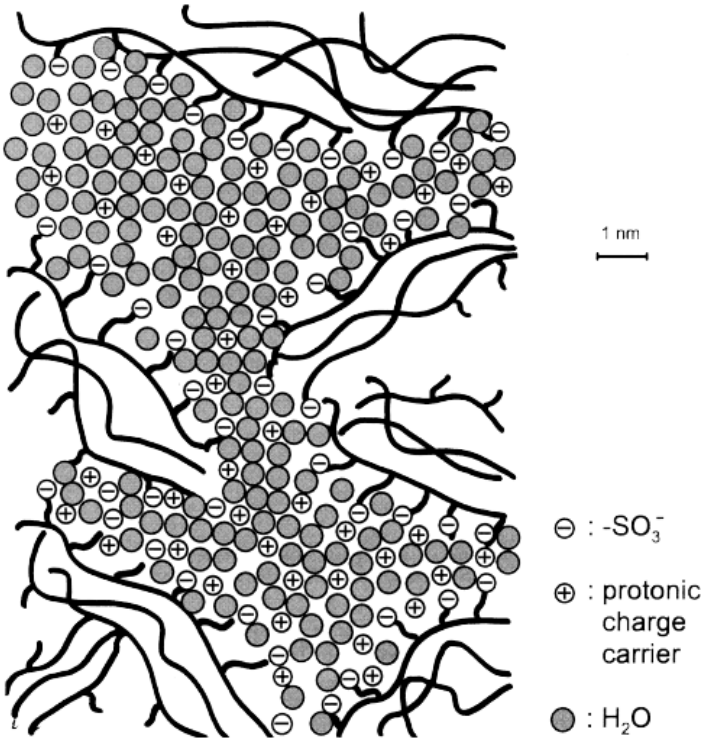

Figure 1.5. Scheme of the microstructure of Nafion® for intermediate water content. Adapted from[28].

It has been subsequently suggested that the models discussed above do not fit the obtained SAXS data. Figure 1.6 depicts the alternative structural model presented by Schmidt-Rohr and Chen,[29] where the structure of hydrated Nafion® is represented by parallel rod-like water channels (diameter between 1.8 and 3.5 nm) and length of approximately 20 nm (Fig 1.6 A and B). The cylindrically shaped inverted micelles, aligned with hydrophilic groups are supported by the PTFE backbone. The larger water channel diameter explains more suitably the high water diffusion coefficient of Nafion® and also the electro-osmotic drag of water inside the membrane. Additionally, this model incorporates 10 vol. % crystallites that lie parallel to the water channels (Fig. 1.6 C). Using a newly developed algorithm that simulates SAXS measurements based on the model, these authors apparently matched previously published SAXS pattern of Nafion®.[30] This model is quite suitable for hydrated Nafion®, however, it is not clear if it can represent also the dry or scantily hydrated membrane.[31]

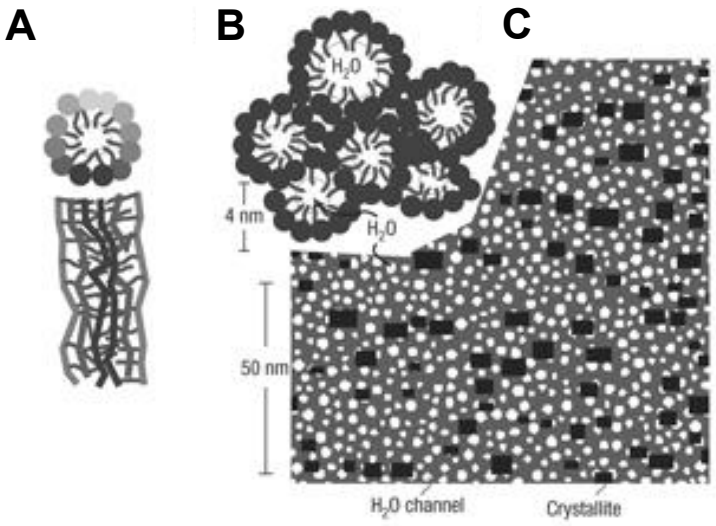

Figure 1.6. Scheme of Nafion® morphology according to the parallel water-channel model: A) transversal and cross section view of an inverted micelle cylinder; B) Parallel packing of inverted micelles cylinders; C) Cross section of the membrane showing the water channels in white, the crystallite in black and the amorphous Nafion® matrix in grey.

A recent paper by Kreuer and Portale[32] focuses on checking the consistency of the parallel cylinder model for membranes with variable levels of hydration. According to these authors, the Schmidt-Rohr and Chen's algorithm[29] is most certainly biased due to a large uncertainty concerning the measured water content in the membrane. The data interpretation by Kreuer and Portale[32] suggests a flat morphology for the pores, as opposed to cylinders. The thin films of water formed at the surface of the pores may act as electrostatic "glue", forcing the approximation of the oppositely charged polymeric structures. The formation of cylindrically shaped pores, with negative charge at the surface and positive charges inside, would correspond to a significant separation of the charges and huge accumulation of positive charge in the structure. The partial collapse of the cylinder into a flatter shape would be more energetically favourable as long as the separated charges are not totally immersed in water.

In a companion paper, Kreuer[33] discusses the role of internal pressure as an additional thermodynamic degree of freedom (to the r.h. and temperature) in the hydration and transport properties of Nafion®. In the low r.h. conditions (Fig. 1.7 A), the presence of hydrophilic sulfonic acid groups in a superficial "open" microstructure

may allow the entrance of hydration water (represented by arrows). As the hydration increases (Fig. 1.7 B), the membrane softens and the internal pressure builds up while the outermost polymer chains organize in a closed hydrophobic layer (dotted region in Fig. 1.7 B) with much lower ability to permeate water.

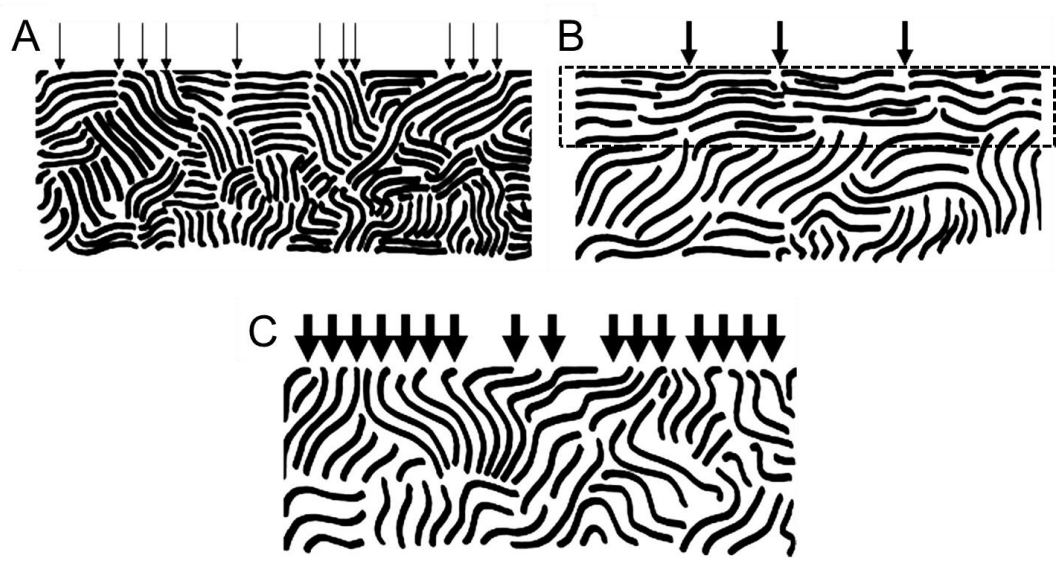

Figure 1.7. Schematic representation of the anisotropic dry "skin" formation in Nafion®. A) at low r.h., B) as the hydration level increases the anisotropic "skin" tends to form (dotted region) and C) the internal pressure is released when the surface "skin" is opened by contact with liquid water. Adapted from[33].

This very low concentration of hydrophilic defects reduces drastically the ability of the membrane to uptake more water below the dew point. However, direct contact with liquid water (Fig. 1.7 C) may open the skin, releasing the internal pressure and allowing the contact between the external water and the water inside the membrane. This might explain the higher λ of Nafion® observed when the material is in contact with liquid water in comparison to when it is exposed to a saturated water vapour atmosphere, as discussed earlier. This puzzling effect actually occurs in many other polymers and is known as the Schroeder's paradox.[34]

1.3.1.2 Proton transport mechanisms and the role of water

There are several mechanism by which protons can migrate from the anode to the cathode inside PFSA membrane and they all depend on the level of hydration. Protons can be transported *via*: i) surface diffusion along the functional groups (itself of structural diffusion type), ii) Grotthus mechanism (structural diffusion *via* water molecules) and iii) vehicular mechanism or the molecular diffusion of hydronium ions.

The first mechanism, depicted in Fig. 1.8 can occur for very low humidity levels, where the water molecules are preferably located around the perfluoroether side-chains, strongly bounded to the charged SO_3^- sites, creating a non-freezable or surface water layer.[35] The proton needs to transfer through the void space to an adjacent charged site. Although some authors state that the distance between the acid sites in Nafion® is too high for a direct transfer (~7 to 12 Å) ,[36] other authors state that the perfluoroether side-chain can be flexible and vibrate enough in the void to shorten this distance, effectively allowing the direct transfer between adjacent charged sites.[37]

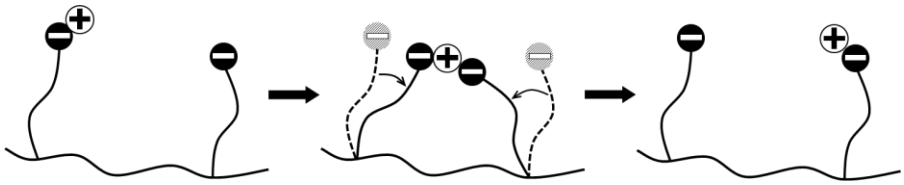

Figure 1.8. Scheme of the proton transport between adjacent charged sites in Nafion®. Adapted from[37].

It is well known that the high values of proton mobility inside PEM structures are highly dependent on the presence of water. Therefore, it is sensible to continue the discussion of the proton transport in PEM by first discussing the transport phenomena in bulk water. The mobility of protons in water is unusually high when compared to other cations such as Li^+ or K^+. The only way to explain this huge difference is by assuming a proton transport mechanism that involves the hydrogen-bond pattern of water, that is, a structural diffusion of water. The excess charged region (proton defect) could be described as a hydrated H_3O^+ in the form a $H_9O_4^+$ (Eigen) ion or by a smaller $H_5O_2^+$ (Zundel) ion.[38] Molecular dynamics simulations (MD) performed by

Tuckerman *et al.*[39,40] and nuclear magnetic resonance (NMR) data provided by Agmon[41] individually proposed a mechanism that addresses the issue of proton excess diffusion in water, as depicted in Fig. 1.9. An initial hydronium ion (H_3O^+) forms an Eigen-ion ($H_9O_4^+$) by bonding with three water molecules in its proximity. When the excess proton transfers to a place between two adjacent water molecules it forms a Zundel-ion ($H_5O_2^+$) and, afterwards, another Eigen-ion can be formed, and so on. This proton exchange by rapidly breaking and forming hydrogen bonds in between Eigen and Zundel-ions ultimately corresponds to the net displacement of one unit charge, which is known as the Grotthus proton hopping mechanism.[41,42]

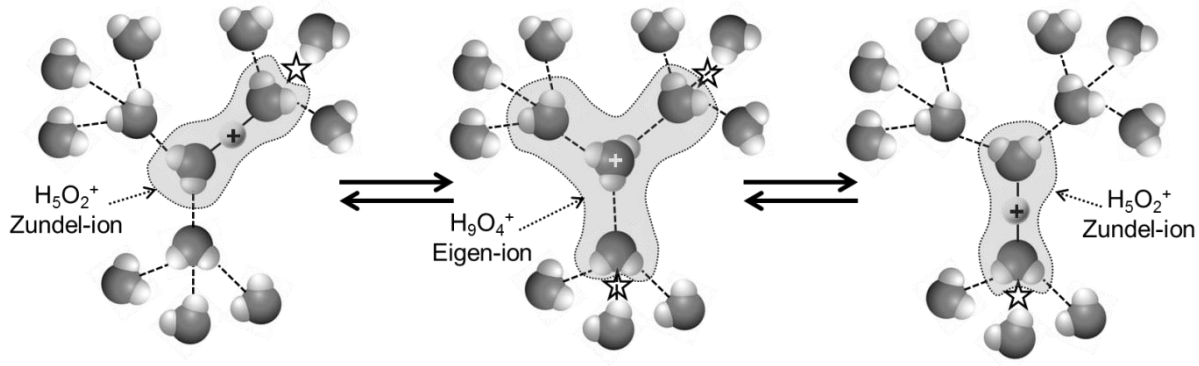

Figure 1.9. Schematic representation of the Grotthuss proton hopping mechanism. Star symbols represent the forming and breaking of hydrogen bonds. Adapted from[37].

There is also a strong correlation between the abnormal proton transport rate and the dielectric relaxation time in water, which can be explained by the dominance of the hydrogen-bond breaking and forming on the global proton transport process.[43]

This mechanism can describe the high mobility of proton in water but water is also a liquid with a high self-diffusion coefficient (2.25×10^{-5} $cm^2 \cdot s^{-1}$ at room temperature). The diffusion of charged water ions (hydronium or protonated water complexes), by "hitching a ride" in moveable water molecules, may contribute to the overall conductivity in bulk water.[44] This so-called vehicle mechanism may represent up to 20% of the total mobility.[45]

Figure 1.10 is a schematic representation of the diffusion of H_3O^+ in bulk water by the vehicle mechanism.

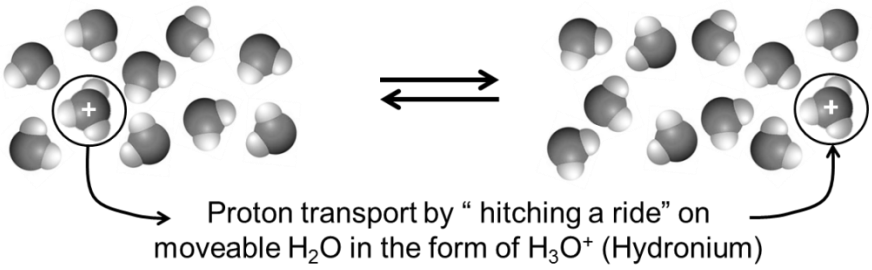

Figure 1.10. Schematic representation of the proton conduction by vehicular mechanism. Adapted from[37].

The coexistence of the various mechanisms is very likely and it is a difficult task to separate their individual contributions to the overall conductivity. Comprehensibly, both mechanisms are dependent on temperature, pressure and on which and how much ions are involved in the process.

Applying these observation to the protonic conductivity in well hydrated acidic polymer membranes, such as Nafion®, one can assume that the structural diffusion is the only mechanism that can explain the high levels of conductivity measured in these materials.[38] In order to have efficient water structural diffusion inside Nafion®, a continuous layer of water must exist between the hydrophilic clusters to successfully transport the protons from the anode to cathode. The discussion around which λ value satisfies the percolation of water inside Nafion® membrane is not consensual.[37,38]

The complex morphology of the polymers associated to the hydrophilic/hydrophobic domain separation and its strong dependence on the hydration provides a variety of configurations where the proton mobility may be significantly different. The nanosized hydrophilic clusters in hydrated Nafion® can adsorb a great amount of water that, besides promoting the solvation of the sulfonic acid groups, provides additional proton diffusion paths with higher mobility, as protons become weakly bounded to the SO_3^- counter-ion. These hydrated clusters can be regarded as dilute acids, where the SO_3^- groups play the role of proton exchange sites.[37]

Several studies were dedicated to understand the distribution and interaction of water in PFSA membranes. Infrared spectroscopy (IR) measurements of Nafion® membrane under increasingly humid atmosphere showed that water clusters start to form inside the membrane for $\lambda > 3$, followed by the aggregation into larger clusters up to $\lambda < 6$ and eventually forming continuous water layers by coalescence of the

clusters beyond this λ value.[46] In a more recent paper by Lu *et al.*,[47] dielectric relaxation spectroscopy was used to study the state of water inside Nafion® as a function of λ. They confirmed the presence of three different water states with distinct dynamics. The study showed the formation of percolated water film between hydrophilic clusters when λ = 9, evidenced by a drastic change of the dielectric constant of the membrane. A quasi-elastic neutron scattering (QENS) study by Pivovar and Pivovar[48] showed two different hydration regimes with turning point at around λ = 7. They found that the fraction of non-diffusing protons rapidly decreased from 0.85 at λ = 1 to 0.20 at λ = 6, reaching a limit of 0.12 for higher λ. These observations were in agreement with the increase of protonic conductivity with increasing water content previously observed.[46,49]. Another QENS study showed a higher value for the fraction of non-diffusing protons (0.5 at λ = 6), which may be due to differences in energy resolution.[50] Perrin *et al.*[51] also used QENS to study the molecular proton motion in Nafion® with λ varying from 3 to 17.5 and found two different proton carriers for time scales of 160-500 ps and 2-8 ps, which are ascribed to slow protons closely bond to the SO_3^- groups, and faster protonic species diffusing in hydration layers away from the acid-functionalized pore surface, where long range diffusion takes place. Eikerling *et al.*[52] performed a simulation study of the protonic conductivity in the pores of a PEM as a function of the hydration and associated dimensional changes (swelling or shrinking).

Figure 1.11A represents the model pore used to calculate the electrostatic contributions to the activation Gibbs energy for the proton migration as a function of several microstructural parameters, notably the pore diameter (L) or the distance between the sulfonic acid groups (l). The model distinguishes two different layers of hydration in the pores: a first monolayer tightly bonded to the pore surface containing the sulfonic acid groups, and the subsequent hydration layers towards the centre of the pore, which behave like bulk water. The equilibrium between the surface and bulk contribution is determined by the distance between the SO_3^- groups and the pore size.

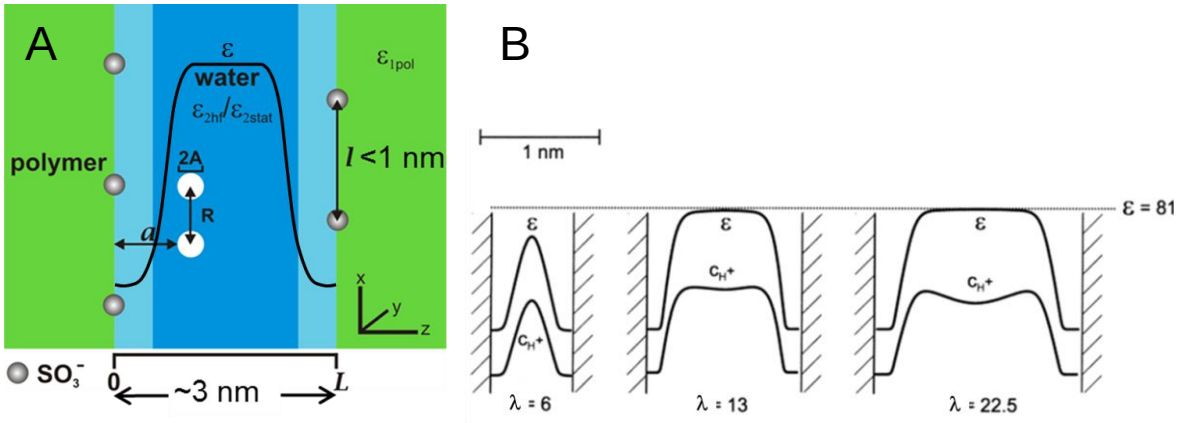

Figure 1.11. A) Representation of a single pore of a PEM used in simulation studies performed by Eikerling *et al.*[52] and B) of the pore size and relative permittivity distribution inside Nafion® as a function of the hydration level.[38]

When the membrane is in a dry state, the presence of a considerable fraction of small pores ($L \leq 10$ Å) with relatively large distance between the SO_3^- sites ($l \geq 15$ Å), gives rise to high values of activation Gibbs energy, affecting negatively the overall conductivity. When the average water content increases, the pore diameter increases due to swelling and the contribution of the proton transport through the bulk-like water is gradually increased.[52]

Simulations of the relative permittivity (ε) distribution within the pore as a function of λ provide a similar picture, as schematized in Fig. 1.11 B.[38,52] In the centre of the pore with $\lambda > 10$, ε approaches the value for liquid water (81), but it is drastically reduced near the surface due to the strong electrostatic interaction with the sulfonic acid groups. The decrease of the pore size for lower λ values leads to the confinement of the water molecules to the pore surface, where it is subjected to the strong influence of the acid groups; consequently the dielectric constant is lowered even at the centre of the pore.[38,52] For $\lambda > 14$, when the material can be seen as a two-phase mixture of free water and the electrostatically bounded polymer/water system, there is a dilution of the charge carrier at the centre of the pore. The high ε stabilizes the proton charge carriers located at the centre of the pores because the solvation energy of protons becomes more negative.

Paddison *et al.*[53] calculated the proton self-diffusion coefficients in Nafion® over a range of hydration levels. They found that the proton carrier H_3O^+ and the diffusion of

water are retarded by the confinement produced by the presence of a substantial density of sulfonate groups. With the same calculation method they also showed that the diffusion of proton for $\lambda > 13$ accounts with the contribution of a structural mechanism.[54,55]

All things considered, the role and state of water on the protonic conductivity in Nafion® are very complex subjects and still motives of debate. However one can surely say that for high water content, the main transport mechanism is surely the structural diffusion.[38] When the water content decreases, the excess proton concentration increases in the aqueous phase, leading to a decreasing intermolecular proton transfer, ultimately affecting the structural diffusion. This was analogously observed in aqueous solution.[56] Consequently, at intermediate and lower levels of hydration the protonic conductivity must rely mainly on the vehicle mechanism.

1.3.2 Other perfluorinated membranes

Many other perfluorinated membranes were developed by manufacturers such as Asahi Glass Co. Ltd (Flemion®), Asahi Chemical Co. Ltd. (Aciplex®), 3M Inc., Dow Chemical and Solvay Solexis (Aquivion® and Hyflon®). In comparison with Nafion®, these perfluorinated membranes possess shorter side-chains and lower EW. The lowering of EW might enhance the acid group concentration and therefore the protonic conductivity of these membranes tends to be slightly higher than Nafion®. However, the short-side-chain (SSC) PFSA membranes normally present lower mechanical integrity and durability due to increased swelling upon water uptake.[13] Nevertheless, the SSC membranes show higher crystallinity at certain EW and elevated T_g, which allow higher working temperatures.

Kreuer *et al.*[57] characterized a PFSA membrane from Dow (EW of 858 with and 1084 with thicknesses of 80 and 90 μm respectively) comparing water sorption and diffusion, electro-osmotic drag effect, protonic conductivity, microstructure and visco-elastic behaviour with Nafion® 117. At high λ (higher than 15) the water diffusion is similar in all membranes but as it decreases, the water diffusion decrease is more significant in the Dow membrane than Nafion® 117. Nevertheless, at $\lambda > 10$, the Dow

membrane, with lower EW than Nafion® 117, shows an enhanced conductivity by a factor of 0.4, with similar methanol crossover and electro-osmotic drag. The high ion exchange capacity brought by the high protogenic group concentration may explain this observation. However, the different thicknesses of the membrane used in this study may also explain the change in the performance of the membranes. Du *et al.*,[58] actually suggested that the properties of Nafion® are significantly increased as the membrane thickness is decreased.

Merlo *et al.*[59] tested the fuel cell performance of a 25 cm^2 MEA using Aquivion® as PEM at 75 °C and 120 °C, obtaining a voltage of 0.75 V at current density of 0.8 $A \cdot cm^{-2}$. They found a lower H_2 crossover than Nafion® 112 and superior protonic conductivity in very cold conditions (-40 °C), which is necessary for cold start. Recently, Arico *et al.*[60] also tested the Aquivion® membrane in fuel cell environment, confirming a better conductivity, water retention and mechanical stiffness above 100 °C, when compared to Nafion®. They also showed that this membrane is more suitable for fast start-up in cold conditions.

1.3.3 Aromatic backbone membranes

The non-fluorinated PEM materials are normally composed of aromatic hydrocarbons. They are capable alternatives to Nafion®, offering simple processability, easy chemical tuning, mechanical and chemical stability and lower production cost. Figure 1.12 represents the most widely studied aromatic backbone PEM that include poly (ether ketone) (PEK with one or more ether (E) and ketone (K) functionalities), poly (ether sulfone) (PES) and poly (benzimidazole) (PBI).[13,18,19]

In a comparative SAXS study of Nafion® and a sulfonated PEEKK membrane, Kreuer *et al.*[28] suggested that the later shows narrower diffusion pathways that could reduce the electro-osmotic drag and water permeation.

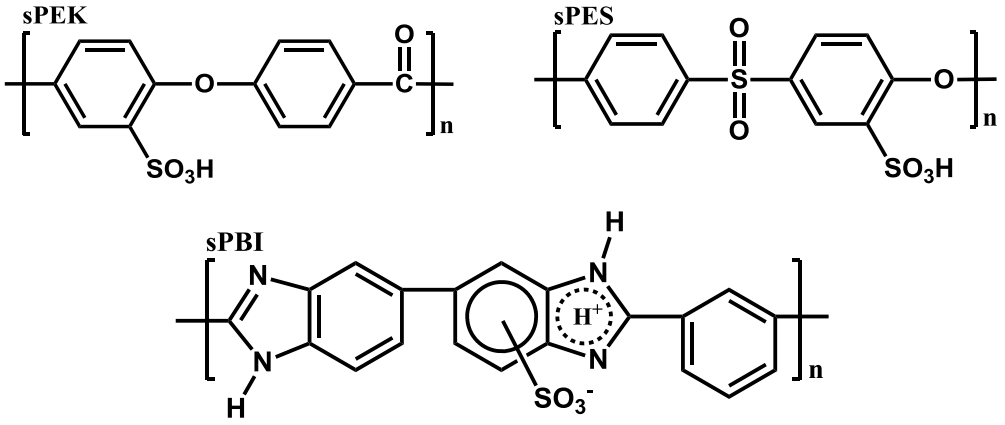

Figure 1.12. Molecular structures of popular non-fluorinated PEM materials. The lower-case "s" stands for sulfonated.[19]

However, the less connected hydrophilic clusters and the larger separation between protogenic groups lead to a steeper decrease of protonic conductivity with decreasing λ. By blending SPEEKK with other polymer (PES or PBI) they managed to overcome some of these drawbacks. Although non-fluorinated PEM materials are prospected to be valuable alternatives to PFSA membranes in PEMFC, mainly due to lower water/methanol crossover and cost, this type of polymeric membranes still suffer from a high swelling behaviour with increasing water level, which is detrimental to the electrode/electrolyte interface in a fuel-cell environment and show lower durability.[14]

Polymer blending has been used as a versatile way to tune the desired properties of aromatic backbone PEMs. The favouring of specific interactions between the different polymers (ionic interaction, hydrogen bonding or ion-dipole interactions) enhances the miscibility and cross-linking of the blend, leading to a better control of the swelling behaviour, without decreasing the flexibility of the membrane.[19] The use of multiblock copolymers as substitute for PFSA membranes, with their specific sequential chain arrangements and control of the hydrophilic/hydrophobic microdomain size and orientation, have shown positive results in terms of improved conductivity, when compared to the random copolymer equivalents. By cross-linking the non-ionic block microdomain in ion-containing block copolymer it is possible to improve the proton and methanol selectivity to the highest values reported for sulfonated polymer membranes.[61]

Einsla *et al.*[62] compared the electrochemical properties of an alternating sulfonated poly(arylene ether ketone) (Ph-PEEKDK), a random sulfonated poly(arylene ether sulfone) (BPSH-35) and a multiblock copolymer made of hydrophobic polyimide block and a hydrophilic poly(arylene ether sulfone) (BPSH-15-PI-15). The multiblock copolymer showed the best performance under fuel cell testing at 100 °C and 40% relative humidity (r.h.), yielding similar results to Nafion®.

In a more recent study, Meyer *et al.*[63] studied a family of fully sulfonated hydrophilic poly (phenylene sulfone) and hydrophobic poly (phenylene ether sulfone) segments. They obtained materials with $[H^+]$ values ranging from 1.2 to 1.7 $mmol \cdot g^{-1}$ and a distinct phase separation with correlation lengths of ~15 nm. This combination results in high conductivity values with increased visco-elastic properties, especially at higher temperatures. The well separated microstructure of the multiblock copolymers allow a superior proton transport and stability of the hydrophilic constituent and the morphological stability of the hydrophobic phase, showing a great potential to be used in high temperature PEMFC. Nevertheless, the other state-of-the-art components of the fuel cell, namely the electrodes, would have to be adjusted to cope with the different chemical nature and the significantly lower hydrodynamic transport properties.

1.3.4 Anhydrous membranes

Another approach investigated for the development of high temperature PEMFC involves the replacement of water by a proton solvent liquid with high boiling point, on a polymeric matrix with high thermo-chemical resistance. In one of the earlier reported examples, Bouchet and Siebert[64] compared the conductivity of PBI membranes doped with H_3PO_4, H_2SO_4 and HBr . They found that both H_3PO_4 and H_2SO_4 act as proton solvent in PBI membrane, which provides the necessary mechanical stability. These membranes showed protonic conductivities of 10^{-4} $S \cdot cm^{-1}$ and 7×10^{-6} $S \cdot cm^{-1}$, in dry state and at 30 ºC, for (PBI - 3.25 H_2SO_4) and (PBI - 3.05 H_3PO_4), respectively. Figure 1.13 depicts the suggested hopping mechanism for proton transport in these acid functionalized membranes.

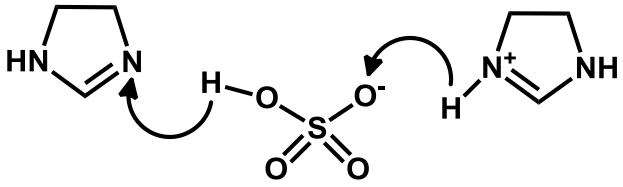

Figure 1.13. Proton hopping mechanism for acid doped PBI membranes.Adapted from[64].

Since the first studies on this type of composite membrane, extensive research in the polymer synthesis, casting of the membranes, characterization and fuel cell application have been made. For example, the use of ionic and covalent cross-linking or inorganic–organic composites development was extensively reported.[65]

So far, the acid-doped PBI membranes are the most successful membranes for application in HT-PEMFC, up to 200 ºC, preferably under atmospheric pressure. However, there are important drawbacks that are still to address such as the difficult processing, the need for high acid load ($[H^+]$) to have decent conductivity values (which can ultimately affect the chemical stability of the other fuel cell components), the leaching of the acid at high temperature, the low conductivity values at low temperatures (important for cold-start) and the slow oxygen reduction kinetics (caused by the strong surface adsorption of acid anions and low solubility of oxygen).[14,65]

Ünsal and Kiefer developed a PEM based on a PBI matrix where polyvinylphosphonic acid (PVPA) is used as the polyelectrolyte, immobilized in the matrix by interpenetration, cross-linking and covalent bonding, which led to the development of the commercial PEM Celtec-V.[66,67] The new improved structure of this membrane prevents the leaching of the electrolyte when in contact with liquid, which is especially desirable for the application in DMFC. The fuel-cell performance of these PBI-based membranes can be sustained to a higher methanol flow with half the methanol cross-over, in comparison to Nafion® 117. However, the ohmic resistance and the cathode/PEM interface (where higher losses are observed with increasing current density) could still be improved.

The patent was bought by BASF® which further developed the material delivering a series of MEAs based on this PBI-H_3PO_4 membrane under the commercial family name Celtec-P®. For the membrane Celtec P-1000® a study performed by Boaventura and Mendes[68] showed conductivity values of 5.6×10^{-2} $S\cdot cm^{-1}$ at 160 ºC and 5% r.h.

Another commercial option available is based on a pyridine containing PES impregnated with H_3PO_4 with the commercial name Advent®.[69] The authors claim that this copolymer, easily processed and with high thermal stability (400 ºC), shows a conductivity of 0.01 $S \cdot cm^{-1}$ at temperature higher than 130 ºC.

More recently, Weber *et al.*[70] studied the protonic conductivity of H_3PO_4 impregnated mesoporous crosslinked PBI structures. The mesoporous PBI was synthesised by a solvent-mediated hard-templating method which yielded PBI networks with defined pores of ~10 nm and S_{BET} up to 190 $m^2 \cdot g^{-1}$.[71] They observed that the protonic conductivity of these acid filled mesoporous PBI membranes showed an important improvement up to ~10^{-2} $S \cdot cm^{-1}$ at 180 °C. The optimal microstructure was found in PBI membrane with 10 - 20 % mol in cross-linker, which corresponds to a suficiently stabilized microstructure with connectivity between the pores.

In the quest for anhydrous PEM, protic ionic liquids (PIL) were also incorporated in polymer matrices. These molten salts mixtures, which usually show low melting point, allow the transfer of proton from a Brønsted acid to a Brønsted base.[72] One of the many studies published was performed by Watanabe's group[73] in which they used sulfonated polyimides as matrices for the incorporation of PIL diethylmethylammonium trifluoromethanesulfonate. For a content higher than 67 % of the protic ionic liquid, the conductivity was in the order of 10^{-2} $S \cdot cm^{-1}$, at 160 ºC and anhydrous conditions.

Solid acids have also been proposed to raise the working temperatures of PEMFC. Many of these crystalline materials are also denominated as "superprotonic conductors" because they normally undergo a phase transition that is translated as a drastic rising of protonic conductivity of about 2-3 orders of magnitude, reaching values of up to 0.1 $S \cdot cm^{-1}$.[19] These non-polymeric membranes could work at temperatures between 100 and 300 °C.[13,19]

The most widely studied solid acid for the application in fuel cell is probably $CsHSO_4$. Early work by Haile *et al.*[74] evaluated the viability of this solid acid for electrolyte material in PEMFC. The super-protonic phase of this material is situated above 140 °C with protonic conductivity of ~10^{-2} $S \cdot cm^{-1}$. In a posterior study, membranes of CsH_2PO_4 solid acid showed a conductivity of 0.022 $S \cdot cm^{-1}$ at 240 °C with the super-protonic transition occurring at 230 ºC.[75] This particular material undergoes a

transition from monoclinic (space group $P\,2_1/m$) at room temperature to cubic (CsCl-like of space group $Pm\text{-}\bar{3}m$) superprotonic phase at 230 ºC. The proton conduction in oxyanion solid acids is not related to the migration of hydronium ions, which is why these materials are, in principle, independent from the presence of water. The transition to super-protonic phase normally implies changes to the network of hydrogen bonds that connect the oxyanion groups, forming dimers, chains, layers or three-dimensional structures. The dramatic increase in protonic conductivity is then caused by a dynamic disordering of the hydrogen bond network.[76]
Some models have been suggested to explain the protonic conductivity in this type of materials, but much work is needed still to fully understand the underlying mechanisms and the membrane degradation at elevated temperatures.

1.4 Periodic Mesoporous Silicas (PMS) and Organosilicas (PMO)

1.4.1 Synthesis

Si-based materials with mesoporous structure (IUPAC classifies a material as mesoporous whenever the pore size ranges between 2-50 nm[77]) have been widely studied, mainly for their potential of application in catalysis, adsorption, gas chromatography, sensors and hydrogen storage.[78,79] The synthesis of periodic mesoporous silicas (PMS) using a template was firstly presented by Kresge, Beck and co-workers in 1992.[80,81] The MCM-41, a member of the so-called M41S family developed at Mobil Co. (MCM stands for Mobil Composition of Matter), was obtained using alkyl trimethylammonium bromide surfactant with a 16 carbon alkyl chain (C16) as structure directing agent (SDA), and tetraethylorthosilicate (TEOS) as the silica precursor. This material has a particular highly ordered hexagonal array of pores (space group *P6mm*) with very high S_{BET} (> 700 $m^2 \cdot g^{-1}$), whereas the silica pore walls are amorphous. The pore size distribution is narrow, with the average pore sizes varying from 2 to 10 nm, depending on the surfactant used.
The assembly of this type of materials can occur by two different mechanisms. In the true liquid-crystal template mechanism, the SDA molecules are self-organized in

micelles above a certain critical micelle concentration (Fig. 1.14 A). Spherical micelles start to elongate, forming rod-like structures in a lyotropic phase, which is a liquid crystal-like structure with various possible structural arrangements (hexagonal liquid-crystal, cubic or lamellar liquid-crystal) depending on the concentration, temperature and pH, without requiring the presence of precursor framework materials.[78]
Alternatively, the liquid-crystalline phase may be formed at lower SDA concentration in the presence of inorganic framework precursors in a cooperative self-assembly process (Fig. 1.14 B).[78]

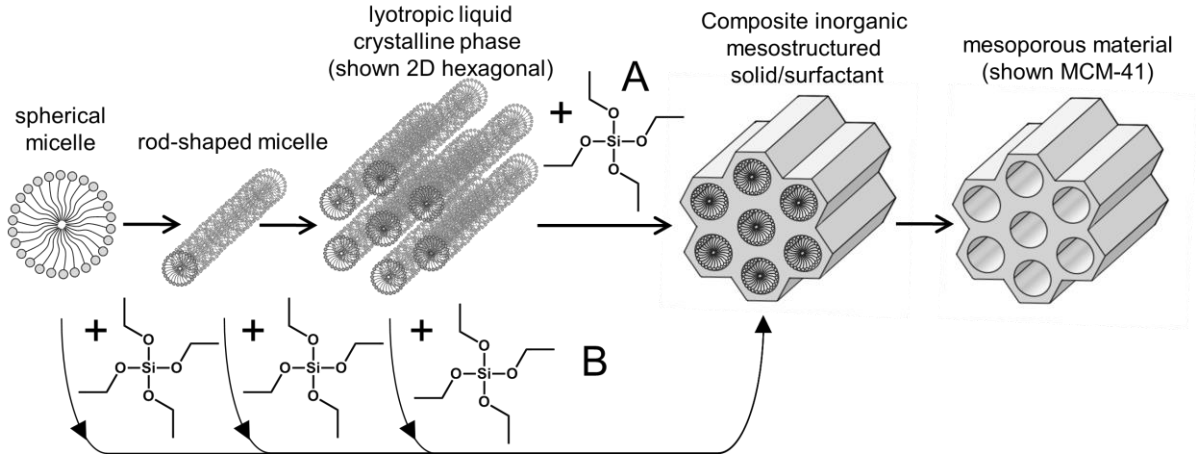

Figure 1.14. Representation of the A) true liquid-crystal template mechanism and B) cooperative self-assembly mechanism for the formation of mesoporous silica materials. Adapted from[78].

In 1998, a new family of materials called SBA (from University of Santa Barbara) was prepared using tri-block copolymers as SDA.[82,83]
These materials show increased pore size compared to M41S materials (up to 30 nm) and thicker pore walls (up to 6 nm). SBA-15, the best known member of this family, is synthesised using tri-block copolymer poly(ethylene glycol)-block-poly(propylene glycol)-block-poly(ethylene glycol) - $EO_{20}PO_{70}EO_{20}$ (Pluronic® P123) and it is characterized by an hexagonal array of pores (space group *P6mm*), with the presence of interconnecting micropores between the main hexagonally-spaced pores.
After the synthesis of the first mesoporous silicas, much attention was given to the incorporation of organic functionalities providing useful properties to PMS. This was primarily achieved by grafting or co-condensing organosiloxilane groups as R'-$Si(OR)_3$ (R' is the organic functional group) inside the pore wall. However, the homogeneity of

the distribution and the conservation of the mesostructure integrity upon the organic loading were fairly poor.[78] This has been finally demonstrated for the incorporation of ethane organic moiety in the framework of the pore wall via hydrolysis and condensation of the bridged organosilane precursor 1,2-bis(trimethoxysilyl)ethane as $(OEt_3)Si\text{-}CH_2\text{-}CH_2\text{-}Si(OEt)_3$, giving rise to the PMO family.[84-86] The integration of the organic moiety in the walls of the mesoporous materials through bridged bissilylated precursors allows higher organic loadings, homogeneously distributed along the material walls. PMO materials are characterised by narrow distribution of pore sizes, high stability and a greater flexibility in framework composition and morphology.[78,87]

Several bridged organosilane molecules were then used to form PMO.[78,88] In an effort to enhance their functionality, Inagaki *et al.*[89] studied the incorporation of benzene as bridging organic moiety of the organosilane (1,4-bis(triethoxysilyl)-benzene, BTEB), which led to the formation of a phenylene PMO (Ph-PMO). This new material showed a hierarchical ordering, comprising the well-defined hexagonal array of pores in the nano-scale (lattice constant of 5.25 nm with mesopores of 3.8 nm in diameter) and also a molecular scale periodicity along the pore wall (spacing of 0.76 nm). The combination of the hydrophilic character brought by the silica layers, and hydrophobic behaviour from the benzene layers with high π-π electron conjugation on the ring, can explain the crystal-like wall structure of this PMO. Figure 1.15 shows TEM micrographs collected along directions parallel (Fig. 1.15 A) and perpendicular (Fig. 1.15 B) to the pore channels of the Ph-PMO and a 3D schematic representation of the particles microstructure (Fig. 1.15 C).

Bion *et al.*[90] synthesised Ph-PMO using different alkyl trimethylammonium halide surfactants from C14 to C18. This showed to be an effective way of tuning the pore size of the hybrid particles (3.2 to 3.9 nm in diameter) without losing the hexagonal array of pores and periodicity in the pore wall.

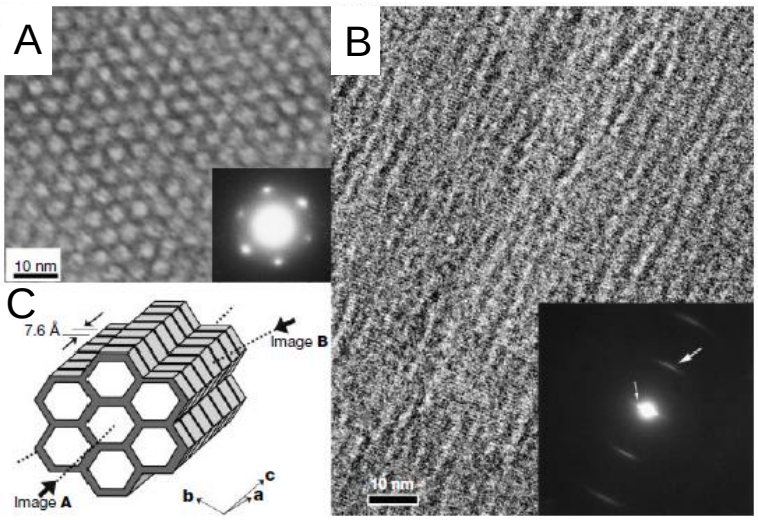

Figure 1.15. TEM images and diffraction patterns of the Ph-PMO in which it is possible to see: A) the hexagonal array of the pores; B) the molecular scale periodicity in the pore wall; and C is a schematic representation of the particle microstructure.[89]

1.4.2 Surface functionalization methods

The incorporation of functional groups into PMS or PMO can be achieved by two main routes (Fig. 1.16). The first is a post-synthetic method in which the inner surface of the already formed PMS or PMO pores are modified by the grafting of the functional groups.

The grafting has the advantage of retaining the mesoporous structure of the starting material, although it can reduce drastically the porosity due to pore blockage. Another potential disadvantage is the preferential grafting of the mouth of the pores, leading to heterogeneous distributions of the functional groups.[78,88] Nevertheless, the method is highly flexible since the organic moiety used (R'-Si$(OR)_3$) allows the functionalization with a variety of organic R' groups.

These include thiol (later oxidized to sulfonic acid),[89,91-97] carboxylic acid,[98,99] perfluorosulfonic acid,[100] and several nitrogen compounds (diamino, triamino, imidazole),[101-108] to cite a few. There are also several examples of grafting various types of inorganic acids, such as H_2SO_4, H_3PO_4, $HClO_4$, $CsHSO_4$ or heteropoly acids.[109-117]

Sharifi *et al.*[97] synthesized three different types of S-Ph-PMOs using the grafting method. The first S-Ph-PMO presented oxidized MPTMS groups anchored on the silica site, the second showed SO_3H groups anchored on the phenylene ring and a third sample showed a combination of both functionalization options. The $[H^+]$ of the samples were of 1.14, 1.42 and 1.61 $mmol \cdot g^{-1}$, respectively. In spite of the increase in $[H^+]$, the samples maintained its hexagonal array of pores and periodicity along the pore wall.

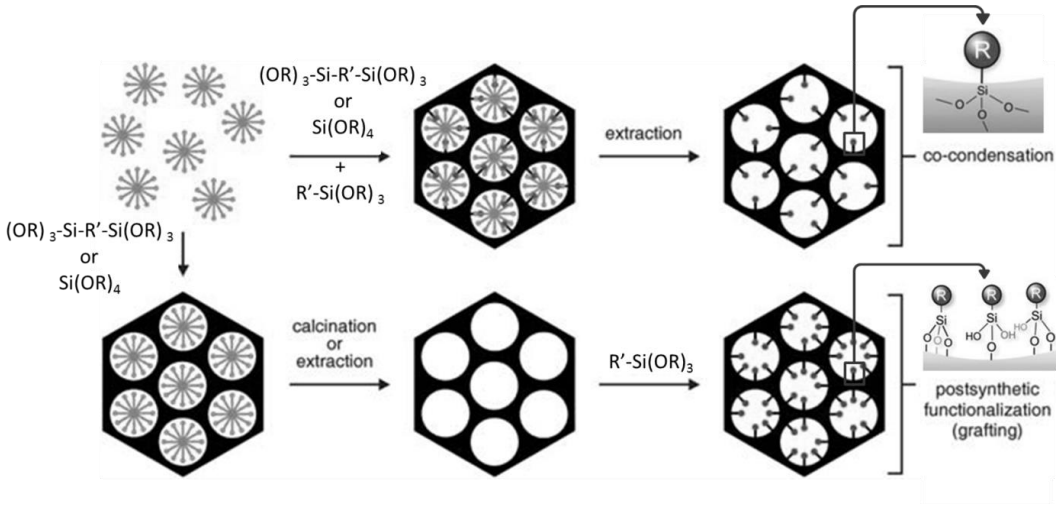

Figure 1.16. Scheme of the functionalization of PMS and PMO by co-condensation (top) and grafting (bottom). Adapted from[79] and[118].

The second method is the co-condensation by the simultaneous addition, to the SDA solution, of the silica framework precursor (or bridged organosilane) and of a trialkoxyorganosilane compound of the type R'-$Si(OR)_3$ containing the desired functional group (or its precursor), which will then be covalently bonded to the surface of the pore wall (Fig. 1.16).[78] The pore blocking in materials prepared by this one-pot synthetic approach is minimized in comparison to grafting. However, due to the simultaneous condensation of the framework units and functional groups, the mesoscopic order tends to decrease with increasing concentration of the functional group. The concentration of functional groups in the materials is dependent on the kinetics of hydrolysis and condensation of the different precursors. The SDA is usually removed by solvent extraction to prevent the destruction of the organic functionality.[78] Just like for the grafting method, a variety of functional groups such as alkyl,[119-122] amino and diamino,[123-126] thiol (subsequently oxidized to

sulfonic acid)[127-135] or phosphonic acid[136-139], have been incorporated in PMO and PMS materials by co-condensation.

Inagaki *et al.*[89] studied the incorporation of sulfonic acid groups inside the pore wall of Ph-PMO (referred to as S-Ph-PMO), adopting two different synthetic routes (Figure 1.17). Using the post-synthetic grafting method, the sulfonic acid groups were added to the phenylene groups of the already synthesised Ph-PMO particles by using fuming sulphuric acid at 110 °C. Both the hexagonal array of pores and the molecular scale periodicity were retained. The $[H^+]$ was of 0.4 $mmol \cdot g^{-1}$, which corresponds to the sulfonation of ~10 % of the phenylene groups inside the pore walls. The alternative material was prepared by the hydrothermal co-condensation of BTEB and 3-mercaptopropyl-trimethoxysilane (MPTMS) in a cationic surfactant template basic medium, followed by surfactant extraction in acidic media and oxidation of the thiol group to sulfonic acid by reaction with HNO_3. The mercaptopropyl groups are linked to the silica. They studied the increase of the nominal ratio of BTEB/MPTMS and, for the sample with 67% MPTMS, the $[H^+]$ was of 0.70 $mmol \cdot g^{-1}$, corresponding to an oxidation of 41.7% of the -SH to $-SO_3H$.[130] They also found that the increase of the initial concentration of MPTMS, with corresponding increase of $[H^+]$, tends to reduce the extension of the pore order.

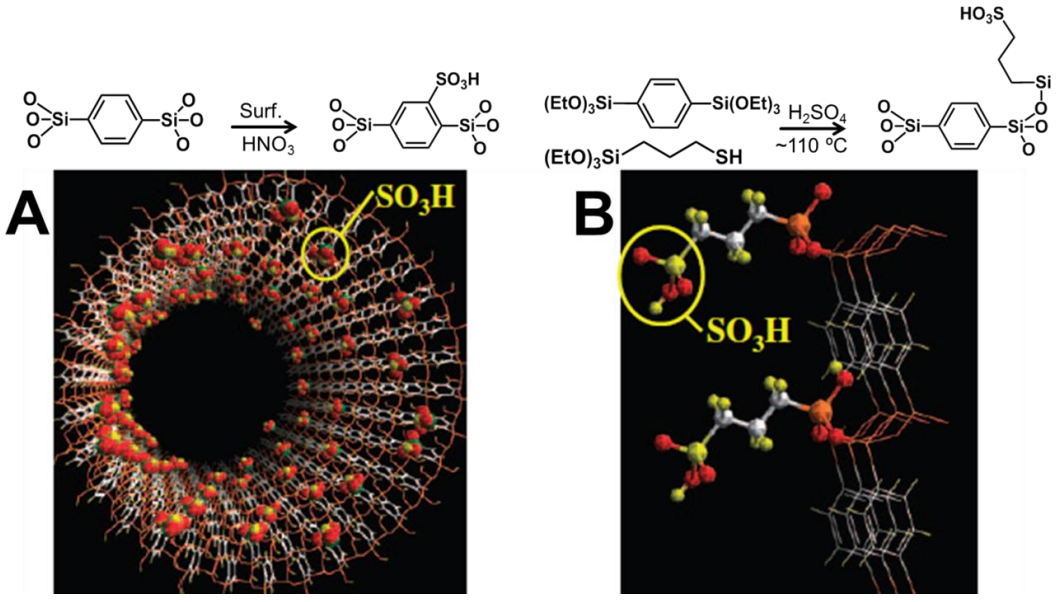

Figure 1.17. Synthetic route and schematic representation of sulfonic acid functionalized Ph-PMO particles synthesized via A) grafting and B) co-condensation. Adapted from[140].

Marschall *et al.*[141] have shown that for SO_3H-functionalized MCM-41 materials the co-condensation method shows higher [H^+] and conductivity. The same materials were analysed by SANS coupled to in-situ adsorption of water (42:58 H_2O/D_2O).[142] The neutron scattering length densities of the 42:58 H_2O/D_2O water and SiO_2 are almost identical, so when the pristine material fills up with water, the SANS signals are quenched by the presence of the water. In the case of the co-condensed sample, no quenching was observed, indicating that the SO_3H groups are well distributed along he pores. On the other hand, the grafted SO_3H-MCM-41 showed an incomplete quenching, which means that the distribution of the acid groups was not homogeneous throughout the pores, probably concentrated at the pore mouth.

1.4.3 Microwave synthesis of PMS and PMO

The complete synthesis cycle of PMS and PMO materials comprising the self-assembly, hydrothermal treatment, solvent extraction and oxidation steps is a time consuming process. In the specific case of S-Ph-PMOs the synthesis can last from 66 up to almost 140 h in total.[97,130] From an economical and environmental point of view, the reduction of synthesis time is obviously of great importance. Microwave (MW) energy has been successfully used to accelerate chemical reactions since the early studies developed in 1986 by Gedye *et al.*[143] for organic chemistry reactions. Ever since, the use of microwave radiation as a substitute of conventional heating spread throughout several fields of chemistry including the synthesis of mesoporous silica materials.[144-147]

In the case of liquid phase synthesis, the conventional procedure of heating the reactants in a furnace or oil bath leads to slow and somewhat inefficient heating since heat transfer relies on convection currents and on the thermal conductivity of vessels and reactants. On the other hand, MW radiation produces a simultaneous and uniform increase of the temperature throughout the whole volume of the synthesis vessel, according to the ability of the solvent used to absorb microwave energy and convert it into heat. However, it also shows some drawbacks like high cost of the MW devices and reactors, limited size of the reactors (due to the short penetration depths of the MW radiation, ultimately affecting the scale-up of the reactions) and difficulty to

monitor the formation and growth of the nano/mesoporous particles *in situ*.[146,147] Nevertheless, the studies of the synthesis of PMS and PMO by MW are numerous, in particular those assessing the effects on the hydrothermal treatment, template extraction and functionalization.[148-162]

The first report on the synthesis of PMOs using microwave as heat source was performed by Ahn and colleagues to produce ethane-bridged PMO by applying MW heating in the hydrothermal treatment step (with C16 as SDA).[152,157] The synthesis time was substantially shorter in comparison to conventional heating (4 to 6 h instead of 21 h), whereas the obtained particles were smaller due to the higher nucleation rate induced by the MW.

Grabicka and Jaroniec[158] used MW for the synthesis of ethane- and dissulfide-bridged PMO using P123 as the SDA. The MW energy was used in both the hydrothermal treatment and in the precedent self-assembly step. The total synthesis time was reduced from 72 h (24 h of self-assembly and 48 h of hydrothermal treatment) to 36 h for samples produced under MW (12 h of self-assembly and 24 h hydrothermal treatment). In the case of the dissulfide-bridged sample, the S_{BET} tends to decrease slightly (from 1040 to 960 $m^2 \cdot g^{-1}$) with increasing MW time (6 to 24 h) whilst for the conventional sample it was a bit lower (865 $m^2 \cdot g^{-1}$). The pore size was just slightly decreased by the MW (from 8.1 to 7.4 nm).

Of special relevance for this thesis is the report from Smeulders *et al.*[161] on Ph-PMO produced using MW as heat source in all the steps of the synthesis (self-assembly, hydrothermal treatment and solvent extraction). The self-assembly step was of 2 h for both conventional and MW stirring, but the duration of the hydrothermal treatment could be reduced from 24 h in conventional oven down to 3 h under MW, and the extraction step could be performed in only 15 min, instead of the several hours required in a conventional solvent reflux (at least 4). The total synthesis time was reduced by more than 40 h under MW. The authors observed an increase of S_{BET} by 25% for the MW samples (up to ~1000 $m^2 \cdot g^{-1}$), whereas the pore size, the hexagonal array of pores and the molecular scale periodicity along the pore wall remained virtually unchanged. The same research group later found that the faster MW heating profiles of the hydrothermal treatment render sphere-like particles with higher S_{BET} (around 20%), higher pore volume and more uniform pore size distribution.[152]

1.5 Protonic conductivity in mesoporous silica-based materials

This sub-chapter is dedicated to review the relevant protonic conductivity studies of silica-based mesoporous materials. It should be noticed, however, that many other equivalent studies on non-silica based mesoporous materials have been performed, e.g. phosphates,[163-169] titania[170-175] or alumina[176-178].

1.5.1 Pure mesoporous silica

Pure silica porous materials, such as silica glasses and xerogels, do show some reasonable protonic conductivity (Table 1.1), which is mainly related to the concentration of Si-OH groups at the pore surface, where significant amounts of water molecules can be accommodated.

Table 1.1. Protonic conductivity, E_a, S_{BET} and pore size for various types of pure porous silicas.

Sample	conditions	E_a kJ·mol^{-1}	σ (S·cm^{-1})	S_{BET} (m^2·g^{-1})	Pore size (nm)	ref
Porous Silica Glasses with High Water Content	30 ºC 90% r.h.	-	1×10^{-3}	690-900	1.6-1.7	[179, 180]
Nanopore SiO_2 ceramic membranes	92 ºC 81% r.h.	15.8	4×10^{-3}	489	3.5	[181]
High porosity silica xerogel treated in acid	81 ºC 80% r.h.	-	4×10^{-3}	579	3.5/6.0 (a)	[182]
Controlled pore silica glass	50 ºC 80% r.h.	-	4×10^{-3} 4×10^{-5}	-	4.2 2.0	[183]
Mesoporous silica film treated with O_2 plasma	50 ºC 90% r.h.	-	6×10^{-4}	-	3.0	[184]
Ordered Mesostructured Silica Monoliths	98 ºC 100% r.h.	0.6	9.1×10^{-3}	-	-	[185]
High porosity silica xerogel	80 ºC 81% r.h.	-	0.02	534	3.7	[186]

a) Bimodal pore size distribution

Nogami *et al.*[179,180] reported a study of the influence of water content on the protonic conductivity of porous silica glasses with high S_{BET} (700 - 900 m^2·g^{-1}), which reached values up to 10^{-3} S·cm^{-1} at room temperature. For the glasses subsequently treated at high temperatures, the concentration of SiOH groups is lowered and thus is also the conductivity, paired to an increase of the activation energy (E_a) from ~60 to ~120 kJ·mol^{-1}.

Daiko *et al.*[183] synthesized several silica glasses with different pore sizes (2-24 nm) and studied their protonic conductivity. They found that the volume fraction of pores occupied by water in glasses exposed to 80% r.h. at 50 °C drops from 0.95 to 0.11 as the pore size increases from 2 to 24 nm. This effect is in agreement with Kelvin's equation (eq. 2.3), which states that, as the pore size decreases, the r.h. at which water condenses also decreases. Interestingly, the conductivity of the sample with pore size of 2 nm is lower than for the sample with 4.3 nm pore size (Table 1.1). The pulse-field gradient NMR spectroscopy analysis of these samples revealed that the proton diffusion coefficient is almost twice higher for the sample with larger pores. This suggests that the diffusion of the proton is somewhat restricted in smaller pores, where they are strongly chemically bonded to the surface hydroxyl groups.

Colomer *et al.*[186] studied the protonic conductivity of porous, acid-free silica xerogels with pore size close to 4 nm and a S_{BET} of 534 $m^2 \cdot g^{-1}$. A water uptake (W) experiment showed that the water concentration inside the xerogel increases sharply up to 75% r.h. and moderately afterwards, indicating a two-regime process for the adsorption of water, in agreement with Dubinin's theory of volume filling for vapour adsorption.[187] According to this theory, at low r.h., a layer of clusters of water molecules is formed at the wall of the interconnected pores and, while the r.h. increases, new layers of water molecules start to fill the remaining pore space via capillary condensation, until a saturation effect is observed. Interestingly, the conductivity increases 4 orders of magnitude with increasing r.h., in a very similar trend as for the *W*. The E_a decreased from 31 $kJ \cdot mol^{-1}$ at 33% r.h. down to 7.7 $kJ \cdot mol^{-1}$ at 75% r.h.[41,188]

1.5.2 Inorganic functionalized ordered mesoporous silica

Mesoporous silicas turned out to be satisfactory proton conductors on their own, but the introduction of acid groups into the pores was regarded as an opportunity to further increase the conductivity by enhancing proton diffusion. The functionalization of PMS with inorganic acids, heteropolyacids or solid acids is widely reported in literature. The conductivity values and other relevant data for several examples are shown in Table 1.2, some of which are analysed in the following paragraphs.

Table 1.2. Protonic conductivity, E_a, S_{BET} and pore size for mesoporous silica with various types of inorganic acid groups in the pores.

Sample	conditions	*E*a kJ·mol^{-1}	σ (S·cm^{-1})	S_{BET} (m^2·g^{-1})	Pore size (nm)	ref
Mesoporous silica-gel vs conventional silica-gel impregnated with H_2SO_4	25ºC dry N_2 meso. conv.	-	 1×10^{-4} 9×10^{-9}	 1215 293	 3.0 2-8	[109]
Mesoporous silica-gel impregnated with H_2SO_4 (SDA with different alkyl chain length)	85 ºC 60% r.h.	- - -	C14 – 0.21 C16 – 0.24 C22 - 0.29	1089 1227 1248	2.6 3.3 4.0	[110]
Porous Silica Gels Impregnated with Sulphuric Acid.	80 ºC 60% r.h.	-	0.4	1254	2.1	[111]
Mesoporous SiO_2: xZrP: yH_3PO_4 composites	100 ºC 30% r.h.	-	0.04	700	4	[112]
$H_5GeW_{11}VO_{40}$ heteropoly acid (HPA) supported on SBA-15	23 ºC 85% HPA	-	3.1×10^{-3}	-	-	[113]
Phosphosilicate films prepared using non-ionic surfactant $C_{16}EO_{10}$	80 ºC 70% r.h.	-	7.5×10^{-3}	1028	2.5	[189]
$CsHSO_4$-SiO_2 nanocomposite membranes	100ºC dry N_2	-	1.6×10^{-4} 2×10^{-6}	-	4 290	[190]
$CsHSO_4$/mesoSiO_2 composite (evaporation-to-dryness method)	100 ºC 200 ºC (dry Ar)	- -	2.8×10^{-4} 0.015	- -	- -	[191]
Mesoporous Silica/Phosphate Composite Films Prepared by Vapour Phase Method using C16 as SDA	90ºC 80% r.h.	-	0.55	-	2.4	[192]
Mesoporous Silica/Phosphate Composite by Vapour Phase Method and Brij-30 as template.	200 ºC 100 ºC 100%r.h.	- -	0.38 0.15	- -	- -	[193]
25 wt.% HPW/Si membrane	100 ºC 100% r.h.	-	0.076	-	3.2-3.5	[194]
HPW/MCM-41 Composites	150 ºC 100 ºC 100% r.h.	8 -	0.045 0.033	- -	2.7 -	[114]
Al doped MCM-41	100ºC 100% r.h.	-	3.2×10^{-5}	785	2.3	[195]
HPW/meso-silica composites (P123 as template)	100 ºC 100% r.h.	13	0.08	-	3.5	[196]
self-assembled 25 wt.% HPW-meso-silica	100ºC 100% r.h.	14	0.09	346	3.9	[115]
Self assembled HPW/silica mesoporous nanocomposites	100 ºC 100% r.h.	-	0.076	-	3.2 -3.5	[197]
HPW/meso-silica composites with cubic bicontinuous structure.	80 ºC 100% r.h.	14.5	0.11	252	3.7	[116, 198]
Nd_2O3–SiO_2 composites	91 ºC 29% r.h.	-	4×10^{-4}	132	9.5	[199]

Nishiwaki *et al.*[109] studied the influence of the impregnation of H_2SO_4, $HClO_4$ and H_3PO_4 on the protonic conductivity of conventional and surfactant-templated silica-gels. The best conductivity results were always obtained when H_2SO_4 was used as impregnating agent. The amount of H_2SO_4 impregnated in the ordered samples was

superior to the one in silica gel (~2.5 times larger), leading to a protonic conductivity which is 4 orders of magnitude higher than the conductivity of acid functionalized silica-gel.

Matsuda *et al.*[110] studied the influence of the alkyl chain length of several alkyl ammonium bromide surfactants (C14, C16 and C22) on the protonic conductivity of similar silica-gels. As the alkyl chain length increased, they found materials with higher S_{BET} (from 1089 to 1248 $m^2 \cdot g^{-1}$) and larger pore size distribution (from 2.6 to 4.0 nm). In terms of conductivity, the result also showed a slight increase with increasing number of carbon in the alkyl chain. Samples impregnated with H_2SO_4 and $HClO_4$ have the highest conductivity (up to 2.9×10^{-1} S·cm-1 at 85 °C and 60% r.h., Table 1.2).

The same authors have also found that the conductivity increases with increasing concentration of H_2SO_4 in the solution used for the impregnation (5 M H_2SO_4 yielded conductivity values up to 4×10^{-1} $S \cdot cm^{-1}$ at 60% r.h., which is 2 orders of magnitude higher than for a sample treated with a 0.5 M H_2SO_4 solution).[111]

Heteropolyacids are known to be good solid conductors at near ambient temperature.[200] Jin *et al.*[113] took advantage of this property and introduced $H_5GeW_{11}VO_{40}$ (HPA) with a Keggin structure into the mesoporous silica molecular sieve SBA-15.

A conductivity value of 3.1×10^{-3} $S \cdot cm^{-1}$ was obtained at 23 °C, which is slightly higher than for the pure HPA.[201] The provenience of the protonic conductivity could be from the HPA itself, from the hydrolysis of water molecules connected to both HPA crystal and the wall of the SBA-15, or from the ionization of the superficial silanol groups. The large number of micro and mesopores in SBA-15 enhances the good dispersion of the HPA, allowing the adsorption of more water than for pure HPA and thus facilitating proton transport. The existence of HPA inside the pores of SBA-15 also led to a strong interaction with the silanol groups, making the ionization of these groups much easier than for pure SBA-15.

Yet another composite material based on mesoporous silica was prepared by incorporating $CsHSO_4$.[190] This solid acid undergoes a phase transition at 140 °C and its conductivity is dramatically increased from 10^{-6} to 10^{-2} $S \cdot cm^{-1}$. This still restrains the working temperature for solid acid based fuel cells to temperature above the phase transition temperature.[74] However, it has been shown that it is possible to

stabilize the high temperature phase at low temperature by synthesizing $CsHSO_4$ composite electrolyte with high content of porous oxides (TiO_2 or SiO_2) and by assuring that the $CsHSO_4$ is in an amorphous phase, which depends not only on the oxide content but also on the shape and pore size of the oxides. Interesting XRD and thermal analysis data showed that the $CsHSO_4$ inside the composite with the smaller pores (~4 nm) was characterized by an amorphous phase with dispersed crystallites, whereas the sample with bigger pores (290 nm) consisted of crystallized bulk phase with amorphous interfaces. Comparing to the sample with 290 nm pore size and to pure $CsHSO_4$, the sample with smaller pores showed an increase of conductivity by 2 orders of magnitude.

Zeng *et al.*[116,198] studied the protonic conductivity of 12-phosphotungstic acid ($H_3PW_{12}O_{40}\cdot nH_2O$ or HPW) impregnated mesoporous silica materials with a bicontinuous cubic symmetry. Samples impregnated with up to 80% HPW showed conductivity levels of 0.07-0.11 $S\cdot cm^{-1}$ at 25-90 ˚C and 100% r.h., which is 3 orders of magnitude higher than for the pure mesoporous silica, and comparable or even higher than for Nafion®. The relatively low E_a (14.5 $kJ\cdot mol^{-1}$) and high conductivity values are related with proton hopping mechanism mediated by water, avoiding the formation of the transition state from the rearrangement of the Keggin structure of the HPW.

1.5.3 Organic functionalized ordered mesoporous silica

The use of organic acid groups (such as sulfonic, phosphonic or carboxylic acid and imidazole) for the functionalization of mesoporous silica is also heavily present in the literature. Table 1.3 presents the characteristic data for a few examples.

Table 1.3. Protonic conductivity, S_{BET}, pore size, W and $[H^+]$ for organic functionalized mesoporous silicas.

Sample	conditions	σ ($S\cdot cm^{-1}$)	S_{BET} ($m^2\cdot g^{-1}$)	Pore size (nm)	W (%)	$[H^+]$ $mmol\cdot g^{-1}$	ref
Functionalized mesoporous silica (SBA 15) with MPTMS. 1) 20% and 2) 10%	90 ºC 100% r.h.	20% - 0.03 10% - 0.01	615 521	12.2 12	56.7 53.8	1.1 0.5	[129]
Meso-SiO_2-$C_{12}EO_{10}OH$-CF_3SO_3H thin films	25 ºC 90% r.h.	5×10^{-4}	-	4.85	-	-	[202]

Table 1.3 (continued)

Mesoporous polyaniline / SBA-15 composites	25 °C 100% r.h.	0.022	555	3.8	42	-	[203]
Mesostructured silica films with aluminosilica and PFSA	100 °C 100% r.h.	0.02	-	-	-	-	[204]
Surface sulfonated $_{(1-x)}PhSiO_{3/2}$-$_{(x)}MeSiO_{3/2}$ particles with (1) and without (2) mesoporous structure	80 °C 80%r.h.	1) 5.5×10^{-3} 2) 1.5×10^{-3}	- -	- -	31 20	1.05 0.90	[205]
Post synthetic sulfonation of MCM-41(1), SBA-15 (2) and SBA-16 (3) with MPTMS	100 °C 100% r.h.	1)9.16×10^{-5} 2)1.28×10^{-5} 3)4.36×10^{-6}	1031 769 792	2.7 7.9 7.2	- - -	1.16 - -	[95]
Co-condensation of MCM-41 with 40% MPTMS. MW energy for template extraction and oxidation in one step.	100 °C 100% r.h.	0.016	-	-	-	2.3	[156]
Immobilized imidazole in MCM-41	100 °C 100% r.h.	1×10^{-6}	-	-	-	0.56	[107]
Functionalized MCM-41 and MCM-48 containing phenyl sulfonic acid (S-PE), propyl sulfonic acid (S-MP) and ethyl phosphonic acid (P).	25 °C 100% r.h.						[206]
	P-48	1.1×10^{-3}	-	-	-	0.36	
	S-MP-48	2.7×10^{-3}	-	-	-	0.23	
	S-PE-48	3.9×10^{-3}	-	-	-	0.28	
	P-41	2.0×10^{-3}	-	-	-	n.a	
	S-MP-41	4.2×10^{-3}	-	-	-	0.68	
	S-PE-41	8.3×10^{-3}	-	-	-	0.87	
Phosphonic acid functionalised porous silica nanospheres	100 °C 100% r.h.	0.014	899	0.96	-	1.3	[137]
Phosphonic acid functionalized silicas	100 °C 100% r.h.	0.026	20	-	-	-	[138]
Nanoparticles of Mesoporous SO_3H-functionalized Si-MCM-41	100 °C 100% r.h.	3.9×10^{-3}	1135	2.1	-	1.78	[135]
Imidazole functionalized MCM-41	100 °C 100% r.h.	1×10^{-5}	349	2.0	-	-	[108]
MPTMS functionalized SBA-15	120 °C 100% r.h.	1×10^{-3}	-	-	-	-	[207]
P_2O_5-SiO_2-PWA inorganic membrane matrix functionalized with MPTMS and glutaraldehyde	100 °C 50% r.h.	0.085	-	-	-	-	[208]
Periodic ordered sulfonated-silica nanoelectrolytes with 2D hexagonal structure	100°C 100% r.h.	0.23	-	-	-	-	[209]
Sulfonic acid functionalized MCM-41 (20 wt. %)	100 °C 100% r.h.	5.7×10^{-3}	428	2.16	-	2.82	[210]
Sulfonic acid functionalized MCM-41 (40 wt. %)	100 °C 100% r.h.	0.016	380	2.01	-	3.2	[211]
Sulfonated Arene Mesoporous Ethane silicas using Brij-56 as SDA	25°C 160 wt.% H_2O	0.016	1040	3.3	-	1.21	[212]
MPTMS functionalized Benzene-PMO grafted at the 1) silanol site, 2) benzene ring and 3) both locations.	100°C 100% r.h.	1)3.9×10^{-6} 2)1.8×10^{-4} 3)9.8×10^{-3}	834 420 348	3.5 2-4 2-4	- - -	1.14 1.42 1.61	[97]
Highly ordered mesoporous sílica films functionalized with MPTMS using different alkyl chain surfactant.	25 °C 90 % r.h.	C12) 0.27 C18) 0.21	830 760	2.7 3.4	- -	1.8 1.5 (theor.)	[213]

Mikhailenko *et al.*[129] pioneered the study of the protonic conductivity in hybrid functionalized PMS. They synthesised the mesoporous organosilicas by co-condensing TEOS and different amounts of MPTMS (0, 10 and 20% mol), using P123 as SDA, in acidic conditions. The protonic conductivity was found to be extremely dependent on water content, enhancing up to 6 orders of magnitude from dry to fully hydrated state. At room temperature, the fully hydrated functionalized silica showed conductivity above 10^{-2} S·cm^{-1}. The conductivity in water vapour saturated conditions followed an Arrhenius tendency, with an apparent E_a of 6.9 kJ·mol^{-1} for the membrane with best protonic conductivity (20% mol. substitution). This value is comparable to the enthalpy of water diffusion (4.8 kJ·mol^{-1}).[200]

Marschall *et al.*[95] studied the conductivity of PMS functionalized with 5 to 20% mmol·g^{-1} of SO_3H via the post-synthetic MPTMS grafting of MCM-41, SBA-15 and SBA-16. For low levels of functionalization, the wide pores of SBA-15 seem to justify its high conductivity. Interestingly, at high [H^+], this material overtakes the others by one order of magnitude, which can be due to the superior S_{BET}, which allows a high degree of acid functionalization. The high density of acid groups in the more confined pores of MCM-41 may facilitate the proton hopping. As expected, the conductivity is highly dependent on the r.h. reflected as an increase in 4 orders of magnitude from dry state to fully hydrated. Still, the best result obtained was a modest 9×10^{-5} S·cm^{-1} at 100 ˚C and 100% r.h. The same group published another paper on the conductivity of highly functionalized PMS (20 to 40 mmol·g^{-1}) obtained by the co-condensation of MCM-41 with MPTMS.[156] The 2.3 mmol·g^{-1} of [H^+] achieved by this method turned out to be crucial for the enhancement of conductivity. More than one SO_3H group per nm^2 was achieved at the inner surface, which promoted the direct proton diffusion between acid sites. At 100 ˚C and 100% r.h. the best result obtained was of 1.6×10^{-2} S·cm^{-1}. MD simulations showed that the functionalized samples obtained by grafting are more dependent on the water transport than the co-condensed ones.[141] Due to the less homogeneous distribution of water in scarcely humidified conditions, for a sample with a low loading of acid groups, the proton transport barrier varies greatly with the λ, whereas for samples with greater level of [H^+], the small distance between the protogenic groups minimizes the effect of the low λ.

As mentioned before, Sharifi *et al.*[97] studied the protonic conductivity of sulfonic acid functionalized Ph-PMO. The temperature dependence of the conductivity follows an Arrhenius behaviour with E_a of 117 kJ·mol^{-1} for a material grafted on the silica, 63 kJ·mol^{-1} for the sample with SO_3H groups at the benzene and 54 kJ·mol^{-1} for the sample with acid groups in both sites. The authors justify the higher E_a of the silica grafted material because of the inhomogeneous distribution of the MPTMS groups inside the material, as mentioned in a previous study.[156] The high reactivity of the acid precursor leads to a preferential anchoring at the pore mouths, hindering the conductivity along the channels.[78,135,156] The sample with both functionalities showed the best conductivity result of 0.08 S·cm^{-1} at 140 °C and 100% r.h. These authors also performed computational simulations for the characterization of the water environment using radial distribution function obtained from MD simulation. These results suggest that the isolated SO_3H acid groups located at the benzene ring should act as a proton trap under scarcely humidified conditions. However, the combination with neighbouring flexible propyl chain of the acid functionalities at the silanol lowers the proton barrier. If sufficient acid groups are provided, the proton conduction along the pore wall by hopping from adjacent acid functionalities may compete with the bulk water vehicular mechanism, in dry conditions.[97]

Very recently, Fujita *et al.*[213] studied the protonic conductivity of several highly ordered mesoporous silica structures with MPTMS functionalization, and using cationic surfactants with different alkyl chain lengths (C12, C14 and C18). The materials were grown over a Si substrate by an evaporation induced self-assembly process. Materials with pore sizes varying from 2.2 to 3.9 nm and [H^+] from 0.78 to 2.3 mmol·g^{-1} could be obtained. All samples show a sharp increase of conductivity with increasing r.h. up to a certain r.h. value, where the subsequent increase is more moderate. Water sorption measurements are used to explain this sharp increase, which is related with the adsorption and clustering of water molecules up to a point where condensation occurs, driven by capillarity. The transition between the two conductivity regimes is shifted to lower r.h. as the acid functional density increases and the pore size decreases, in agreement to Kevin's equation (eq. 2.3). The best performing sample showed high conductivity values even at low water filling ratio of the mesopores (20% or $\lambda = 2$).

The potential of phosphonic acid functionalized PMO for proton conduction has also been investigated. Jin *et al.*[137,138] synthesised porous silica nanospheres functionalized with phosphonic acid by the co-condensation of variable amounts of diethylphosphatoethyl trimethoxysilane (DPTS) (in P/Si nominal ratios of 10, 20, 30 and 40%) and TEOS, using C16 as SDA. It was observed that the conductivity increases with increasing acid content and that the elevated S_{BET} helped raising the conductivity at low water content. The sample with 40% nominal functionalization rate exhibited a $[H^+]$ of 1.3 mmol·g^{-1} and the highest protonic conductivity at 130 °C of 3×10^{-4} up to 0.015 S·cm^{-1} from 20% to 100 % r.h respectively. The presence of phosphonic acid groups inside the pore wall may create a continuous pathway for the proton to diffuse in a Grotthuss mechanism in reduced water content conditions. Moreover, the amphoteric characteristic of this acid enables intrinsic protonic conductivity, which can be advantageous comparing to sulfonic acid.[214]

1.6 Composite Nafion®-based membranes

Since Nafion® is still the best choice as electrolyte material for PEMFC in terms of performance and durability, much effort has been made in order to modify this PEM with the purpose of rising the working temperature and lessen the chronic dependence on the presence of water. The incorporation of hygroscopic phases into the polymer matrix is probably the most explored approach to improve water retention capacity of the polymer and hence the conductivity. The fillers also contribute to improve the thermo–mechanical stability of the polymer.[215] A huge variety of filler materials has been tested including SiO_2, TiO_2, SnO_2, ZrO_2, $Zr(HPO_4)_2$ and heteropolyacids (e.g. $H_3PW_{12}O_{40}$ and $H_4SiW_{12}O_{40}$).[13,215]

The following analysis is focused on composite Nafion® membranes with silica-based fillers. Selected examples of these composites are listed in Table 1.4, including data of conductivity, *W* and swelling. The membrane conductivity is preferred over alternative indicators of performance such as the power output because there is a huge influence

of the electrode composition and electrode/electrolyte interface on the fuel cell measurements, that is difficult to account for and, thus, difficult to compare.

Table 1.4. Protonic conductivity, W and swelling of Nafion®/SiO_2 composite membranes, including filler properties [H^+], S_{BET} and pore size.

Sample	Condit.	Conductivity ($S \cdot cm^{-1}$)	W (wt.%)	Swell. (%)	Filler properties			ref
					[H^+] ($mmol \cdot g^{-1}$)	S_{BET} ($m^2 \cdot g^{-1}$)	Pore size(nm)	
3 wt.% SiO_2 particles in recast Nafion®	100 °C in air	0.19 (a)	-	-	-	200	12(b)	[216]
SiO_2 particles in various % added to preformed 1)Nafion® 115 and 2) recast Nafion®	130 °C 90-100% r.h.	1) 2% - 0.28 6% - 0.23 10% - 0.26 2) 3% - 0.42 6% - 0.46 (a) 10%-0.26	-	-	-	-	-	[217]
Composite Nafion® recast membrane with 1) perfluoroalkyl sulfonic acid functionalized mesoporous SiO_2 and 2) pristine mesoporous SiO_2 (L64 copolymer as SDA).		1) 1% - 0.11 3% - 0.12 6% - 0.11 2) 1% - 0.10 6% - 0.07	79.8 75.8 70.5	48.3 44.1 39.1	1.52 -	304 568	2.4 4.5	[218]
Composite Nafion® membranes with 1) bulk SiO_2 particles, 2) pristine mesoporous SiO_2 and 3) SO_3H functionalized mesoporous SiO_2.	80 °C 95% r.h.	1) 0.08 2) 0.12 3) 0.13 (d)	10.6 15.7 22.3	-	0.06 0.38 0.46	89 837 717	18-84(b) 6.7 6.7	[219]
1 wt.% MCM-41 in recast Nafion®	80 °C 100% r.h.	0.2	24.2	(e)		970	2.5	[220]
4 wt.% polyelectrolyte grafted SiO_2 nanoparticles in recast Nafion®	80 °C	0.041	9.7					[221]
13 wt.% (in Si) sulfonated organically modified silicas grown in situ in recast Nafion.	95 °C 95% r.h.	0.029	56 λ=31	16	0.98 (f)			[222]
5 wt.% in situ grown SiO_2 nanoparticles in recast Nafion®.	60 °C 100%r.h.	0.09	λ=7 60 °C					[223]
Nafion® recast membranes of 1) phosphonic acid functionalized porous SiO_2 nanoparticles and 2) colloidal SiO_2	85 °C 50% r.h.	1) 5% - 0.025 10% - 0.026 15% - 0.022 2) 5% - 0.014 10% - 0.009			1.25 1.29 1.39(f)	700	2.5 20 (b)	[224]
10 wt.% Sulfonated SBA-15 in recast Nafion®.	80 °C 100% r.h.	0.011			0.36		8	[225]
5 wt.% in situ formed SiO_2 in recast Nafion®	100 °C 100% r.h.	0.02	27.2					[226]
20 wt. % in situ sol-gel formation of acid-functionalized Polysilsesquioxane in recast Nafion®	80 °C 90% r.h.	0.09	30.2 λ=13		1.28 (f)			[227]
10 wt.% of a SiO_2-TiO_2-Catechol sulfonate salt (ratio of 1:01:0.025) in recast Nafion® (P123 as SDA)	100 °C 80% r.h.	0.039	17			313		[228]
3 wt.% mesoporous sulfonated-Ph-SiO_2 in recast Nafion®	25 °C 100% r.h.	0.013	60		0.94 (f)	617	6.9	[229]

(a) contact resistance in $\Omega \cdot cm^2$, (b) particle size, (c) without acid functionalization, (d) composite membranes with 5 wt.% filler, (e) less than Nafion® reference, f) for the membrane.

Early work made by Antonucci *et al.*[216] investigated a 3 wt% SiO_2/Nafion® composite membrane at 145 °C, in which the silica was added to a solution of Nafion® ionomer before recasting. They reported a cell resistance* of 0.19 $\Omega \cdot cm^2$ at 100 ºC in air with improved water retention and lower methanol cross-over. A different approach for the synthesis of the composite membranes was introduced by Adjemian *et al.*[217], by addition of commercial SiO_2 particles (Aerosil 200, Degussa) to a preformed Nafion® 115 membrane (using an impregnation method via sol-gel processing of TEOS) and to recast Nafion® membrane, using various amounts of SiO_2 fillers. The composite membrane with preformed Nafion® 115 showed, at 130 °C, a minimum contact resistance of 0.23 $\Omega \cdot cm^2$ for the sample with 6 wt.% SiO_2, increased water retention and thermal durability in comparison to the pristine Nafion® 115 membrane.

The membranes with recast Nafion® showed enhanced properties up to 10 wt.% SiO_2 loadings with a minimum resistance observed of 0.26 $\Omega \cdot cm^2$. The optimal filler content thus seems to be higher for the recast membranes, probably due to the phase-separated microstructure in the membranes, since in the recast Nafion® the hydrophilic domains could restructure as the SiO_2 polymer was forming, thus accommodating more filler. The incorporation of more than 10 wt.% fillers led to mechanical instability of the membranes. An investigation by Lin *et al.*[218] compares composite Nafion® membranes using perfluoroalkyl sulfonic acid functionalized mesoporous silica particles (S-$MSiO_2$) and pristine mesoporous SiO_2 particles ($MSiO_2$) as fillers. The recast S-$MSiO_2$/Nafion® membranes containing up to 6 wt.% hybrid fillers showed reduced methanol permeability, W and swelling as function of filler content increase. The authors state that the probable cause of the increase in conductivity for the composite membranes is due to the increase of $[H^+]$ of the membranes caused by the presence of the functionalized S-$MSiO_2$ in the matrix. Interestingly, the improvement in conductivity from 0.10 to 0.12 $S \cdot cm^{-1}$ is maximized for 3 wt.% filler. The authors suggest that the conductivity drop for higher filler contents is mainly due to phase-separated microstructure in the membrane. On the other, the addition of pristine $MSiO_2$ leads to a quasi-linear decrease in conductivity from the first 1 wt.% addition up to 6 wt.%.

* - area-specific resistance, which is the cell resistance multiplied by the electrode area.

Tominaga *et al.*[219] studied the incorporation of SiO_2 fillers using various types of silicas: bulk nanosized SiO_2 (p-SiO_2), pristine mesoporous SiO_2 ($MSiO_2$) and sulfonated mesoporous SiO_2 (S-$MSiO_2$). Composite membranes with the S-$MSiO_2$ fillers showed improved conductivity with the increase of filler content up to 5 wt.%, and decreasing thereafter. Contrary to the observation of Lin *et al.*,[218] they also observed an increase of conductivity with additions of pristine M-SiO_2. They justify the higher conductivity in the $MSiO_2$ comparing to pristine Nafion® and composite with p-SiO_2 by the presence of the mesoporosity which can lead to higher W of these composite membranes (the pristine $MSiO_2$ filler has a S_{BET} more than 50% higher than for the $MSiO_2$ from Lin *et al.* – Table 1.4). In the specific case of S-$MSiO_2$, the presence of hydrophilic sulfonic acid could also contribute to higher migration of proton in the composites. The visible decline in conductivity from 5 wt.% upwards was explained by the increasing presence of an insulating phase composed by agglomerates of mesoporous SiO_2 domains, which ultimately hinder the conductive nature of the Nafion® matrix. On the other hand, the composite membranes with p-SiO_2 particles show a decline in conductivity right from the first addition of 1 wt.% in filler.

Pereira *et al.*[222] used an *in-situ* sol-gel process to synthesise mesoporous hybrid organic-inorganic SiO_2-based particles in a Nafion® matrix. The membranes were made by the co-condensation of TEOS and 10 mol % of a sulfonated organo-alkoxysilane, using an organic surfactant as directing agent, in the presence of the ionomer. The co-condensation reactions and cooperative self-assembly organization occurred during solvent evaporation of the membrane recast process. This *in-situ* sol-gel method allowed a better definition of pore dimension and a homogeneous distribution of the particles in the polymer matrix. The composite membrane with hybrid silica particles content of 13 wt.% was found to be the best performing membrane. The protonic conductivity of the hybrid membrane at 95 °C and 90% r.h. is 0.029 $S \cdot cm^{-1}$, which is more than 5 times the conductivity of Nafion® 112 reference used in this work (0.006 $S \cdot cm^{-1}$). The authors state that the high $[H^+]$ of the hybrid membrane associated to the enhanced W and reduced swelling can explain this increase. However, when compared to other conductivity values published in the

literature, which are usually close to 0.1 $S \cdot cm^{-1}$ in similar conditions, the improvements reported by Pereira *et al*. seem indeed modest.

Phosphonic acid functionalized mesoporous particles have also been added to Nafion®. The use of this acid instead of sulfonic acid seems to be advantageous because of the potentially higher charge carrier concentration, thermal stability and resistance to oxidation. The dependence on liquid water can also be diminished because of the amphoteric behaviour of this protogenic group (it can act as a proton donor and as proton acceptor), forming dynamic hydrogen bond networks where proton can be transported by the quick formation and breaking of hydrogen bonds.[214]

A research developed by Wang *et al.*[224] compared the performance of phosphonic-acid functionalized silica particles/Nafion® composite membranes with colloidal silica/Nafion® and pristine Nafion® membranes. The functionalized silica particles composite membranes with 10 wt.% of loading showed an improvement of 24% in protonic conductivity at 85 °C/ 50% r.h. As observed by other authors cited above, the increase of conductivity with increasing filler amount goes through a maximum. The authors also speculate, as for Lin *et al.*[218], that this effect is related to the phase-separated microstructure of the membranes. Changes in the hydrophobic/hydrophilic domains could thus affect the proton transport in the membrane.

From the analysis made so far, there seems to be a maximum filler content that renders the greater conductivity increase of the composite membranes conductivity comparing to pristine Nafion®, normally under the 10 wt. % threshold. Although the great variability in the structure and microstructure of the different fillers used in the literature may not allow a straightforward correlation, one can say that there is a limit to the incorporation of fillers in Nafion®. Several authors seem to agree that this effect is related to changes if the microstructural phase-separation of the Nafion® membrane. The majority of the works in the literature used the recast method to incorporate the fillers inside the polymer matrix with promising results. The composite membrane where the filler present higher $[H^+]$ allied to high S_{BET} tend to show better conductivity values of the composite membranes.

The majority of the studies of Nafion® composite membranes explain the enhancements in conductivity solely by the increase in W and water retention ability

introduced by the presence of the hygroscopic fillers. Kreuer[33] recently suggested that the presence of foreign bodies in Nafion®, mainly those that stand at the surface, could create a perturbation of the observable surface skin, helping to release the built-up internal pressure and allowing the incorporation of additional water, just like it happens in membranes that are in direct contact with liquid water (the so-called Schroeder paradox presented in section 1.2.1.1).

To the best of our knowledge, this thesis reports for the first time the incorporation of sulfonic acid functionalized benzene-bridged PMO in composite Nafion® membranes. Moreover, the study of the influence of the characteristics of PMOs ($[H^+]$, S_{BET}, pore volume, pore order) on the conductivity as function of both temperature and relative humidity is also scarce in the literature. The choice of benzene-bridged PMO as hybrid filler for composite Nafion® membranes is not arbitrary. It has been chosen because it offers a stable rigid structure for the conduction of proton which is independent of r.h. and should not suffer from the confinement effect caused by the shrinkage of the pores, as it happens in Nafion®.[38,52] Moreover, the structure of the acid functionalized PMO makes it a good model of the structure of Nafion® pores in its hydrated form, with similar pore width and distance between acid sites.[52] It is expectable that the swelling of the composite membrane is reduced as a function of the filler content because the mesoporous particles can offer the free volume necessary for the incorporation of excess hydration water, limiting the expansion of the Nafion® matrix, as observed by other authors.[218] The choice of the protogenic group is also matter of discussion: sulfonic and phosphonic acids are thus investigated. The former was chosen because it has been largely used in the functionalization of PMSs and PMOs, with good results in terms of protonic conductivity and W. Sulfonic acid is therefore a safe choice as protogenic group.[214] The phosphonic acid group was selected due to its novelty in the functionalization of Ph-PMO and to some promising results found in the literature on the phosphonic acid functionalization of mesoporous silicas.[137,138,206]

2 MATERIALS AND METHODS

In this chapter the syntheses of the various precursors, of the acid functionalized periodic mesoporous organosilicas and of the composite Nafion® membranes are described. The techniques and methods used to characterize the composition, structure and microstructure of the hybrid mesoporous silica powders and composite membranes are also described.

2.1 Synthesis of the acid functionalized PMO precursors

Two of the basic precursors for sulfonic and phosphonic acid functionalized PMO were synthesized in-lab, mainly due to the high cost and relatively low purity of the products available in the market.

2.1.1 Synthesis of 1,4-bis(triethoxysilyl)benzene (BTEB)

The synthesis of the benzene-bridged organosilane BTEB (scheme 2.1) was prepared according to the procedure described in the literature.[230]

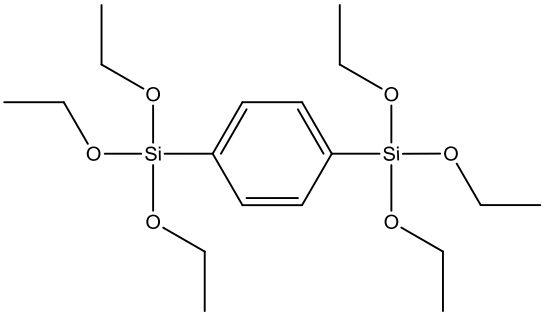

Scheme 2.1. Structure of BTEB.

This Barbier-Grignard synthesis started by the addition of 3 small iodine crystals (Fluka, *purum*) to a mixture of 5.14 g of previously air-dried magnesium chips (Aldrich, *purum*), 60 ml of tetraethoxysilane (TEOS, Aldrich, 98%) and 40 ml of tetrahydrofuran (THF, Sigma-Aldrich, ≥99.5%, over molecular sieves) under nitrogen atmosphere, to which a solution containing 16.45 g of 1,4-dibromobenzene (Aldrich, 98%) dissolved in 31 ml of THF was added drop by drop at 50 ºC. The reaction mixture was kept at reflux overnight (75 ºC). After the reaction time, the THF was evaporated in vacuum and 80 ml of dry n-hexane (Sigma-Aldrich, ≥99%, over molecular sieves) was added in order to precipitate any remaining Mg salts in solution. The obtained light yellow solution was filtered in a glass frit filter funnel, under nitrogen. After the subsequent evaporation of the n-hexane under vacuum, the resulting yellow oil was transferred to a special round-bottom flask for low pressure distillation in a Kugelrohr apparatus. The unreacted chemicals were distilled up to 155 ºC and 200 Pa, and the colourless BTEB was collected at 180-190 ºC and 147 Pa (30% yield). The structure of BTEB was confirmed by ^{1}H NMR (300 MHz, $CDCl_3$) δ: 7.60 (4 H, s, ArH); 3.80 (12 H, q, J = 7.02 Hz, $OC\underline{H}_2CH_3$); 1.16 (18 H, t , J = 7.02 $OCH_2C\underline{H}_3$).

2.1.2 Synthesis of diethyl 4-(trimethoxysilyl)benzylphosphosphonate (PSiP)

The PSiP precursor (scheme 2.2) was prepared using a modified version of the method described in reference[231].

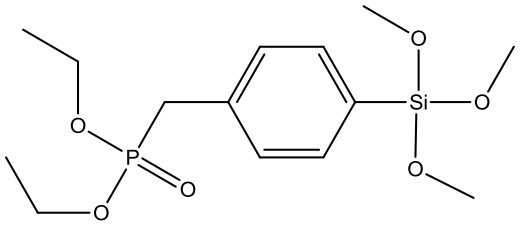

Scheme 2.2. Structure of PSiP.

The synthesis starts by the addition of 4.41 ml of (p-cloromethyl) phenyltrimethoxysilane (ABCR, 95%) to 4.20 ml of triethylphosphite (Aldrich, 98%). The mixture was then stirred and heated in reflux at 150 ºC in nitrogen atmosphere, overnight. After cooling down to room temperature, part of the unreacted compounds was removed by evaporation under vacuum. The remaining liquid was then distilled at low pressure in a Kugelrohr apparatus, under nitrogen. The unreacted compounds where distilled up to 200 ºC at ~330 Pa and the colourless PSiP oil was collected at 230 ºC, also at 333 Pa (77% yield). The structure of PSiP was also only confirmed by ^{1}H NMR (300 MHz, $CDCl_3$) δ: 7.65 (2 H, d, J = 7.68 Hz, ArH); 7.38 (2 H, dd, J = 8.10; 2.43 Hz, ArH); 4.10-4.00 (4 H, m, $OC\underline{H}_2CH_3$); 3.65 (9 H, s, $OC\underline{H}_3$); 3.19 (2 H, d , J = 22 Hz, $PC\underline{H}_2$); 1.27 (6 H, t , J = 7.13, $OCH_2C\underline{H}_3$).

2.2 Synthesis of acid functionalized Ph-PMO

The synthesis of Ph-PMO functionalized with sulfonic or phosphonic acids followed similar pathway as the number of steps is the same for both acids. The syntheses were all made by the co-condensation method, where the silica and acid precursors were added in the same synthetic step and allowed to condensate simultaneously.

2.2.1 Functionalization with sulfonic acid

The synthesis of sulfonic acid functionalized Ph-PMO samples (S-Ph-PMO) was carried out following the procedures reported in the literature,[89,90] with some minor adjustments as schematized in scheme 2.3 (path 1).

In a typical synthesis, 1.86 g of cationic surfactant octadecyl trimethylammonium bromide (C18, Aldrich, 98%) was dissolved in 50 ml of distilled H_2O and 1.33 ml of 6M NaOH (EKA chemicals) aqueous solution at ~50 ºC. 0.67g of BTEB are added to 0.32 ml of (3-mercaptopropyl)trimethoxysilane (MPTMS, Sigma-Aldrich, 95%) and ultrasonicated for 5 min. The chemicals ratios used in the synthesis are BTEB:MPTMS:C18:NaOH:H_2O 1:1:2.87:4.83:1716.

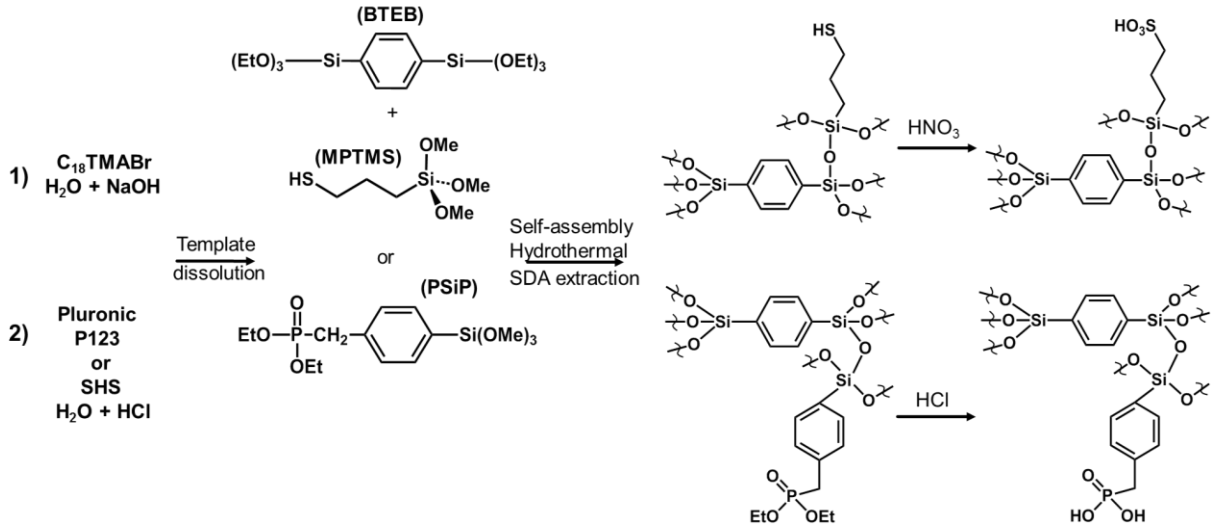

Scheme 2.3. Typical synthesis pathway for 1) S-Ph-PMO and 2) P-Ph-PMO.

This mixture was then added dropwise to the surfactant solution at room temperature and under vigorous agitation. After the addition of the precursors, the mixture was ultrasonicated for 5 minutes and transferred to a PTFE lined stainless steel autoclave. The self-assembly process was allowed to occur, in which the precursors organize around the lyotropic liquid-crystalline phase formed by the supramolecular aggregates of the surfactant micelles. The process was conducted at room temperature under vigorous agitation, for 24 or 48 h. Then, the autoclave was inserted in an oven at 100 ºC for 24 h of hydrothermal treatment to further consolidate the mesostructure and the pore walls. The resulting mesostructured hybrid powders were filtered and washed with warm distilled H_2O, dried at 60 ºC and the remaining template extracted overnight using a 100 ml solution of 1:9 HCl/EtOH (typically for 0.5 g of co-condensed powders, 100 ml of EtOH was used) at reflux temperature. Finally, after a thorough washing in EtOH and distilled H_2O and subsequent drying at 60 ºC, the

oxidation of the SH groups to SO_3H was performed by wetting about 0.5 g of the sample with 1 ml of distilled water, followed by 5 ml of 20 mol % HNO_3 solution and finally by the slow addition of 10 g of concentrated HNO_3 (Sigma-Aldrich, 65%). The mixture was left at room temperature under vigorous stirring during 24 h. The shortest time spent in this conventional synthesis (discounting filtering and drying inter-steps) was 84 h.

In order to reduce the synthesis time and the amount of solvent used, a series of experiments was designed to explore the potential of MW radiation as an alternative heat source on the various steps of the synthesis (self-assembly, hydrothermal treatment, extraction and oxidation).

The MW synthesis of S-Ph-PMO was inspired in the MW synthesis of acid-free Ph-PMO reported in the literature,[161] exploiting the effect of time on the various synthetic steps. According to the synthesis path in question, different self-assembly times were performed (2, 6, 12 and 24 h for conventional stirring and 0.5, 1, 2, 4, 6 and 12 h stirring in MW at 40 °C). Subsequently, the mixture was poured into a MW vial and heated at 100 ºC for the desired hydrothermal treatment time (1, 3 or 5 h). The remaining surfactant was extracted also in the MW oven at 100 ºC for 15 min using half of the solvent quantity typically used in the conventional extraction. The oxidation step was accomplished by reaction with HNO_3 for 30 min in MW at 40 °C. The MW syntheses were performed using microwave systems model MARS-5 (CICECO, University of Aveiro) and MARS-X (LACCO, University of Poitiers), both from CEM Corporation.

The samples notation system follows the acronym S-AxByZ, where “S” refers to the sulfonic acid functionalization, “A” refers to the conditions used in the self-assembly step (“C” for conventional stirring at room temperature or “MS” for microwave treatment at 40 °C under stirring), “B” is related to the conditions used in the hydrothermal treatment (“C” for conventional oven and “M” for microwave treatment) and “Z” denotes the specific sample condition at the moment of characterization, including (as) as-synthesized and (ext) extracted; when “Z” is not mentioned, the acronym refers to the final oxidized form. The “x” and “y" indicates the duration of the specific step, in hours. As an example, S-C24M3 corresponds to a

24 h conventional self-assembly step, followed by a 3h hydrothermal treatment with MW. The sample was then extracted and oxidised.

2.2.2 Functionalization with phosphonic acid

The synthesis of Ph-PMO samples functionalized with phosphonic acid (P-Ph-PMO) was carried out by the co-condensation of PSiP and BTEB in several proportions using a triblock-copolymer EO_{20}-PO_{70}-EO_{20} (Pluronic P123, Aldrich) or anionic surfactant n-hexadecylsulfuric acid sodium salt (SHS, ABCR, includes 40% sodium stearyl sulfate salt) as structure directing agents. Although the synthesis of P-Ph-PMO samples was also attempted with cationic surfactants of the trimethylammonium bromide family (C14, C16 and C18), these did not result in any condensation of the PSiP group, as assessed by acid-base titration. These samples are denoted "Px-y", where x stands for the nominal molar percentage of PSiP and y represents the acronym of the structure directing agent (P123 or SHS). The second path in scheme 2.3 represents the synthetic pathway for the synthesis of P-Ph-PMO using co-polymer P123 as structure directing agent. For example, P20-SHS corresponds to a sample with a 20 % PSiP and 80 % BTEB, using SHS as SDA, and synthesised with conventional stirring, hydrothermal treatment, extraction and acidification steps.

In a typical synthesis 0.75 g of P123 was dissolved in a mixture of 29 ml of distilled H_2O and 0.2 ml of concentrated HCl (37 wt.%). The mixture was stirred and heated at 50 ºC until a clear solution was obtained. A mixture of BTEB and PSiP, in 1:9, 1:4 and 1:1 molar proportion (totalling 2.46×10^{-3} mol of total precursors in each batch and corresponding to samples P10%-P123, P20%-P123 and P50%-P123 respectively) was kept for 5 minutes in an ultrasonic bath and added dropwise to the copolymer solution, under vigorous agitation and at room temperature. After the addition, the reaction mixture was kept for 5 minutes in an ultrasonic bath, poured in a PTFE autoclave and left for 24 hours at room temperature, under vigorous agitation for the self-assembly step. After this time, the vial was placed in an oven at 100 ºC for 24 hours. The solid product was recovered by filtration, washed with hot distilled H_2O

and dried in the oven at 60 ºC. The remaining surfactant was extracted from the co-condensed P-Ph-PMO using a mixture of EtOH/HCl (66.6:1) in reflux at 75 ºC and overnight. The remaining solid was washed with EtOH and distilled H_2O, and finally dried at 60 ºC. The sample was wetted with 2 mol of distilled H_2O and the free phosphonic ether groups were transformed to phosphonic acid groups by the acid-catalysed hydrolytic dealkylation. This was achieved by addition of 40 ml of concentrated HCl, leaving the reaction at 80 ºC in reflux for 2 h. This reaction time was found to yield the highest level of acid incorporation, as assessed by acid-base titration and ^{31}P high-power decoupling technique (HPDEC) magic-angle spinning (MAS) NMR.

The synthesis of P-Ph-PMO with the anionic surfactant SHS is in all similar to the synthesis of P-Ph-PMO with copolymer P123, apart from minor adjustments in the quantities of the reactants. The molar ratio BTEB:PSiP for the P-SHS used were 1:9, 1:4, 1:2.3 and 1:1, which corresponds to samples P10%-SHS, P20%-SHS, P30%-SHS and P50%-SHS respectively.

2.3 Preparation of composite Nafion® membranes

An aliquot of Nafion® dispersion (Aldrich, 20 wt.% dispersion in n-propanol, ethanol and water) was heated up to 45 ºC in order to remove the solvents and redispersed in N,N-dimethylacetamide (DMAc, Aldrich, ≥ 99%). For a typical composite membrane with 5 wt.% of S-Ph-PMO in relation to the dry weight of Nafion®, a dispersion was prepared with 0.3730 g of dry Nafion® polymer in DMA. In parallel, the selected S-Ph-PMO powder was ultrasonicated for 10 min in 20 ml of EtOH, then thoroughly ground in an agate mortar and dried in oven at 60 ºC. 0.0196 g of this powder was then added to the Nafion®-DMA dispersion. The mixture was homogenised in an ultrasounds bath for 5 min, and vigorously stirred overnight at room temperature. Adjustments in the quantity of Nafion® and filler were made for composite membranes with 10 and 20 wt. % S-Ph-PMO powders. The obtained slurry was poured into a 5 cm in diameter petri dish and, in order to prevent the precipitation of

the particles, the viscosity of the mixture was increased by drying some of the solvent in a hot plate at ~80 ºC and under constant agitation. Vacuum was then applied for 1 h in order to facilitate solvent evaporation and to remove air bubbles. The as-prepared membranes were fully dried in an oven at 100 ºC for 5 h, and then at 60 ºC overnight. For comparison purposes, a pure Nafion® membrane was also prepared by the same method.

All the prepared membranes were hot-pressed at 120 ºC under 10 MPa for 10 minutes to improve their mechanical robustness. Finally, the membranes were washed and activated using a series of treatments in boiling 3 vol. % H_2O_2 (Alfa Aesar, 29-32 wt. %), 0.5 M H_2SO_4 (Panreac, 96%) and high purity H_2O. The membranes were stored in high purity H_2O.

The composite membranes were denoted as "S-AxBy-C%" where the first part "S-AxBy" specifies which S-Ph-PMO material was used and "C%" is the nominal wt.% in relation to the dry weight of Nafion®.

2.4 Characterization of composition, structure and microstructure

2.4.1 X-ray diffraction

X-ray diffraction (XRD) is a key technique for identification and characterization of the crystalline phases in a material, which relies on the fact that the wavelength is in the same order of magnitude than the bond distance between atoms in a crystalline material. The crystal can be regarded as a set of regularly spaced scattering centres, which can be portrayed as planes of lattice points, as depicted in the left side of Fig. 2.1.[232] The planes of scattering centres that make up the crystal are separated by a distance *d*, but there can be several different planes, depending on which atoms are regarded, each with its specific *d* inter-planar distance. A diffraction maximum occurs when the crystal is specifically orientated regarding both the X-ray source and the detector, in such a way that there is a constructive interference of the X-rays scattered by the atomic planes of the sample.

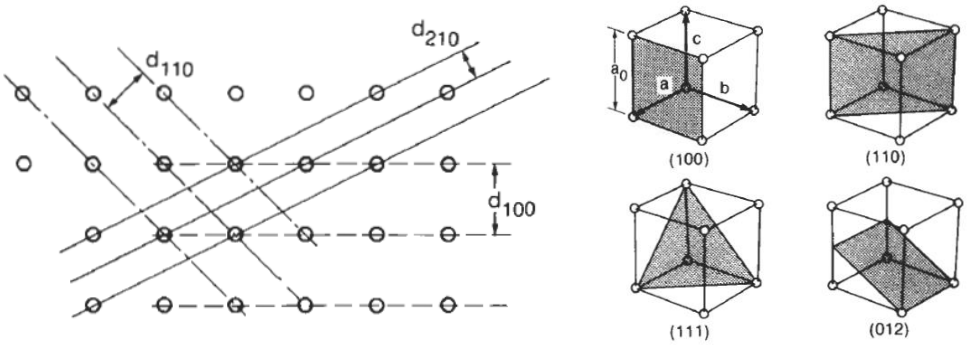

Figure 2.1. Representation of some of the atomic planes and their *d*-spacings in a simple cubic crystal (left) and Miller indices of atomic planes in a simple cubic crystal (right). Adapted from ref[232].

Bragg's law determines that for this to occur, the angle of incidence must be equal to the scattering angle and that the path difference must be a whole number multiple of the wavelength, according to:

$$n\lambda_{Cu} = 2d\ \sin\theta \qquad \text{eq. 2.1}$$

in which n is an integral multiple of the wavelength, λ_{Cu} is the wavelength of the X-ray (in this case a Cu Kα signal), d is the inter-planar distance and θ is the incidence angle.

In the case of the materials studied in this work, there are no crystalline arrangements of the atoms; in fact, these materials may be considered as amorphous. However, the X-ray diffraction technique is also sensitive to the electron density contrast created by the organization and distribution of the pores, which in this case have 2D hexagonal symmetry.[89] The lattice constant, a_0, which refers to the constant distance between unit cells, can be calculated from d_{100} according to:

$$a_0 = 2d_{100}/\sqrt{3} \qquad \text{eq. 2.2}$$

as depicted in fig. 2.2 . Additionally, for samples that use ionic surfactants as SDA (S-Ph-PMO and P-PH-PMO-SHS) the XRD can also show an additional peak related to

a molecular scale periodicity, due to the stacking of hydrophobic and hydrophilic layers, represented by the interplanar distance d_{001} in fig. 2.2.

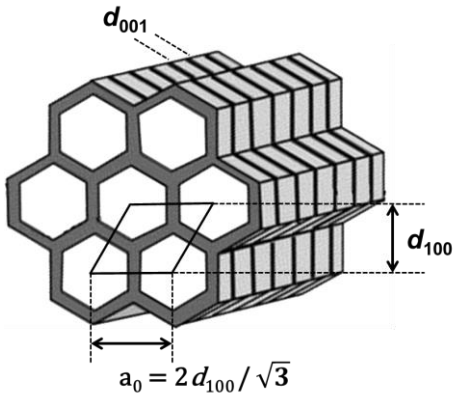

Figure 2.2. Schematic representation of the hexagonal arrangement of pores and the molecular scale periodicity of the pore walls of Ph-PMO. Adapted from[89].

The majority of the XRD analyses performed for this work were obtained in a Rigaku Geigerflex D/Max – C series, equipped with a monochromatic Cu Kα radiation (λ_{Cu} = 1.5406 Å). The diffractograms were collected from 1 to 16 º in 2θ, with step size of 0.02 º and acquisition time of 2 s. A Phillips X'pert MPD diffractometer, using Cu Kα, was also used to perform some measurements on an extended low angle range from 0.5 to 16 º in 2θ, with a step size of 0.02 º and variable acquisition times (1 to 5 s).

2.4.2 -196 ºC nitrogen sorption isotherms

The study of the adsorption of gases by porous materials is useful for the characterization of the structural and microstructural features, namely the S_{BET} and the volume and size distribution of the pores. When a porous solid (adsorbent) is exposed to a vapour phase at a precise partial pressure, inside a defined closed space, it will adsorb some of that vapour. After achieving equilibrium, the amount of gas adsorbed can be calculated from the fall of the pressure or from the weight increase of the material.

The sorption isotherm is then a plot of the amount of adsorbed gas as a function of the increasing and subsequent decreasing of the relative vapour pressure. In the case of

mesoporous materials the typical shape of the sorption isotherm pattern is of type IV, according to the IUPAC classification, which has a characteristic hysteresis loop between the adsorption and the desorption branch as depicted in fig. 2.3.[233] At the beginning of the plot, in the low relative pressure region, the adsorption branch (full line in the fig. 2.3) starts with a curve (ABC) that represents the formation of a monolayer followed by a multilayer of the absorbate gas. The curve then deviates upwards (CDE) until the slope decreases (EFG) and the condition of saturation vapour pressure is attained.

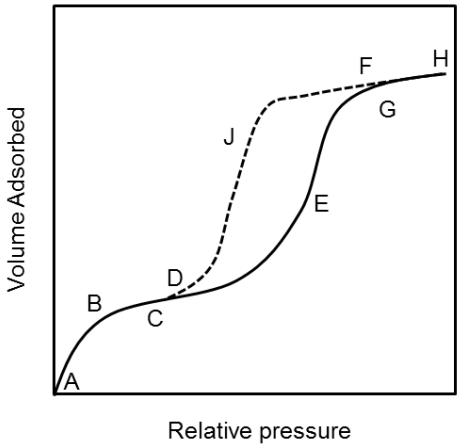

Figure 2.3. Typical isotherm adsorption (full)/desorption (dashed) curve for mesoporous materials (IUPAC isothermal sorption curve of type IV). Adapted from[233].

The saturation in normally represented by a little variation in the amount of absorbed gas (FGH). In the desorption branch (dashed line), a characteristic hysteresis loop is observable (FJD). This hysteresis loop is due to the capillary condensation taking place in the mesopores and its mathematical interpretation allows a reasonable estimate of the specific surface and an approximate assessment of the pore size distribution.

The vapour pressure due to the curved liquid/vapour interface follows the Kelvin equation, which can be represented as:[233,234]

$$\ln\frac{p}{p_0} = -\frac{2\psi V_L \cos\phi}{RTr} \qquad \text{eq. 2.3}$$

where ψ is the surface tension, V_L is the molar volume of the liquid condensate, ϕ is the contact angle between the pore surface and the water molecules and r is the radius of the pore. It is possible to calculate the S_{BET} using the Brunauer, Emmett and Teller (BET) method, which is based on the multilayer adsorption phenomenon described above.[235]

The calculation of the pore size distribution and pore volume is usually obtained using the Barret, Joyner and Halenda (BJH) method, which was initially developed for absorbents with relatively wide pores and pore size distribution. The algorithm used in this model assumes that the pores have a cylindrical shape and also uses a modified Kelvin equation. The discovery of PMS materials brought the opportunity for the development of gas adsorption measurements since a new family of mesoporous materials with a simple pore geometry, tuneable pore size, well-defined microstructure and reproducible surface properties was available.[236] Based on the BJH method, Kruk, Jarionec and Sayari (KJS) developed a more comprehensive method for pore size analysis.[236] They used N_2 sorption isotherms and XRD measurements of MCM-41 materials as a way of establishing correlations between the pore width and the condensation pressure, and between the statistical film thickness and the equilibrium pressure. They later extended the KJS method to include PMS samples with a broader pore size range and cylindrical pores interconnected with micropores (e.g. SBA-15).[237] The pore size distribution curves obtained from the KJS method were quite similar to the pore size distribution curves calculated using nonlocal density functional theory (NLDFT), both for large and small pores. Since its development, the KJS method has been successfully used for the characterization of several ordered mesoporous materials.

The -196 ºC N_2 sorption isotherms measurements of the S-Ph-PMO and P-Ph-PMO samples presented in this work were performed in a Micromeritics Gemini 2370 equipment. The samples were degassed overnight at 120 ºC and the measurements were performed at -196 ºC. The S_{BET} was calculated using the BET method and the pore size distribution was determined by the BJH method with the KJS correction implemented in the Micromeritics Gemini V2.00 software.

2.4.3 Electron microscopy

Scanning and transmission electron microscopies (SEM and TEM, respectively) are key techniques for the observation of materials at nano and atomic scales. In an electron microscope, instead of visible light photons, electrons are used as incident radiation. The electron microscope works by emitting a beam of electrons from an electron gun through electromagnetic lenses, which are the equivalent of the glass lenses in the optical microscope. As a result of the interaction of the electron beam with matter, a large number of scattered signals can emerge. If the incident electrons conserve their energy, the scattering process is considered elastic, and only their direction of propagation is modified by the interaction with the samples atoms. Back-scattered electrons arise from such interaction and can be used for imaging and for diffraction analysis. Inelastic scattering is the other fundamental scattering process in which the kinetic energy of the incident particle is lost or gained. A small portion of the energy lost may escape as characteristic X-rays, secondary electrons or Auger electrons and these can be extremely useful for imaging and structural analysis.[238]

In SEM mode, the electron beam is focused by the electromagnetic lenses onto the sample and a deflecting unit controls the beam that scans the selected area line-by-line. For mesoporous samples, SEM is useful to study the surface, shape, topography, size and the level of aggregation of the powder particles.

In TEM mode, the electrons that travel through the sample and manage to exit on the other side are used directly to replicate the pattern onto a screen (e.g. digital sensor or fluorescent screen). In this work, TEM is used to detect visually the channelled microstructure of the mesoporous particles as well as perceiving the hexagonal arrangement of the pores, which may be useful to correlate to the data obtained by XRD. High-resolution TEM (HR-TEM) allows a theoretical resolution of up to 0.2 Å, well in the range of atomic bond length. This TEM mode is especially useful to distinguish and characterize atomic arrangements in crystalline materials, but in the case of Ph-PMO samples, it is possible to detect the molecular scale periodicity along the pore wall, as shown also in Fig. 1.15.

When an electron of the inner shells of the samples atoms is pulled out by inelastic scattering process, an electron from the outer shells will fall down to fulfil that electron hole, emitting an X-ray photon in the process, which is characteristic for the energy gap between the electron shells and to the element that was interacted with. These photons can be counted by an energy dispersive X-ray spectroscopy (EDS) detector and the signals are processed and converted into a plot of number of counts vs. X-ray energy. The peaks correspond to the specific decays of specific elements, which makes this a powerful tool for the chemical characterization of the samples, including mapping areas of different elemental composition.[238,239]

When possible, the interplanar distance d_{100} was measured on the TEM images and compared to the XRD result, using the software Image J (version 1.45s).[240] The measurements were made in samples with observable channelled microstructure by measuring the distance between peaks in a grayscale profile drawn perpendicularly to the channels. A minimum amount of 10 measurements were made for each sample, where the standard deviation was an average of 8% for all measurements.

The TEM used in this work was a Hitachi H-9000 equipped with a Quantax 400 EDS detector from Bruker. The typical acceleration voltage used in the experiments was limited to 200 kV (the microscope delivers a maximum of 300 kV), to avoid damaging the samples and to minimize the drifting caused by charge accumulation. The preparation of the samples for TEM observation consisted in a simple submersion of 400 mesh holy-carbon coated TEM copper grids (Agar Scientific) in an EtOH suspension of the mesoporous materials. Prior to making the suspension, the materials where thoroughly grinded in an agate mortar and ultrasonicated to promote disaggregation of the particles.

The SEM micrographs were obtained in a Hitachi SU-70 microscope equipped with a Quantax 400 EDS detector from Bruker. The acceleration voltage was kept between 4 to 10 kV to avoid destruction of the mesoporous materials and composite membranes. The powder samples were observed by SEM using the same TEM copper grids, whereas the composite membranes were observed on specific aluminium holder using carbon conductive tape as adhesive. The membranes were lightly covered with conductive carbon coating, using a vacuum evaporator (Emitech K 950 x).

2.4.4 Solid state nuclear magnetic resonance

Solid-state nuclear magnetic resonance (NMR) is a technique used to structurally characterize materials that works by measuring the nuclear shielding, or electron density, of specific elements. The chemical environment affects this nuclear shielding and different adjacent atoms will perform different influences on a targeted nucleus. For an element to be seen in NMR it has to present a spin state greater than 0. When a sample with an eligible nucleus is inserted in the NMR apparatus, the applied magnetic field will cause the spin state to split. A nucleus with a spin state of ½ splits into two states, and the number of split states increases with increasing spin (spin of 1 will divide in 3 states and so on).

In solids, and contrary to liquids or gases, the atoms are spatially confined (e.g. in certain lattice positions) and chemical shift anisotropy can occur due to the different orientation of the molecules towards the spectrometer. The fact that the atoms in the lattice are not always equally distanced can also lead to additional noise in the spectra due to fluctuations in the levels of dipolar interactions. Moreover, nucleus with spin higher than ½ may display quadrupolar interactions, shifting energy levels and creating additional resonance frequencies.[241] These interactions may be reduced using the magic-angle spinning (MAS) technique. There is a simple geometric factor that is common to the three types of interactions and this it can be reduced to zero when the sample is tilted 54.74º in relation to the applied magnetic field. By tilting the sample and spinning it at high frequency, the solid samples will behave similarly to a liquid. Another important technique, normally coupled to MAS, is the Cross-Polarization (CP), which is useful to counteract the sensitivity and low natural abundance of certain targeted atoms analysed by solid state NMR. In this work, these techniques were applied to obtain the ^{13}C and ^{29}Si NMR spectra. In the case of ^{31}P spectra the high-power decoupling technique (HPDEC) was applied to eliminate the heteronuclear dipolar interactions and the heteronuclear scalar coupling interactions.[242]

The NMR spectrum consists of peaks located at different chemical shifts δ, in Hz or ppm, relatively to a reference. This information can elucidate on the chemical

environment of the targeted nucleus. For example, in ^{29}Si NMR the spectra are expected to reveal T^n type signals (according to R-$(OSi)_nSi(OH)_{3-n}$), which are an indicator of the levels of condensation of the R-SiO_3 tetrahedra inside the hybrid materials. For these signals, the peaks with higher "n" correspond to a better incorporation of the R-SiO_3 tetrahedra in the walls of the structure, whereas structure with n < 3 correspond to Si nucleus connected to pending OH groups. The relative intensity of the several peaks could give some insight about the overall level of structural order of the materials. The expected absence of Q^n signals, which are originated by the presence of substructures $(OSi)_nSi(OH)_{4-n}$ would be an indication that the Si-C bond did not break during the multiple steps of the synthesis of the PMOs.[86,130,243] The signals expected for the ^{13}C NMR spectra would be an intense benzene ring carbon nucleus and also carbon signals from the -CH_2 and -CH_3 groups of the acid precursor chains. The presence of 4 signals in the oxidized S-Ph-PMO samples could indicate that the -SH groups were not totally converted to SO_3H in the oxidation step.[128,244] The analysis of P-Ph-PMO samples using ^{31}P NMR techniques should reveal a peak assigned to the free R-P(O)$(OH)_2$ acid groups and another peak assigned to the acid bounded to surface silica as R-P(O)(OH)(OSi) or R-P(O)$(OSi)_2$ where R represents the organic group. The higher relative intensity of the first peak is desirable because it suggests that the acid groups are pending inside the pore instead of bonded to the silica surface.[245,246]

In this work, the ^{29}Si, ^{31}P and ^{13}C Solid-State NMR experiments were performed at 79.49 MHz for ^{29}Si and 161.98 MHz for ^{31}P on a Bruker Avance 400 spectrometer and at 125.76 MHz for ^{13}C on a Bruker Avance 500 spectrometer. ^{29}Si CP-MAS NMR spectra were recorded with a 4.75 μs ^{1}H 90º pulse, a contact time of 8 ms, a spinning rate of 5 kHz and 5 s recycle delays. ^{13}C CP-MAS NMR spectra were recorded with 3.5 μs ^{1}H 90º pulses, a contact time of 2 ms, a spinning rate of 12.0 kHz (P-Ph-PMO) and 15.0 kHz (S-Ph-PMO) and 5 s recycle delays. ^{31}P HPDEC NMR experiments were recorded with a 6.5 μs ^{1}H decoupling pulse, a spinning rate of 12 kHz, a 3 μs ^{31}P 90 º pulse with a flip angle of 90 º and 60 s recycle delay.

2.4.5 Dynamic mechanical analysis

The dynamic mechanical analysis (DMA) technique is widely used to study the visco-elastic properties of polymers. This technique is based on the application of a dynamic sinusoidal stress to the sample, which responds with a sinusoidal strain shifted by a certain angle (φ) with respect to the stress wave. Figure 2.4 is a schematic representation of the stress/strain chart. From φ and the amplitude of the strain curve one can calculate the modulus, the visco-elastic properties and the damping of the studied material. The strain curve is defined by a complex modulus, which can be expressed by its in-phase component, the storage modulus (E') and its out of phase component, the loss modulus (E''). The E' is a measure of the stiffness of the material and it is proportional to the energy that is stored during one period under load, that is, the materials elastic behaviour.

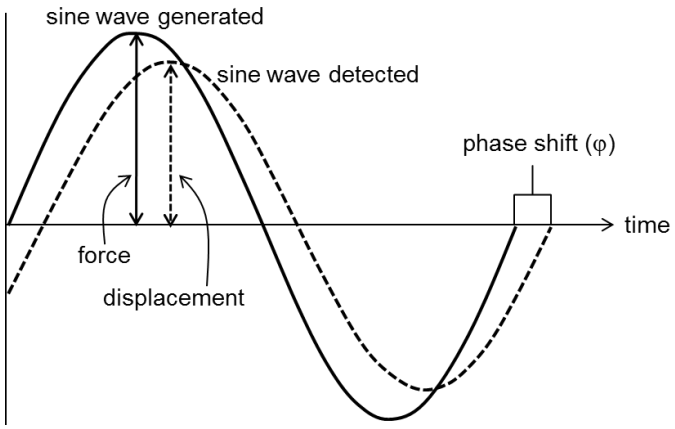

Figure 2.4. Schematic representation of the applied stress wave (full line) and strain response (dotted line) of the real material, in a fixed frequency experiment. Adapted from[247].

The E'' measures the ability of a material to deform without breaking and it is proportional to the work that is lost or dissipated during one period under load. The ratio between the energy dissipated by internal friction and the elastic energy is the mechanical damping factor, and is expressed by the loss factor tan $\varphi = E''/E'$. A material that shows a high E'' displays a large inelastic fraction response to the applied

mechanical stress while a material with a low *E*'' refers to a more elastic behaviour.[247]

Coupling a temperature sweep to the DMA technique is a good way to characterize the several thermal transformations that occur in polymers, for example the T_g, which is the temperature above which the materials will show a rubbery behaviour instead of glassy properties, characterized by a dramatic drop in the stiffness. This is portrayed by a significant decrease of the *E*' and a maximization of *E*'' with a consequent peak of tan φ. The technique is also useful to characterize other phase shifts, displacements and modifications that occur while the temperature rises. In the case of Nafion® and similar perfluorosulfonated polymers, water plays the role of plasticizer inside the structure, influencing enormously the DMA results.[33,248-250] The segmental motion of the main chain of physically cross-linked perfluorocarbon phase (the genuine T_g of Nafion®) is expected at ~20 ºC, but it can occur at 0 ºC or even lower temperatures, depending on the water content of the material.[248] The weakening of electrostatic network involving the aqueous domains allows the occurrence of a α relaxation which is attributed to the long-range motion of both the main and the and sulfonic acid side chains.[33,250]

In this work, the DMA apparatus (Tritec 2000 DMA) was used for the analysis of the visco-elastic behaviour of the prepared Nafion® and composite membranes upon heating at constant rate and to study the effect of the filler fraction. The dimensions of the sample were of ~30 (height) × 5 (width) × 0.1 (thickness) mm. The sinusoidal tensile deformation applied corresponds to a 20 μm displacement. The data were collected with at 1 Hz during heating from -100 °C to 160 °C at 2 °C·min^{-1}. The samples were firstly placed in the DMA chamber and cooled down to -110 °C by flowing liquid nitrogen within the chamber walls. The cooling rate is not controlled, but the conditions were selected in order to obtain the fastest cooling time possible (slightly more than 5 min). There was no control of the r.h. in the chamber. Before the measurements, all samples were kept in a conditioning cabinet at 30 °C under 50% r.h. for at least 48 h.

2.4.6 Fourier transform infrared spectroscopy

Fourier transform infrared spectroscopy (FTIR) is a characterization technique that helps to identify the presence of certain functional groups. The basic FTIR experiment determines intensity changes in an IR beam after interaction with a sample, as a function of wavelength or frequency. At a specific frequency, and when it matches the vibrational frequency of a characteristic bond or functional groups, the material will absorb the IR wave and the amplitude of the molecular vibration will change. This fluctuation in vibrational energy states as a function of wavelength (or the wavenumber, as is usually used) is the actual IR spectrum, and the bands that emerge can be indexed to specific vibrational modes (stretching or bending) of specific bonds or groups of atoms.[251]

The FTIR spectra were obtained on a FTIR Mattson-7000 infrared spectrometer with 2 cm^{-1} resolution. The samples in the powder form were mixed with KBr and the mixture was then shaped into disks on a stainless steel die by applying uniaxial pressure.

2.4.7 Thermal analyses

Thermogravimetric analysis (TGA) and Differential scanning calorimetry (DSC) are very useful and common techniques used to study the thermal behaviour and composition of materials. On a TGA experiment, the weight loss of a sample under controlled conditions of temperature and atmosphere is measured. This technique is particularly helpful to study the different thermal stages at which water leaves the materials and also to study the overall thermal stability.

The DSC technique is based on the difference in heat necessary to change the temperature between the sample and a reference, which is monitored as the temperature increases continuously at a fixed rate. This technique is very useful to study phase transitions in materials and to know if these transitions are exothermic or endothermic.[252]

Before the measurements, the samples (in the form of powder) were kept in a closed glass desiccator with a aqueous solution saturated in K_2SO_4, defining an equilibrium r.h. of ~98% r.h. at 25 ºC.[253] The samples were equilibrated in this atmosphere for about 48 h, then quickly transferred to the TGA/DSC sample holder to carry out the respective measurements. These were made in TGA-50 Shimadzu apparatus and DCS-50 Shimadzu apparatus respectively, in both cases using a heating rate of 5 $^{o}C \cdot min^{-1}$ in air and N_2 atmospheres.

2.4.8 Acid load

The acid load ($[H^+]$) expressed in mmol of H^+ equivalent per gram of dry sample, was measured by a simple acid-base back titration. For the powder samples, the weighted amount of dry sample ($W_d \approx 20$ mg) was dispersed in 20 ml of 0.1 M KCl, ultrasonicated for 5 min and vigorously stirred for 30 min to allow the exchange of the proton for K^+. The suspension was then titrated with a 0.01 M KOH aqueous solution, following the pH evolution with a WTW Sentix 41 pH electrode wired to a WTW pH 330i pocket meter. The $[H^+]$ was calculated as:

$$[H^+] = \frac{[KOH] \times V_{KOH}}{W_d} \qquad \text{eq. 2.4}$$

where [KOH] and V_{KOH} are the concentration and the volume of the KOH solution added to reach the equivalence point.

The procedure to measure the $[H^+]$ of the membranes was analogous, soaking the membranes in 2 M NaCl solution at room temperature under magnetic stirring for 24 h in order to promote the exchange of the protons by Na^+. After removing the membrane, the solution was then titrated with a diluted NaOH solution.

2.4.9 Hydrolytic properties (water uptake, hydration level and swelling)

The water uptake capacity (W) of the acid functionalized Ph-PMO was measured in powder compacts by comparing the wet weight W_w of the pellet, after stabilization in a closed vessel exposed to high r.h., and the dry weight W_d of the sample after drying under vacuum at 60 ºC for 4 h. It was found that this method provided more consistent and reproducible results than the TGA data. So this weighting method was the one chosen for calculating W.

For the membrane materials the method used was in all similar but the W_w was obtained by soaking the membrane in ultrapure water at room temperature for 24 h. Before weighing the W_w of the membranes, these were lightly pressed between two sheets of absorbent paper to remove excessive surface water. The W was then calculated as:

$$W = \frac{W_w \times W_d}{W_d} \times 100 \qquad \text{eq. 2.5}$$

The swelling of the membranes (upon adsorption of water) was calculated from the difference in thickness (measured with a micrometer - precision of 0.01mm) between the swelled membrane (kept in saturated water vapour conditions until stabilization) and the dry membrane (dried under vacuum for 4 h at 60 ºC). For the calculation of the swelling %, an analog to eq. 2.5 was used.

The hydration level (λ) of the membranes, which represents the number of water molecules per acid group, was calculated based on the measure of W and $[H^+]$ of the membranes as:

$$\lambda = \frac{W}{MH_2O} \times \frac{1000}{[H^+]} \qquad \text{eq. 2.6}$$

where M H_2O is the molar mass of water (18.02 g·mol^{-1}).

2.4.10 Dynamic light scattering

The dynamic light scattering (DLS) technique was used to assess the average particle size of the acid functionalized Ph-PMO particles. All the suspension of particles or molecules experiences Brownian motion. Upon the illumination with a laser beam, the different particles in suspension will scatter the light with different intensities, which is dependent upon the size of the analysed particles. The analysis of these intensity variations enables the calculation of the Brownian motion velocity and the diffusion coefficient can be retrieved using the Stokes-Einstein relationship. The size of the particles is then calculated using:

$$D = \frac{kT}{6\pi\eta r} \Leftrightarrow d_p = \frac{kT}{3\pi\eta D} \qquad \text{eq. 2.7}$$

where d_p is the average diameter of the particles, k is Boltzmann's constant, η is the viscosity of the media and D is the diffusion coefficient. The particle diameter estimated from the DLS measurements is in fact a hydrodynamic diameter and it is related to the way that the particles diffuse within a fluid. The actual value of the diameter obtained by this technique is that of a spherical particle that shows the same translational diffusion coefficient as the particle analysed.[254]

The DLS measurements were carried out on a Zetasizer Nano ZS (Malvern instruments). Prior to the measurements, the samples where thoroughly grinded in an agate mortar, lightly dispersed in ultrapure water and finally ultrasonicated for 10 min. DLS measurements where repeated for at least five times for each sample.

2.5 Electrochemical impedance spectroscopy

The electrical behaviour of powder compacts and composite membranes was carried out by electrochemical impedance spectroscopy (EIS), which was one of the most extensively used techniques in this work.

2.5.1 Fundamentals

Electrochemical impedance spectroscopy is a powerful technique for the electrochemical characterization of electrolytes and electrolyte/electrode interfaces, particularly because it allows conveniently separating the contributions of these processes to the total impedance, each with a distinct time constant (or characteristic relaxation frequency ω_0). The use of an alternate current (AC) minimizes the impact of the electrode polarization.

The basic principle of this technique consists in applying a small sinusoidal signal *v(t)* with amplitude V_m

$$v(t) = V_m \sin(\omega t) \qquad \text{eq. 2.8}$$

at a frequency $f=\omega/2\pi$, resulting in alternate current

$$i(t) = I_m \sin(\omega t + \vartheta) \qquad \text{eq. 2.9}$$

where ϑ represents the phase angle between the applied voltage and the resulting current. It is perhaps interesting to notice the analogy between the EIS and DMA.

The concept of impedance is a more general concept than resistance because it takes into account the differences in phase. A planar vector in an orthogonal system can have its magnitude and direction represented as a complex number:

$$Z = Z' + iZ'' \qquad \text{eq. 2.10}$$

in which $i = \sqrt{(-1)}$, *Z'* is the real part of *Z* in the direction of the x axis and *Z''* is the imaginary part along the y axis. Figure 2.5 represents the impedance as a planar vector with rectangular and polar coordinates.

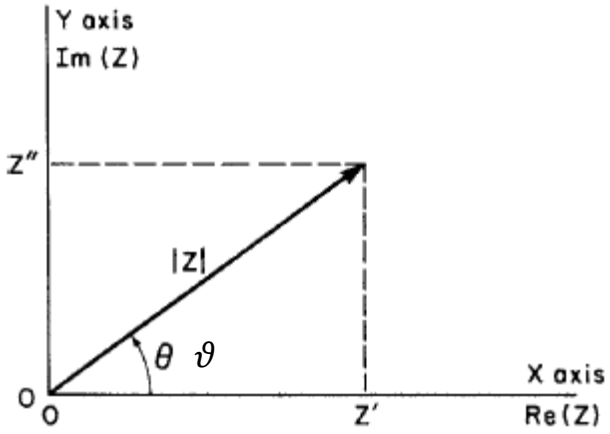

Figure 2.5. Impedance plotted as a planar vector. Adapted from[255].

The rectangular coordinates can be calculated as:

$$Z' = |Z| \cos \vartheta \qquad \text{and} \qquad Z'' = |Z| \sin \vartheta \qquad \text{eq. 2.11}$$

where,

$$\vartheta = \arctan (Z''/Z') \qquad \text{eq. 2.12}$$

One of the possible ways to represent an impedance plot is an extension of Fig. 2.5, where a series of points are taken from the magnitude and direction of the impedance vector as a function of frequency, normally in the range from few Hz to few MHz (Fig. 2.6). These so-called Nyquist plots are useful to identify physical processes occurring in the cell assembly during the measurements.

In most practical cases, the electrochemical cell can be represented as an equivalent circuit displaying the same impedance as the cell measured. In these circuits, a resistor element can represent the ohmic resistance associated to charge mobility or transference (e.g. accounting for the conductivity of the electrolyte or even a step in the electrode reaction), whereas capacitors and inductors are generally associated to non-ohmic phenomena related to charge accumulation (polarization).

In the case of a pure ohmic resistor, the impedance is independent of the frequency and ϑ=0, hence $Z=|Z|=R$. For a purely capacitive element, the phase shift is –90 º and the total impedance has only an imaginary contribution given by $Z_C = -i/\omega C$,

where C is the capacitance. For an inductor, the impedance has also an imaginary contribution but the phase shift is +90 °, and hence $Z_L = i\omega L$, where L is the inductance.[256] However, real electrode/electrolyte systems are normally composed by ohmic and capacitive contributions, whereas inductive features may be also observed usually resulting from the wires of the experimental set-up.

Different phenomena may have significantly different relaxation frequencies that can be distinguished on an impedance spectrum, provided that the frequency range is large enough. The Nyquist plot presented in Fig. 2.6 is representative of a sample with two phenomena in series. This type of behaviour can be described by an equivalent circuit model comprising a series of two parallel resistor and capacitor elements (RC+RC). The left semi-circle, corresponding to higher values of frequency, is related to the ohmic resistance of the system R_1, that is, to the response of the electrolyte. The other semi-circle can be related to an electrode or electrolyte/electrode interface polarization phenomenon, non-ohmic in nature as the amplitude of the contribution changes with the applied signal amplitude.

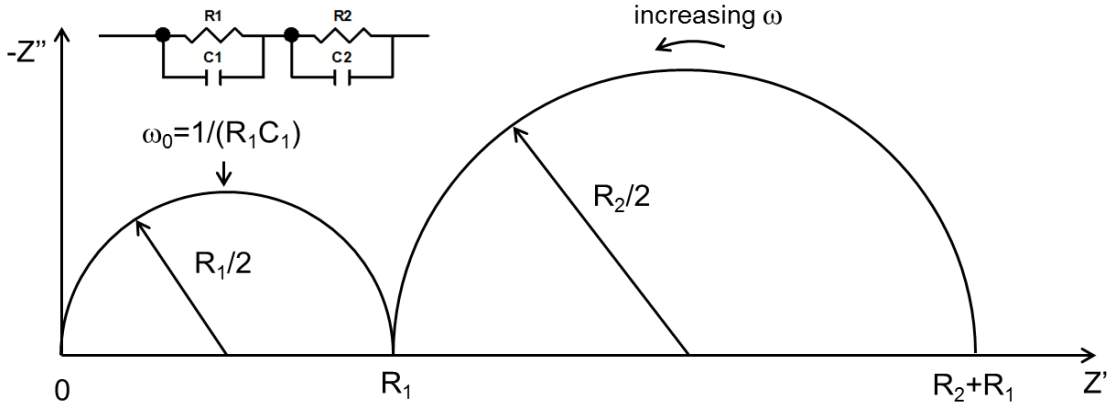

Figure 2.6. Representation of the impedance spectrum of an R_1C_1-R_2C_2 equivalent circuit.

The dielectric relaxation frequency in both cases is given by:

$$\omega_0 = \frac{1}{RC} \qquad \text{eq. 2.13}$$

which corresponds to the frequency value at the peak of the semicircle (*Z*'' maximum). It may be seen as a characteristic fingerprint of the phenomenon originating the impedance.

In many cases, as in the majority of the measurements obtained in this work, the relaxation frequency of the proton conduction phenomenon through the electrolyte is so high that the complete semicircle is not (or only partly) observed within the frequency range available. This affects the accuracy of the determination of *R* and is the main reason for the use of an alternative setup for the EIS study of the membrane, as discussed in the next sub-section.

The semicircles related to the impedance of the electrolyte, when visible, are quite often depressed in the sense that the centre of the semicircle lies below the real axis of the spectrum, with which it describes a specific angle τ. This depression can occur due to the contribution of several phenomena with different relaxation frequencies for the impedance semicircle, moving the system away from ideality (Fig. 2.7)

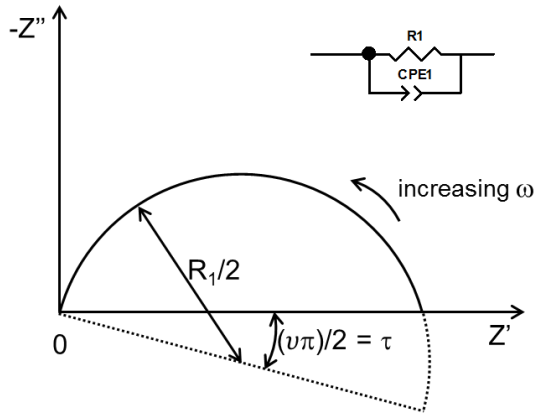

Figure 2.7. Representation of the semi-circle depression affecting the impedance of the electrolyte.

In the special case of a polymer electrolyte this happens quite often due to the presence of non-conductive regions, which makes the path of the charge carriers longer than the distance between the electrodes.[257] From a mathematical point of view, the capacitor in the equivalent circuit can be replaced by a constant phase element (CPE). The physical interpretation of this element varies, but it has been often used in the analysis of electrochemical systems. The impedance of the CPE is defined by:

$$Z_{CPE} = \frac{1}{Y_0(i\omega)^a} \qquad \text{eq. 2.14}$$

where Y_0 is the admittance and

$$a = 1 - \frac{2\tau}{\pi} = 1 - \upsilon \qquad \text{eq. 2.15}$$

represents the angle shift between the centre of the semicircle and the real axis of the complex plane. The relaxation frequency is related to these two parameters as:

$$\omega_0 = (RY_0)^{\frac{1}{a}} \qquad \text{eq. 2.16}$$

It is possible to calculate the true capacitance:

$$C = R^{\frac{1-a}{a}} Y_0^{\frac{1}{a}} \qquad \text{eq. 2.17}$$

and the impedance of an equivalent circuit composed by a CPE and a resistor can be described as:

$$Z_\omega = \frac{R}{1 + \left(i\frac{\omega}{\omega_0}\right)^{1-\upsilon}} \qquad \text{eq. 2.18}$$

where $0 \leq \upsilon \leq 1$.

2.5.2 Measurements with different sample geometries

The electrochemical impedance spectroscopy analysis of the acid-functionalized Ph-PMO was carried out in disc-shaped powder compacts obtained by pressing ~50 mg of powder in a 1 cm dye using 150 MPa of uniaxial pressure, and then with 300 MPa of isostatic pressure to enhance the mechanical stability and the density of the pellets. The apparent density of the compacts was ~0.9 g·cm^{-3}, calculated from the mass and

geometry of the pellets. Electrodes were applied to both sides of the pellets by painting a conductive silver paste (Agar Scientific) and drying in an oven at 60 °C overnight, to evaporate the organic solvents and to cure the paint. The area of the electrodes was calculated from a scaled photography, using the software Image J (version 1.45s).[240] The pellets with the silver electrodes were sandwiched between two pieces of carbon paper GDL and two carved graphite pieces (for better distribution of water vapour) before being installed between the two platinum current collectors (see Fig. 2.8 A).

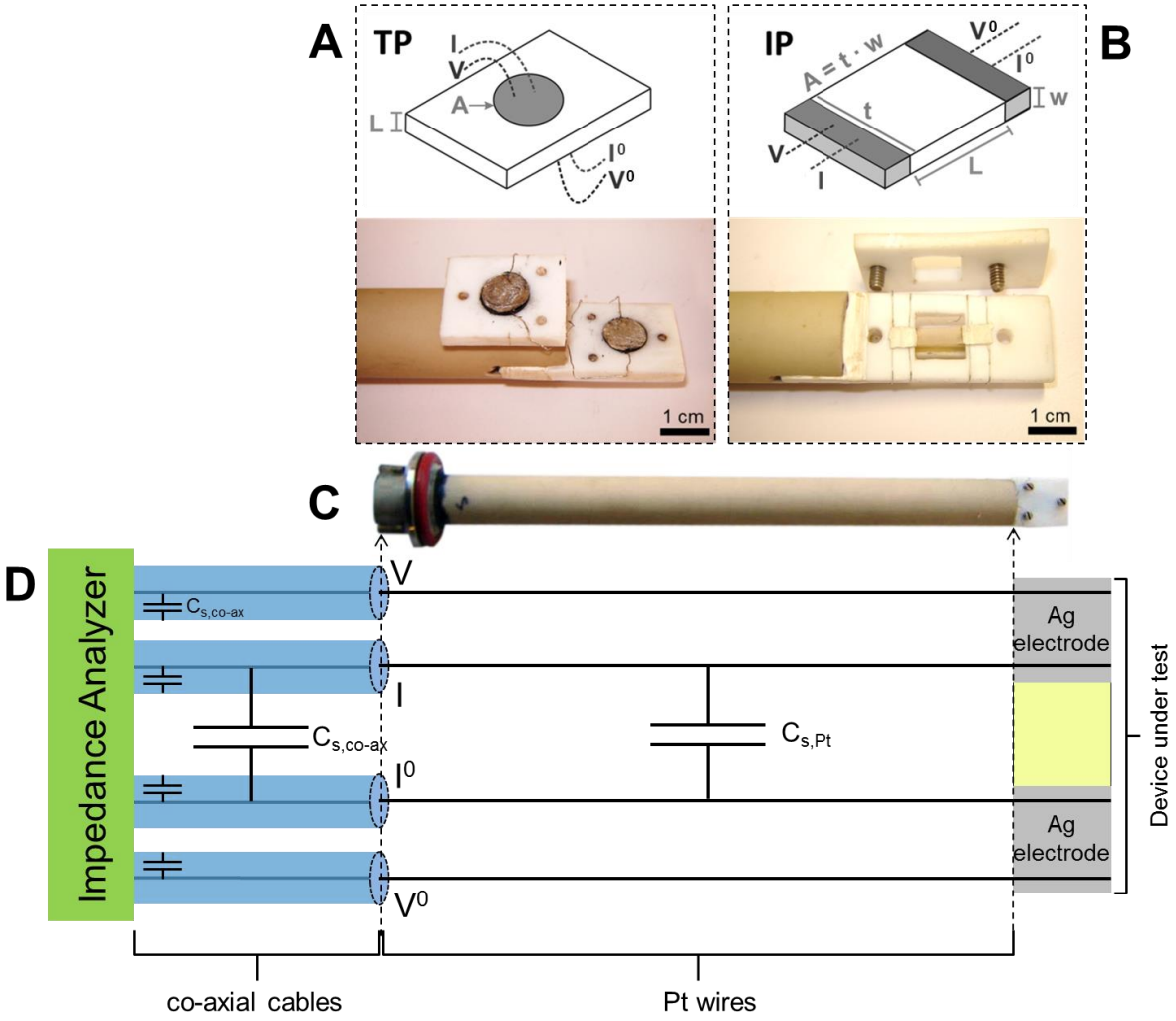

Figure 2.8. Schematic representation and photograph of the tip of the used in this work in the A) TP and B) IP configurations. C) photograph of the entire sample-holder and D) schematic representation of the sample-holder, portraying the inner Pt wires connected to the device under test to the right and to the co-axial cable to the left, which are then connected to the impedance analyser. Cables I and I^0 are twisted around each other to minimize the stray capacitance $C_{s.co\text{-}ax}$.

In the case of the membranes, the same general procedure of electrode application was used for the preparation of the samples for the through-plane (TP) measurements. For the in plane (IP) measurements, the sample consisted of a strip of membrane with ~1.5 cm in length by 0.5 cm in width. The tips of these pieces were fully covered by the silver paste and a free length of ~1 cm was left between these two electrodes. After drying the solvents overnight, the membranes were finally mounted in the sample holder, as depicted in the IP configuration of Fig. 2.8 B.

The measurements were made with a 4 cable configuration in order to keep the connection between the impedance spectrometer terminals and the electrodes separated right up to the closest as possible to the sample, in what is known as a pseudo 4-electrode configuration. Figure 2.8 (C and D) represents the entire sample-holder and a scheme of the internal wiring, depicting Pt wires (0.25 mm in diameter and ~22 cm in length) connected to the device under test on one side and to the co-axial cables (~1 m) on the other side, which are then connected to the impedance analyser. The scheme also represents the several stray capacitances expected from this type of configuration (inside co-axial cables, between co-axial cables and between Pt wires).

The impedance spectrometer used in this work was an Agilent E4980A, and the spectra were collected between 20 Hz and 2 MHz with variable test signal amplitude between 100 mV and 1 V.

The protonic conductivities of the samples were calculated using:

$$\sigma = \frac{1}{R} \times \frac{L_{el}}{A} \qquad \text{eq. 2.19}$$

where, R is the resistance of the powder compact or membranes, L_{el} is the distance between the electrodes and A is the area of the electrode, or the cross-section area of the membrane in the IP configuration (see fig. 2.8 A and B).

The precise determination of the membrane resistance needs some particular attention, especially due to the huge differences caused by the increase of r.h. on the shape of the obtained spectra. As the r.h. increases (normally above 40 - 60 %) the impedance spectra of the powder compacts and of the membrane in TP configuration are very similar and do not show the semi-circle contribution related to the ohmic

resistance of the electrolyte (inset in fig. 2.9) due to a high ω_0, well above the upper limit of the meter used in this work. The spectra are characterized by a dominant contribution assigned to the impedance of the electrode, which can be projected in the high frequency region to intercept the real axis, defining the value of *R* for the electrolyte. Additionally, the high conductivity of the materials combined with the reduced thickness of the samples (~0.1 cm for the powder compacts and ~100 μm for the membranes) leads to *R* values in the order of few Ω, or even less than 1 Ω in the membranes under high r.h. This is regarded as an important limitation that ultimately can affect the precision of the measurement.[258] A more precise determination of the resistance of the membranes is possible by using the IP measurement configuration. Due to higher L_{el} and lower *A* (eq. 2.19) the expected *R* is up to 2-3 orders of magnitude higher in the same temperature and r.h. conditions, which can be determined without the need to extrapolate high frequency data. In fig. 2.9 one can see the typical impedance spectra for powder compacts and membranes in the TP and for the membranes in IP configuration at 80ºC and 40 % r.h.

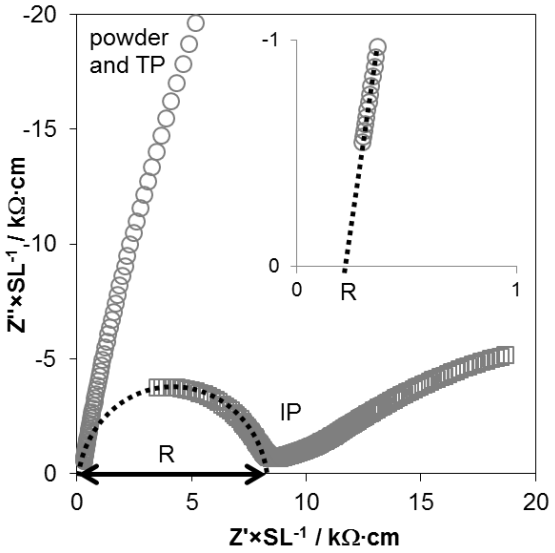

Figure 2.9. Typical impedance spectra for powder compacts and membranes in TP and IP configuration.

The IP spectra are constituted by a semicircle in the high frequency regions followed by a large contribution related to the impedance of the electrode. The values of *R* were calculated by fitting the spectra with an equivalent circuit model consisting of a series

association of two parallel R/CPE elements, using the software ZView version 3.0 (Scribner Associates).

Interestingly, the capacitive response of the system due to the proton relaxation phenomena in this kind of material (with ε in the range of 20 to 80) should be much lower than the capacitance predicted for the particular TP or IP sample geometry (as presented in table 2.1) according to:

$$C = \varepsilon \times \varepsilon_0 \times \frac{A}{L_{el}} \qquad \text{eq. 2.20}$$

where ε_0 is the vacuum permittivity. Likewise, the sample resistance can be estimated based on typical conductivity values using eq. 2.19, which can be combined with the capacitance values to obtain ω_0 (eq. 2.13). These estimates are also shown in table 2.1.

Table 2.1. Predictions of R, C and ω_0 for the different electrode configurations.

ε_r	TP configuration			IP configuration			
	$R(\Omega)$[b]	C(pF)	ω_0(GHz)	$R(\Omega)$[a]	C(fF)	ω_0(GHz)	ω_0^{stray}(MHz)[b]
20	4	2.82	88.5	6.67×10^4	2.82	5.30	1.5
40		1.41	177		1.41	10.6	1.5
60		0.94	266		0.94	15.9	1.5
80		0.71	354		0.71	21.2	1.5

TP (L_{el} = 100 μm and A = 0.5 cm^2) and IP (L_{el} = 1 cm and A = 3×10^{-3} cm^2).

a - calculated assuming σ = 0.05 S·cm^{-1} at 94 ºC and 40 % r.h.

b - calculated from a typical stray capacitance of 10 pF.

For the IP configuration, the predicted ω_0 values are in the GHz range, which is 3 orders of magnitude higher than the maximum frequency of the impedance spectrometer used in this work (2 MHz). This means the high frequency semi-circle observed in the IP spectra cannot be attributed to the electrolyte. The most likely explanation for this contribution is a stray capacitance (C_s) associated to the sample holder, more specifically the capacitance of the co-axial cables (about 1 pF) and particularly that resulting from the parallel Pt wires used to route the electrical signals to and away from the sample (see fig. 2.8 D). This C_s was measured with a dummy cell

and it was found to be ~10 pF which is very similar to the capacitance measured for the membranes with the IP configuration. Since C_s is in parallel and much higher than the expected sample capacitance (Table 2.1), the equivalent capacitance of the system ($C_{eq}=C_s+C$) will be dominated by C_s. As the IP resistance is much higher than the TP measurement, the resulting ω_0 related to the C_s is found in the frequency range of the impedance spectrometer (1.5 MHz, see table 2.1), resulting in the observable semicircle. The spectra obtained in the TP configuration, without detectable bulk capacitive contribution (inset in fig. 2.9), are in agreement with the predictions (table 2.1).

In some cases, normally at lower r.h., the TP membrane and powder compact measurements can also show a semicircle in the high frequency region, but in this case it can be actually related to the electrolyte because R is a few orders of magnitude higher. For these contributions, the R values are retrieved using the same equivalent circuits as for the membranes in IP configuration.

2.5.3 Measurements under variable temperature and relative humidity

As said in the first chapter, the conductivity of the acid functionalized Ph-PMO and the Nafion® based membranes is highly dependent on the λ and on temperature, showing typical Arrhenius behaviour. Therefore, the study of the conductivity in different temperature and r.h. conditions is crucial to fully characterize the transport properties of these materials. The samples were analysed by EIS in the temperature range from 40 ºC up to 140 ºC and r.h. from 20% up to 98%.

Two climatic chambers were used for these measurements. One specially assembled in-lab, as depicted in Fig. 2.10, consisting of a stainless steel cylindrical chamber surrounded by a heating cartridge controlled by a proportional-integral-derivative controller (Eurotherm 3216). Next to this chamber, and connected to it by a series of Swagelok type 1/8'' tubing and fittings, are two stainless steel vessels mounted on a rack, being one of these vessels filled with a desiccating agent (silica-gel, Panreac), and the other with distilled water (Fig. 2.10).

An air stream generated by an electric pump with a controlled flow (measured in a rotameter and controlled by needle valves) is driven to one or the other vessel, ultimately forcing wet or dry air into the climatic chamber. The temperature of the wet vessel was independently controlled in order to adjust the relative humidity inside the chamber. This vessel temperature was kept slightly above the dew point to account for some temperature drop between the wet vessel and the climatic chamber.[259] Both the temperature and the r.h. were constantly monitored in the vicinity of the sample using a Rotronic HC2-IC102 probe, equipped with a Pt100 resistance thermometer (accuracy of ± 0.2 ºC) and a Hygromer®IN1 capacitive humidity sensor (accuracy of ± 1 to 2.5% from 0 to 100% r.h.).

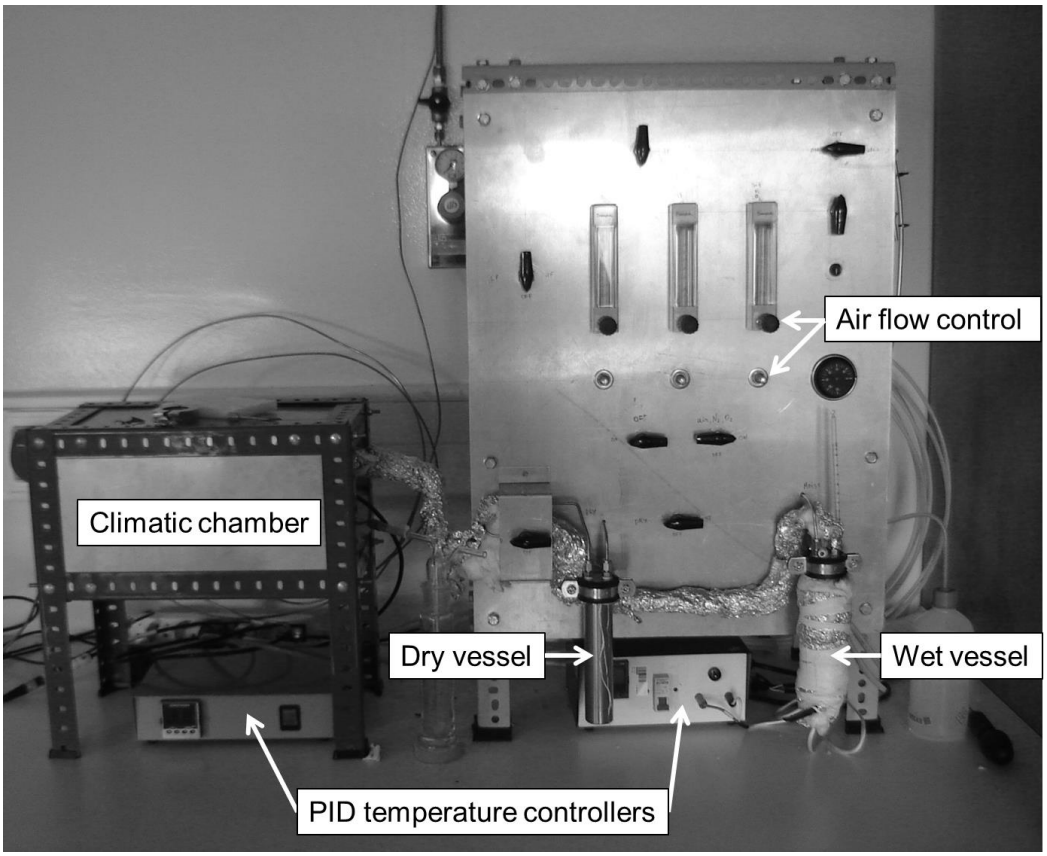

Figure 2.10. Climatic chamber apparatus for EIS measurements as a function of temperature and r.h.

An ACS Discovery 110 climatic chamber (T accuracy of ± 0.3 ºC and r.h. accuracy of ± 1 to 3% from 10 to 98% r.h.) was used at later stages of the research of powder compacts and for the great majority of the membrane samples, offering the possibility

of measuring 3 samples simultaneously (Fig. 2.11). The sample holders are connected to the impedance analyser via an electronic switch and the acquisition of data (with varying temperature and r.h.) can be made automatically.

Both systems are not adapted to operate under pressurized conditions, and thus the measurements above 100 °C were carried out only at the maximum possible r.h., corresponding to a water vapour partial pressure (pH_2O) of 1 atm (~40% and ~20% r.h. for 120 ºC and 140 ºC, respectively).

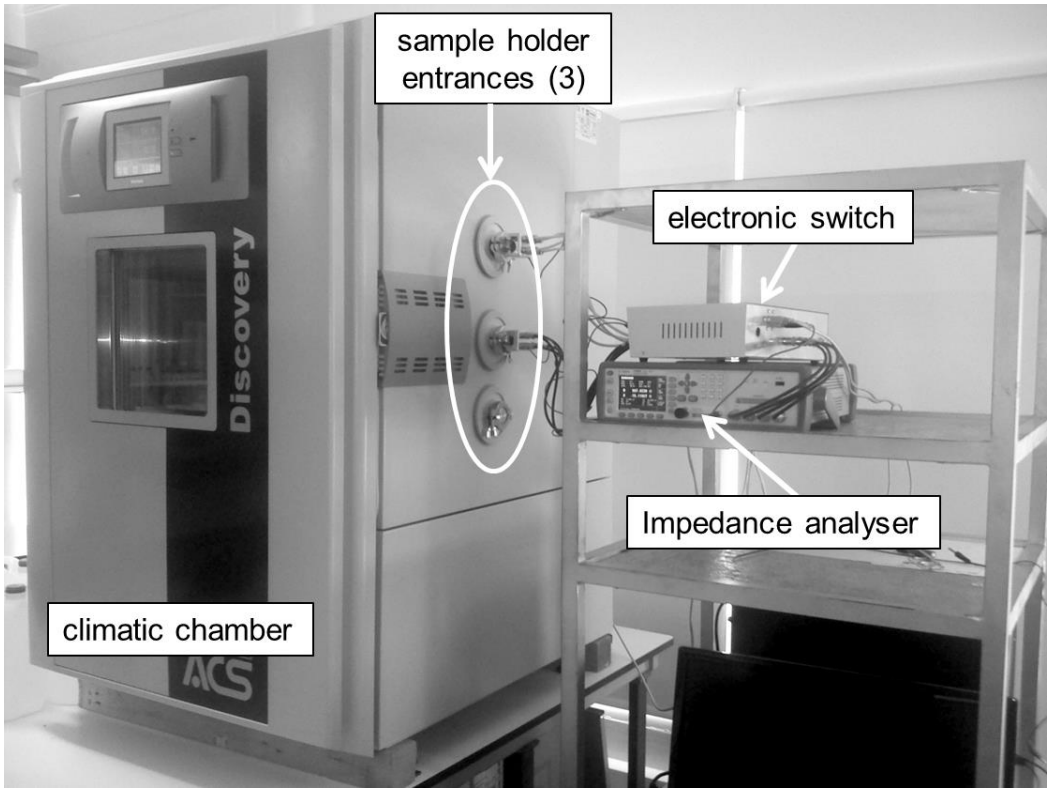

Figure 2.11. Setup for the EIS automatic data acquisition system, using the ACS climatic chamber.

3 RESULTS AND DISCUSSION

This chapter is divided in four main sub-chapters. The process of the choice of the protogenic group to functionalize the Ph-PMO, to be posteriorly used in composite membranes, is presented and discussed in the first sub-chapter. The second sub-chapter is dedicated to the structural and microstructural characterization of the S-Ph-PMO synthesized by both conventional and microwave heating methods, including a multivariate analysis of the influence of microwaves on the reaction kinetics. The relationships between the structure, microstructure and the protonic conductivity of S-Ph-PMO are analysed in the third sub-chapter, as a function of temperature and relative humidity. The most conductive fillers were used to prepare composite S-Ph-PMO/Nafion® membranes and their microstructure/property relationships are analysed in the last sub-chapter, again as a function of temperature and relative humidity.

3.1 The choice of the protogenic group

The choice of the protogenic group was made from two initial options: sulfonic acid, as the most common option found in the literature, and phosphonic acid, so far not used to functionalize Ph-PMO. The synthesis and characterization of the two types of mesoporous materials is described in this section based on a preliminary study of the structure, microstructure and protonic conductivity.

The full list of the prepared samples is presented in Table 3.1 according to the acronyms defined in section 2.2 and including a summary of the synthetic conditions, whereas Table 3.2 summarises the main obtained results.

Table 3.1. List of prepared Ph-PMO samples functionalised with sulfonic (prefix S-) and phosphonic (prefix P) acid groups.

Sample	acid precursor (mol. %)	SDA	self-assembly		hydrothermal treatment		Extraction type	Oxidation/ acidification type
			time (h)	type	time (h)	type		
S-C2M3	MPTMS(50)	C18	2	C	3	M	M	M
S-MS2M3	MPTMS(50)	C18	2	MS	3	M	M	M
S-C24M3	MPTMS(50)	C18	24	C	3	M	M	M
no-acid	n.a	C18	24	C	24	C	C	C
P10%-P123	PSiP (10)	P123	24	C	24	C	C	C
P20%-P123	PSiP (20)	P123	24	C	24	C	C	C
P50%-P123	PSiP (50)	P123	24	C	24	C	C	C
P10%-SHS	PSiP (10)	SHS	24	C	24	C	C	C
P20%-SHS	PSiP (20)	SHS	24	C	24	C	C	C
P50%-SHS	PSiP (50)	SHS	24	C	24	C	C	C
P50% no-surf.	PSiP (50)	n.a	24	C	24	C	C	C

Table 3.2. Summary of the main obtained results, including a_0, S_{BET}, average pore size, wall thickness, $[H^+]$, W, protonic conductivity at 94 ºC and 98% r.h. and corresponding E_a.

Sample	a_0 (nm)*	S_{BET} ($m^2 \cdot g^{-1}$)	Avg. pore size (nm)	Wall thickness (nm)	$[H]^+$ ($mmol \cdot g^{-1}$)	W (%)	σ ($S \cdot cm^{-1}$)	E_a ($kJ \cdot mol^{-1}$)
S-C2M3	4.95	774	3.37	1.58	0.30	48.3	8.9×10^{-4}	11.9
S-MS2M3	4.55	715	3.15	1.40	0.58	66.5	2.6×10^{-3}	18.7
S-C24M3	5.15	623	3.15	2.00	0.77	64.6	1.0×10^{-2}	6.43
no-acid	5.20	757	2.80	2.4	0	69.8	5.4×10^{-4}	24.1
P10%-P123	8.86	616	3.34	5.52	0.24	45.4	2.1×10^{-4}	34.4
P20%-P123	10.3	506	3.99	6.31	0.62	39.2	4.2×10^{-5}	n.a.
P50%-P123	11.9	82.0	3.42	8.48	1.83	27.3	4.1×10^{-6}	11.6
P10%-SHS	7.61	1000	**	n.a.	0.25	60.8	3.1×10^{-4}	n.a.
P20%-SHS	6.98	730	**	n.a.	0.55	56.8	9.1×10^{-4}	n.a.
P50%-SHS	n.a.	28.0	n.a.	n.a.	1.05	26.9	3.8×10^{-6}	23.9
P50% no-surf.	n.a.	27.0	n.a.	n.a.	1.54	46.0	4.1×10^{-6}	49.8

* $a_0 = 2d_{100}/\sqrt{3}$ ** large distribution.

3.1.1 Composition, structure and microstructure

The XRD patterns presented in Fig. 3.1 show the main diffraction peak at $2\theta \approx 2^\circ$ for S-Ph-PMO (Fig. 3.1 A), at $2\theta \approx 1^\circ$ for P123 P-Ph-PMO (Fig. 3.1 B), and at $2\theta \approx 1.3^\circ$ for the SHS P-Ph-PMO samples (Fig. 3.1 C). In all cases this peak corresponds to the (100) reflection of the hexagonal array of pores (space group *P6mm*).[89,130] The additional (110) and (200) reflections could not be detected, probably due to the small coherent diffraction ordered domains of the materials.

For several samples, the hexagonal array of pores was confirmed by TEM and one can thus confidently index the XRD patterns in the *P6mm* space group in order to estimate the lattice parameter, a_0, listed in Table 3.2.

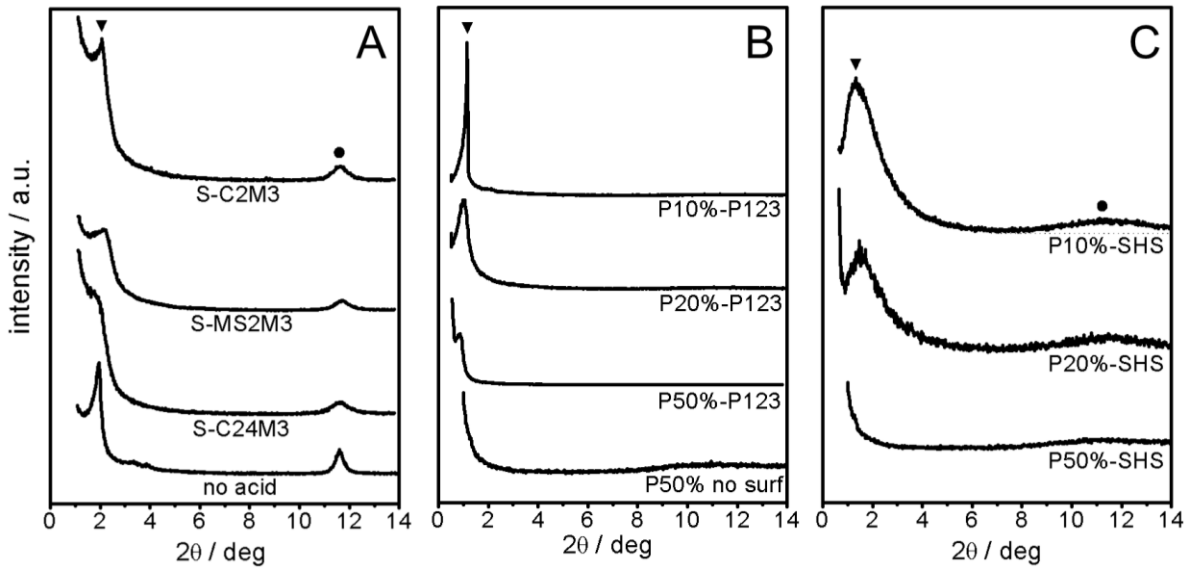

Figure 3.1. XRD diffractograms of a) S-Ph-PMO, b) P-Ph-PMO (P123) and c) P-Ph-PMO (SHS) samples.

The a_0 values of the P-Ph-PMO materials can be explained primarily by the much larger size of the P123 template molecule when compared to C18. Likewise, the intermediate size of the SHS leads to intermediate a_0 values. Other factors such as the nature of templates (neutral amphiphilic P123, and cationic surfactant C18) and the pH of the synthesis media (acidic for P123 and basic for C18) may also have a deciding effect.

The sulfonic acid-based materials are characterized by hierarchical structural order, combining the organized hexagonal pore structure with a molecular-scale periodicity along the pore wall, which is apparent in characteristic peak at $2\theta \approx 11.6^{\circ}$. Conversely, the phosphonic acid-based samples synthesized with the P123 as SDA did not show any additional diffraction peaks besides the one due to the hexagonal array of pores. The lack of periodicity along the pore wall was expected since the supramicellar structure of the non-ionic tri-block co-polymer P123 does not favour the alignment of the hydrophobic and hydrophilic domains in such a way that the coherent volume is enough to cause a diffraction peak to appear in the diffractogram.[260] In the case of P-Ph-PMOs prepared with SHS as SDA, the diffraction patterns display a broad bump in the angles corresponding to the meso- and molecular-scale periodicity, but their

intensity is indeed very low to actually be considered indicative of a constructive diffraction.

As expected, the final concentration of the acid groups increases with increasing concentration of the acid precursor (clear in the case of the P-Ph-PMO materials) or with the extension of the reaction time (visible in the S-Ph-PMO series). The $[H^+]$ has a significant impact on the shape of the XRD patterns, showing a decrease of the intensity of the pore order peak with higher incorporation of acid groups (Table 3.2). This may be a real structural effect or, as suggested by others,[130,261] it may be due to the reduction of the X-ray scattering contrast between the organosilica walls and the pore-filling ligand. Furthermore, in the case of the S-Ph-PMO, the reduction of the intensity of the peaks may be due to the fact that the MPTMS precursor has only three hydrolysable groups versus six in the BTEB precursor. Consequently, when MPTMS is co-condensed with the BTEB, the degree of cross-linking decreases, leading to a less ordered mesostructure.[262] This issue will be discussed again in face of N_2 sorption and TEM data.

Figure 3.2A shows the solid state ^{13}C CP-MAS NMR and ^{29}Si CP-MAS NMR spectra of the sample S-C2M3ext. The expected chemical environments of benzene, mercaptopropyl and silicate groups are confirmed. The ^{29}Si CP-MAS NMR spectrum depicts three signals at $\delta \approx$ -80.9, -70.5 and -59.4 ppm, that can be assigned to the connectivity of Si to benzene (T^3 at $\delta \approx$ -80.9 and T^2 at $\delta \approx$ -70.5 ppm), and to the mercaptopropyl group ($T^{3'}$ at $\delta \approx$ -70.5 and $T^{2'}$ at $\delta \approx$ -59.4 ppm) where T^n and $T^{n'}$ signals are for benzene and mercaptopropyl respectively (R groups) according to the general formula $R\text{-}Si(OSi)_n(OH)_{3-n}$. The attribution of the phenylene linked Si peaks is based on observations made by Yang *et al.*[130] in S-Ph-PMO materials. The attribution of the mercaptopropyl linked Si peaks is analogous to the one made in this reference also, and it can be confirmed by the observations made by Margolese *et al.*[128] and Nakamura *et al.*[263] in pure Si mesoporous materials functionalized with MPTMS. They identified $T^{3'}$ and $T^{2'}$ ^{29}Si NMR signals, with peaks at $\delta \approx$ -65 and $\delta \approx$ -57 ppm, which are somehow deviated from our values but still in accordance, taking into account the different chemical environment introduced by the altered framework composition.

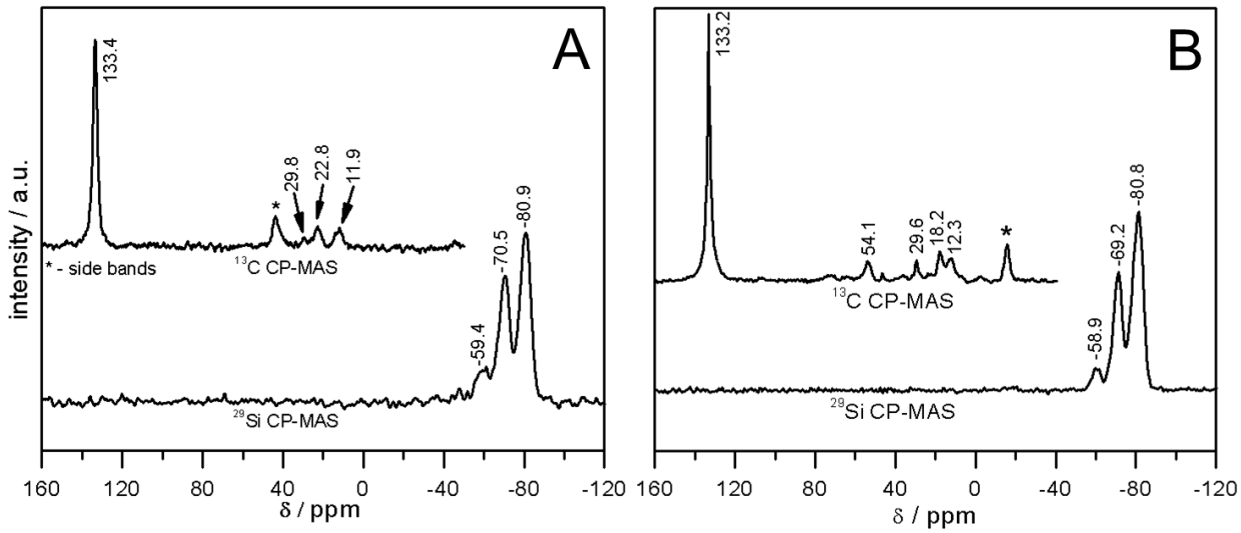

Figure 3.2. ^{13}C and ^{29}Si CP-MAS NMR spectra for sample A) S-C2M3ext and B) S-C2M3ox. Peaks indicated as * in D are spinning side-bands.

No Q^n signals, corresponding to silicon atoms connected entirely to the OSi and/or OH units are detected, which indicates that the Si–C bond cleavage did not take place during synthesis.[86, 130] The ^{13}C CP-MAS NMR spectrum displays the main peak at 133.4 ppm due to the carbon atoms of the benzene ring, and three other peaks at 29.8, 22.8 and 11.9 ppm that can be assigned, respectively, to the -CH_2- linked to the thiol group; -CH_2- in the middle of the propyl chain and the -CH_2- bonded to the Si atom of the mercaptopropyl ligand.[128,130,264]. Looking at Fig. 3.2 B, which shows the solid state ^{13}C CP-MAS NMR and ^{29}Si CP-MAS NMR spectra of the sample S-C2M3ox, the only obvious difference is the presence of an extra peak on the ^{13}C CP-MAS NMR spectrum due to a high chemical shift of the terminal -CH_2- ($\delta \approx 54.1$ ppm) in this case linked to a -SO_3H group instead of -SH. However, the enduring peak at $\delta \approx 29.6$ can be assigned to the resonance of the -CH_2- connected to the remaining -SH groups which is an indication that the oxidation process did not occur completely.[128]

Typical solid-state NMR spectra for the P-Ph-PMO acidified samples are shown in Fig. 3.3, again for few representative examples (A and B - P20%-P123; C and D – P20%-SHS).

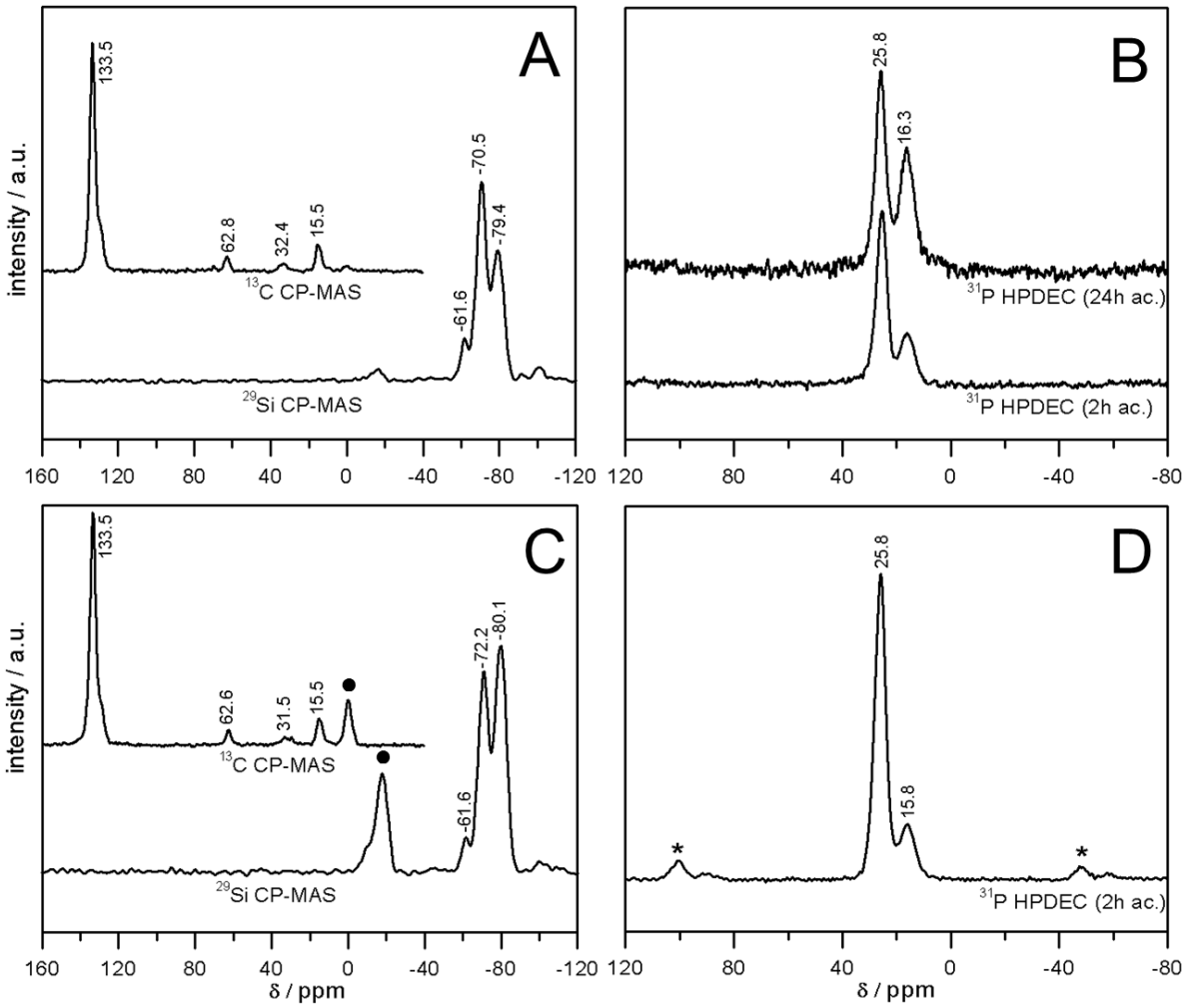

Figure 3.3. ^{13}C and ^{29}Si CP-MAS NMR spectra for sample A) P20%-P123 and C) P20%-SHS. ^{31}P HPDEC NMR spectra for sample B) P20%-P123 acidified for 2h and 24h and D) P20%-SHS acidified for 2h. Peaks marked with ● in C are relative to silicone grease used in the synthesis of the precursors.[265,266] Peaks indicated as * in D are spinning side-bands.

The ^{29}Si CP-MAS NMR spectra for both sample (Fig. 3.3 A and C) depict three resonance peaks at $\delta \approx$ -80, -71 and -62 ppm that can be assigned to T^3, T^2 and T^1 substructures respectively (T^n – Ph-Si$(OH)_{3-n}(OSi)_n$).[138,245] The absence of Q^n signal confirms the preservation of the Si-C bond during the co-condensation and consecutive steps. The ^{13}C CP-MAS NMR spectra for the same samples show resonances a $\delta \approx$ 133.5 ppm (benzene ring carbon), $\delta \approx$ 63 (carbon of the P-O-$\underline{C}H_2$- of the remaining ethoxyl groups), $\delta \approx$ 32.5 ppm (carbon connected to the phosphorous atom P-$\underline{C}H_2$-Ph) and $\delta \approx$ 15.5 ppm (-CH_3 carbons connected of the remaining ethoxyl

group).[244] The peaks at $\delta \approx 63$ and $\delta \approx 16$ ppm are an indication that the acidification has not been completed.

The ^{31}P HPDEC MAS NMR spectra of sample P20%-P123 (Fig 3.3B) shows a peak at $\delta \approx 26$ ppm that can be assigned to the free R-P(O)(OH)$_2$ acid groups, and another peak at $\delta \approx 16$ ppm assigned to the acid bonded to surface silica as R-P(O)(OH)(OSi) or R-P(O)(OSi)$_2$. The intensity of the ~16 ppm peak increases with increasing acidification time, suggesting that free acid groups reacted with the silica surface,[245,246] thus lowering the overall [H$^+$]. For this reason, we decided to use the 2 h acidification process for all the P-Ph-PMO samples, as depicted in Fig. 3.3 D.

Figure 3.4 presents the N_2 sorption isotherms for the several studied samples. The data for S-Ph-PMO and the P-Ph-PMO-P123 depict type IV sorption isotherms, typical for mesoporous materials.[233]

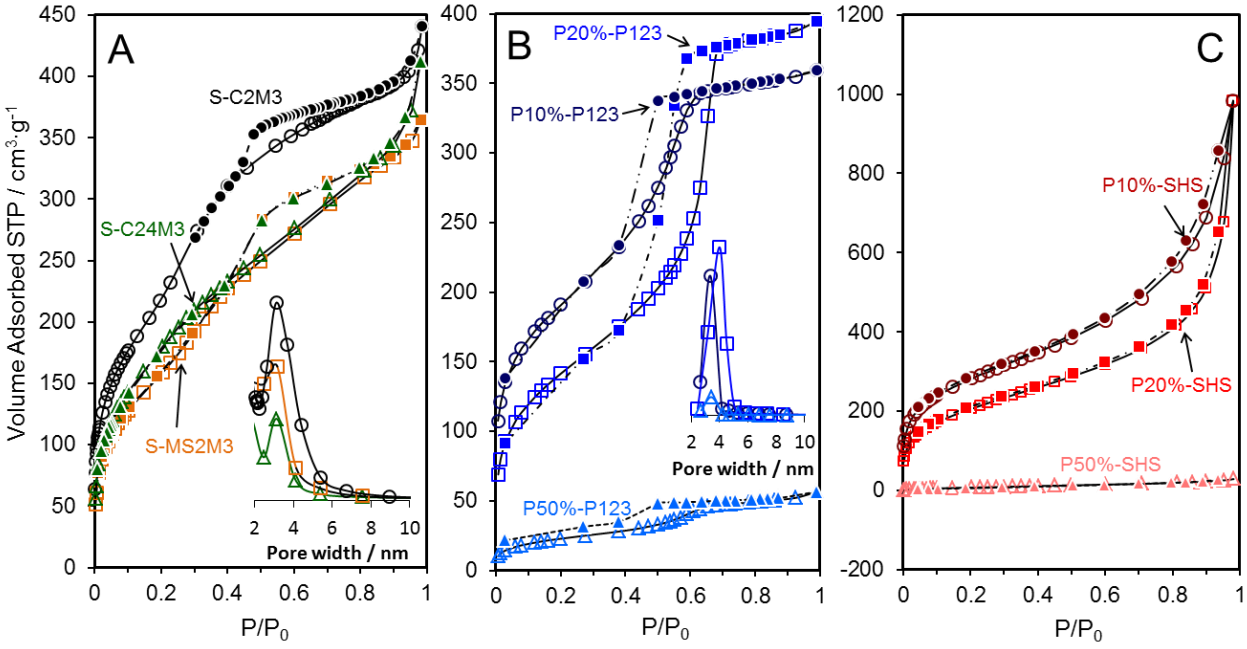

Figure 3.4. N_2 adsorption/desorption isotherms collected at -196 °C for the acid-functionalised materials: A) S-Ph-PMO-SO$_3$H, B) P-Ph-PMO-P123 and C) P-Ph-PMO-SHS samples. Empty symbols represent the adsorption data while full symbols represent the desorption data. The insets show the respective pore size distribution.

Although, according to XRD, there are no major differences between the structure of P-Ph-PMO made with P123 or SHS as SDA, the shape of the N_2 isotherms is fairly

different. The P-Ph-PMO-SHS show an atypical type IV N_2 sorption isotherm, much more similar to the type II isotherms. The hysteresis loop is very small, indicating that the condensation did not occur, or has occurred just in a small amount. The lack of a plateau in the high partial pressure region, right after the sharp increase of volume adsorbed, can be due to the presence of large pores, preventing the system of attaining saturation within the vapour pressure conditions of the measurement.

In fact, the pore size distribution of P-Ph-PMO-SHS samples show several broad peaks (not shown), unlike the clear unique peak observed for S-Ph-PMO and P-Ph-PMO-P123. The adsorbed N_2 volume at the intermediate flat region, corresponding to the monolayer formation, is clearly higher for the SHS samples than for the P-Ph-PMO-P123, thus suggesting a much larger micropore volume. Actually, the *t*-plot analysis of the sample P10%-SHS suggests a microporosity of 102 $m^2 \cdot g^{-1}$. Consequently, the total mesoporous volume should be smaller and probably less ordered, in agreement with the XRD patterns (Fig. 3.1 C). Nonetheless, the S_{BET} values for the samples with the lowest acid loading (10% and 20% sample) are quite high. Increasing the amount of the phosphonic acid precursor to 50% precludes the action of both SDAs (P123 and SHS) leading to very low values of S_{BET} and disordered structures, in agreement with the XRD diffractograms shown in Fig. 3.1 B and C. Obviously, the control sample P50%-no surf, synthesized without any SDA, showed the lowest S_{BET}. Since the average pore diameter is similar for both the S-Ph-PMOs and the P-Ph-PMO-P123 (Table 3.2), the thickness of the pore walls (taken as a_0 minus the pore diameter) is considerably larger in the phosphonic acid-based materials (~5-6 vs. ~2 nm). This large difference suggests a much less dense material in the case of the P-Ph-PMO when compared to the S-Ph-PMOs.

The overall description of the structure and microstructure obtained from the combined XRD and N_2 sorption data is fully confirmed by the TEM images shown in Fig. 3.5. The micrographs of S-Ph-PMO materials (Figs. 3.5 A and B) depict the expected channelled mesoporous microstructure and the hexagonal array of pores, looking down the (001) direction (insets). Similar channelled patterns are observed in the TEM images for P-Ph-PMO-P123 as SDA (Fig. 3.5 D), whereas the P-Ph-PMO-SHS samples are essentially disordered (Fig. 3.5C).

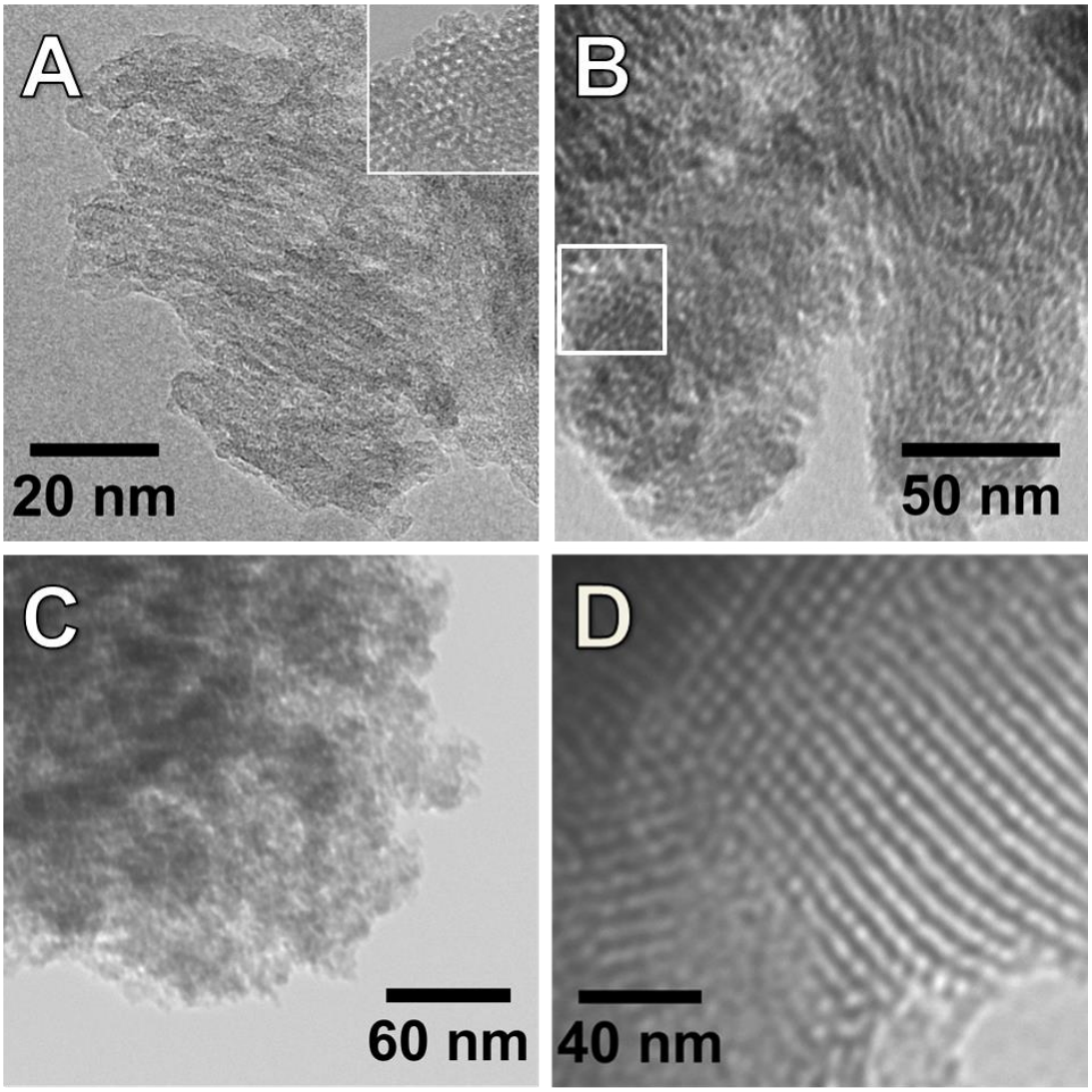

Figure 3.5. TEM micrographs of samples: A) S-MS2M3, B) S-C24M3, C) P10%-SHS and D) P20%-P123.

3.1.2 Protonic conductivity

The samples considered for this preliminary study were analysed by EIS in the form of powder compacts under variable temperature (40 to 100 ºC) and r.h. (20 to 98%) conditions. It should be noticed that due to experimental limitations, the measurements at the lowest temperature and nominal 98% r.h. were actually carried out at 94% r.h. Nonetheless, the influence of this difference should not be significant

and would always be pointed towards lower levels of conductivity than the real ones, also leading to slightly higher E_a.

A normalized representation of Nyquist plots is shown in Fig. 3.6 to illustrate the influence of r.h. on the shape of the impedance spectra. These are dominated by a large semicircle with amplitudes in the MΩ range (scale not shown due to normalization) at low r.h., being strongly reduced with increasing humidity.

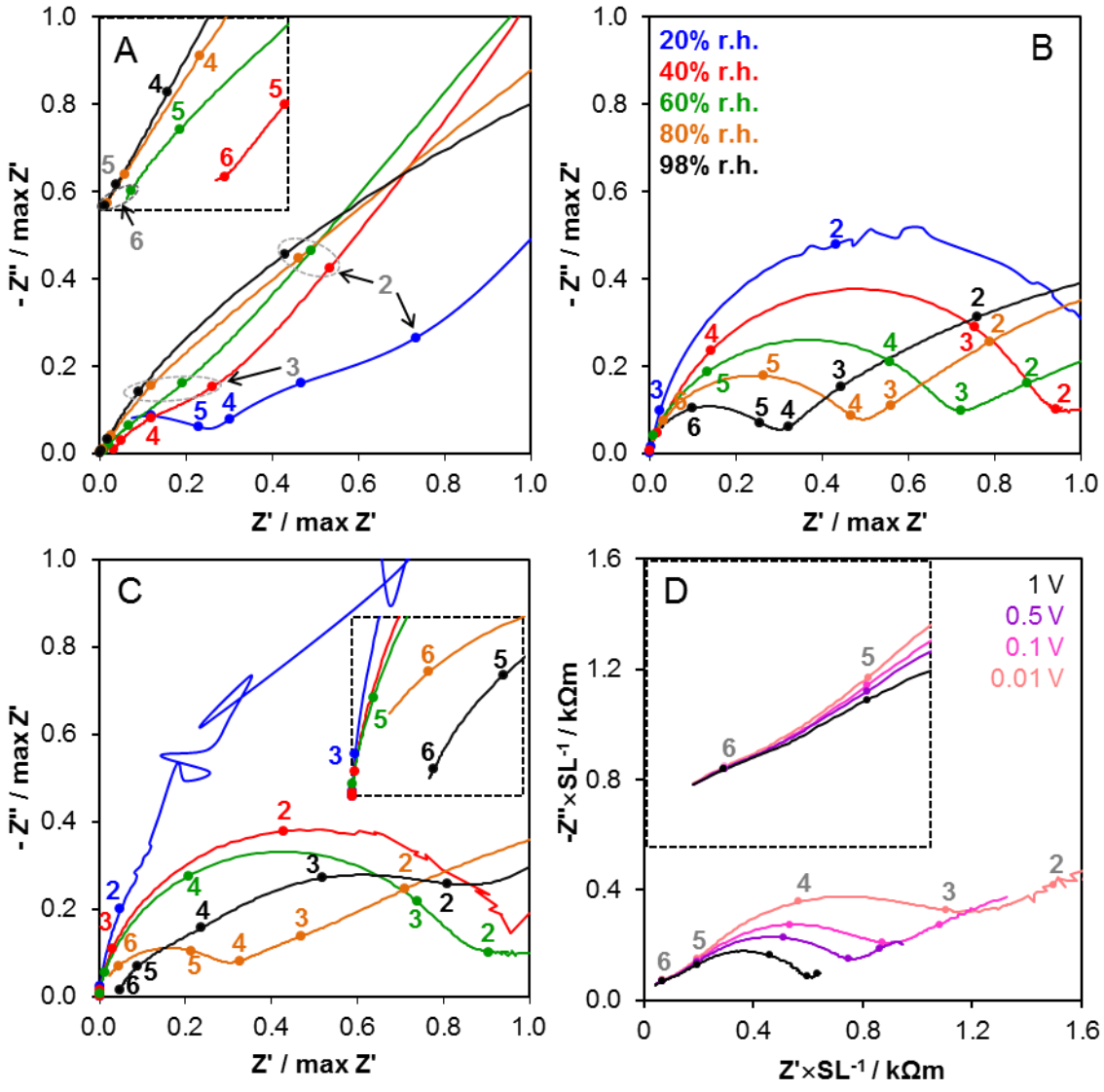

Figure 3.6. EIS spectra collected at 80 ºC showing the evolution of the shape with increasing r.h. for several representative samples: A) S-C24M3, B) P10%-P123 and C) P20%-SHS (obtained with a test signal amlpitude of 0.1 V). D) shows spectra for P-10%-P123 at 98% r.h. with variable test signal amplitude (numbers represent powers of 10 of frequency in Hz).

However, there are obvious differences in the shape of the spectra of S-Ph-PMO and P-Ph-PMO. In the former, the high frequency semicircle is no longer observed for r.h. ≥ 60%, depicting one single contribution that can be ascribed to the electrode impedance. These spectra do not intercept the real axis at high frequency (inset in Fig. 3.6 A), and thus the ohmic resistance may be assumed as the Z' value at the lowest phase angle, in the high frequency region.[129] The evolution of the P-Ph-PMO-P123 spectra follows a similar trend. However, under nearly saturated conditions, the spectra still displays three different contributions at high, intermediate and low frequencies with some degree of overlapping (Fig. 3.6 B). The behaviour of the P-Ph-PMO-SHS samples is similar to that of the P123-based materials, but with more overlapping phenomena (Fig. 3.6 C).

While the separation of the ohmic resistance of S-Ph-PMO materials is relatively straightforward (simply the high frequency intercept with the real axis), a fitting procedure was applied to the spectra obtained with different test signal amplitudes in the case of materials functionalized with phosphonic acid.

It was found that the high frequency contribution is independent of the test signal amplitude, as shown in Fig. 3.6 D. This is a strong indication that the intermediate and low frequency contributions are related to electrode phenomena, whereas the high frequency contribution corresponds to the ohmic resistance of the material. Due to the strong overlapping of the contributions and considering the complexity and the absence of a physical model for this particular system, the spectra were fitted with a simple equivalent circuit composed by two (RC+RC) series components (C is actually a CPE - constant phase element - to account for some depression of the semi-circle). The estimated resistance was then used to obtain the conductivity by taking into account the geometry of the samples (eq 2.18).

The conductivity data for P-Ph-PMO and S-Ph-PMO at 98% r.h. is plotted against the inverse of the temperature, and in several cases it indeed shows the expected Arrhenius behaviour, as depicted in Fig. 3.7. In general, the conductivity increases with increasing S_{BET} and $[H^+]$. For a similar $[H^+]$ and S_{BET} values, the highest conductivity registered is for materials with sulfonic acid as protogenic group.

The effect of the concentration of the acidic functional groups is best illustrated by the significant increase of conductivity (by more than 1 order of magnitude) in the series of three S-Ph-PMO samples (Fig. 3.7 A), which all have relatively similar S_{BET} values in the range of 620-780 m^2g^{-1}. Analogously to PFSA membranes, this demonstrates the active role of the acid groups in retaining water in the structure and ensuring proton solvation. In fact, the conductivity of the sample prepared without the acid precursor is comparable to that of the sample with the lowest $[H^+]$ (0.3 $mmol \cdot g^{-1}$), which suggests the existence of a critical percolation concentration above which the proton structural diffusion along the aqueous domains is facilitated. The E_a for the conductivity is lower than 20 $kJ \cdot mol^{-1}$ in all cases, which is similar to that measured for Nafion® in similar conditions. There is a slight tendency for a decrease of E_a with increasing $[H^+]$, although the differences are relatively small. For comparison, the Fig. 3.7 also shows the values obtained for Nafion® in the same conditions.

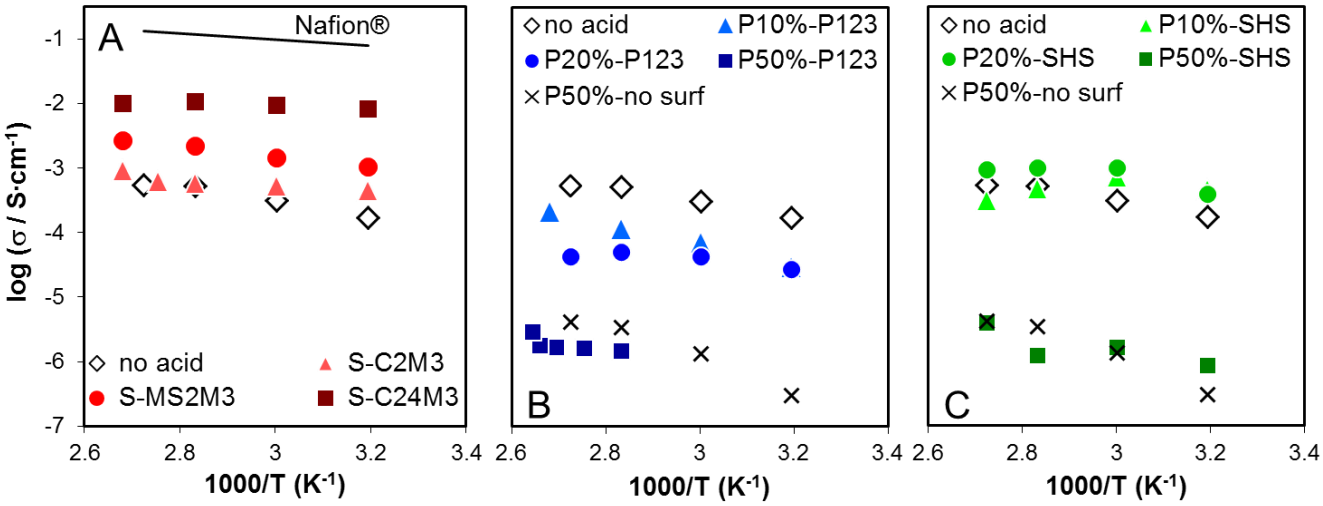

Figure 3.7. Arrhenius plots of the conductivity of several samples tested in the preliminary study, measured with increasing temperature at 98% r.h: A) S-Ph-PMO; B) P-Ph-PMO-P123; C) P-Ph-PMO-SHS.

The data for the P-Ph-PMO-P123 (Fig. 3.7 B) show the key influence of S_{BET}, with the lowest conductivity being paired to the lowest S_{BET} in sample P50%-P123 (82 $m^2 \cdot g^{-1}$ when the other samples have all more than 500 $m^2 \cdot g^{-1}$), in spite of the highest $[H^+]$ (1.83 $mmol \cdot g^{-1}$). This means that most of the functional groups are not accessible to the water vapour, thus drastically lowering the water uptake capacity of the material (Table 3.2) and hence the protonic conductivity of this sample.

The data in Fig. 3.7 C, for the P-Ph-PMO-SHS, also illustrates this effect, with samples P50%-SHS and P50%-no surf showing the lowest levels of conductivity due to the low S_{BET}, in spite on the considerably high $[H^+]$.

Surprisingly, the sample P20%-P123 does not show any increase in conductivity when compared to P10%-P123, although it has twice the $[H^+]$ and similar S_{BET}. Moreover, there is a clear deviation from the Arrhenius behaviour for r.h.> 40% for the sample with higher $[H^+]$, displaying an apparent decrease of E_a. One possible explanation for this somewhat unexpected behaviour is the degradation of the particle-particle contact with increasing r.h., negatively impacting the phase contiguity necessary for the ionic transport. However, no obvious modification of the sample microstructure could be detected after the measurements, and alternative explanations for this behaviour should be considered. Indeed, a similar trend is observed in the behaviour of the P-Ph-PMO-SHS, although with slightly higher conductivity values. The conductivity enhancement of the sample P20%-SHS with respect to P10%-SHS is surprisingly small, in spite of the much higher $[H^+]$. A deviation from the Arrhenius behaviour with apparent negative activation energy for r.h. higher than 40% is also observed, but in this case for both the P10%-SHS and P20%-SHS samples.

It is important to notice the slight advantage of the conductivity values of the SHS-based samples, very likely resulting from their higher S_{BET} in comparison to the P123-based materials, since the $[H^+]$ is similar.

All the mesoporous materials have been found to be difficult to press into handleable pellets. On the other hand, the densities of these pellets are all rather low at around 0.9 $g \cdot cm^{-3}$, certainly due to high volume of macro, meso and micropores. So, it is sensible to say that the conductivity values obtained for pelletized samples are underestimated.

Nonetheless, the comparison of S-Ph-PMO and P-Ph-PMO samples with similar $[H^+]$ and S_{BET} (e.g., S-C2M3 and P10%-P123) shows considerably better transport properties for the S-Ph-PMO. This may be due to the higher water retention capacity and to the strongest acidic characteristics of the sulfonic acid group, which is able to provide more extensive proton solvation in the presence of large amounts of water.[214]

The potential advantage of the more amphoteric character of phosphonic acid under low humidity conditions is here severely limited by the difficulties in obtaining materials with sufficiently high acid concentrations and high specific surface areas. In

fact, the conductivity values of the P-Ph-PMOs with the highest acid load (nominal 50% acid) are actually lower than that of the sample without acid (Fig. 3.7 A).

The dependence of the conductivity on r.h. is shown in Fig. 3.8. For the P-Ph-PMO samples, the data suggests a quasi-linear increase of the conductivity with increasing r.h., becoming sharper near saturated conditions, whereas the S-Ph-PMO shows a steep increase in conductivity between 20 and 60 % r.h., followed by a more moderate increase up to ~100%. These results, combined with the strong correlation of high S_{BET} / high conductivity, suggests that the water condensed on the mesoporous structure is the main contributor for the observed conductivity of P-Ph-PMO. It also means that the intrinsic proton mobility in P-Ph-PMO materials should be rather low. The most obvious explanation for such behaviour would rely on structural arguments, but the essentially amorphous structure prevents any analysis based on the available XRD, NMR and FTIR data. It may be speculated that the low proton mobility in the P-Ph-PMO is due to a structural arrangement that does not allow hopping between adjacent phosphonic acid groups, despite their relatively high concentration (Table 3.2)

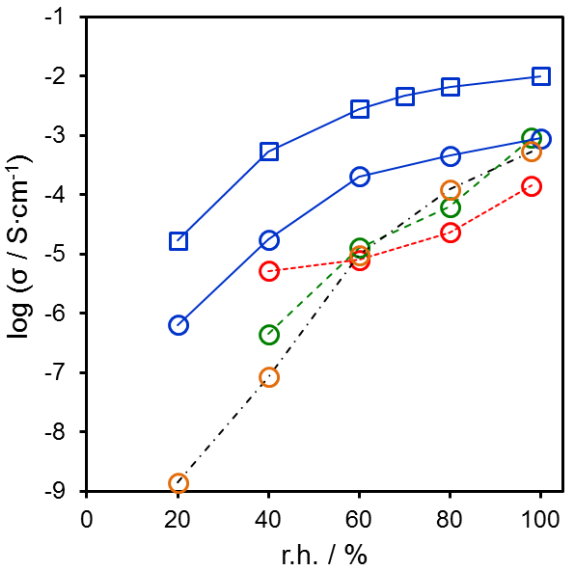

Figure 3.8. Influence of r.h. on the conductivity of □) S-C24M3, ○) S-C2M3, ○) P10%-P123, ○) P20%-SHS and ○) no-acid. Lines are for visual guidance.

The noticeable low conductivity of the P-Ph-PMO materials represents a severe disadvantage of these materials regarding their prospective application as fillers in improved Nafion® membranes. This had also implications for the work plan of the thesis, initially placing significant expectations in this new type of materials combining

the ordered mesoporous structure with the potential of the phosphonic acid as protogenic group. The work plan thus became primarily focused on the S-Ph-PMO materials.

3.2 Synthesis and characterization of S-Ph-PMO: effect of microwaves

This section presents and discusses the synthesis and the properties of S-Ph-PMO produced with a wide array of [H^+], S_{BET} and microstructural order, by conventional hydrothermal method and using MW as heat source. The complete list of the prepared samples and the processing conditions is shown in Table 3.3.

Table 3.3. List of prepared S-Ph-PMO samples divided in three groups according to the type of self-assembly and hydrothermal treatments.

Sample	self-assembly		hydrothermal		Extraction	Oxidation	Group
	time (h)	type	time (h)	type	type	type	
S-C24C24	24	C	24	C	C	C	A
S-C48C24	48	C	24	C	C	C	
no surf	24	C	24	C	C	C	
no-acid	24	C	24	C	C	C	
S-C0M1	0	C	1	M	M	M	B
S-C0M3	0	C	3	M	M	M	
S-C2M3	2	C	3	M	M	M	
S-C6M3	6	C	3	M	M	M	
S-C12M3	12	C	3	M	M	M	
S-C24M3	24	C	3	M	M	M	
C0M5	0	C	5	M	M	M	
C6M5	6	C	5	M	M	M	
C12M5	12	C	5	M	M	M	
S-MS0.5M3	0.5	MS	3	M	M	M	C
S-MS1M3	1	MS	3	M	M	M	
S-MS2M3	2	MS	3	M	M	M	
S-MS4M3	4	MS	3	M	M	M	
S-MS6M3	6	MS	3	M	M	M	
S-MS12M3	12	MS	3	M	M	M	

It is possible to separate the samples studied in three different groups, depending on the synthesis steps and the type of heating source. A first group (A) includes the samples produced using conventional heating in all the steps of the synthesis (acronyms of type CxCy). This group also includes control samples "no-acid" (S-Ph-PMO without any acid precursor) and "no surf" (material made in absence of SDA). The second group (B) consists of samples processed with a combination of conventional heating during the initial self-assembly step and MW for the all the other steps (CxMy). Finally the third group (C) includes the samples that were totally synthesized using MW (MSxMy).

3.2.1 Surfactant extraction and oxidation

According to the literature, the as-synthesized Ph-PMO powders need a EtOH/HCl reflux treatment of at least 8 h to fully remove the surfactant from the pores.[90] Moreover, in the case of C18, the procedure must be repeated. Smeulders *et al.*[161] successfully used a single MW step of 15 min to perform the extraction of the surfactant in pristine Ph-PMO. In the case of our acid-functionalized materials, the application of MW in the surfactant extraction of S-Ph-PMO was also successful. The FTIR spectra depicted in Fig. 3.9 for samples S-C12M3as and S-C12M3ext show a drastic decrease of the intensity of the peaks related to -CH_2- groups of the long alkyl chain of the surfactant (stretching vibrational modes ν_s – 2852 cm^{-1}; ν_{as} – 2923 cm^{-1} and bending modes δ_s – 1467 cm^{-1}[267]) after the SDA extraction under MW.

The pattern of the extracted sample shows residual peaks in the same position which can be ascribed to the presence of the -CH_2- groups of the MPTMS precursor. For comparison, Fig. 3.9 also shows the FTIR spectra of a reference sample prepared before and after extraction by the conventional reflux method (S-C24C24as and S-C24C24ext). It is thus possible to infer that a short 15 min MW treatment is as efficient as an overnight reflux of about 14 h.[268]

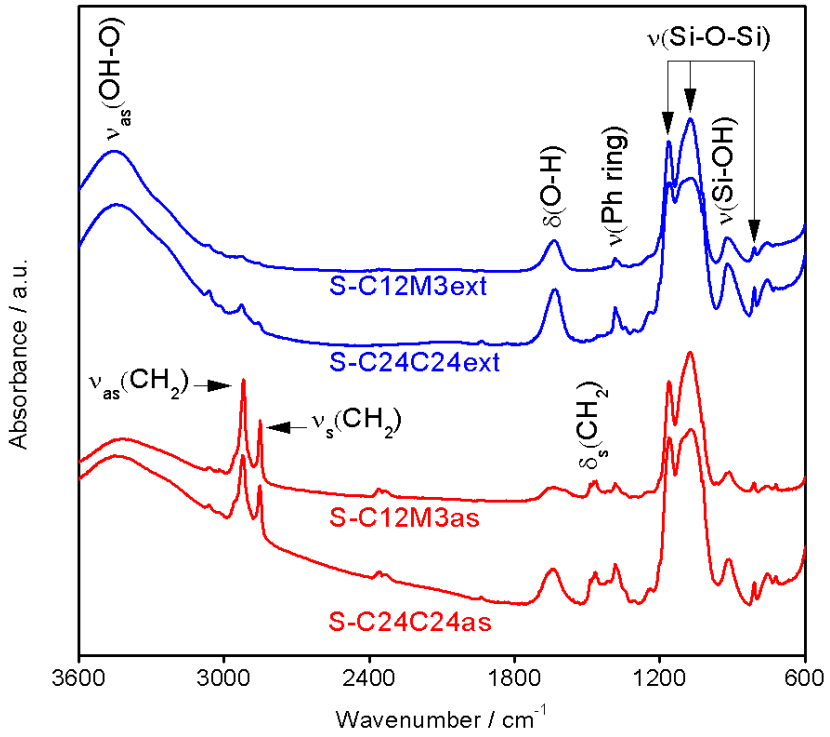

Figure 3.9. FTIR spectra of sample S-C12M3 and S-C24C24 before (as) and after (ext) surfactant extraction. The vanishing peaks after extraction are ascribed to the -CH_2- of the alkyl chain of the surfactant.

Besides confirming the good extraction of the SDA, the FTIR analysis was also useful to assess the presence of specific functional groups that confirm the desired structure of the samples. Indeed, the samples show the characteristic vibrational band that corresponds to the stretching mode of Si-OH at ~920 cm^{-1}.[269] One can also notice the presence of the Si-O-Si vibrational stretching modes at ~810, 1075 and 1165 cm^{-1}.[270] The broad band at ~3460 cm^{-1} and the band at ~1637 cm^{-1} are due to the asymmetrical OH-O stretching and to the O-H bending modes of water, respectively.[271] The peak at ~1385 cm^{-1} is due to vibrational modes of the benzene ring.[269] Unfortunately, the peaks for –SH are not observable. Typically, the stretching modes of the S-H bond appear in the 2550-2600 cm^{-1} range and is quite weak, probably hidden by the background signal.[267]

The oxidation step under MW at 40 ºC was proven to be as efficient as conventional stirring at room temperature. This could be verified in a series of S-C2M3ext samples oxidized during different amounts of time under MW or conventional heating. A sample with 30 min of MW oxidation was found to have similar [H^+] and microstructural features than the sample with a conventional 24 h oxidation step.

These findings are a strong indication that the use of MW heating is an efficient way to drastically reduce the synthesis time, especially in the extraction and oxidation step, contributing for a total reduction of the synthesis time by nearly 36 h.

3.2.2 Self-assembly and hydrothermal treatment

Table 3.4 presents the structural and microstructural characterization data obtained for the materials prepared under variable conditions of self-assembly and hydrothermal treatment.

Table 3.4. Physico-chemical properties of the prepared S-Ph-PMO samples

Sample	S_{BET} ($m^2 \cdot g^{-1}$)	Pore size (nm)	Pore volume ($cm^3 \cdot g^{-1}$)	a_0 (nm)	Wall thickness (nm)	χ[a]	$I_{(001)}$[b]	$[H]^+$ ($mmol \cdot g^{-1}$)	W (%)	Particle size (nm) [c]
S-C24C24	724	3.40	0.98	5.48	2.08	10.6	162	0.93	64.1	837
S-C48C24	471	4.28	0.64	5.00	0.72	1.20	166	1.61	57.2	652
no-surf	223	n.a.	0.65	n.a.	n.a.	n.a.	49.5	1.26	68.9	431
no-acid	757	2.80	0.83	5.20	2.4	3.13	348	0	70.0	682
S-C0M1	733	2.90	0.30	4.81	1.91	12.4	313	0.27	n.t.	n.t
S-C0M3	931	3.14	0.89	4.72	1.58	10.4	506	0.24	n.t.	n.t
S-C2M3	774	3.10	0.49	4.95	1.85	4.42	280	0.30	53.6	799
S-C6M3	991	3.10	0.93	4.81	1.71	4.57	205	0.46	63.3	559
S-C12M3	1023	3.18	1.04	5.05	1.87	4.61	140	0.63	n.t.	594
S-C24M3	623	3.15	0.46	5.15	2.00	2.78	243	0.77	64.6	559
S-C0M5	792	3.21	0.33	4.76	1.55	3.29	887	0.42	n.t.	n.t.
S-C6M5	826	3.20	0.40	4.81	1.67	2.17	165	0.36	59.9	598
S-C12M5	1199	3.13	0.71	4.90	1.77	1.37	166	0.58	59.7	483
S-MS0.5M3	763	3.17	0.52	4.90	1.73	4.30	564	0.24	n.t.	n.t.
S-MS1M3	854	3.18	0.44	4.72	1.54	2.75	585	0.27	n.t.	n.t.
S-MS2M3	715	3.15	0.66	4.55	1.40	3.60	416	0.58	66.5	782
S-MS4M3	857	3.15	0.42	4.95	1.80	7.42	687	0.56	59.4	611
S-MS6M3	862	3.16	0.55	5.05	1.79	1.38	825	0.62	56.6	641
S-MS12M3	48.9	3.13	0.09	n.a.	n.a.	n.a.	93.2	1.35	n.t.	814

[a] χ is an arbitrary factor that represents the ratio between the intensity of the XRD peak for the hexagonal array of pores and the intensity of the peak related to the molecular scale periodicity along the pore wall.

[b] $I_{(001)}$ represents the relative intensity of the molecular scale periodicity along the pore wall XRD peak.

[c] particle size in diameter, assuming spherical particles. n.a. - non appreciable. n.t. - not tested

As expected, the concentration of sulfonic acid groups increases with increasing self-assembly time for both conventional and MW heating. However, the reaction kinetics is strongly enhanced by the MW in comparison to conventional heating, allowing a reduction of up to ~80% of the time necessary to attain similar acid loads.

Figure 3.10 depicts the evolution of $[H^+]$ as a function self-assembly time for both conventional and MW routes. The $[H^+]$ is showed normalized to the maximum acid incorporation, defined by the stoichiometry of the reaction (~1.77 $mmol.g^{-1}$). The samples with 5 h (dotted circles) and 3h (solid lines) of hydrothermal treatment show a similar tendency.

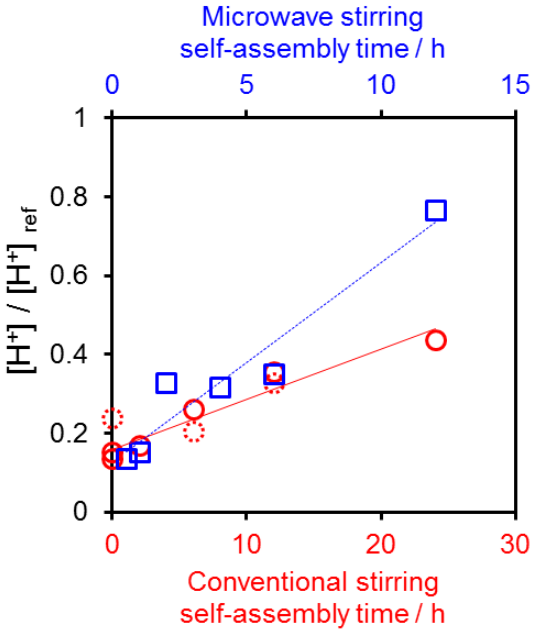

Figure 3.10. Evolution of $[H^+]$ as a function of self-assembly time: (○) conventional stirring (open symbols and dotted symbols are for samples with 3 h and 5 h of hydrothermal treatment, respectively). (□) MW stirring (all samples where hydrothermally treated in MW for 3 h).

The XRD patterns of several oxidized samples are shown in Fig. 3.11. The diffractograms are presented as raw data, but to effectively retrieve diffraction angles and the relative intensities of the two peaks, the baselines were subtracted. Most patterns are typical of ordered mesoporous materials, with the diffraction maxima at $2\theta \approx 2°$ being assigned to the (100) reflection of the hexagonal distribution of the pores, and the smaller (001) reflection at $2\theta \approx 11.6°$ due to the molecular scale periodicity in the pore wall.

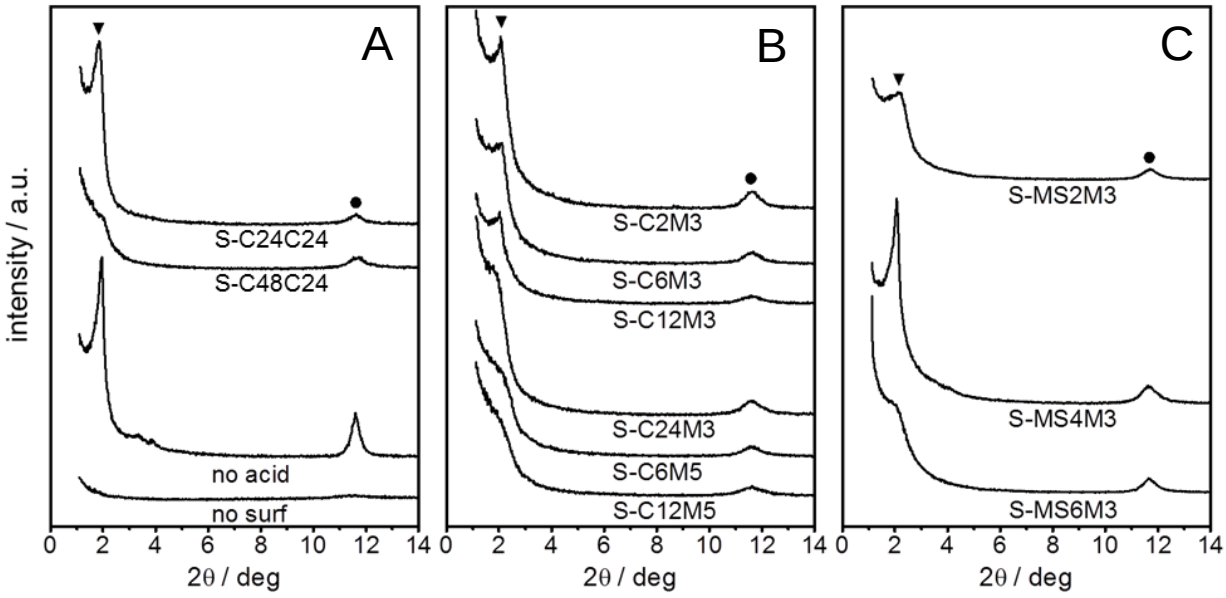

Figure 3.11. XRD diffractograms for the several oxidized S-Ph-PMO samples: A) conventional heating and control samples; B) samples with MW heating in the hydrothermal step and C) samples fully synthesized using MW energy. The triangles identify the pore order reflection (100) and circles denote the (001) molecular scale periodicity.

As expected, the "no-acid" control sample shows a clear pattern with high intensity peaks due to the absence of the acid precursor, whereas the sample "no surf" does not show any evidence of organized pores due to the lack of SDA in the synthesis. The hexagonal cell parameter a_0 (Table 3.4) increases slightly with increasing self-assembly time for the samples of group B and C. This effect can be related to the increasing incorporation of the acid precursor inside the pore wall. A slight increase of a_0 with increasing $[H^+]$ was also observed by Inagaki *et al.*[130] for Ph-PMO samples prepared with conventional heating.

One of the major differences between the patterns of samples prepared with at least one MW step (B and C) and those prepared by the conventional method (A) is the marked decrease of the intensity of the pore order reflection ($I_{(100)}$) for the samples S-C6M5 and S-C12M5. This suggests that the use of MW during the hydrothermal step for more than 3 h tends to decrease the coherent ordered volume that causes the diffraction.

One can also notice the decrease of $I_{(100)}$ with increasing $[H^+]$ in the materials of group B, suggesting a decrease of the extension of the pore order due the acid incorporation, also in agreement with the literature.[97,130,213,268] The behaviour of the group C samples does not follow exactly the same trend, with sample S-MS4M3 (with intermediate MW self-assembly step duration) showing an apparent higher order than sample S-MS2M3, although the $[H^+]$ is lower in S-MS4M3 than in S-MS2M3 (Table 3.4). Nevertheless, sample S-MS6M3 follows the trend observed for group B, clearly displaying the lowest $I_{(100)}$ of the C samples. The causes for this apparent dispersion may be related to the lack of control on the MW energy delivered to the samples. Since the self-assembly temperature (40 ºC) is quickly attained under MW, significant differences may indeed occur between the nominal duration of the treatment and the time that MW were effectively targeting the reactants.

In order to rationalise the observed correlations, it is useful to introduce an order factor χ representing the ratio between $I_{(100)}$ and $I_{(001)}$. In Fig. 3.12A these values are presented normalized to the highest value of all samples (χ_{ref}=12.4 for sample S-C0M1). Likewise, it is also useful to consider $I_{(001)}$ as an indication of the extension of the molecular scale order along the pore walls, also presented in Fig. 3.12B, normalized to the highest $I_{(001)}$ from all samples ($I_{(001)ref}$ = 887 for S-C0M5).

For the samples of group B (circles in Fig. 3.12), both χ and $I_{(001)}$ tend to decrease with increasing self-assembly time. The values of $I_{(001)}$ for sample S-C24M3 is a bit off the tendency, probably due to the long self-assembly time (24h), enabling significant molecular periodicity, but not the long range hexagonal order.

For the samples in group C (square symbols), the trend is similar for χ (Fig.3.12A), which essentially is linked to the increase of $[H^+]$. As noticed above, the exception for S-MS4M3 may be related to the uncertainty on the effective MW dosage. Interestingly, the $I_{(001)}/I_{(001)ref}$ ratio in group C samples (squares in Fig. 3.12 B) seems to deviate from this trend for intermediate MW stirring times (4 and 6 h). In the absence of plausible and reasonable explanation for this apparent maximum, one could invoke the effect of uncontrolled parameters during the XRD analysis. Besides differences in

background contributions for patterns collected in different days, the packing of the powder in the sample holder and the atmospheric conditions are likely to introduce variability in XRD data obtained for this particular type of highly hygroscopic mesoporous samples.

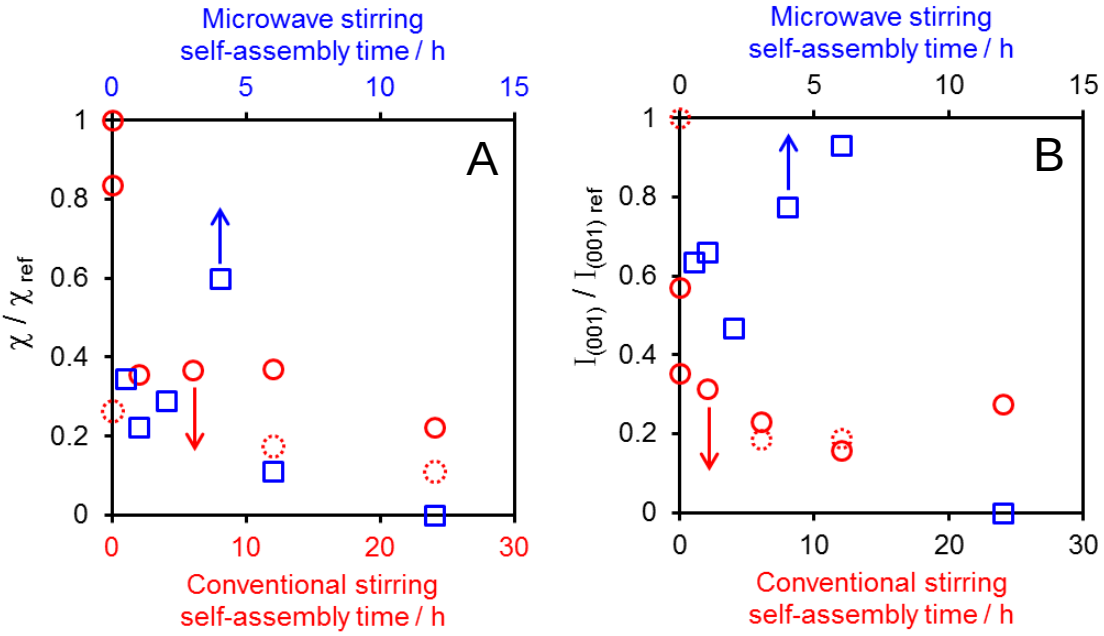

Figure 3.12. Evolution of the A) χ and B) $I_{(001)}$ as a function of self-assembly time: (○) conventional stirring (open symbols and dotted symbols are for samples with 3 h and 5 h of hydrothermal treatment, respectively). (□) MW stirring (all samples where hydrothermally treated in MW for 3 h).

The N_2 sorption isotherms of several representative samples are presented in Fig. 3.13 with insets of the respective pore size distribution (Table 3.4 contains the full data obtained from such sorption measurements). The pore size distribution was calculated with the adsorption branch using the BJH method and KJS correction (see section 2.4.2). All curves show the typical adsorption/desorption pattern for mesoporous materials, which is classified as type IV by IUPAC.[233] The obvious exception from the group is the sample synthesized without surfactants ("no surf"), which shows low S_{BET} and no discernible pore size distribution peak.

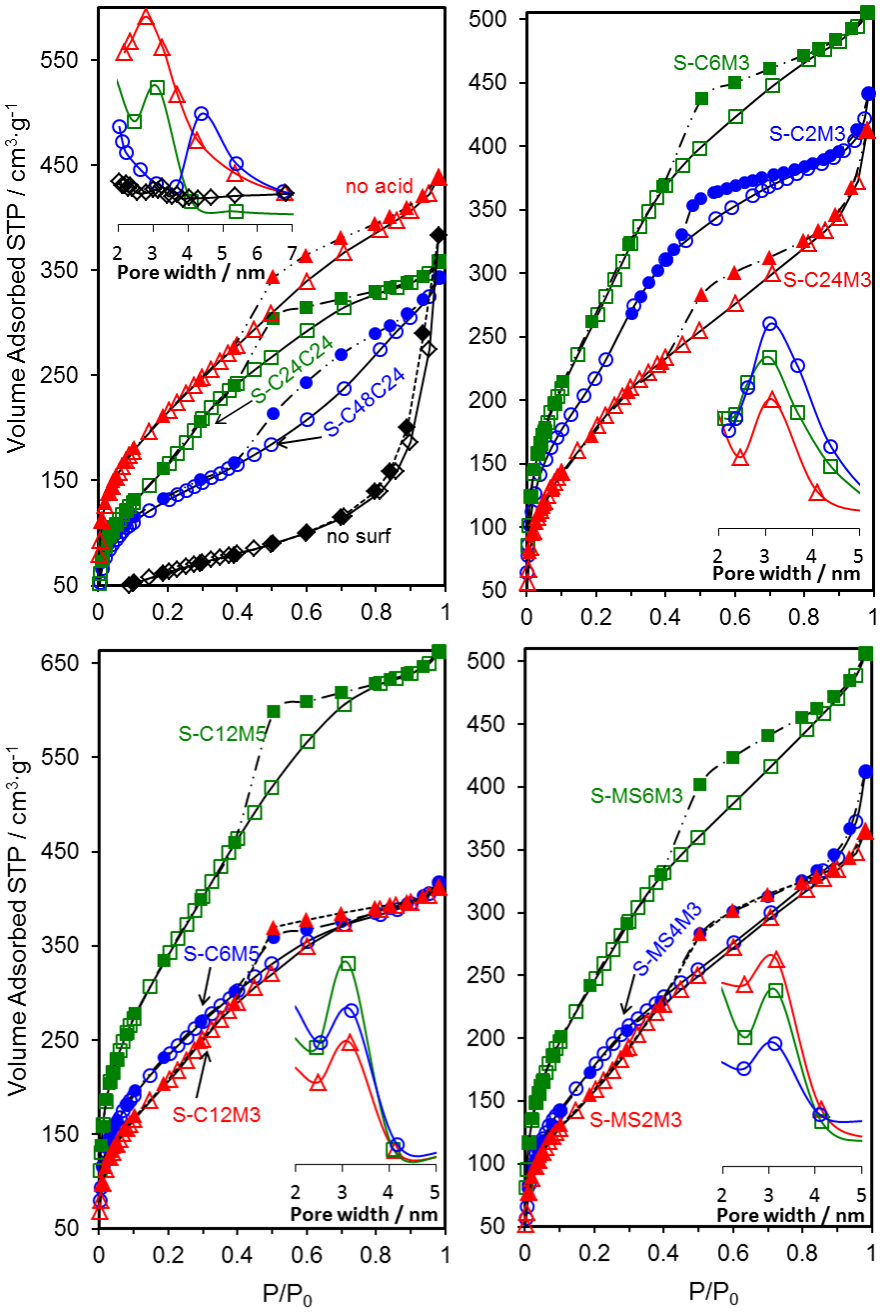

Figure 3.13. N_2 adsorption/desorption isotherms collected at -196 °C of the several S-Ph-PMO and control samples. Insets in each graph represent the pore size distribution.

The S_{BET} values of the samples synthesized in the presence of surfactant are much higher, but also quite variable (from 470 up to 1200 $m^2 \cdot g^{-1}$). The pore size distribution is less affected by the processing conditions, with average pore size between 2.9 and 3.2 for samples processed with MW (Fig. 3.13 B_1, B_2 and C).

The samples synthesized using the conventional heat source in all steps (group A) show somewhat larger pores than samples made with MW (3.40 and 4.28 nm,

increasing with increasing self-assembly time). This may be due to the higher [H^+] in these samples, leading to more open structures.

The wall thickness, calculated by the difference between the cell parameter a_0 and the pore size, for samples of groups B and C (Table 3.4), are all in the interval between 1.5 and 2.0 nm.

As expected and in agreement with literature,[97] there is a general tendency for increasing pore volume with increasing S_{BET}, as depicted by Fig. 3.14.

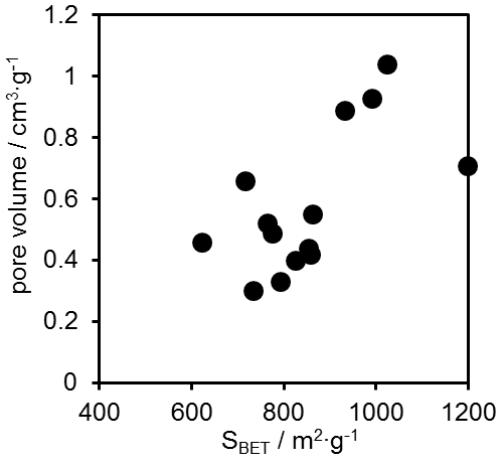

Figure 3.14. Evolution of the pore volume as a function of the specific surface area.

Figure 3.15 shows TEM micrographs of some representative S-Ph-PMO samples to complement the examples already provided in Fig. 3.5. As expected, the sample "no-acid" (Fig. 3.15A) shows a clear channelled microstructure, with long, organized channels, while sample "no surf" (Fig. 3.15B) is completely disordered with no perceivable presence of mesoporous channels. This observation is in agreement with the XRD and N_2 sorption results.

A reduction of the size of the ordered channels is perceptible with the increase of the self-assembly time and the consequent increase of [H^+] (Fig. 3.15C and D for samples S-C2M3 and S-C24C24, respectively), confirming the observed progressive decrease of χ and $I_{(001)}$ with increasing conventional self-assembly time (Fig. 3.12B).

It should be noticed that only for a few samples was it possible to find particles oriented in the [001] direction in such a way that it would allow to verify the hexagonal array of pores.

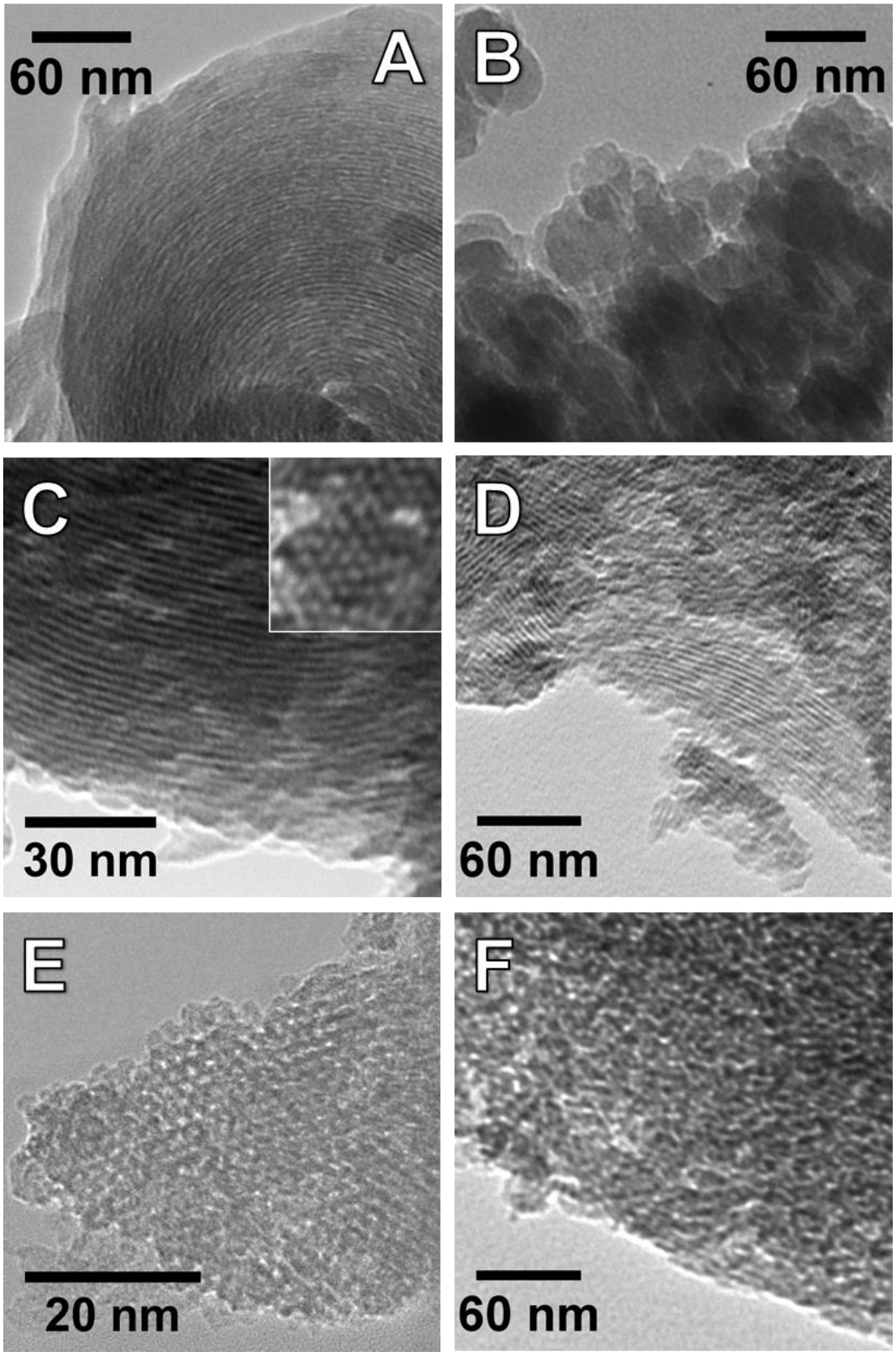

Figure 3.15. TEM images of samples A) no-acid, B) no surf, C) S-C2M3, D) S-C24C24 E) S-MS2M3 and F) S-C12M5.

TEM observation of sample S-MS2M3 (Fig. 3.15 E) show that the use of MW in the self-assembly step does not significantly affect the pore order. However, more than 3 h of MW treatment in the hydrothermal step leads to the collapse of the channelled microstructure, as observed in Fig. 3.15 F for sample S-C12M5. This observation is in full agreement with the N_2 sorption and XRD data.

The d_{100} values obtained from the TEM images were used to calculate the hexagonal cell parameter a_0. The values obtained by TEM are ~20% smaller than the a_0 calculated from the XRD data. Such difference is systematic and may be related to purposively overfocusing the images to enhance contrast. The overfocus was intended to be very slight, even though it may explain the differences in the a_0 values. Data reported for mesoporous silica KIT-6 reveal a similar trend, although the difference is about 7%.[272]

Unfortunately, it was not possible to detect the molecular scale order along the pore wall as presented by other authors[89] due to the great instability of the materials under the electron beam, which disabled the use of high resolution.

Under static conditions, the S-Ph-PMO particles have a tendency to form aggregates, as shown by the SEM micrographs of Fig. 3.16 for some representative S-Ph-PMO samples.

Isolated particles are quite difficult to find in SEM, but some occasional observations revealed a random shape and a significant roughness of the surface (Figs. 3.16 B and 3.16 D). The high level of agglomeration inhibits a proper assessment of the particle size from these images, although some observations of isolated particles show that they are clearly submicrometric. The average diameter of the particles estimated by DLS was found to be in the range between 431 and 800 nm, with a median of 629 nm and standard deviation of 10.4%.

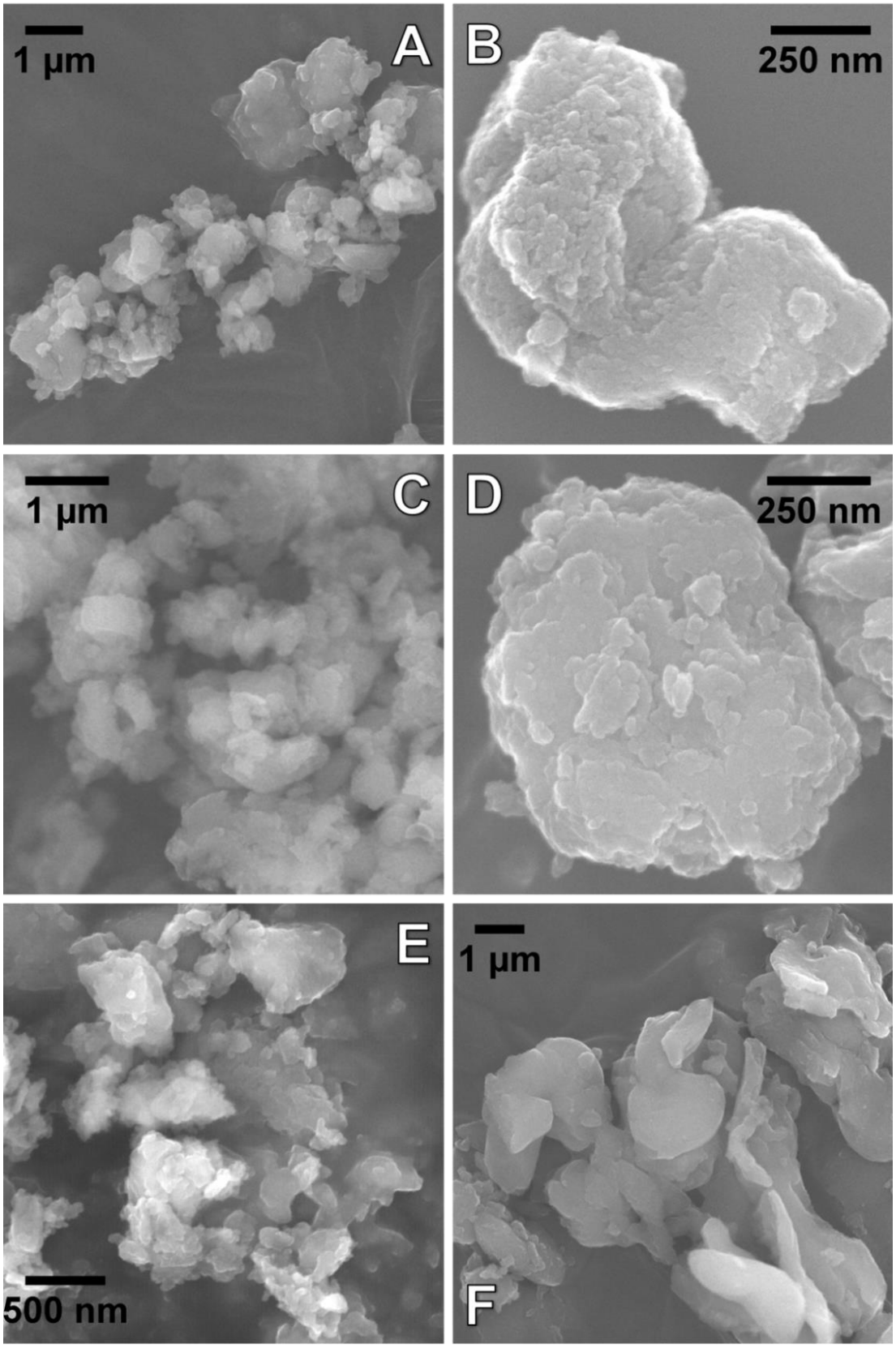

Figure 3.16. SEM micrographs of samples: A, B) S-C2M3; C, D) S-MS2M3; E) S-C24M3 and F) S-C24C24.

Solid state NMR results are presented in Fig. 3.17 showing basically the same features regardless of the heating source used during synthesis. The ^{29}Si CP-MAS spectra (Fig. 3.17, left) of the S-Ph-PMO and control samples "no-acid" and "no surf" depict three signals at $\delta \approx$ -80.8, -69.2 and -58.9 ppm, with minor shifts for the different samples. These signals, based on the report of Yang *et al.*[130], can be assigned to the Si connectivity to benzene (T^3 at $\delta \approx$ -80.8 and T^2 at $\delta \approx$ -69.2 ppm) and to the connectivity of Si to the mercaptopropyl group ($T^{3'}$ at $\delta \approx$ -69.2 and $T^{2'}$ at $\delta \approx$ -58.9 ppm where T^n = C-Si$(OSi)_n(OH)_{3-n}$). The predominance of T^3 and $T^{3'}$ signals are a good indication that the majority of the ethoxy groups are well condensed into the walls of the PMO, with few connections to -OH groups. Q^n signals corresponding to silicon environments = $Si(OH)_{4-n}(OSi)_n$ atoms connected entirely to OSi and/or OH units were not detected, which indicates that the Si–C bond cleavage did not take place during the materials formation. The ^{13}C CP-MAS NMR spectra (Fig. 3.17, right) show a resonance peak at $\delta \approx$ 54.1 ppm that can be assigned to the -$^1CH_2$- linked to the SO_3H group.

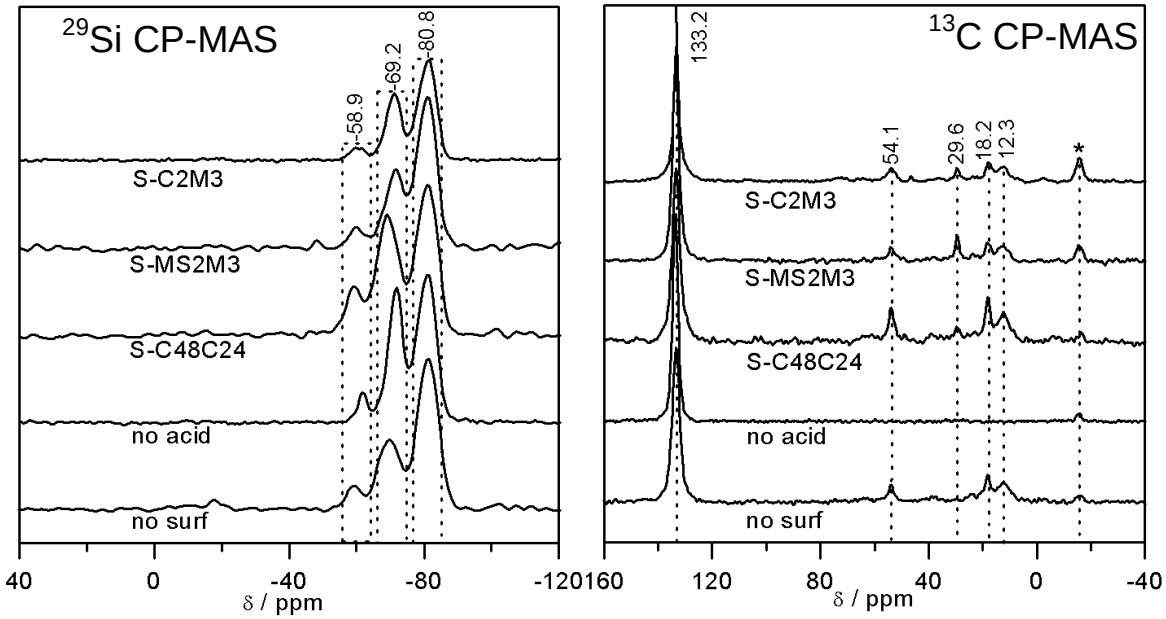

Figure 3.17. ^{29}Si CP-MAS (left) and ^{13}C CP-MAS (right) solid state NMR spectra of representative samples of the S-Ph-PMO family.

The resonance at $\delta \approx 18.2$ ppm is related to the -$^{3}CH_2$- bonded to the Si atom and the signal at $\delta \approx 12.3$ ppm corresponds to the -$^{2}CH_2$- resonance in the middle of the propyl chain (-Si-$^{3}CH_2$-$^{2}CH_2$-$^{1}CH_2$-SO_3H). The enduring peak at $\delta \approx 29.6$ can be assigned to the resonance of the -CH_2- connected to the remaining -SH groups, here indicating that the oxidation process did not occur completely.[128] As expected, the sample "no-acid" did not show any resonance peaks in the ^{13}C CP-MAS besides the peak related to the benzene carbons, due to the absence of any other source of carbon.

In a parallel investigation in collaboration with the Solid State NMR research group of the Chemistry Department of the University of Aveiro, a study of hydrated and dehydrated S-Ph-PMOs with variable acid loading (from 0.21 up to 1.30 mmol·g^{-1}) by advanced high-resolution solid state magic-angle spinning (MAS) NMR was conducted. The objective of such work was to attempt an explanation for the high catalytic activity of these materials in the acid condensation of indole with benzaldehyde in water.[273] The observed displacement of the propyl sulfonic –SO_3H protons to high chemical shifts with increase of the sulfonic acid strength suggested the formation of hydrogen bonds involving neighbouring –SO_3H groups. The acid strength of the materials was lowered by the presence of water for [H^+]> 0.40 mmol·g^{-1}, whereas samples with low [H^+] were very little affected. A plausible explanation for this negligible effect was advanced based on the proximity of the hydrophobic phenyl ring to the sulfonic site, with the former playing an important role in protecting the acid sites against solvation by water. For higher acid loads, the protection is no longer efficient and the extensive proton solvation occurs. For loadings above 0.40 mmol·g^{-1}, there is a linear relationship between the turn over frequency and the [H^+], which in turn is proportional to the ^{1}H chemical shift of the SO_3H. The formation of increasingly strong intermolecular –SO_3H···O_3(H)S hydrogen bonds for S-Ph-PMOs with [H^+] above 0.4 mmol·g^{-1} may explain the enhancement of the catalytic activity with increasing [H^+]. The higher catalytic activity in the presence of water may also be related to the percolation of the aqueous domains stabilized around sulfonic acid groups, which tend to increase significantly when the concentration of acid groups is high enough to enable percolation. The enhanced mobility of the protons in these domains may thus favour the oxidation of the indole. Here it is perhaps interesting to recall the above mentioned effect of the acid load on the protonic conductivity of S-

PMOs (section 3.1.2), where percolation was also invoked to explain the enhanced protonic conductivity above a certain [H^+] value, which is essential for a good conductivity, very much as it happens in PFSA polymers.[23,24,26] The fact that the conductivity increases slightly between the sample with no acid and the sample with [H^+] = 0.3 mmol·g^{-1} suggests that there is a critical percolation concentration above which the proton structural diffusion along the aqueous domains is facilitated.

Figure 3.18 shows the TGA and DSC results for samples S-C2M3 and S-MS2M3, obtained under air and N_2 atmospheres.

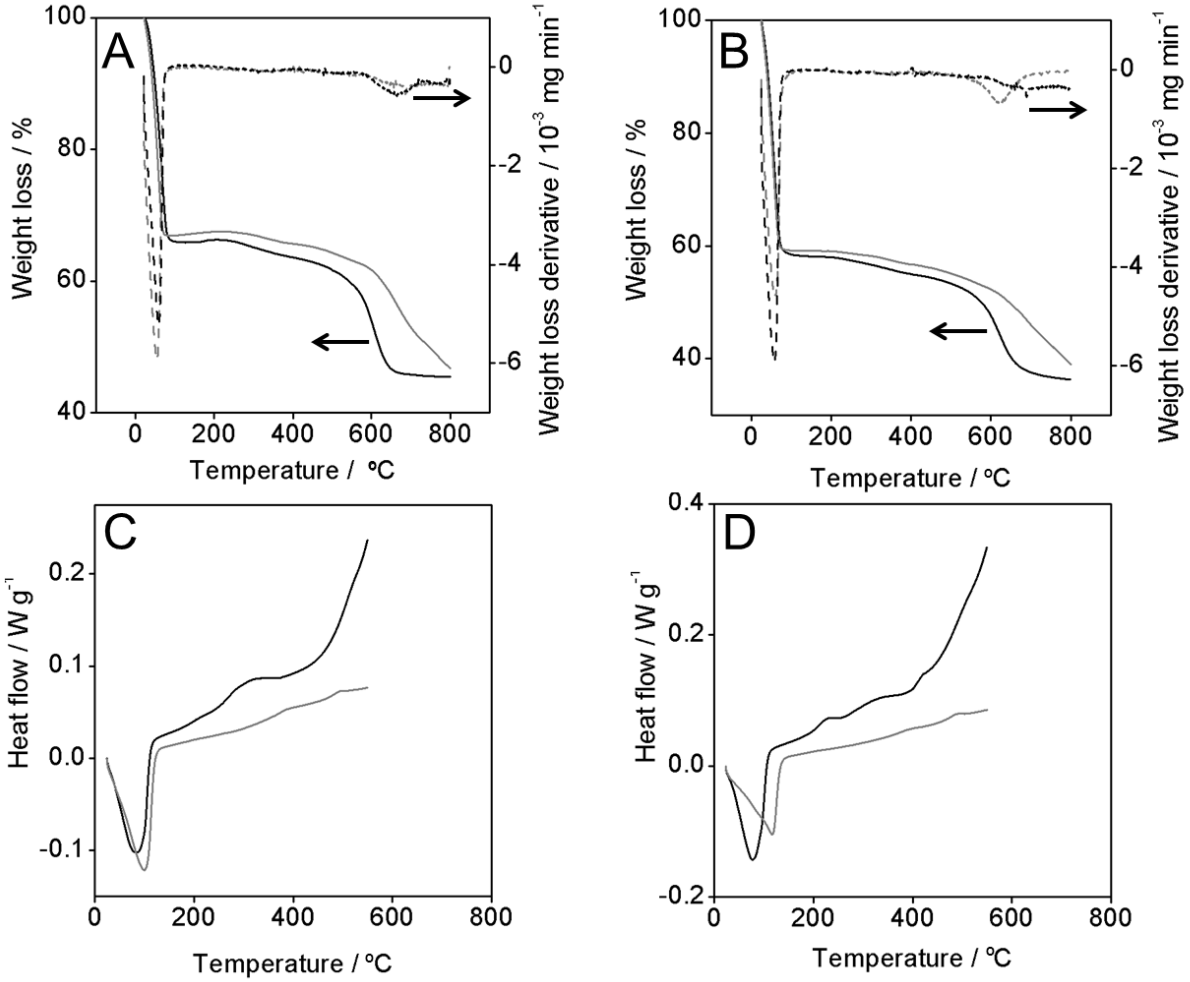

Figure 3.18. TGA (full lines) and derivative (dashed lines) curves for sample A) S-C2M3 and B) S-MS2M3 in air (black) and N_2 (grey) atmospheres. DSC curves in air (black lines) and N_2 (grey lines) for sample C) S-C2M3 and D) S-MS2M3. The heat flow was normalized by the weight of he sample.

The TGA data depict a rapid weight loss at ~100 ºC, which corresponds to the loss of physisorbed water. The lack of appreciable weight loss from 100 to ~250 ºC, similarly to S-Ph-PMO grafted materials from Yang *et al.*[274], is a good indication that the surfactant was completely removed in the extraction step.

A slight weight loss and shallow exothermal peaks in the DSC from ~250 ºC up to ~550 ºC can be assigned to the decomposition of the propylsulfonic acid functionality, as mentioned for MPTMS functionalized SBA-15[128] and S-Ph-PMO[274] materials, together with the decomposition of the residual SDA.

The decomposition of the phenyl rings lodged in the pore wall can be pointed to start at ~550 ºC, alongside with the decomposition of the propylsulfonic acid residue.[274] As expected, these decompositions are enhanced and occur at lower temperature in the presence of oxygen.[90]

The water uptake capacity of the prepared materials (data also listed in Table 3.4) is represented in Fig. 3.19 as a function of the acid load and the volume of pores. The *W* values are quite high and they tend to increase with increasing [H^+] and pore volume. The apparent scatter in the representation of Fig. 3.19 reflects the large variety of structural and microstructural characteristics of the prepared S-Ph-PMO materials.

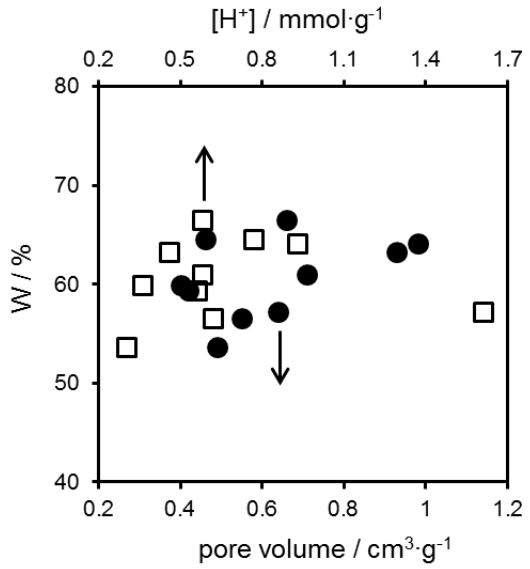

Figure 3.19. Evolution of *W* with increasing [H^+] and pore volume.

3.2.3 Multivariate analysis of the reaction kinetics

It has been shown that that MW can indeed speed up the production of S-Ph-PMOs with similar acid load and specific surface area, allowing a reduction of the synthesis time by ~80%. However, MW also has a tremendous impact on the structure and microstructure of the materials, namely by decreasing the length scale of the pore order. In addition, the synthesis of S-Ph-PMO is a complex process, involving various reaction steps, where MW can be used independently. The quantification of the influence of each variable on the kinetics of such processes is thus extremely challenging, implying a large number of experiments with a much larger combination of conditions than those explored in this thesis.

This section describes a first attempt to parameterize the kinetics of the multi-step synthetic reactions of S-Ph-PMO. The underlining model assumes linear dependencies between the type and time of the self-assembly and hydrothermal steps on three selected characteristics of the final material, which are the acid concentration and the two order parameters extracted from the XRD data (χ and $I_{(001)}$).

The objective is to obtain a set of time constants based on a limited number of experiments, which allow predicting the optimal conditions for the synthesis of a specific S-Ph-PMO (with a given $[H^+]$ and pore order) using MW energy. This approach implies the calculation of a parameter matrix **P** with the kinetic coefficients from a matrix **V** containing the time variables for the different experiments made (a combination of self-assembly time and type - C or MS - and microwave hydrothermal treatment time), and a matrix **R,** with the obtained experimental results of $[H^+]$, χ and $I_{(001)}$, according to[275]:

$$\mathbf{P} = (\mathbf{V}' \mathbf{V})^{-1} (\mathbf{V}' \mathbf{R}) \qquad \text{eq. 3.1}$$

where **V**' is the transpose of **V**. Predictions of a results matrix $\mathbf{R_s}$ with $[H^+]$, χ and $I_{(001)}$ can then be made for a given set of experimental conditions defined by the duration (in hours) of the self-assembly and hydrothermal steps, simply by using:

$$\mathbf{R_s} = \mathbf{V} \times \mathbf{P}. \qquad \text{eq. 3.2}$$

Figure 3.20 exemplifies the application of the method to some experiments listed in Table 3.4, including the difference between the prediction and the experimental results, expressed as a fraction of the latter (error). The simulated values of $[H^+]$ calculated using the model are quite similar to the experimental values. This is actually a surprisingly good result considering the complexity of the multistep approach and the assumed linear dependences. The errors are substantially larger for the structural parameters, especially for $I_{(001)}$, where differences of more than 40% were observed in the results of 7 experiments. Interestingly, the errors are smaller for the C samples fully synthesised under MW. Differences in the pore order parameter are somewhat lower than for $I_{(001)}$. While these deviations may reflect an oversimplified model, it should be noticed, as previously mentioned, the XRD intensities are not the most reliable and reproducible parameter in this type of material.

V				×	P			=	R_s			error (%)		
self-assembly			hydrothermal											
C(h)	MS(h)	M(h)							$[H^+]$	χ	$I_{(001)}$	$[H^+]$	χ	$I_{(001)}$
1	24	0	3		0.24	12.6	297		0.80	2.76	23	3.75	0.47	90.5
1	12	0	3		0.02	-0.16	-16.9		0.55	4.69	226	13.4	1.75	61.8
1	6	0	3		0.06	-0.69	63.1		0.42	5.66	327	9.01	23.9	59.7
1	2	0	3		0.02	-1.99	44.0		0.33	6.30	395	11.3	42.6	41.2
1	0	0	1						0.26	10.6	341	3.62	14.6	8.86
1	0	0	3						0.29	6.62	429	21.6	36.3	15.3
1	0	0	5						0.32	2.63	517	23.0	19.9	41.8
1	6	0	5						0.45	1.67	415	25.0	23.1	152
1	12	0	5						0.58	0.70	314	0.54	48.5	88.6
1	0	0.5	3						0.32	6.28	460	34.6	46.0	18.4
1	0	1	3						0.35	5.93	492	31.2	116	15.9
1	0	2	3						0.42	5.25	555	28.2	45.7	33.5
1	0	4	3						0.54	3.87	681	3.34	47.8	0.92
1	0	6	3						0.67	2.50	807	7.43	81.7	2.18

Figure 3.20. Matrices of the original time constants (V) and correspondent simulated values (R_s) obtained using the parameter matrix (P). The matrix on the right contains the fractional difference of the simulations with respect to the measured values.

Nevertheless, the predictions made using the model can at least qualitatively describe the trends in Figs. 3.10 and 3.12. Figure 3.21 shows 3D plots of the simulated $[H^+]$, χ

and $I_{(001)}$ as a function of the duration of the self-assembly and hydrothermal treatment steps for both self-assembly experimental conditions (C in blue and MS in red). It can be clearly seen that $[H^+]$ increases with increasing self-assembly time, for both MS and C stirring self-assembly methods, but with a clearly higher slope for the red plane of MS (Fig. 3.21 A). The SO_3H concentration is also slightly increased with increasing hydrothermal time for both methods. These results are in fair agreement with Fig. 3.10.

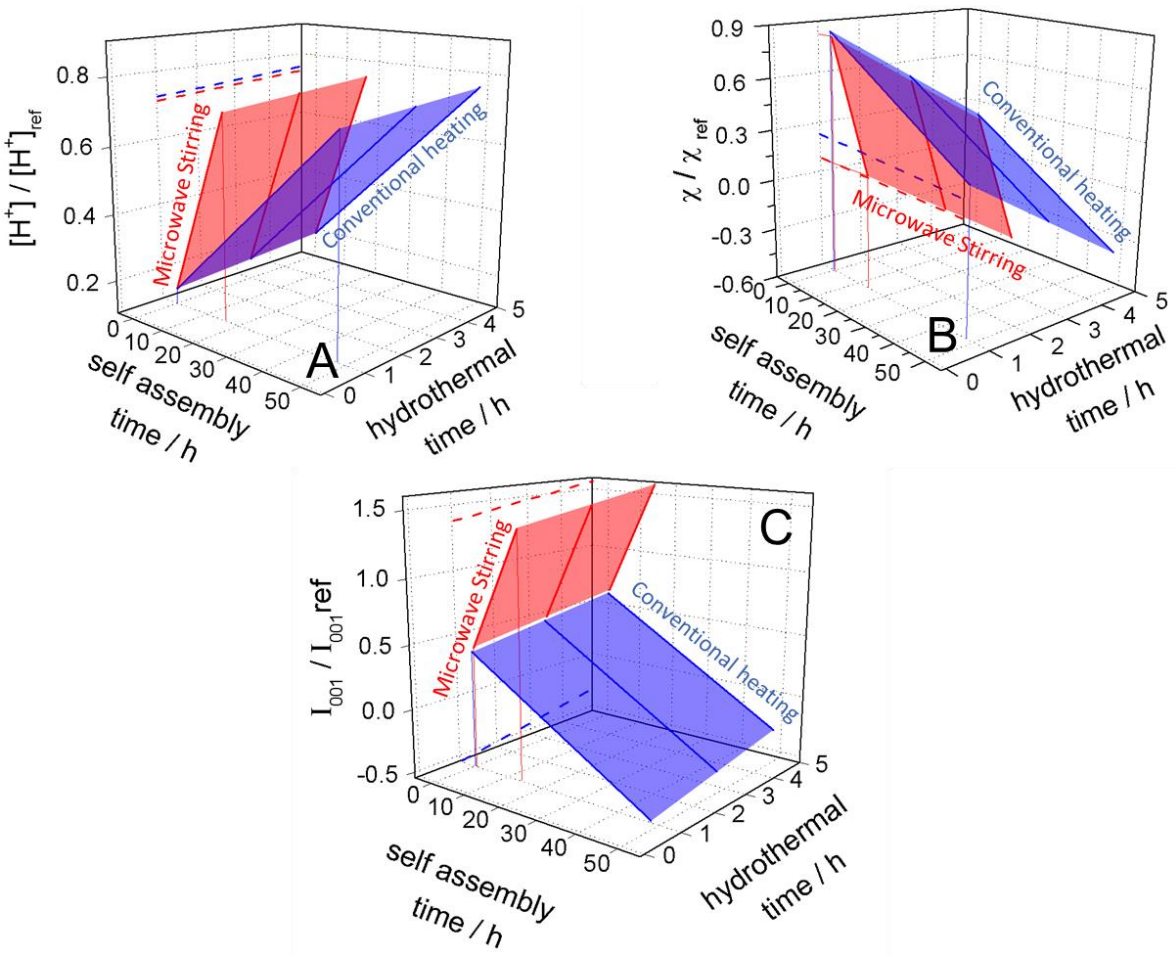

Figure 3.21. 3D plots of the evolution of simulated values of: A) $[H^+]$; B) χ and C) $I_{(001)}$ as a function of self-assembly time and hydrothermal treatment time for both self-assembly types (MS in red and C in blue). The dashed lines are projections of the surface edges (values of higher self-assembly time) on the parameter/hydrothermal time plane.

These projected results show that S-Ph-PMO with a concentration of sulfonic acid groups in excess of 70% of nominal stoichiometry (1.77 $mmol \cdot g^{-1}$) can be obtained after about 16 h of self-assembly and 3 h of hydrothermal treatment under MW. A similar material would only be obtained after 48 h of self-assembly using conventional heating. In terms of the total duration of synthesis, the MW sample could be obtained in less than 20% of the time.

Fig. 3.21 B predicts a progressive decrease of χ with increasing self-assembly time and increasing hydrothermal treatment for both MS and C heating sources, with a larger effect for the microwave method. These trends are also in agreement with the experimental data (Fig. 3.12).

Likewise, and despite the significant errors, the trends projected for $I_{(001)}$ (Fig. 3.21 C) are also consistent with the observed results (Fig. 3.12), showing the increase of $I_{(001)}$ with increasing MW self-assembly time and a decrease of $I_{(001)}$ with increasing conventional self-assembly time. Additionally, there is a slight increase in $I_{(001)}$ with increasing hydrothermal treatment time.

To validate the model projections of the effect of MW, a sample S-MS12M3 was synthesized according to the conditions in Table 3.4. The $[H^+]$ = 1.35 $mmol \cdot g^{-1}$ obtained for this sample is somewhat higher than the predicted value (1.04 $mmol \cdot g^{-1}$), but still a fair agreement overall. This sample revealed a totally disordered pore structure by XRD and TEM, in excellent agreement with the predicted $\chi \approx 0$. However, the model fails when predicting a material with considerably more order at the molecular level ($I_{(001)}$=1185) than the actual experimental result ($I_{(001)}$= 93). This result confirms that the assumed linear dependence is able to provide reasonably accurate predictions of the acid load and the pore order as a function of the reaction time under MW.

3.3 Electrochemical characterization of S-Ph-PMO

The smart use of the MW and conventional heating on the various synthetic steps of S-Ph-PMOs allowed the design of materials with a large variety of compositional and microstructural characteristics. In this section, an attempt is made to identify solid correlations between these intrinsic characteristics and the protonic conductivity of the materials, and how they are influenced by extrinsic factors such as temperature and relative humidity.

The samples electrical resistance was estimated from impedance spectra collected under variable external conditions following the procedures already described in section 3.1.2. Figures 3.22 A, B and C represent the typical evolution of these spectra for several representative S-Ph-PMO samples at 40, 60 and 100 °C respectively (please refer to Fig. 3.6 A for the S-Ph-PMO sample at 80 °C).

In general, the spectra display two contributions, one at high frequency due to the sample bulk resistance and a low frequency semi-circle associated to the electrode impedance. At sufficiently low r.h. and low temperature, the bulk impedance of the samples with the highest resistance consists of a semicircle. This semicircle vanishes with increasing r.h. and temperature, until it eventually disappears. In this case, the bulk impedance is described by a pure ohmic resistance corresponding to the high frequency intercept of the electrode semicircle. The most conductive samples tend to display the latter shape throughout the entire range of r.h. and temperature.

Figure 3.22 D is a collection of spectra obtained with variable test signal amplitude. It is possible to see that the high frequency semi-circle is not affected by the applied voltage, whereas the low frequency tail is reduced. This confirms the assignment of the high frequency phenomenon to the ohmic resistance of the material, and the low frequency contribution to the electrode impedance.

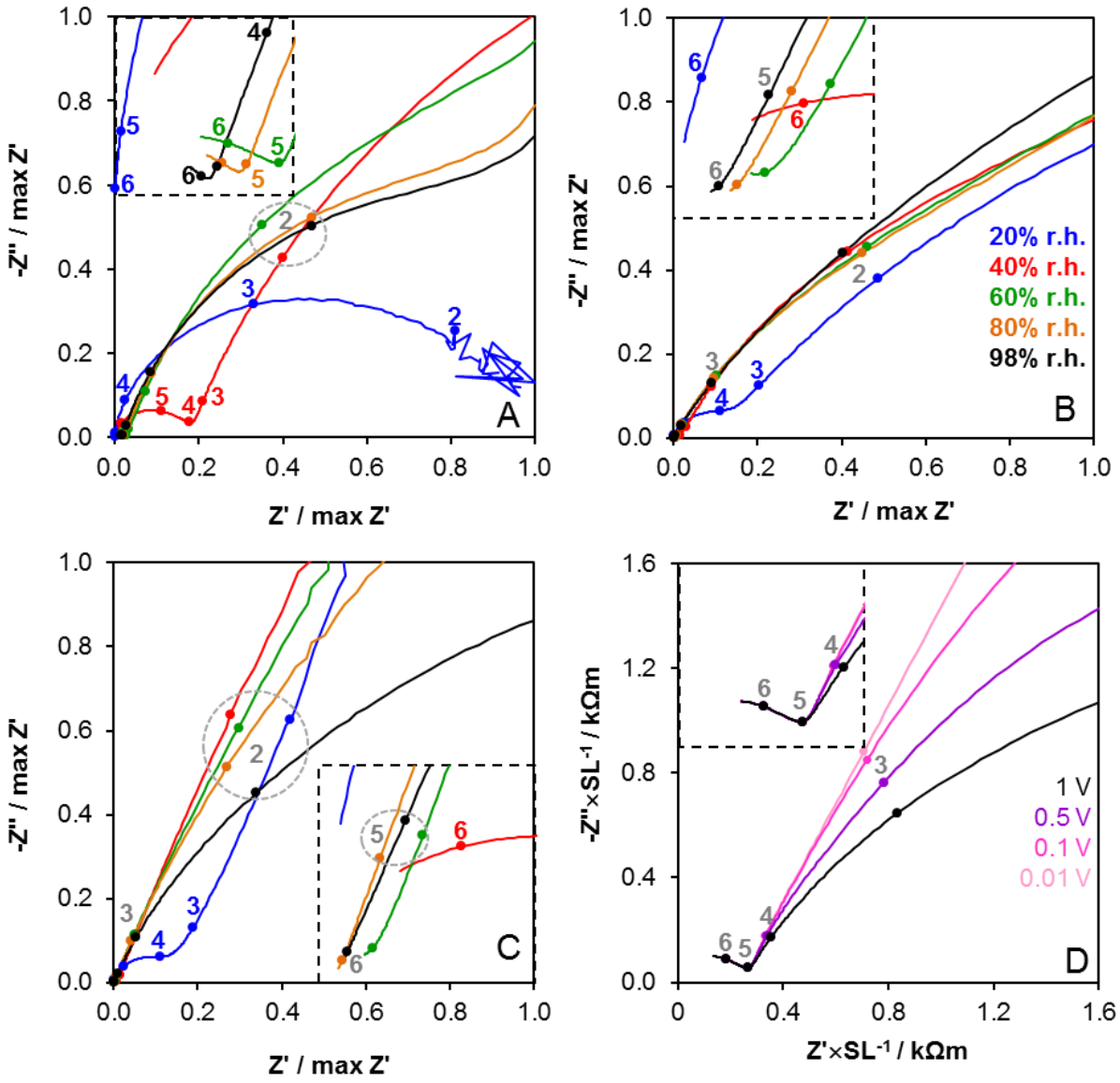

Figure 3.22. EIS spectra for several representative samples showing the evolution of the shape of the impedance spectra with increasing r.h. at A) 40 ºC (no-acid), B) 60 ºC (S-MS4M3) and C) 100 ºC (S-C2M3). Please consider Fig. 3.6 A for sample S-C24M3 at 80 ºC. D) Influence of test signal amplitude on the shape of the impedance spectra for sample S-C2M3 at 60°C and 60% r.h. (numbers represent powers of 10 of frequency in Hz).

3.3.1 Influence of extrinsic factors on conductivity: temperature and relative humidity

Figure 3.23 depicts Arrhenius type plots of the conductivity of several representative samples obtained with increasing r.h. The highest conductivity value is 0.11 $S \cdot cm^{-1}$ for

S-C48C24 at 80 ºC and 98 % r.h., which is comparable to Nafion® in similar conditions.

As expected, the conductivity increases with increasing r.h. for all samples, regardless of the temperature, due to an increasing amount of the proton concentration in the material. However, it is also immediately apparent that in some cases the data for low humidity and low temperature tend to deviate from the Arrhenius behaviour.

This is particularly obvious for the sample prepared without any acid, which nicely illustrates the trend observed for other samples. Since this sample has no acid functionalization, the protonic conductivity is in principle only due to water molecules physisorbed at the surface of the material. Increasing the temperature will naturally decrease the concentration of the adsorbed water, hence decreasing the conductivity. The magnitude of this effect is expected to be larger for low r.h. conditions, when pH_2O is lower.

Conversely, increasing the r.h. at a fixed temperature increases the driving force for the physisorption, and thus the conductivity increases. Therefore, the apparently positive slope in the Arrhenius plot at 20% r.h. becomes progressively less positive as r.h. increases, eventually becoming negative for 98% r.h. The E_a in these humidity conditions, close to 25 $kJ \cdot mol^{-1}$ (Table 3.5), is in the range reported for the structural diffusion of protons as the underlining transport mechanism.[38,41,188]

On the other hand, the sulfonic acid groups in the sample processed without SDA (no surf) are solvated by the adsorbed water molecules, which in this case are also chemisorbed to the surface of the material. Consequently, the water molecules can be retained in the structure up to much higher temperatures than in the acid-free material. This enables levels of protonic conductivity similar to those measured for Nafion® even at temperatures close to 100 °C. In fact, the Arrhenius behaviour is observed for the entire range of r.h., with similar activation energy (~30 $kJ.mol^{-1}$) for r.h. ≥ 60%.

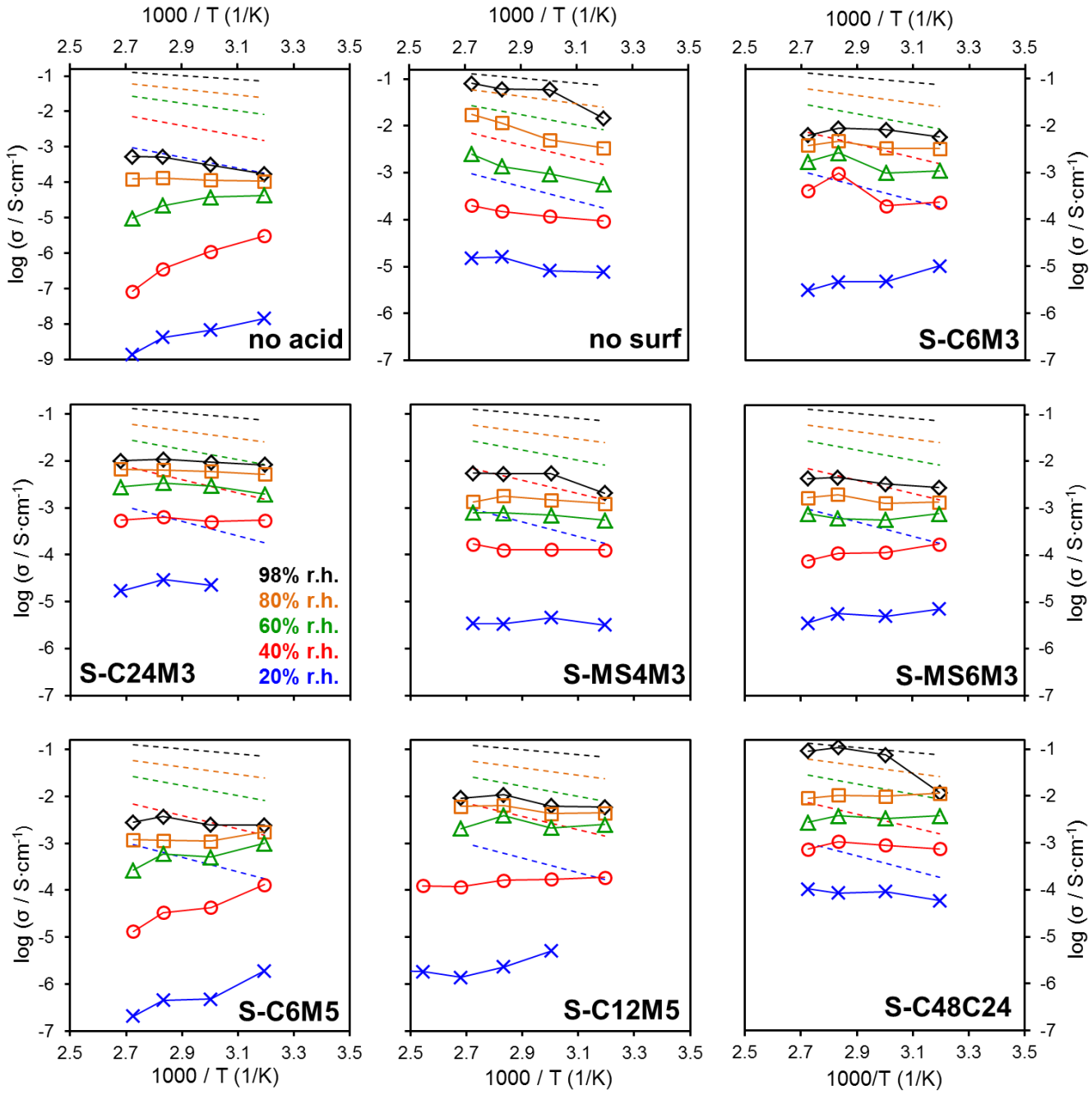

Figure 3.23. Arrhenius plots of several S-Ph-PMO representative samples as a function of r.h. Lines are for visual guidance. Relative humidity: ×) 20%, ○) 40%, △) 60%, □) 80% and ◇) 98%. The dashed lines are for our Nafion® reference, in the same conditions.

The data for the other samples represent a variety of intermediate situations between the behaviour of the previous limiting cases, with the data for samples with lower [H^+] (e.g. S-C6M5) often featuring negative apparent activation energies for low humidity, and samples with highest acid content (e.g. S-C48C24) depicting full Arrhenius behaviour throughout the entire r.h. range. A more detailed analysis of the effect of the

[H^+] and other physico-chemical characteristics of the S-Ph-PMO on the protonic conductivity is provided in sub-section 3.3.2.

Table 3.5. Values of E_a for the conductivity measured under variable r.h. conditions. The S_{BET} and the [H^+] are given to help the discussion.

Sample	S_{BET} ($m^2 \cdot g^{-1}$)	$[H]^+$ ($mmol \cdot g^{-1}$)	σ ($S \cdot cm^{-1}$)[a]	E_a ($kJ \cdot mol^{-1}$)				
				98% r.h	80% r.h.	60% r.h.	40% r.h	20% r.h.
S-C2M3	774	0.30	8.9×10^{-4}	11.9	3.41	10.8	16.8	[b]
S-C6M3	991	0.46	6.3×10^{-3}	5.80	7.80	15.5	21.4	[b]
S-C12M3	1023	0.63	1.6×10^{-2}	14.5	9.60	3.60	[b]	[b]
S-C24M3	623	0.77	1.0×10^{-2}	6.40	6.90	9.00	3.90	[b]
S-C6M5	826	0.36	2.8×10^{-3}	12.5[c]	[b]	[b]	[b]	[b]
S-C12M5	1199	0.58	9.3×10^{-3}	12.3	9.70	3.30	[b]	[b]
S-MS2M3	715	0.58	2.6×10^{-3}	18.7	23.6	27.9	16.3	--
S-MS4M3	857	0.56	5.5×10^{-3}	19.1	5.70	9.50	6.60	2.70
S-MS6M3	862	0.62	4.2×10^{-3}	11.6	8.70	2.60	[b]	[b]
S-C24C24	724	0.93	2.6×10^{-3}	32.7	-	3.88	[b]	[b]
S-C48C24	471	1.61	9.0×10^{-2}	39.1	0.40[c]	2.85[3]	4.05	11.4
no-surf	223	1.26	8.0×10^{-2}	30.6	32.9	28.0	15.8	17.7
no-acid	757	0	5.4×10^{-4}	24.1	6.02	[b]	[b]	[b]

[a] – at 94 ºC and 98% r.h.; [b] – apparent E_a are negative;

[c] – in the range 25-80 °C .

The data in the Arrhenius plots (Fig. 3.23) are replotted in Fig.3.24 to illustrate the effect of r.h. on the conductivity.

For the samples with [H^+] lower than 1 $mmol \cdot g^{-1}$ and S_{BET} higher than 600 $m^2 \cdot g^{-1}$ the conductivity increases sharply with increasing r.h. up to ~60% r.h., and more moderately thereafter. The behaviour of the "no-surf" and "no-acid" samples again represent the two limiting situations, with the remaining materials showing intermediate behaviour.

This bending of the r.h. plots was also noticed by Hamoudi *et al.* for SO_3H functionalized ethane bridged organosilicas,[212,262] and very recently by Inagaki's group on SO_3H functionalized PMS thin films.[213] Based on water sorption isothermal measurements, the later study correlates the sharp increase of conductivity at low r.h. with the adsorption and clustering of water molecules around the acid sites,

which eventually condensate in the mesopores, driven by capillarity, and on the surface of the films above a certain r.h. The humidity threshold leading to condensation is shifted to lower r.h. values with increasing [H^+] and decreasing pore size, in agreement with the Kelvin's equation (eq. 2.3).

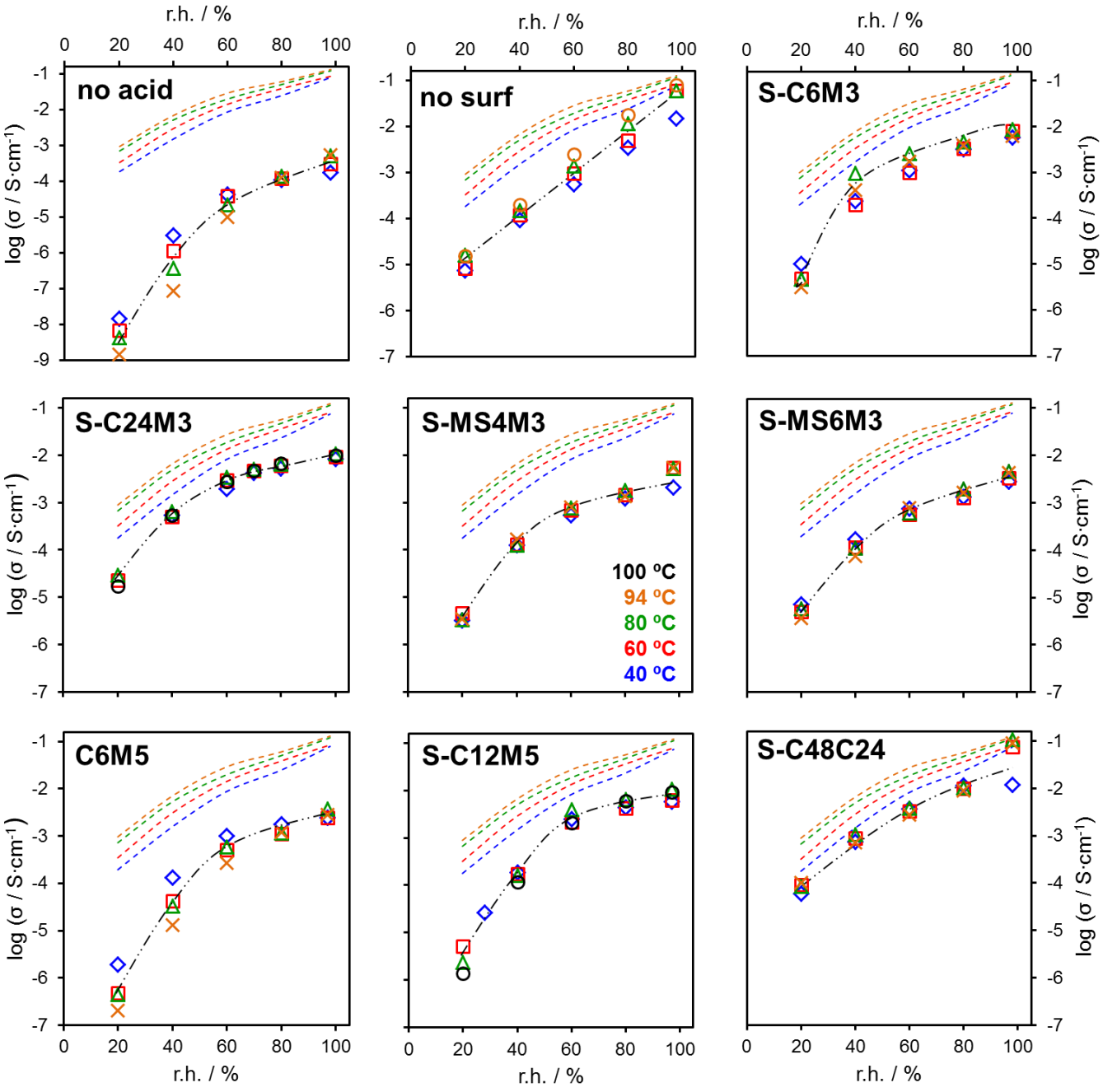

Figure 3.24. Evolution of conductivity as a function of r.h., at different temperatures, for some representative S-Ph-PMO samples. Lines are for visual guidance. Temperatures: ◇) 40 ºC, □) 60 ºC, △) 80 ºC, ×) 94 ºC and ○) 100 ºC. The dashed lines are for our Nafion® reference, in the same conditions.

While the water vapour sorption measurements could not be performed in this work, the conductivity vs. r.h. profiles can be nicely explained by the condensation hypothesis. Indeed, the "no surf" sample shows an almost linear dependence for r.h. lower than 98%, in agreement with the much lower volume of mesopores. Proton transport in this case is mostly occurring along the SO_3H-water domains on the surface of the particles, without major changes in the proton mobility. On the other hand, a transition at around 60% r.h. is observed for the material without acid functionalization, suggesting a change of mechanism, possibly due to changes in proton mobility made possible by the water condensed in the pores.

The S-Ph-PMO samples with higher $[H^+]$ (>1 mmol·g^{-1}) and lower S_{BET} (<500 m^2·g^{-1}) (e.g. S-C48C24) tend to show a more linear increase of conductivity with increasing r.h. This difference can be due to the high concentration of acid groups combined with a somewhat low mesoporosity. Conversely, samples with high mesoporous volume, which, as discussed earlier, is usually paired to low $[H^+]$ and high S_{BET}, tend to depict clearer 2-step σ *vs.* r.h. dependences.

Considering the T and r.h. ranges corresponding to Arrhenius behaviour in Fig. 3.23, (essentially data for r.h. greater than 60% for the majority of samples – see table 3.5) the proton mobility is likely to be constant and the conductivity is thus essentially determined by the proton concentration. As described analogously for Nafion® 117 by Maréchal *et al.*[276], the interaction of the sulfonic acid groups with the hydration water can be described by the solvation equilibrium

$$SO_3^-H^+ + gH_2O \leftrightarrows SO_3^-hH_2O + H^+jH_2O \qquad \text{eq. 3.3}$$

where g is the total number of solvating water molecules, and h and j are the number of water molecules associated to the sulfonate anion and the proton, respectively. If $[SO_3^-hH_2O] = [H^+jH_2O]$, the corresponding solvation constant is

$$K^{solv}_{(T)} = [H^+jH_2O]^2 / pH_2O^g \qquad \text{eq. 3.4}$$

Since we assume that the proton mobility is constant, the protonic conductivity is thus directly proportional to the proton concentration and eq. 3.4 can be rewritten as

$$K^{solv}_{(T)} \propto \sigma^2 / pH_2O^g \qquad \text{eq. 3.5}$$

Since pH_2O = r.h. × $p_{sat}H_2O$, where $p_{sat}H_2O$ is the saturated vapour pressure at a given temperature, one expects a linear relation between log (σ) and log (r.h.) with slope $g/2$. Such dependence is indeed depicted by Fig 3.25 for representative samples with positive E_a values.

The calculated total water molecules involved in the solvation equilibrium vary from $g \approx 6$ for samples with $[H^+] < 1$ mmol·g^{-1} to $g \approx 8$ for samples with higher $[H^+]$. Sample "no surf", which has $[H^+] = 1.26$ mmol·g^{-1} but a low $S_{BET} = 223$ m^2·g^{-1} without apparent mesoporosity, has the highest $g \approx 10$.

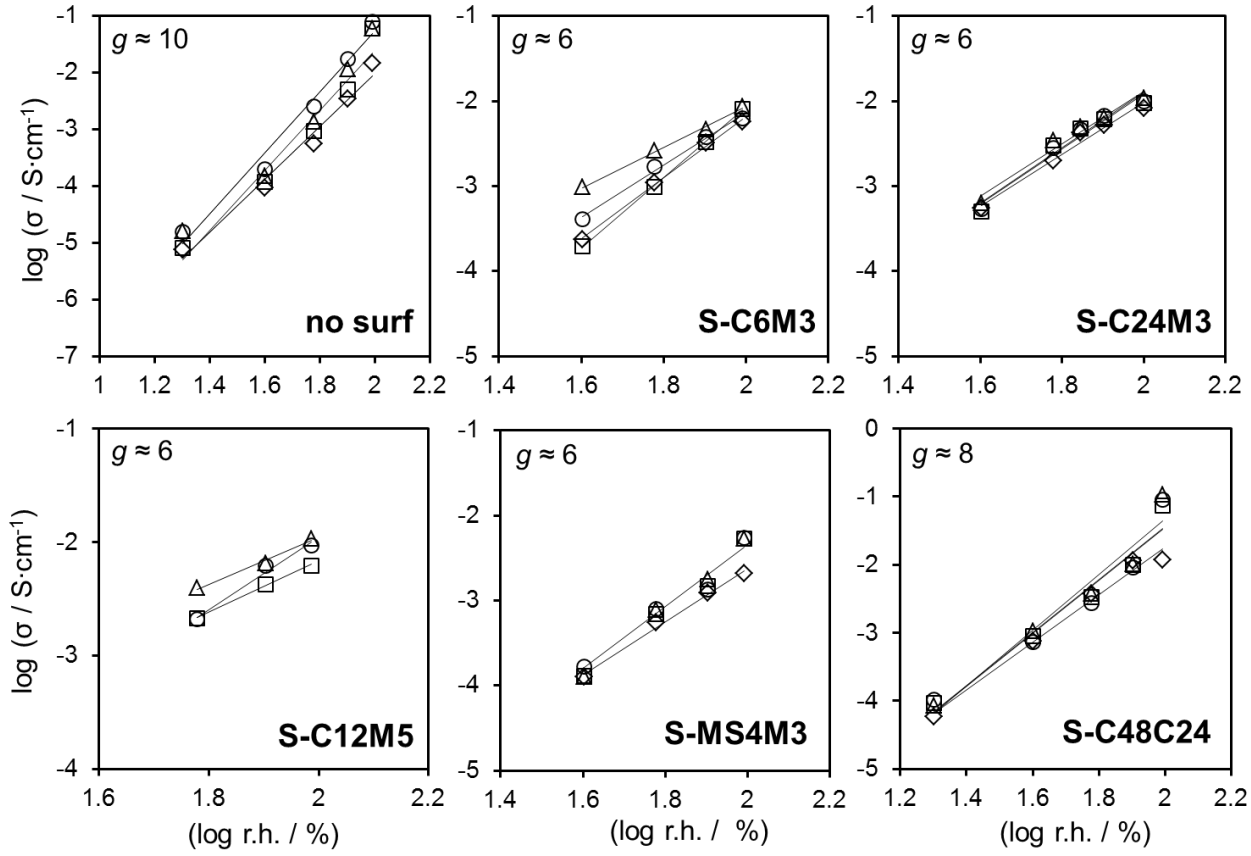

Figure 3.25. Graphical representation of log σ vs log r.h. at different isothermal conditions. ◇) 40 ºC, □) 60 ºC, △) 80 ºC and ○) 94-100ºC.

A similar analysis performed on literature data of MCM-41 materials with 40 % nominal SO_3H ($[H^+]$ = 2.3 mmol·g^{-1}) showed values of $g \approx 6$ at 80 and 100 ºC, in the r.h. range of 50 to 100 %.[156] From the data of Fujita *et al.*[213] on a SO_3H functionalized mesoporous silica oriented film with $[H^+]$ = 1.8 mmol·g^{-1} we calculated $g \approx 4$ for room temperature and r.h. between 45 and 90 % r.h. A value of $g \approx 4$ was also found for Nafion® 117 membranes in a similar range of conditions.[276]

The higher g values obtained with the S-Ph-PMO materials prepared in this work, or those estimated from literature data on similar structures, may be explained by the additional empty space within the rigid, open mesoporous network, in contrast to the soft structure of Nafion®, dimensionally-dependent on the water content.

Equation 3.5 can be used to estimate the solvation enthalpy (ΔH_{solv}) assuming a dependence with the reciprocal temperature

$$\ln(\sigma^2 / p\mathrm{H_2O}^g) \propto (\Delta S_{solv}/R) - (\Delta H_{solv}/RT) \qquad \text{eq. 3.6}$$

where the ΔS_{solv} is an entropy term. Figure 3.26 shows the data represented according to this equation.

The ΔH_{solv} values estimated for our S-Ph-PMO samples tend to become more negative with increasing $[H^+]$, spanning from an average -220 kJ·mol^{-1} for the sample with less $[H^+]$ (S-C6M3) to -300 kJ·mol^{-1} for the sample with the highest $[H^+]$ (S-C48C24). This suggests that the solvation of the proton on the acid sites is facilitated by the presence of more acid sites, justifying also the increase amount of water molecules involved in the solvation process (g values) observed in Fig. 3.25.

A theoretical study on the solvation of SO_3H in a Nafion®/H_3O^+/H_2O system calculated the enthalpy of formation of the complex $–SO3^-\cdots H_3O^+–(H_2O)n$ to be -44.3 kJ·mol^{-1}[277] while in the experimental study by Maréchal *et al.*[276] the calculated value was of -135 kJ·mol^{-1}. Nevertheless, this means that that the proton solvation is more favourable inside our mesoporous materials than in Nafion®.

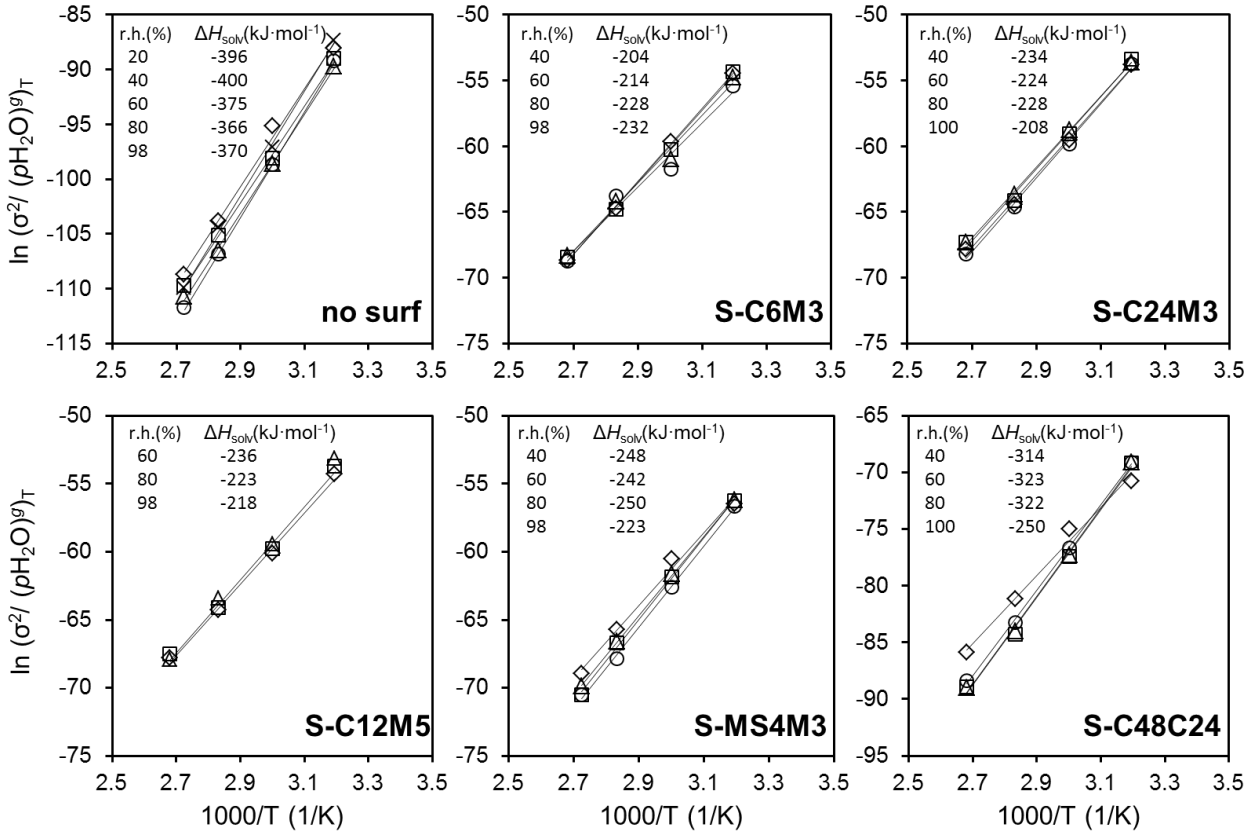

Figure 3.26. Representation of ln $(\sigma^2/(p\mathrm{H_2O})^g)_T$ vs. the reciprocal temperature for several representative samples and different r.h. conditions. ×) 20 % r.h., ○) 40 % r.h., △) 60% r.h., □) 80 % and ◇) 98-100 % r.h.

3.3.2 Influence of intrinsic factors on conductivity: structure, acid load and porosity

Figure 3.27 represents the evolution of the conductivity of the S-Ph-PMO samples as a function of the S_{BET}, for two extreme temperatures (40 ºC and 94-100 ºC) and under two extreme r.h. conditions (40% and ~98%).

The scatter of the data gives an idea of the wide range of conductivity values and reflects the magnitude of the combined effect of the materials physico-chemical properties on the conductivity. As previously noticed, the conductivity increases with increasing S_{BET} for samples with similar $[H^+]$ (full symbols in Fig. 3.27), mainly at high r.h. This is in agreement with the assumption that proton transport occurs essentially at the surface, and hence the effect of the S_{BET} may hide the impact of other factors.

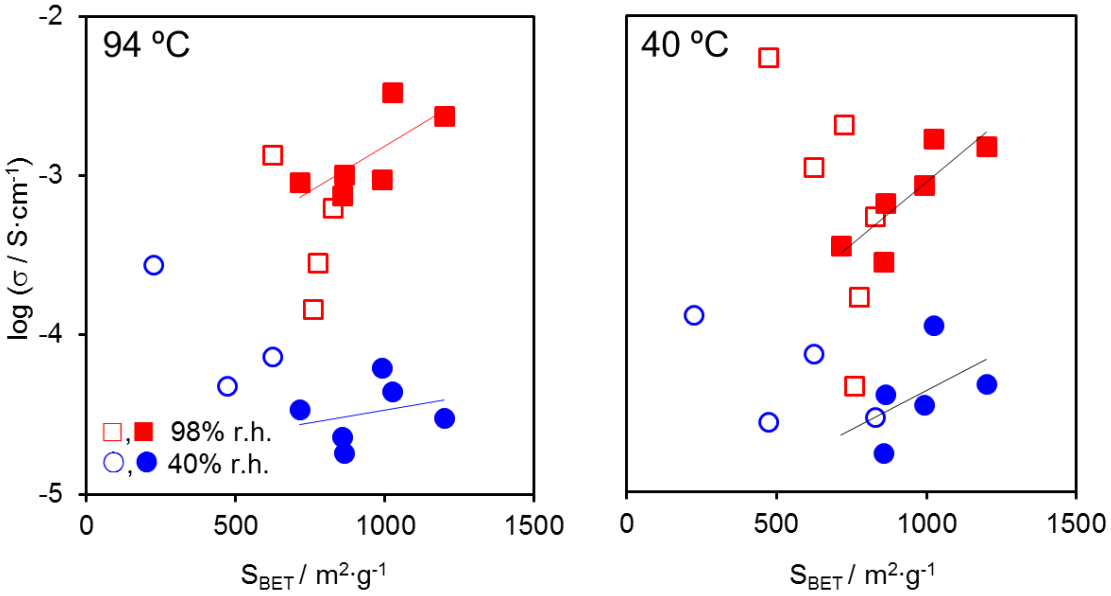

Figure 3.27. Protonic conductivity as a function of S_{BET} measured at 94 and 40 °C combined with 40% and 98% r.h. conditions. Full symbols correspond to samples with similar [H^+] within the range 0.46-0.63 mmol·g^{-1}.

It is thus useful to retain, for the subsequent analysis, the conductivity values normalized by the S_{BET}, in the form of the so-called area-specific conductance (ASC):

$$ASC = \sigma A/(L_{el} S_{BET} m_p) \qquad \text{eq. 3.7}$$

where A is the electrode area, L_{el} is the distance between electrodes and m_p is the mass of the pellet.

Figure 3.28A shows, for the same climatic conditions as in Fig. 3.27, a quasi-linear increase of ASC with increasing [H^+], for 94 °C / 98% r.h. The trend is somewhat scattered for lower temperatures, but unambiguously observed. This strong correlation demonstrates that the [H^+] is indeed the most important factor determining the protonic conductivity of these materials, and reinforces the utility of using ASC instead of the conductivity to further analyse the data. The reason for such strong effect can be found on the higher proton concentration associated to the increasing number of solvated and percolated sulfonic acid groups. Therefore, besides using ASC to account for a possible cross-effect of the S_{BET}, the [H^+] must be also considered when analysing the impact of the other microstructural factors.

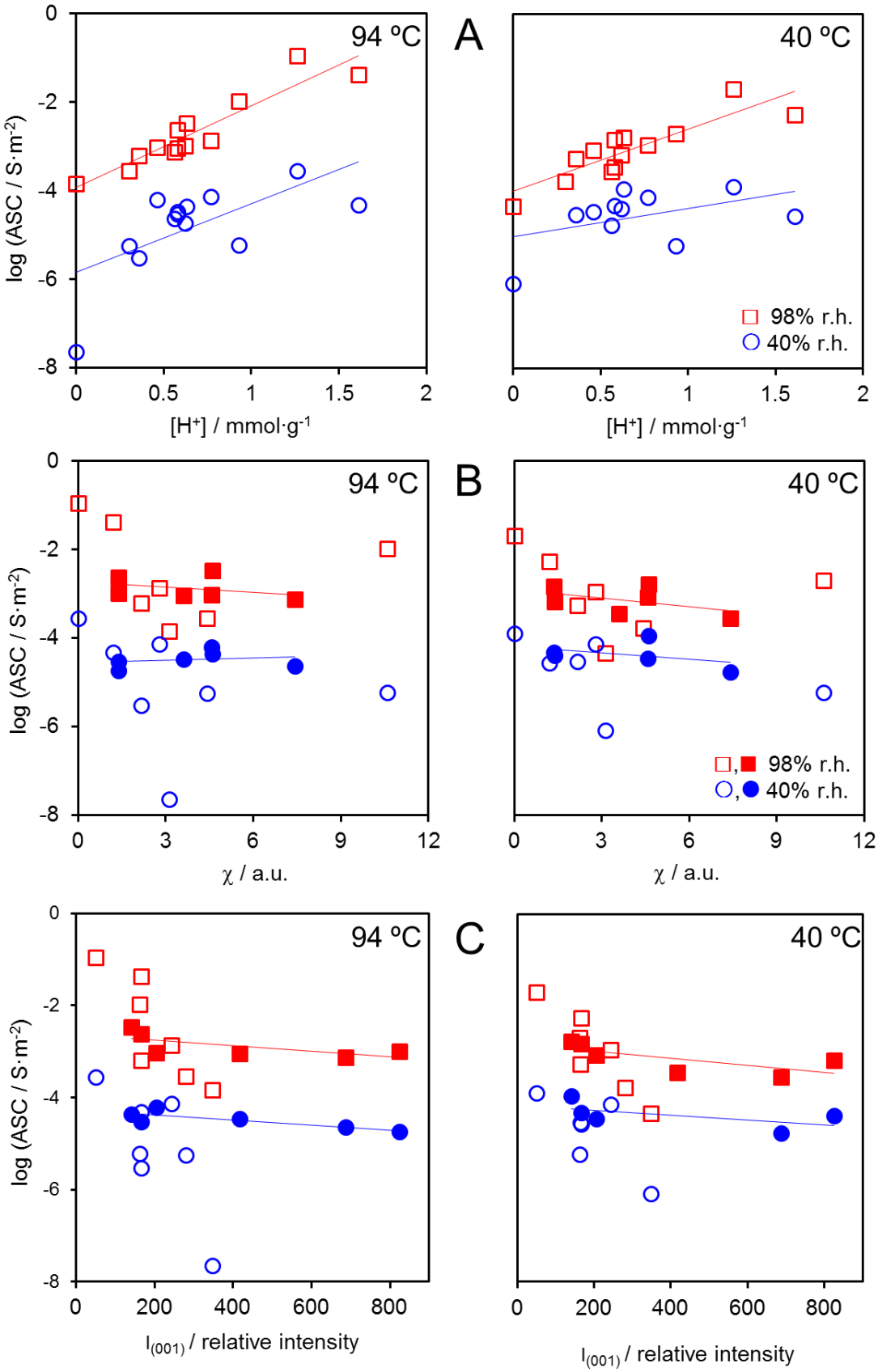

Figure 3.28. ASC as a function of A) $[H^+]$, B) χ and C) $I_{(001)}$. Full symbols identify samples with similar $[H^+]$ within the range of 0.46 to 0.63 mmol·g^{-1}.

The B plots in Fig. 3.28 show highly scattered ASC data for the highly variable pore order factor χ (table 3.4), regardless of temperature and r.h., suggesting that the pore distribution has little or no effect on the conductivity of these materials. This observation is reinforced by the ASC values for samples with similar $[H^+]$, as illustrated by the full symbols located along a quasi-horizontal line parallel to the abscissa of Fig 3.28 B.

Although it was already observed that the $I_{(100)}$ tends to decrease with increasing $[H^+]$ (and ASC thereof),[97,130,213,268] there is no indication in the literature for the use of a similar order factor such as χ.

Figure 3.28 C represents the influence of $I_{(001)}$ on the ASC. Since this peak represents the molecular scale order along the pore wall defined by the alternate stacking of hydrophilic and hydrophobic domains inside the structure,[89] of which one could infer a possible correlation between the conductivity and the distance between adjacent acid groups at the inner surface of the pores. This could ultimately affect the percolation between adjacent acid groups and undermine the protonic conductivity. There is indeed a very weak tendency of decreasing $I_{(001)}$ with increasing ASC for samples with similar acid load (full symbols), specially at high r.h., but this is certainly related to the observed decrease in $I_{(001)}$ with increasing $[H^+]$ (Fig. 3.12 B).

Due to the relatively low distribution of the a_0 cell parameter it is difficult to draw tendencies on the effect of this parameter on the ASC (Fig. 3.29 A). Based on the behaviour of samples with similar $[H^+]$ (full symbols in Fig. 3.29 A), it can be said that the conductivity values are independent of the lattice parameter, within the natural dispersion evidenced by this type of data.

Figure 3.29 B shows the evolution of ASC as a function of the pore volume, calculated from the N_2 isothermal analysis. Focusing again in the samples with similar $[H^+]$ (full symbols), the data show a slight increase of ASC with increasing pore volume. At present there is no study available that compares the protonic conductivity of S-PMO samples with similar $[H^+]$ and largely different microstructural features created by using different synthetic approaches in the self-assembly and hydrothermal treatment steps. The SO_3H functionalized mesoporous silica oriented films explored by Fujita *et al.*,[213] did not show any meaningful effect of the pore volume on the conductivity.

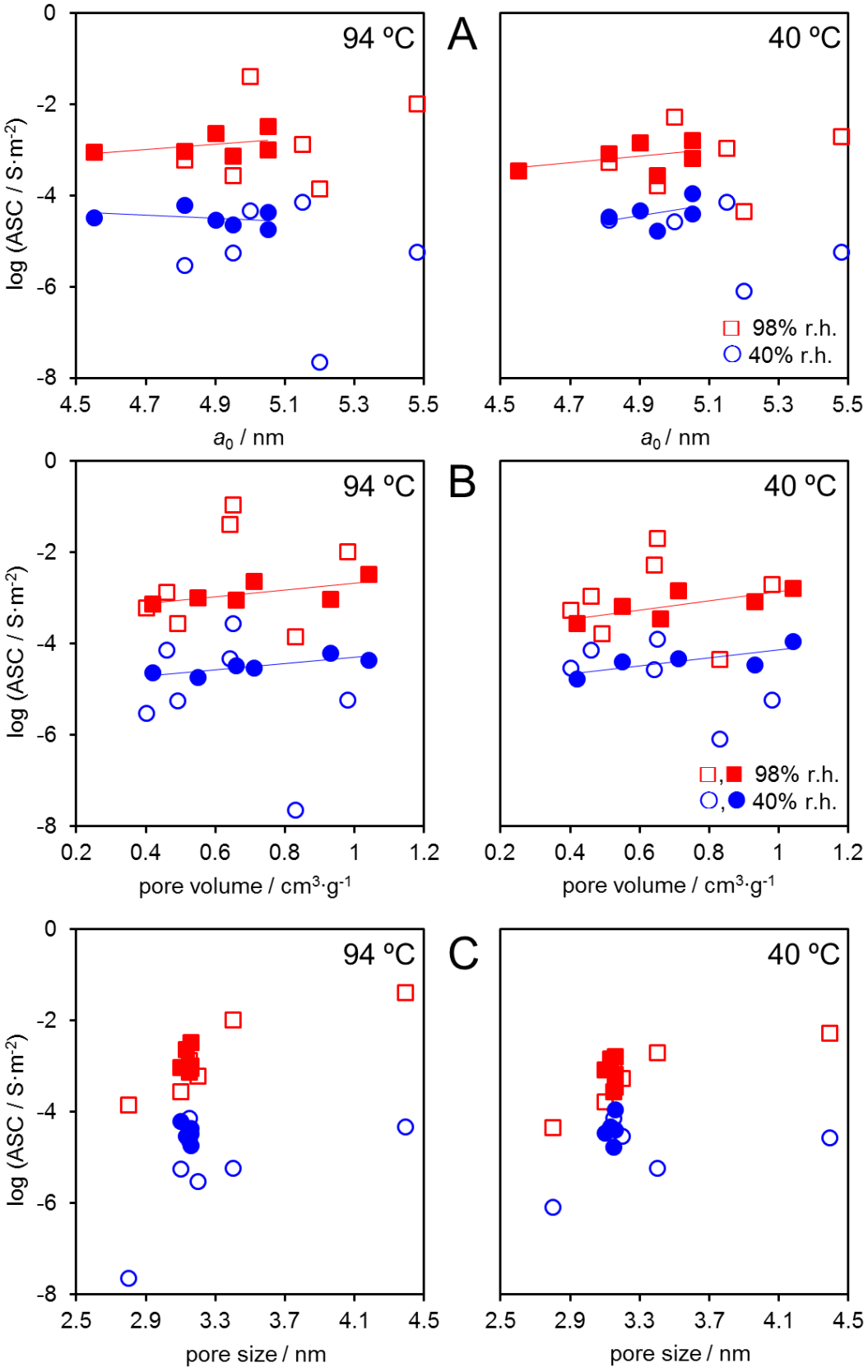

Figure 3.29. ASC represented as a function of A) a_0, B) pore volume and C) average pore size. Full symbols identify samples with similar [H^+] within the range of 0.46 to 0.63 mmol·g^{-1}.

Figure 3.29 C represents the evolution of ASC as a function of the average pore size, also calculated from the N_2 isothermal analysis. In this case, the use of only one surfactant (C18) as SDA for the synthesis of the S-Ph-PMO did not allow having materials with a wide array of pore size. It is, nevertheless, possible to identify a trend for increasing ASC as the average pore size increases, mainly at high r.h. This is at least partly related to the fact that the average pore size increases with $[H^+]$, as previously discussed in section 3.2.2, ultimately affecting positively the ASC (Fig. 3.28A). In fact, samples with similar acid loads have nearly identical pore size (full symbols).

The measurements of water uptake capacity of the materials *W* were made at room temperature, which limits the possibility of confronting these values with the ASC measured at higher temperatures. Nevertheless, it is possible and useful to compare *W* with ASC obtained at 40 ºC and 98 % r.h., the closest climatic conditions to those used to measure *W*. Figure 3.30 depicts the evolution of ASC as function of *W* in such conditions.

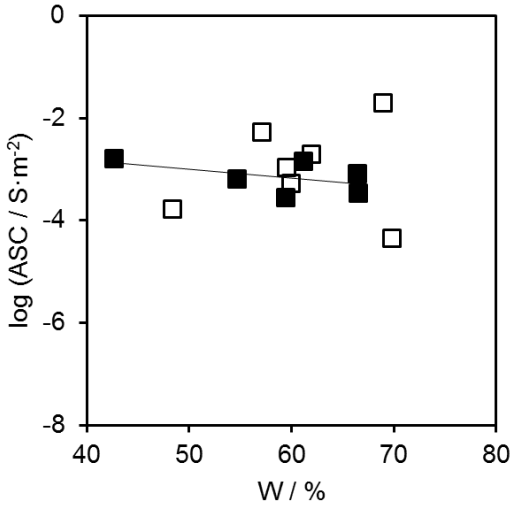

Figure 3.30. ASC at 40 ºC and 98% r.h. plotted as a fucntion of *W* for the S-Ph-PMO samples. Full symbols are for samples with $[H^+]$ in the range 0.46-0.63 mmol·g^{-1}.

It is perhaps important to notice that an increase of ASC with increasing *W* would indeed be expected since the concentration of protonic charge carriers is obviously higher with more water in the material. In fact, it is also surprising that the measured *W* values do not show any strong dependence on the concentration of acid groups in these materials (Fig. 3.19). This may suggest that the adopted procedures to measure

W are not suitable for this type of extremely reactive materials. Measurements of water vapour adsorption−desorption isotherms would certainly be more appropriate, but the lack of suitable equipment prevented this type of studies.

Figure 3.31 represents the E_a for the protonic conductivity at 98% r.h. of the S-Ph-PMO materials as a function of A) $[H^+]$ and B) ASC.

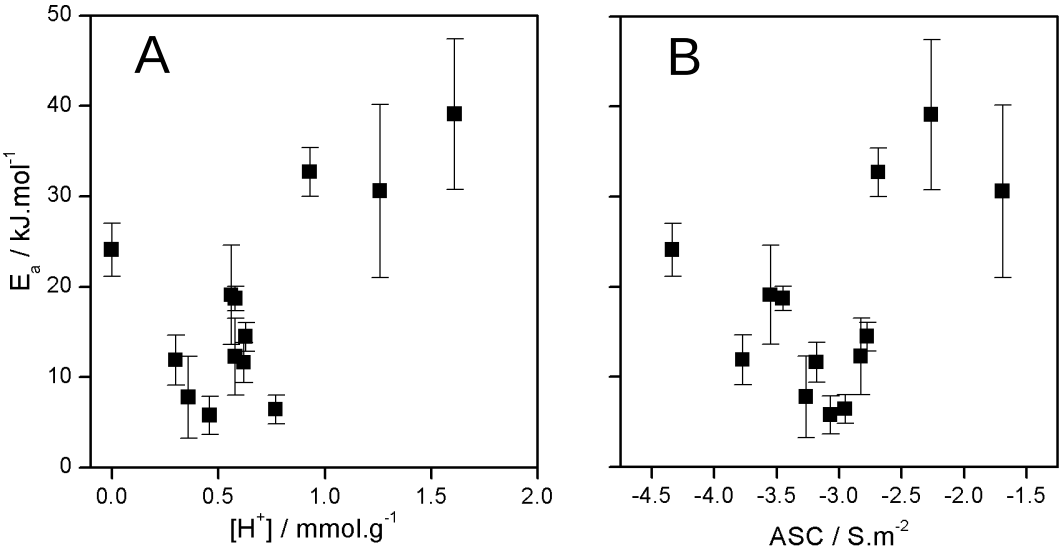

Figure 3.31. Activation energy for the protonic conductivity measured at 98% r.h. plotted as a function of A) $[H^+]$ and B) ASC

The values span from about 5 kJ·mol^{-1} to 40 kJ·mol^{-1}, with the most conductive samples in the upper range of 30-40 kJ·mol^{-1}, in line with what is usually reported for proton structural diffusion in similar hybrid structures[213,278] or in Nafion®.[258,279,280] Although the error bars may be significant in some cases, one can notice that E_a tends to increase with increasing $[H^+]$, and the same observation can be made for ASC. Since the correlation of $[H^+]$ with ASC is quite linear, one would expect such an observation. The high concentration of hygroscopic sulfonic acid group enhances the hydration capacity of the material, hence providing a higher concentration of protons in the bulk. This can lead to a higher fraction of structural diffusion of protons through hopping from neighbouring solvated acid anchor points, which typically shows higher E_a values than the vehicular mechanism.[38,41,188]

Figure 3.32 relates the ASC at 98 % r.h. with the ΔH_{solv} by showing an increase of ASC with increasing absolute values of ΔH_{solv}. Since the solvation of the SO_3H groups is more energetically favourable as the solvation enthalpy becomes more negative, the proton concentration available for transport should also increase, and hence the ASC. This is in agreement with the fact that ΔH_{solv} tends to be more negative with increasing $[H^+]$, as observed earlier, at the end of section 3.3.1 (see Fig. 3.26).

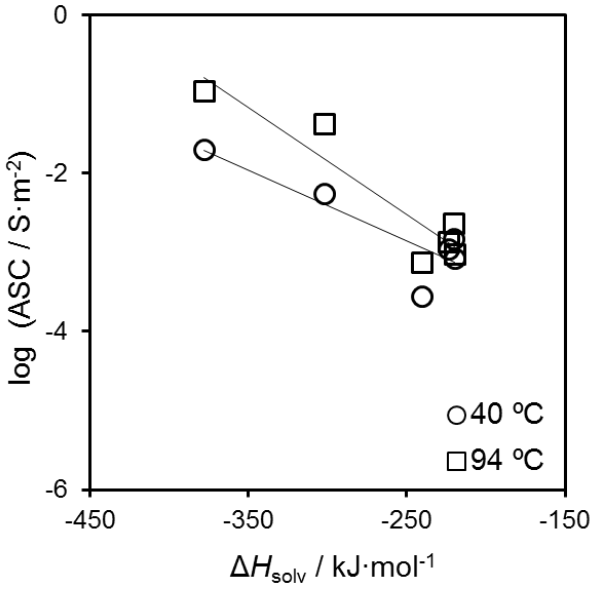

Figure 3.32. Evolution of ASC as a function of enthalpy of solvation.

3.3.3 Co-condensation vs. grafting of sulfonic acid groups: effects on conductivity

It has been shown that the co-condensation of SO_3H functionalized mesoporous silicas yields more efficient materials in terms of catalysis[281,282] and protonic conductivity[142,156,283] than the equivalent material functionalized by a grafting method. However, the co-condensed materials normally show a less organized mesostructure and the thermal stability tends to be inferior.[78]

Figure 3.33 compares the conductivity of the S-Ph-PMO materials prepared in this work, using the co-condensation method, to analogous materials obtained by Sharifi *et al.* using the post-synthetic grafting methods (details in ref.[97]). The protonic conductivity of the co-condensed S-Ph-PMO samples is four orders of magnitude higher than for the corresponding counterpart with the SO_3H group grafted on the silanol (A).

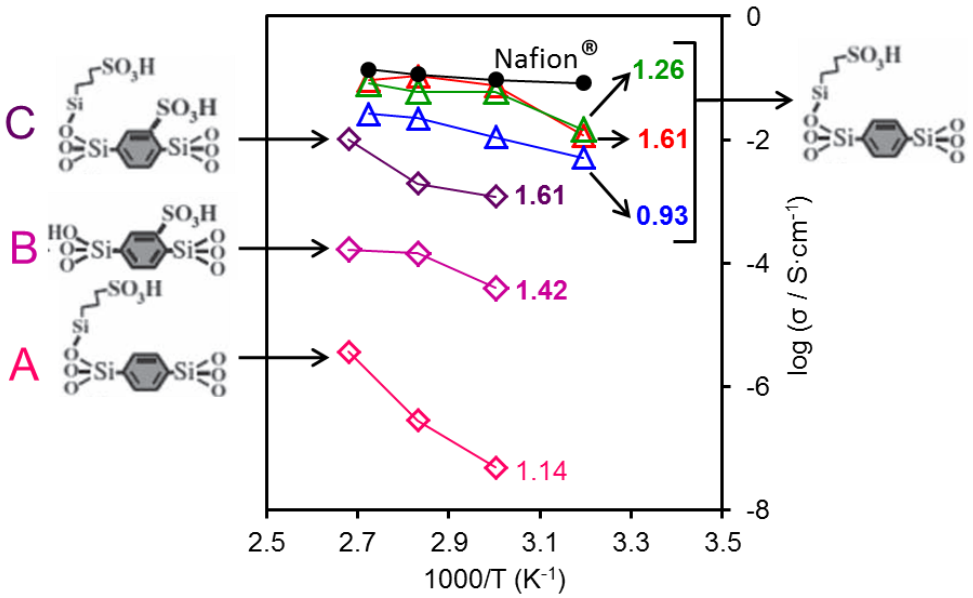

Figure 3.33. Comparison of the protonic conductivity (at 98% r.h.) of S-Ph-PMOs synthesized by co-condensation (△) in this thesis and literature data for samples obtained via post-grafting (◇) in reference [97]. Black full symbols are for Nafion® in the same conditions. The values presented in the graph are the [H^+] of each sample, in mmol·g^{-1}.

The difference is smaller for samples grafted on the benzene ring by treatment under fuming H_2SO_4, but still more than two orders of magnitude. Even the S-Ph-PMO grafted on both the silanol and the benzene ring, showing a [H^+] of 1.61 mmol·g^{-1}, is almost one order of magnitude less conductive. The E_a values for the grafted samples are abnormally high (54, 63 and 117 kJ·mol^{-1}), and clearly larger than for the co-condensed samples (see Table 3.4). One possible reason for this increased conductivity might be related to a more homogeneous distribution of the acid groups along the pore wall in co-condensed samples. This has been suggested to explain similar behaviour for SO_3H functionalized MCM-41, in which the co-condensed samples showed higher [H^+] and also higher conductivity.[141,142] Rác *et al.*[132] studied the influence of the synthetic method on the catalytic performance of several SO_3H functionalized silica-based mesoporous materials and also reported better results for the co-condensed samples. They attributed the worst results of the grafted samples to the non-random distribution of the acid groups, which are surrounded by hydrophilic regions ultimately resulting in the blocking of the active sites by strong adsorption of reactants and intermediates.

As a last note to this section, it is perhaps interesting to highlight the fact that the presented conductivity values are likely to be underestimated, due to the

macroporosity of the powder compacts, hence being potentially very similar or even higher than the conductivity of Nafion®. The other characteristics of S-Ph-PMO samples that make them suitable and desirable to act as fillers in Nafion® membranes shall be discussed in the following section.

3.4 Synthesis and characterization of composite membranes

This sub-section describes the preparation and characterization of composite membranes based on the synthesised S-Ph-PMOs and using Nafion® as matrix. These composites were prepared with a selection of S-Ph-PMOs featuring a variable set of characteristics, including acid load, porosity, and microstructural and structural order. Firstly, the focus is set on the optimization of the processing methodology in order to ensure the homogeneous distribution of the particles within the polymeric matrix. The correct analysis of the impedance spectra is critical to obtain accurate protonic conductivity values. A sub-section is dedicated to this topic underlining the differences between data collected through the plane (TP) and along the plane (or in-plane-IP) of the membranes. An attempt is made to establish correlations between the properties of the S-Ph-PMO fillers and of the corresponding composite membranes. Finally, the effect of the filler fraction on the IP conductivity and the visco-elastic behaviour of the composite membranes are discussed in face of their composition, morphology and hydrolytic properties. The results presented in this section were obtained in close collaboration with several colleagues, namely MSc Nuno Sousa, Dr. Sergey Mikhalev and in particular Dr. Carolina Navarro.

3.4.1 Optimizing the membrane processing

The distribution of the S-Ph-PMO particles in the Nafion® matrix must be ensured and is a key factor for the membrane performance, requiring a strict control of the suspension viscosity through the several processing stages. The first membranes prepared did suffer from sedimentation of the S-Ph-PMO. Figure 3.34 A is a SEM micrograph and respective Si EDS (A') mapping of a composite membrane with 5 wt.% of sample S-C24M3.

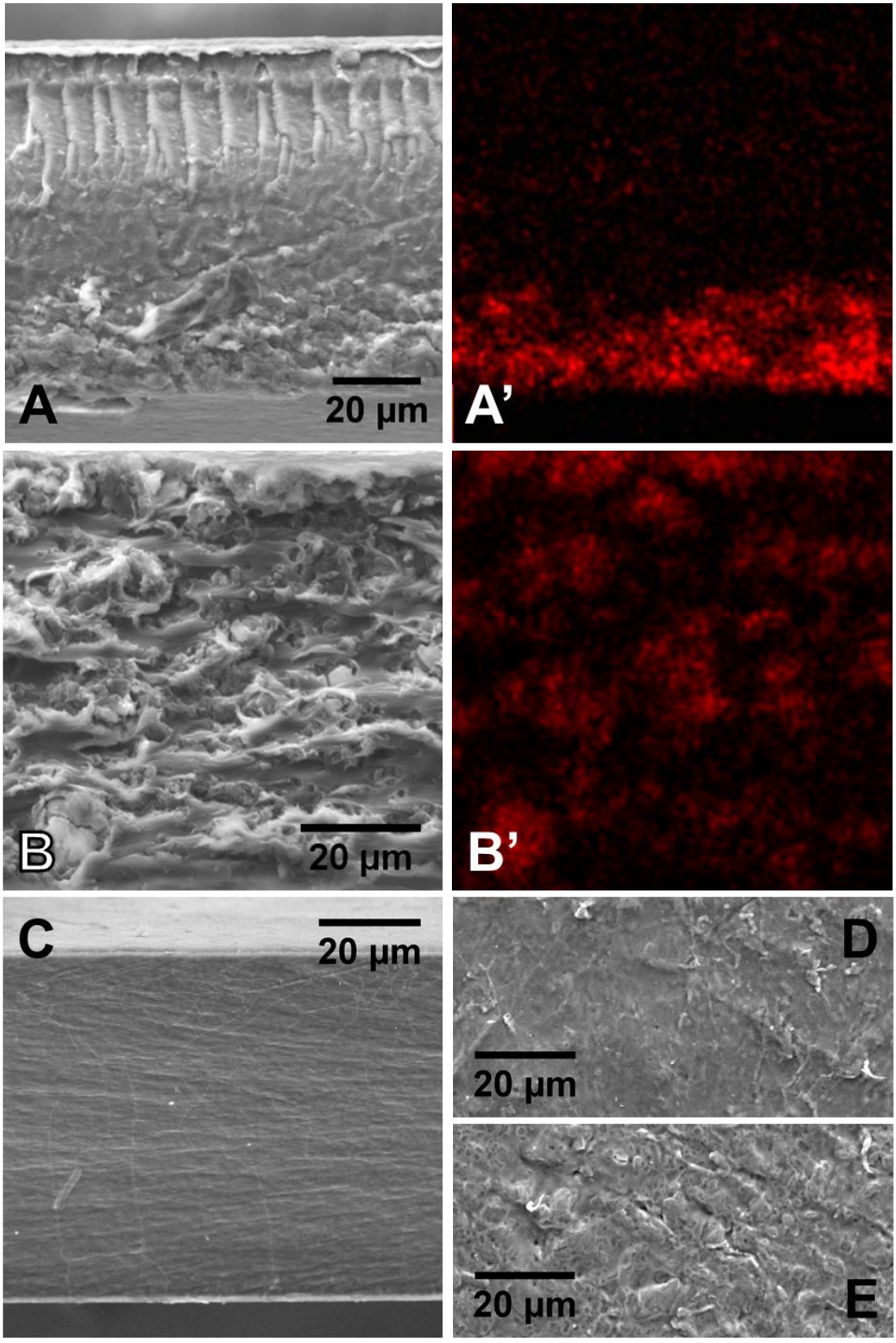

Figure 3.34. SEM micrographs of the cross-section and respective EDS mapping of A) S-C24M3-5% and B) S-C24C24-10%. C) cross section of plain Nafion® membranes. D) top and E) bottom views of S-C24M3-10% composite membrane.

The Si EDS mapping shows a clear predominance of silica-containing particles at the bottom of the membrane, with obvious corresponding morphological differences as illustrated by the SEM micrograph.

According to Stoke's law[284]

$$v_s = \frac{2}{9} \times \frac{\rho_p \rho_f}{\mu} \times g {R_p}^2 \qquad \text{eq. 3.8}$$

the terminal velocity v_s of a spherical particle with density ρ_p, falling in a fluid of density ρ_f is inversely proportional to the dynamic viscosity μ of the liquid and directly proportional to the square of the particle radius R_p. Therefore, in order to hinder the precipitation of the filler particles during the casting of the membrane it is thus necessary to decrease the size of the filler particles to a minimum and increase the viscosity of the dispersing media. The S-Ph-PMO powders were grinded on a mortar for a variable time until a limiting size was attained. The typical average particle size was of the order of 600 nm, but with fairly broad size distributions, as determined by DLS (see Table 3.4). After homogenizing the polymer suspension with the fillers, the viscosity of the slurry was increased up to a certain point by gently heating the slurry, under magnetic stirring.

It is important to monitor closely the slurry to prevent excessive drying, which would impede the casting. The casting conditions were adapted to the various filler content, as the initial viscosity varied significantly with the solids concentration. Crack-free membranes with thicknesses lower than 100 μm could be obtained with a homogeneous distribution of up to 20 wt.% filler particles, which corresponds to a quite significant 36 % of the membrane volume. Fig. 3.34 B is a micrograph of a typical membrane, with the companion Si EDS (B') map demonstrating the homogeneous distribution of the filler particles across the membrane cross-section. The fillers produce a rough surface morphology in comparison to pure Nafion®, as shown in Figs. 3.34 D (surface in contact with air during casting) and 3.34 E (bottom surface in contact with the Petri glass).

Table 3.6 presents the list of the prepared membranes and a summary of the relevant properties, including water uptake, swelling, acid load and hydration level. The $[H^+]$ values were obtained after verifying the effect of the membrane activation time, since it was found that the different membranes had different responses to this activation step. Reproducible results (less than 3% difference) could be obtained for pure Nafion® and the composites with the lowest filler fraction (5 and 10 wt. %) after a 2 h treatment, whereas the membrane with 20 wt.% fillers required a minimum of 3 h of soaking in boiling H_2SO_4 solution for an adequate activation of the acid sites. This is an indication that the particles play a role as barrier to the hydrodynamic transport inside the Nafion® matrix.

The $[H^+]$ obtained for pure Nafion® (0.90 $mmol \cdot g^{-1}$) is marginally lower than the manufacturer's specification (~0.92 $mmol \cdot g^{-1}$ available from a maximum of 0.95 to 1.01 $mmol \cdot g^{-1}$).[285]

Table 3.6. Values for *W*, swelling, $[H^+]$ and λ of composite membranes synthesized with different powder fraction.

membrane sample	Filler Fraction (wt%)[a]	*W* (%)[b]	Swelling (%)[c]	$[H^+]$ ($mmol \cdot g^{-1}$)	λ (nH_2O / nSO_3H)
None	0	54	31	0.90	33
S-MS2M3	10	50	25	0.96	29
S-C12M3	10	52	34	0.93	31
S-C24M3	5	49	28	0.90	30
S-C24M3	10	46	23	0.94	27
S-C24M3	20	47	21	0.85	31
S-C24C24	10	51	28	0.92	31
S-C48C24	10	50	30	0.92	30
S-no-surf	10	57	36	0.76	42
S-no-acid	10	47	26	0.60	43

[a] - The wt.% of the filler fraction is regarding the dry membrane of Nafion®.

[b] - The wet weight in these measurements was taken from membranes immersed in liquid water.

[c] - Taken from membranes exposed to 94ºC and 98% r.h.

Additions of 10 wt.% S-Ph-PMO to Nafion® slightly increase the $[H^+]$, attaining a maximum of 0.96 mmol·g^{-1}. The difference, however, could not be verified as statistically significant. The lower $[H^+]$ of the fillers in comparison to Nafion® (e.g. $[H^+]$=0.77 mmol·g^{-1} for S-C24M3) and invoking a simple mixture rule can explain the $[H^+]$ drop observed for the sample with highest filler content (e.g. S-C24M3-20%). Nonetheless, the data confirms that the acidic sites located at the pore wall of the mesoporous materials remain accessible inside the polymeric matrix. The *W* values are found to be in the range of the specification for the pristine Nafion® membrane, which is of 50%±5%.[285] The value for the pure Nafion® membrane was found to be within the specifications (54%), although some dispersion was observed in the values measured on other Nafion® membranes made in-lab, differences that were also noticed for membranes with different histories, typically varying between 40 and 60%.

3.4.2 Analysis of impedance spectra: through-plane vs in-plane

The first EIS measurements of the membranes were obtained with a TP configuration (section 2.5.2). Figure 3.35 presents typical Nyquist plots obtained with variable r.h. and at different temperatures using this configuration. The spectra have similar shape, dominated by a large contribution in the low frequency range that can be assigned to the impedance of the electrode or electrode/electrolyte interface. The spectra do not intercept the real axis at high frequencies, indicating that the relaxation frequency of the proton transport in the membrane is undetectable by the impedance analyser used in this work. The membranes resistance was thus assumed as the high frequency *Z'* value with the lowest phase angle, similarly to the procedure adopted for the powder compacts at high r.h. (see section 3.1.2 for details).

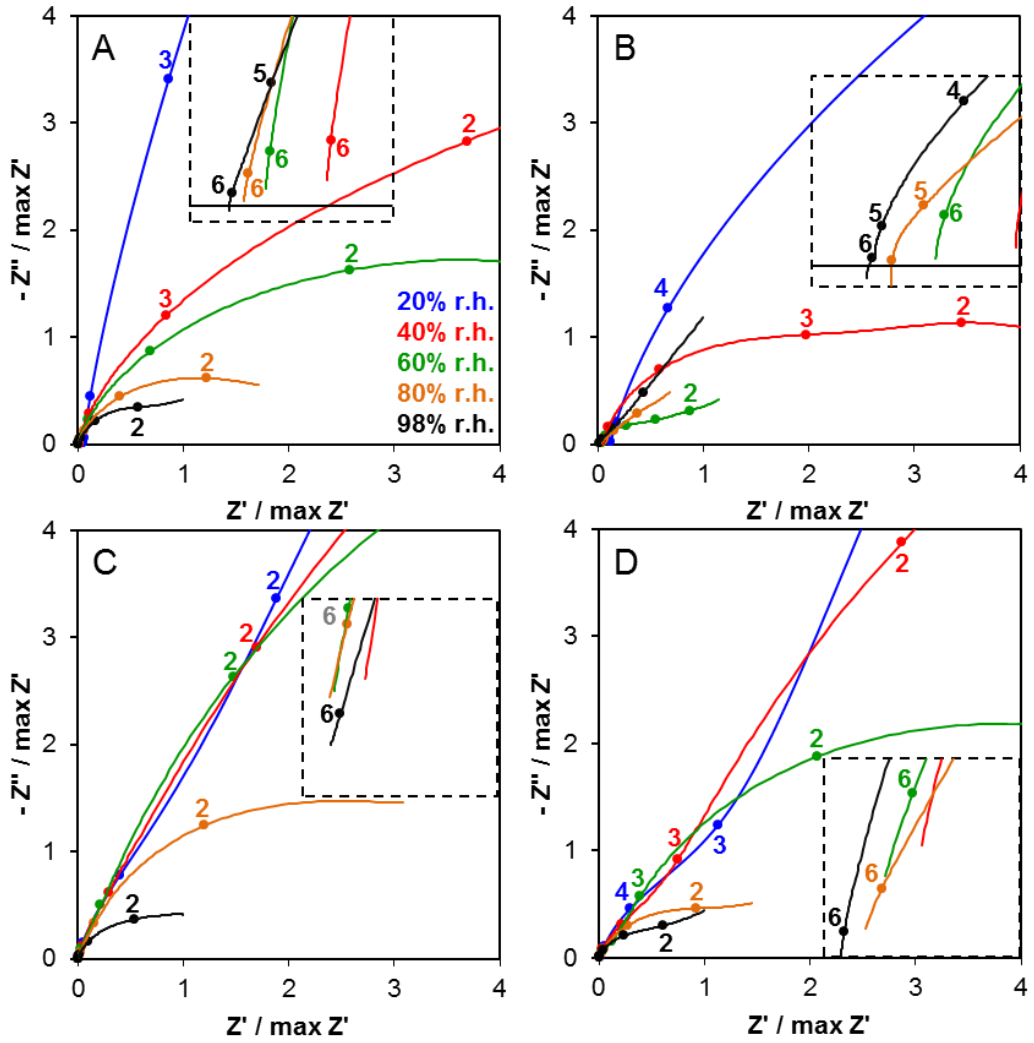

Figure 3.35. Nyquist plots for several representative membranes showing the evolution of the shape of the impedance spectra with increasing r.h. taken in the TP configuration at A) 40 °C (S-MS2M3-5%), B) 60 °C (Nafion®), C) 80 °C (S-C24M3-10%) and D) 94 °C (S-MS2M3-10%).

Fig. 3.36 shows Nyquist plots collected under different r.h. for a set of samples with increasing filler fraction. These spectra depict, for the pure Nafion® membrane, the usual electrode contribution with the high frequency intercept of the Z' axis corresponding to the membrane resistance, whereas for the composites the spectra are shifted to higher frequencies, with the last data point of the frequency (2 MHz) still in the capacitive range. The latter behaviour is similar to that obtained for powder compacts of the pure filler materials,[286] thus suggesting a major role of the filler on the electrical properties of membranes. The ill-defined spectra in the high frequency region decreases the precision with which one can determine the membrane ohmic resistance and hence the conductivity.

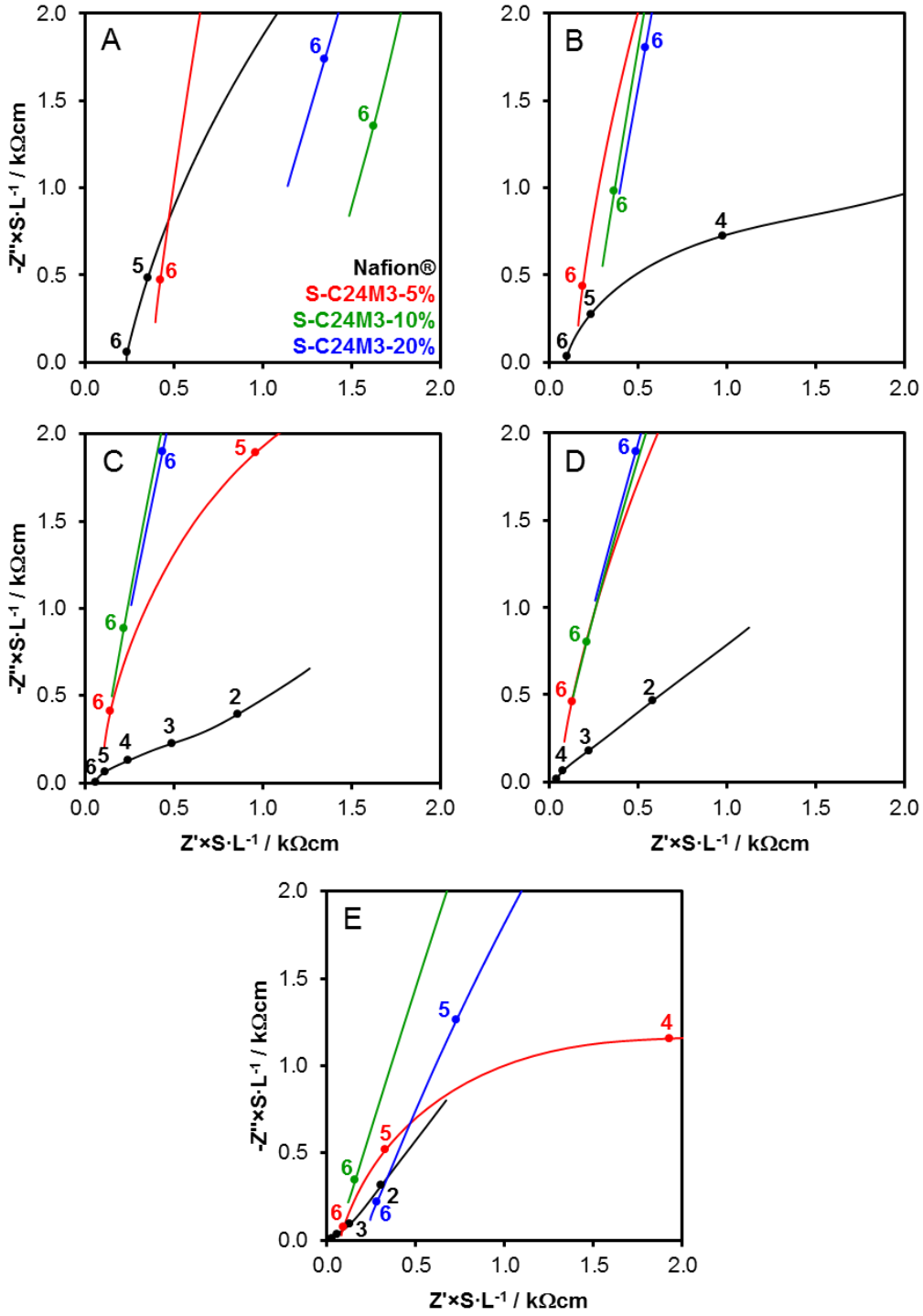

Figure 3.36. Nyquist plots collected at 80 °C and different r.h., for various membranes. A) 20% r.h., B) 40% r.h., C) 60% r.h., D) 80% r.h. and E) 98% r.h., obtained using the TP configuration. Numbers represent powers of 10 of frequency in Hz.

For this reason, the subsequent analysis of the membranes conductivity was based on data obtained using an IP configuration. The spectra obtained using this configuration shows a well-defined series of two semi-circles, as depicted in Fig 3.37. The high-

frequency contribution only starts fading at elevated r.h. conditions. Unlike the information obtained from the TP measurements, the capacitive part of the IP semicircles is solely due to the stray capacitance of the measurement set-up, as discussed in section 2.5.2, and thus one cannot extract from here any conclusion regarding the dielectric constant of the material. The IP spectra are however more adequate to estimate the membrane resistance, corresponding to the amplitude of the high-frequency semicircle.

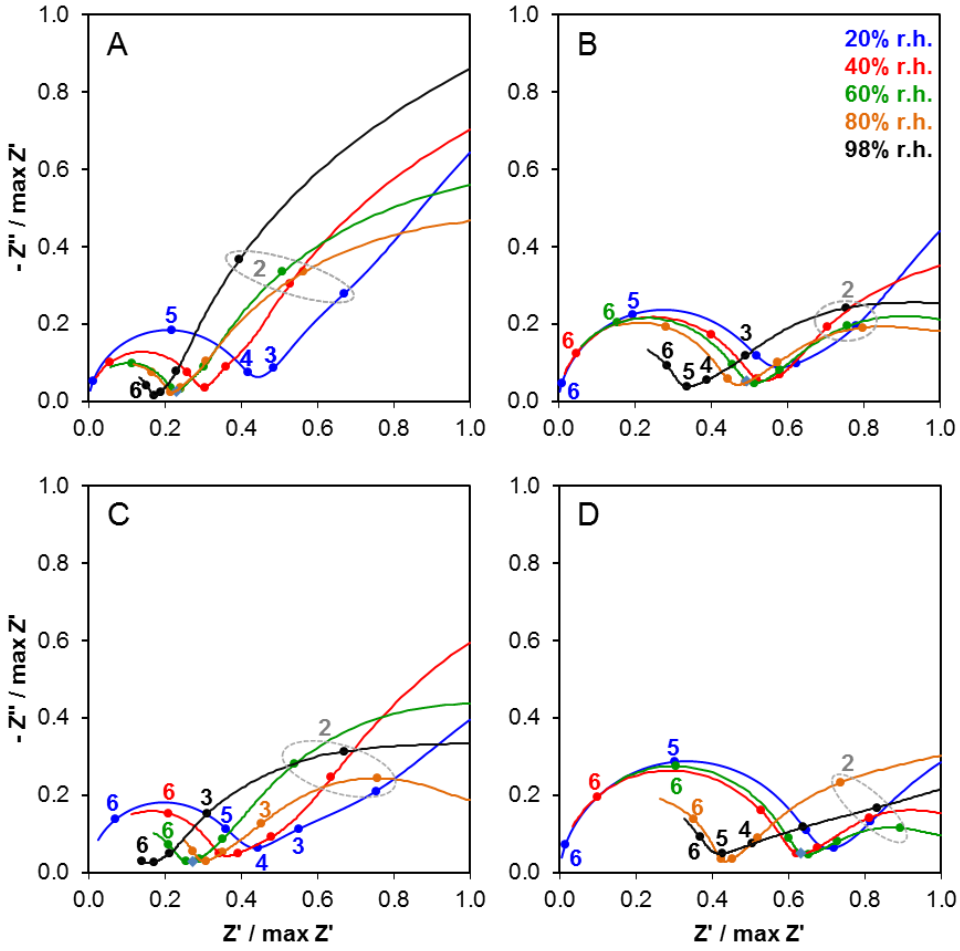

Figure 3.37. Nyquist plots for several representative membrane showing the evolution of the shape of the impedance spectra with increasing r.h. taken in the IP configuration at A) 40 ºC (S-MS2M3-10%), B) 60 ºC (S-C24C24-10%), C) 80 ºC (S-C12M3-10%) and D) 94 ºC (S-C48C24-10%).

Fig. 3.38 shows a collection of Arrhenius plots at different r.h. for composite membranes with 10 wt.% of various fillers, together with data for pure Nafion®. In almost all the conditions of temperature and r.h., the composite membranes show an increased conductivity comparing to pristine Nafion®, with exception for some samples in the almost saturated r.h. condition of 98%.

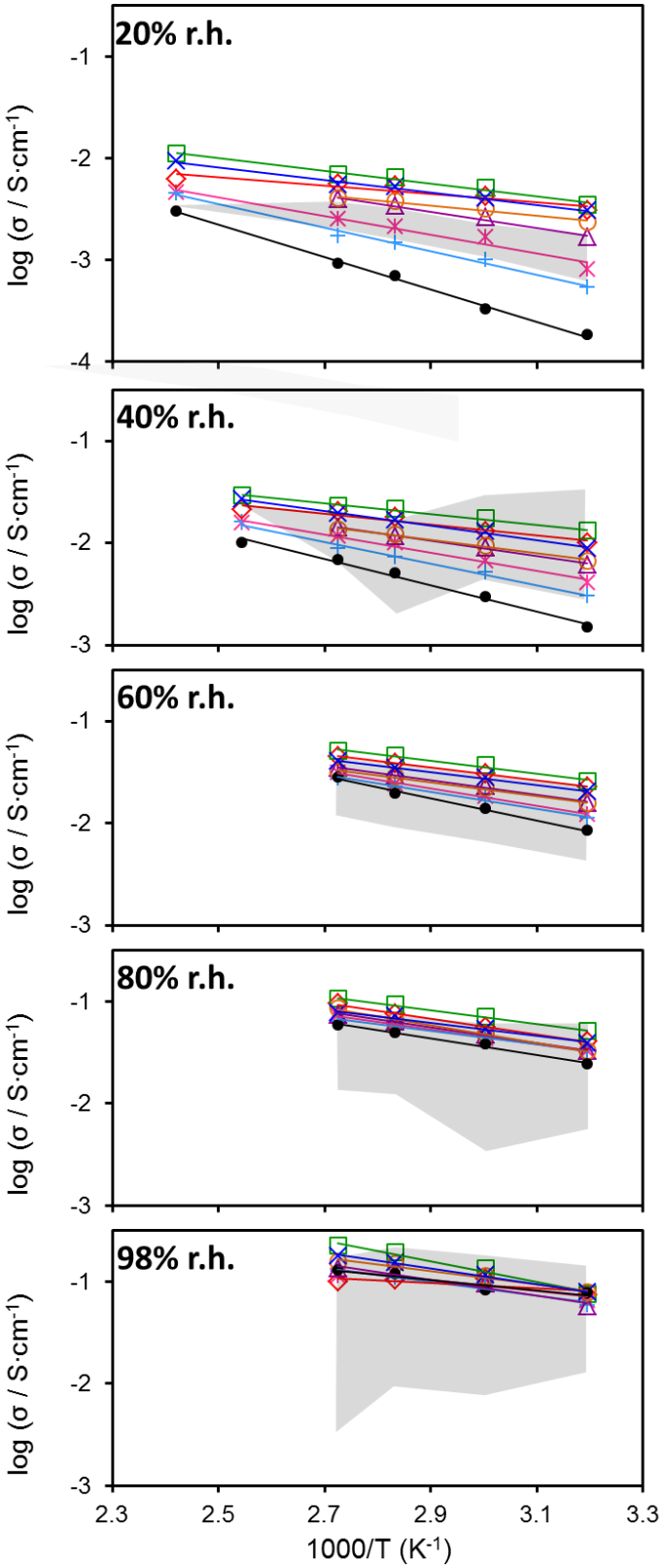

Figure 3.38. Arrhenius plots of membranes with various types of fillers as a function of r.h.●) Nafion®; +) no-acid-10%; ✳) no surf-10%; △) S-MS2M3-10% ○) S-C24C24-10% ×) S-C48C24-10% ◇) S-C12M3-10% □) S-C24M3-10%. The grey areas represent the conductivity range for pure Nafion® found in the literature, for the same conditions.[228,258,271,276,279,280,287-296]

Indeed, at 20% r.h. the conductivity of the composite membrane S-C24M3-10% is more than 19 times larger than the conductivity of the Nafion® reference at 40 ºC. The difference decreases with increasing temperatures (almost 4 times at 140 °C) and particularly with increasing r.h. In fact, the data tend to converge above 80% r.h., although almost all the composite membranes display slightly better performance than Nafion®. Experimentally, it was difficult to control the r.h. at 98% in the ACS Discovery 110 climatic chamber, mainly at T < 60 ºC. This may explain some slight deviation from the expected linearity at lower temperature and 98% r.h.

The measurements were made during heating and with increasing r.h. in order to reduce the duration of the experiments. Nevertheless, a series of preliminary measurements were conducted in order to verify that equilibrium was effectively attained with the adopted protocol, as illustrated by the example in Fig. 3.39.

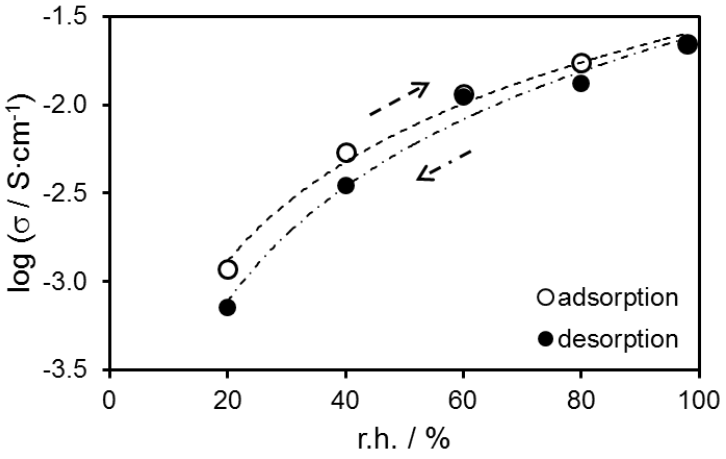

Figure 3.39. Conductivity of composite membrane S-C24M3-10% measured at 60 °C upon increasing (absorption) and decreasing (desorption) of the r.h.

The differences between the data collected during humidification and dehumidification are actually quite low, suggesting that the conductivity values were indeed obtained with the samples in equilibrium with the surrounding atmosphere.

Analogously to the calculations made for the powder compacts in section 3.3.1, the total number of solvating water molecules (g) and the ΔH_{solv} where calculated for the composite membranes and the Nafion® reference. The g and ΔH_{solv} values of the

membranes presented in this work (≈ 4 and ≈ -135 kJmol-1 respectively) are in agreement with the values available in the literature for Nafion® 117.[276]

As the analysis performed for the powders compacts in section 3.3, it is of obvious interest to try to correlate the membrane conductivity with its acid load and hydrolytic properties. This is attempted in Fig. 3.40 for composite membranes with 10 wt.% fillers.

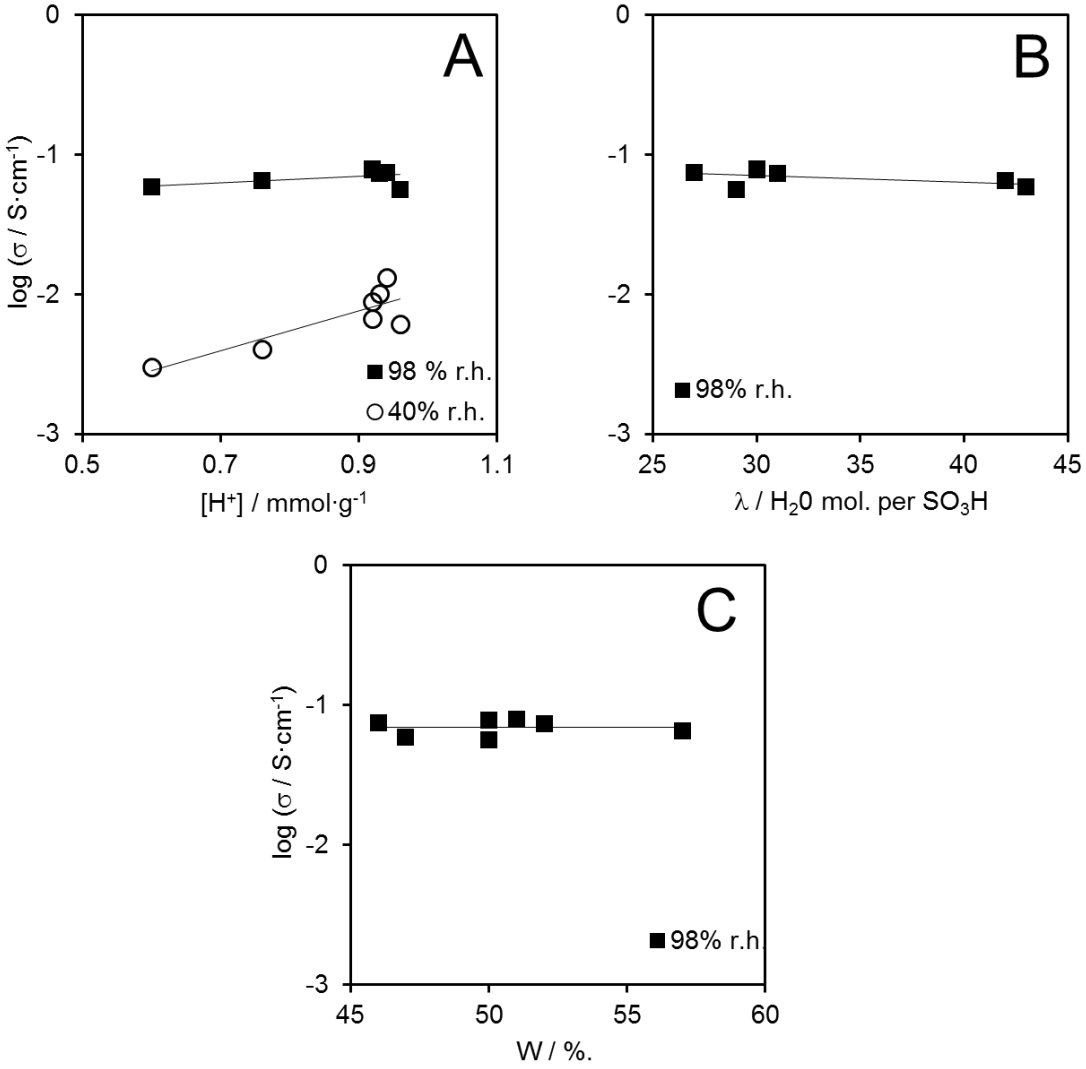

Figure 3.40. Influence of the membranes A) [H^+], B) λ and C) W on their own conductivity (at 40 ºC for membranes with 10 wt.% of fillers).

According to Fig. 3.40 A, at 40 % r.h., the membranes tend to show an increase of conductivity with increasing [H^+], which is expectable since the higher concentration

of acid sites is associated to a higher probability of percolation and consequent easier proton transport, just like it was observed for the powder compacts (see Fig. 3.28 A). Increasing the r.h. to 98% increases the proton concentration in the membrane and the overall conductivity is less dependent on the acid protons. It should be noticed that very similar trends are observed at higher temperatures due to the relatively low activation energy. Likewise, the conductivity of highly hydrated membranes ($\lambda > 25$) does not vary with λ (Fig. 3.40 B).

Since the λ values were calculated from W and $[H^+]$, it accounts for all the water inside the membranes and S-Ph-PMO materials, including the water adsorbed by capillarity and not only the portion solvated around the SO_3H groups. In the case of the composite membrane no surf-10% (see table 3.6), the higher λ value could be due to the high $[H^+]$ of the fillers. However these acid groups might be somehow less available since the S_{BET} is so low, which could explain the observed low $[H^+]$ of the composite membrane. In the case of the composite no-acid-10% (see table 3.6), the absence of SO_3H acid groups in the fillers can partly explain the lower $[H^+]$ value, but not totally since only 10% of the mass correspond to the fillers (a $[H^+]$ value closer to 0.8 mmol g^{-1} is expected for this composite assuming a simple mixture of the two components). The lower $[H^+]$ observed (and higher λ thereof) may indicate some kinetic limitation affecting the protonic exchange.

As expected for heavily hydrated membranes, the conductivity becomes less dependent on the water content (Figure 3.40 C).

3.4.3 Effect of the filler characteristics

This sub-section is dedicated to the analysis of the influence of the fillers structural and microstructural features on the physical and electrochemical properties of the composite membranes.

Figure 3.41 plots the W and $[H^+]$ of the membranes with 10 wt.% of fillers as a function of their $[H^+]$ and S_{BET}.

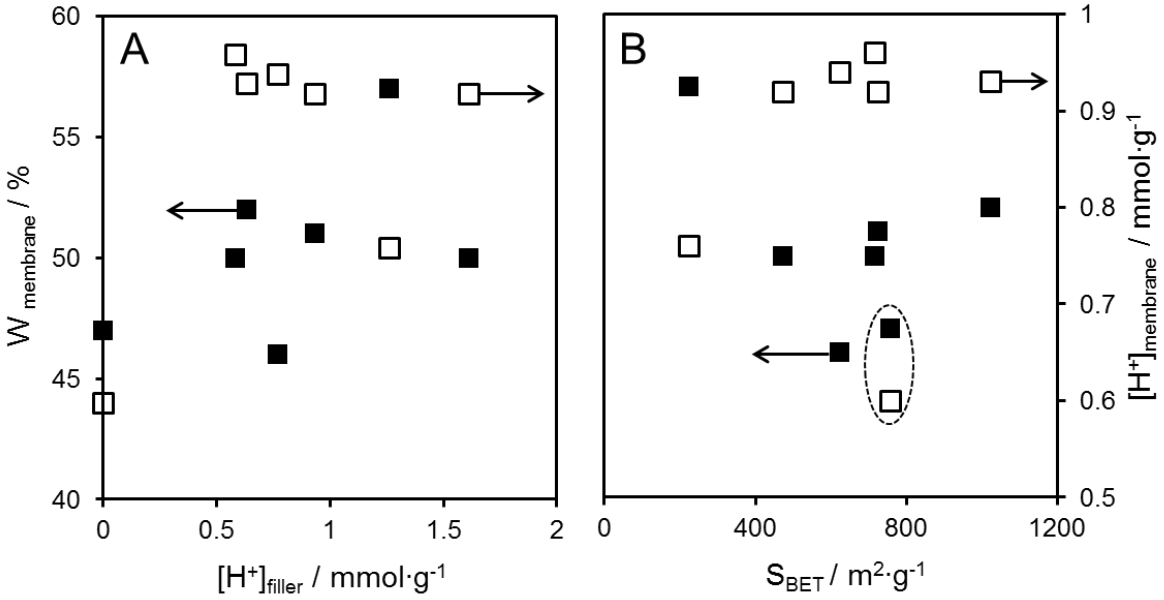

Figure 3.41. Evolution of *W* and [H$^+$] of the membranes (10 wt.% fillers) as a function of the filler properties A) [H$^+$] and B) S_{BET}. Values inside the dotted oval shapes are for composite membranes no-acid-10% and no surf-10%.

There is no direct correlation between the [H$^+$] of the powder and the [H$^+$] of the composite membranes. Ignoring the values for composites no-surf-10% and no-acid-10% one can observe that the acid load of the S-Ph-PMO powders (Fig 3.41 A) does not imply significant changes on the [H$^+$] of the membranes, as expected, considering that only 10% of the membrane mass is replaced by fillers. Similar conclusions can be drawn from the evolution of the [H$^+$] as a function of the fillers S_{BET} (Fig. 3.41 B).

On the contrary, a slight increase of the water uptake is suggested by an increasing surface area of the fillers (Fig.3.41 B). This indicates that the fillers can indeed accommodate a significant amount of water in their mesoporous structure.

Figure 3.42 correlates the conductivity of composite membranes with 10 wt.% fillers with structural and microstructural features ([H$^+$], χ and $I_{(001)}$) of the filler powders. The trends are the expected in face of the behaviour of the fillers themselves, with a slight increase of conductivity with increasing [H$^+$], whereas the structural orders (of pores and pore walls) have no significant effects.

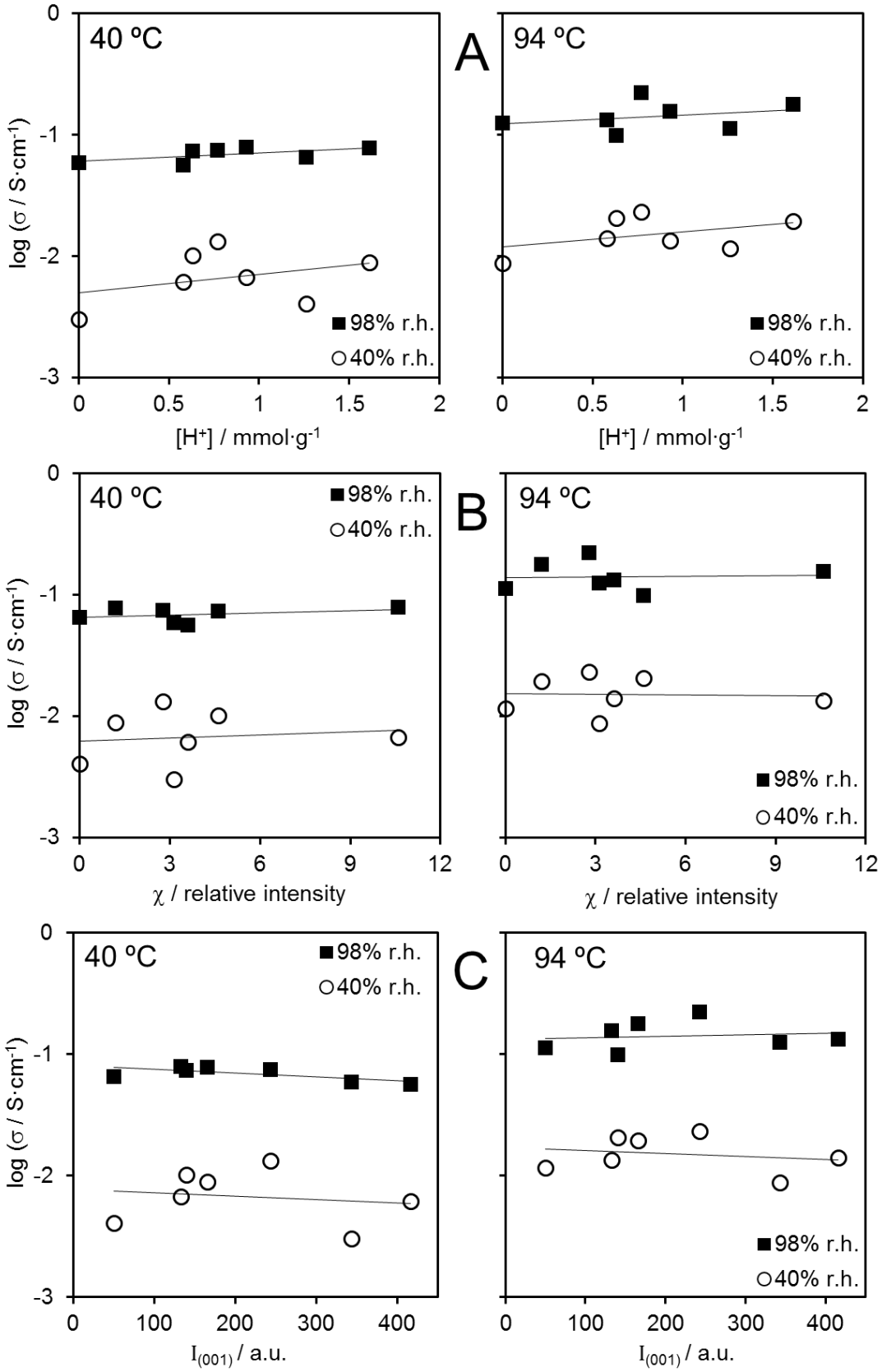

Figure 3.42. Evolution of the protonic conductivity of several 10 wt. % composite membranes as a function of the S-Ph-PMO fillers characteristics A) [H^+], B) χ and C) $I_{(001)}$.

3.4.4 Effect of the filler fraction

So far, the composite sample S-C24M3-10% showed the highest conductivity in low and high r.h. conditions, although the major differences were found at the lower r.h. This sub-chapter presents a study of the effect of the fraction (up to 20 wt.%) of this particular filler on the morphology, hydrolytic properties, [H^+], visco-elastic properties and protonic conductivity of Nafion®-based composite membranes.

3.4.4.1 Morphology, hydrolytic properties and acid load

Looking back to Table 3.6, the data suggest a slight decrease of W with increasing filler content until 10 wt.%, with further additions having no meaningful effect (within the natural dispersion on these kind of measurements). The hydration number reflects this tendency as well, but differences amongst the various membranes are indeed small, with all λ values found on a narrow interval averaged by $\lambda = 30$.

The swelling of the membranes upon hydration show a decrease with increasing filler fraction, as depicted in Fig. 3.43. The trend is somewhat scattered for the data collected at lower temperature, which may be the combined result of insufficient measuring precision (1 μm) and some heterogeneity of the membrane thickness. These limitations are less severe at high temperature, when the membranes expand considerably more, and the data allows a confident linear fit of the dependence of the membrane thickness on the volume fraction of the fillers (circle symbol in Fig. 3.43). This can be explained by the rigid and open mesoporous structure of the S-Ph-PMO which provides the free volume necessary to accommodate the hydration water without expanding the Nafion® matrix, and again confirming that the acidic sites in the pores of the filler are easily accessible in all membranes. The projection of the trend line towards the total substitution of the matrix for the filler suggests that the swelling of the fillers should indeed be virtually inexistent.

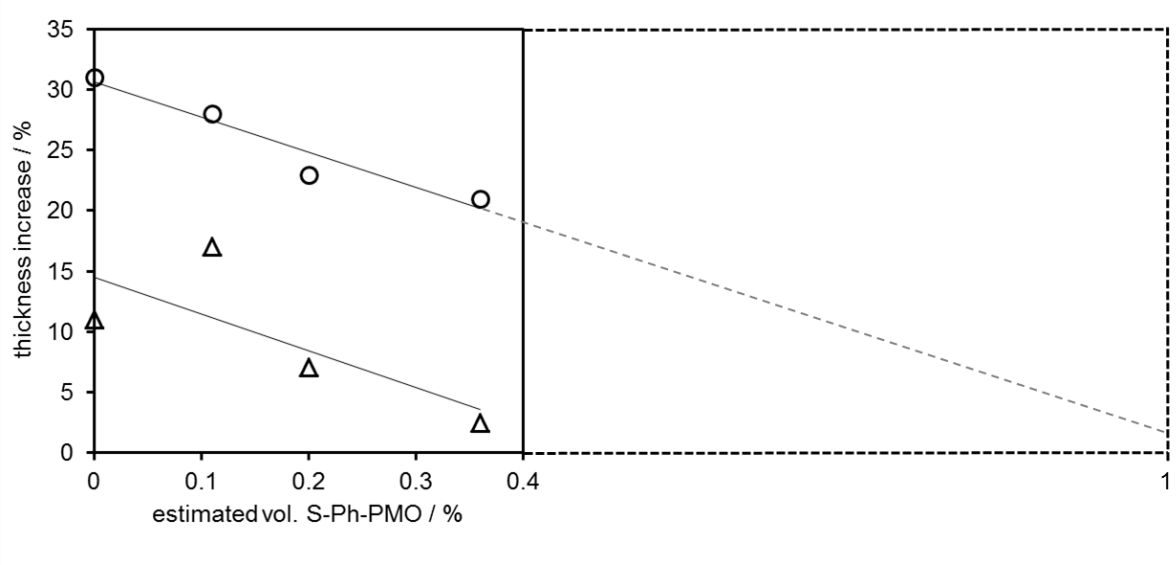

Figure 3.43. Swelling expressed as the fractional increase of the thickness of membranes equilibrated under different temperature (○-94 ºC and △-40 ºC at 98 % r.h). The reference value was obtained with the membrane exposed to 20% r.h. at 40 °C.

Figure 3.44 shows the combined SEM micrographs and Si EDS mappings collected at the cross-section of the various composite membranes. All membranes were obtained with an apparent homogeneous distribution of the filler particles, demonstrating that both the powder agglomeration and the particle precipitation on the bottom side of the casting dish could be minimized. Despite the obvious morphological differences due to the fillers, all membranes were obtained free of cracks and of any major macrostructural defects. The thickness of the dry membranes was in the range of 70 to 80 μm. The cross-sectional view of the membranes with less fillers (5 and 10 wt.%) show some surface holes in the polymeric matrix, resulting from the detachment of filler particles during the preparation of the samples for SEM (Fig. 3.44 A and B). With the increasing amount of filler (20 wt.%), the two phases become difficult to distinguish on the observable rough surface (Figs. 3.44 C). The elemental map for this sample clearly shows the Si percolation, where the occasional spots of higher intensity are most likely due to an effect of topography (Fig. 3.44 C and respective EDS mapping C').

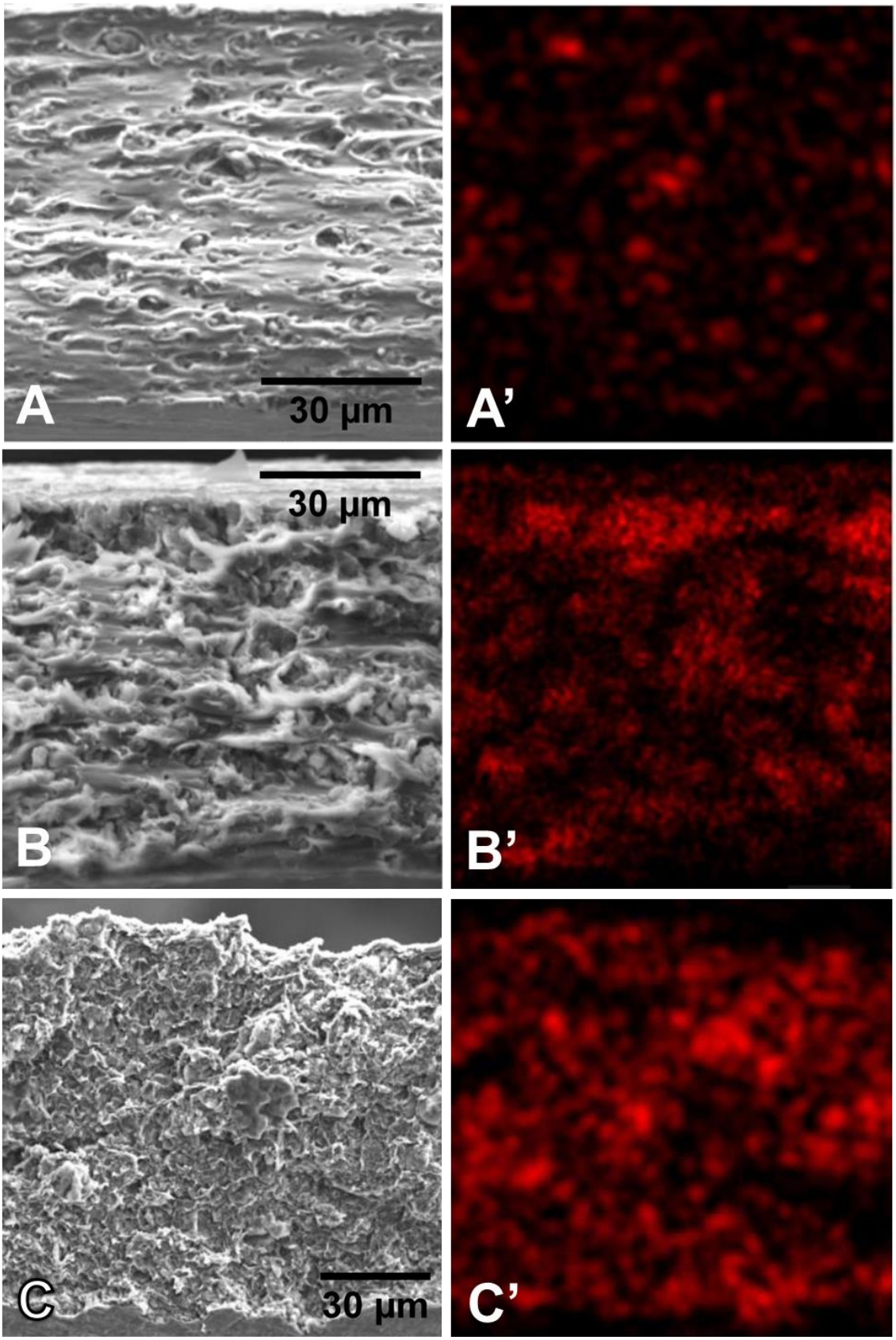

Figure 3.44. SEM micrographs and respective Si EDS mapping taken at the cross-section of composite membranes samples A) S-C24M3-5%, B) S-C24M3-10% and C) S-C24M3-20%

Fig. 3.44 B, taken for the 10 wt.% S-Ph-PMO sample, also shows very intense Si-rich regions, but most of them are surrounded by dark regions, denoting a clearly less percolated structure than in the 20 wt.% membrane. Images of the membrane with 5 wt.% fillers taken at high magnification (Fig. 3.45 A) reveal the presence of agglomerates of the initial submicrometric particles (~0.5 μm) with typical sizes in the range 2-5 μm, although a large faction of the powder remains dispersed in the polymer (see Fig. 3.44 A'). These agglomerates are no longer discernible on the microstructure of the 20 wt.% membrane, which is perhaps better described by a network of interconnecting submicrometric particles with the spaces filled by the polymer (Fig. 3.45 B).

The microstructural features observed on the cross-sections are also apparent on images of the surface of the membranes. Figure 3.45 C (membrane with 10 wt.%) depicts a quite rough surface due to the presence of the fillers within the polymer matrix, shown in detail by Fig. 3.45 D. The Si distribution map shows again the presence of Si regions surrounded by dark areas (Fig. 3.45 E and respective EDS mapping E'), a pattern similar to that observed at the cross-section (Fig. 3.44 B). Some small pore-like voids are topographic features that do not percolate inwards to the bulk of the membrane.

In face of the large impact of the fillers on the membrane morphology, it is important to notice that the moderate weight fractions of fillers (5, 10 and 20%) actually correspond to approximately the double in terms of volume fraction (11, 20 and 36 vol.%), if one considers the usual density of Nafion® of ~2 $g \cdot cm^{-3}$ and ~0.9 $g \cdot cm^{-3}$ for the density of the powders. The latter is an assumption based on the geometric density of the powder compacts, and should thus be an upper value, since the sample volume is somewhat overestimated due to the contribution of macropores inherent to powder packing. In fact, slightly higher densities are reported for ordered mesoporous silica with similar microstructural characteristics, but processed as films with well-defined geometries allowing reasonably accurate estimates of the density.[213]

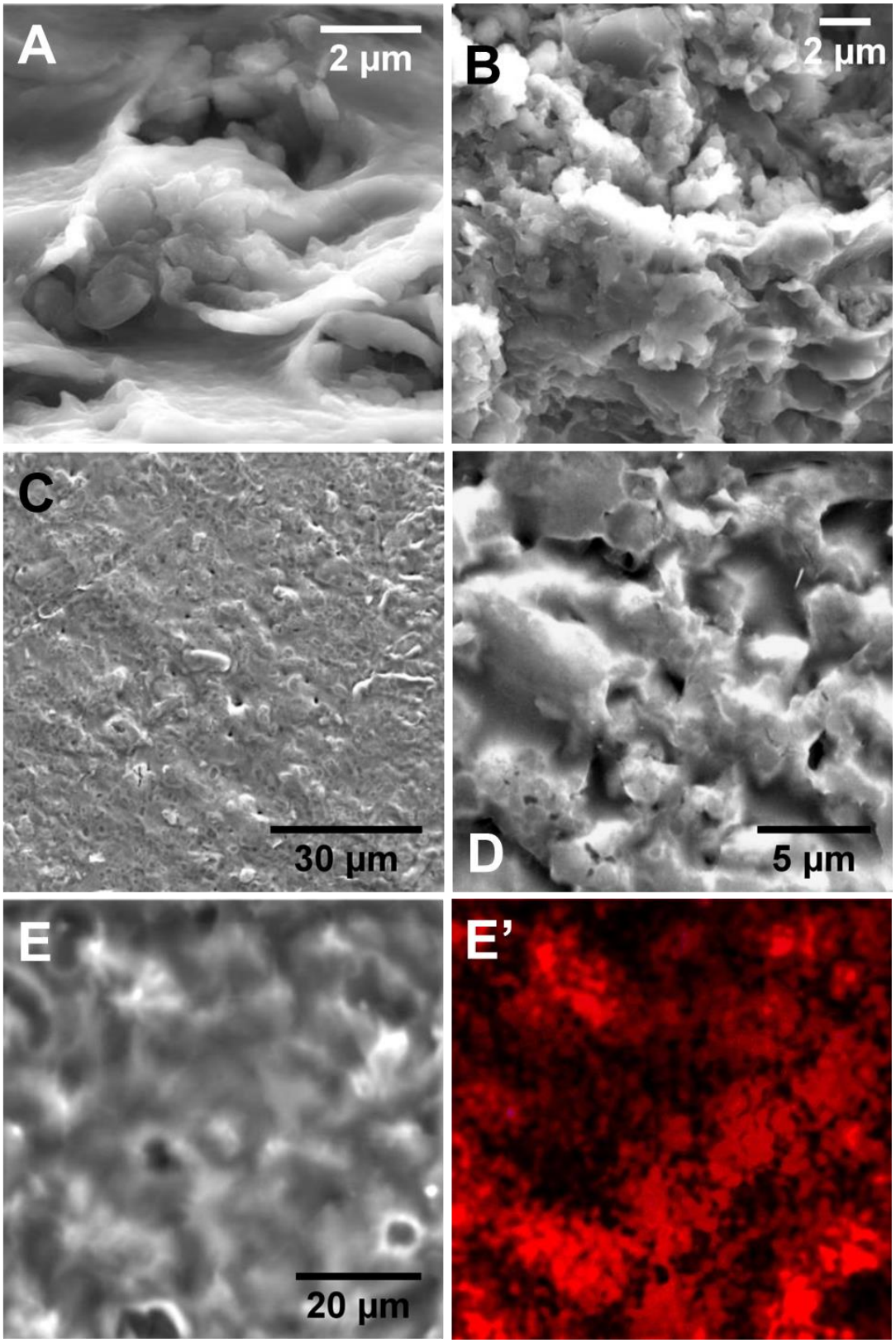

Figure 3.45. SEM micrographs taken at the cross-section of composite membranes A) S-C24M3-5%, B) S-C24M3-20% and at the surface of C,D and E) S-C24M3-10% with the respective Si EDS mapping.

3.4.4.2 Visco-elastic properties

The visco-elastic behaviour of the various membranes was investigated by DMA. The temperature dependence of the storage modulus (*E*') depicts essentially the same features for the 4 membranes, but the 20 wt.% S-Ph-PMO composite shows clearly higher *E*' values than the other samples throughout most of the used temperature range, as depicted in Fig. 3.46 A.

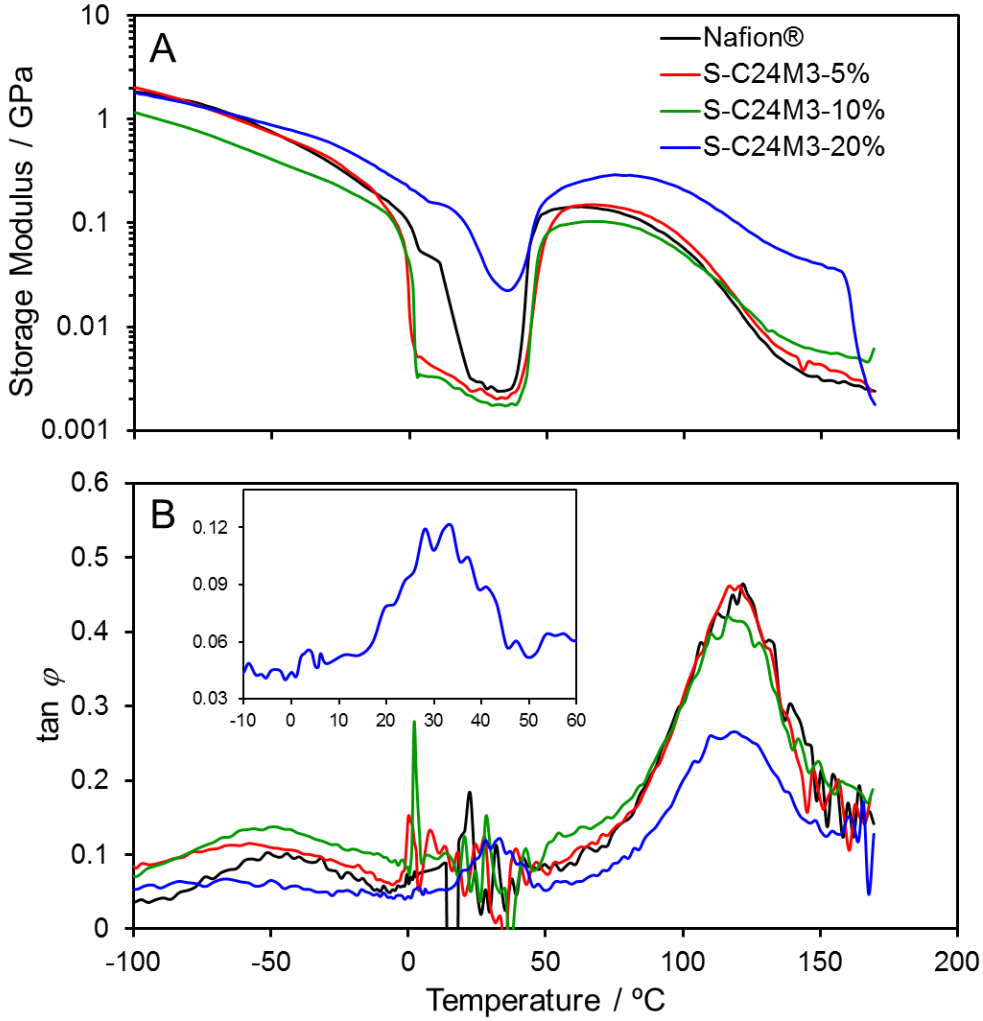

Figure 3.46. Comparison of the A) Storage modulus and B) tan φ obtained by DMA for Nafion® and Nafion®/S-C24M3 composite membranes (the inset is a zoomed view of sample S-C24M3-20%.

The modulus is close to 1-2 GPa at -100 °C, decreasing almost linearly with increasing temperature until ~0 °C, where significant differences between this and the other

membranes are already apparent. While this composite clearly detaches from the other membranes, the positive impact of lower filler quantities on the mechanical properties is also apparent on the progressive increase of *E*' with increasing filler content above 120-130 °C.

A sudden decrease of *E*' is observed above the melting point of water, which is particularly abrupt for the composites with 5 and 10 wt.%. The data show an impressive recovery of *E*' at ~40 °C, depicting a plateau-like behaviour in the range 50-80 °C. Further heating leads to a second linear decrease of *E*' until another plateau is attained above 130-140 °C. The modulus of the 20 wt.% composite is half to one order of magnitude higher than for the other membranes (0.2 GPa at 100 °C, or 0.05 GPa at 140 °C), thus suggesting enhanced mechanical performance of this membrane comparing to the pristine Nafion®. Such type of sudden transition for the sample with the highest filler content is typical of percolation-type behaviour, which is to some extent expected in face of the approximate volume fraction of S-Ph-PMO (36%) and the SEM/EDS observations (Fig. 3.44 C). The existence of a percolating network of the more rigid S-Ph-PMO mesoporous structure (compared to Nafion®) would very likely counteract the destabilization of the electrostatic network responsible for the degradation of the visco-elastic behaviour of Nafion® at these temperatures.[32,33,248-250]

The following analysis of the loss tangent (tan φ) data seems to support this hypothesis. However, some previous remarks about the possible influence of the uncontrolled presence of water in the membranes or in the DMA apparatus (the chamber of the DMA apparatus used in this work does not allow the control of r.h.) are necessary in order to justify the somewhat confusing trends observed for the low temperatures, particularly in the interval between 0 and 50 °C. The water has a plasticizer role and hence an enormous influence on the DMA results.[33,248,249] Since it would have been impossible to maintain the membranes dry during the manipulation and the measurements, a pre-treatment in temperature and r.h. conditions close to normal laboratory environment was carried out.

All samples were thus equilibrated at 25 °C under 50% r.h., which for the Nafion® corresponds to $\lambda \approx 5$ (the exothermally absorbed water).[33,213] Similar hydration values are expected for the composite membranes, as suggested by the observed W (Table 3.6). The DMA studies were performed upon heating, and hence some of the water existing in the chamber may condensate on the membrane surface, since not all the water should be adsorbed due to the kinetic limitations during the fast cooling. This water melts at 0 °C during the slow heating and can be immediately adsorbed by the membrane, with expected drastic effects on the elastic behaviour. Above room temperature, the r.h. decreases and the membranes start to dehydrate until the elastic behaviour is drastically recovered and the normal effect of temperature becomes dominating again. The rigid mesoporous fillers can rapidly accommodate the liquid water at 0 °C, thus limiting potential impacts on the Nafion® matrix when the volume fraction of fillers is sufficiently high, as in the membrane with 20 wt.% S-Ph-PMO. The composites with less filler content seem to be the most sensitive to this effect, judging by the extremely sharp drop, and equally sharp recovery of E' between 0 °C and 40 °C. One can understand this assuming the existence of the already discussed dry and compact hydrophobic "skin" at the surface of Nafion®.[33] The mesoporous materials, functioning as permanently open channels, can perturb this "skin" and ensure a direct access of the surface water to the bulk of the membrane. For the low filler contents, the percolation is either deficient (sample with 10 wt.%) or inexistent (5 wt.%), and hence most of the water is absorbed by the Nafion® matrix, leading to the sharp drop of E'. The higher filler content (20 wt.% ≈ 36 vol.%) ensures percolation and simultaneously a larger mesoporous volume that can accommodate the additional hydration water, thus minimizing the impact of the adsorption on the visco-elastic behaviour of the matrix. The hardly perceived E' minimum at ~0 °C for this membrane puts into evidence a second minimum at approximately 35 °C, which can also be distinguished for Nafion®, although as a much broader peak.

The possible origins of the relaxations observed are better discussed by analysing the tan φ data shown in Fig. 3.46 B. Two well defined peaks are observed, one centred at ~ -50 °C, and the other at ~120 °C. The data in the intermediate temperature interval

between 0 and 50 °C depict a series of spikes. The first spike appearing above 0 °C corresponds to the sharp drop in *E'*, whereas the subsequent, more or less random spikes exceeding the maximum displacement fixed by the instrument (20 μm), correlate with the small oscillations of the signal response (see Fig. 3.46A). The data for the stronger, less strained 20 wt.% S-Ph-PMO composite are less sensitive to this limitation and display a well-defined peak at approximately 35 °C, with the additional small lump at 0 °C (see Fig. 3.46B, inset) suggesting minimum disturbance of the structure by the absorption of the water melted at the surface. These 2 maxima are overlapped in the samples with 5 and 10 wt.% fillers due to the onset of the strong relaxation at 0 °C, whereas Nafion® represents an intermediate situation, still displaying the small peak at 0 °C.

All in all, the same features are present in the 4 samples to various degrees and are thus features of the visco-elastic behaviour of Nafion®. According to previous detailed DMA studies of protonated Nafion®, the peak at around -50 °C (the γ relaxation) is due to short-range motions of the polytetrafluoroethylene-like backbone, and is unaffected by the presence of water.[248,250] The second (β) relaxation at ~20 °C is assigned to the segmental motions of the main-chain of the physically cross-linked perfluorocarbon phase (the genuine T_g of Nafion®). Water (even residual) has a strong influence on the β relaxation by decreasing the temperature down to values close to 0 °C, or lower.[18] Finally, the α relaxation, denoted by a tan φ peak at ~120 °C, is ascribed to the increasing long-range motion of both the main and the sulfonic acid functionalised side chains, made possible by the weakening of the electrostatic network involving the aqueous domains.[33,250] Since all peaks can be ascribed to Nafion®, the overall lower intensity of the tan φ peaks for the 20 wt.% S-Ph-PMO composite can be explained by the lower Nafion® volume contributing to the overall visco-elastic behaviour of this composite membrane. This is also nicely illustrated by the progressive decrease of the intensity of the α relaxation with increasing filler fraction. The fact that the α temperature does not change, even for 20 wt.% S-Ph-PMO, strongly suggests that the softening of the membranes is exclusively due to the

Nafion® matrix. Indeed, one would not expect the long-range motion of any of the structural entities of the hybrid S-Ph-PMO structure within this temperature range. The massive impact of the λ on the behaviour between 0 and 50 °C prevents a similarly solid conclusion, but the observed trends are coherent with the dominating role of the β relaxation of Nafion®, which is strongly dependent on the water content. The γ peak at negative temperatures is also little affected by the presence of small amounts of filler and should thus be due to the short-range motion of the Nafion® -CF_2- backbone. The peak is hardly discernible for the highest filler content, in agreement with the decreasing volume of Nafion® in the composite.

The overall positive role of the fillers on the elastic properties of the composite Nafion®/S-Ph-PMO membranes seems to be a simple bulk effect where the percolation of the particles (and hence of the mesopores) plays an important role. Surprisingly, this is not the case for the protonic conductivity.

3.4.4.3 Protonic conductivity

The previous analysis and observations made for the impedance spectra of Nafion® composite membranes remain valid for the present data. The conductivity of the 3 composite membranes is higher than for Nafion® but the effect of the filler content is not linear across the compositional range, showing a maximum for the sample with 10 wt.% of filler. The Arrhenius plots presented in Figure 3.47 confirm the aforementioned tendency from 40 to 94 °C, and on extended ranges of up to 120 or 140 °C for 40% and 20% r.h., respectively. The important increase of the conductivity of the best composite membrane was already compared to Nafion® and described previously (sample S-C24M3-10%, Fig. 3.38).

The E_a values for the protonic conductivity estimated from the Arrhenius plots are listed in Table 3.7. Conversely to the powder compacts presented in section 3.3, the composite membrane show consistent E_a values over the whole range of r.h.

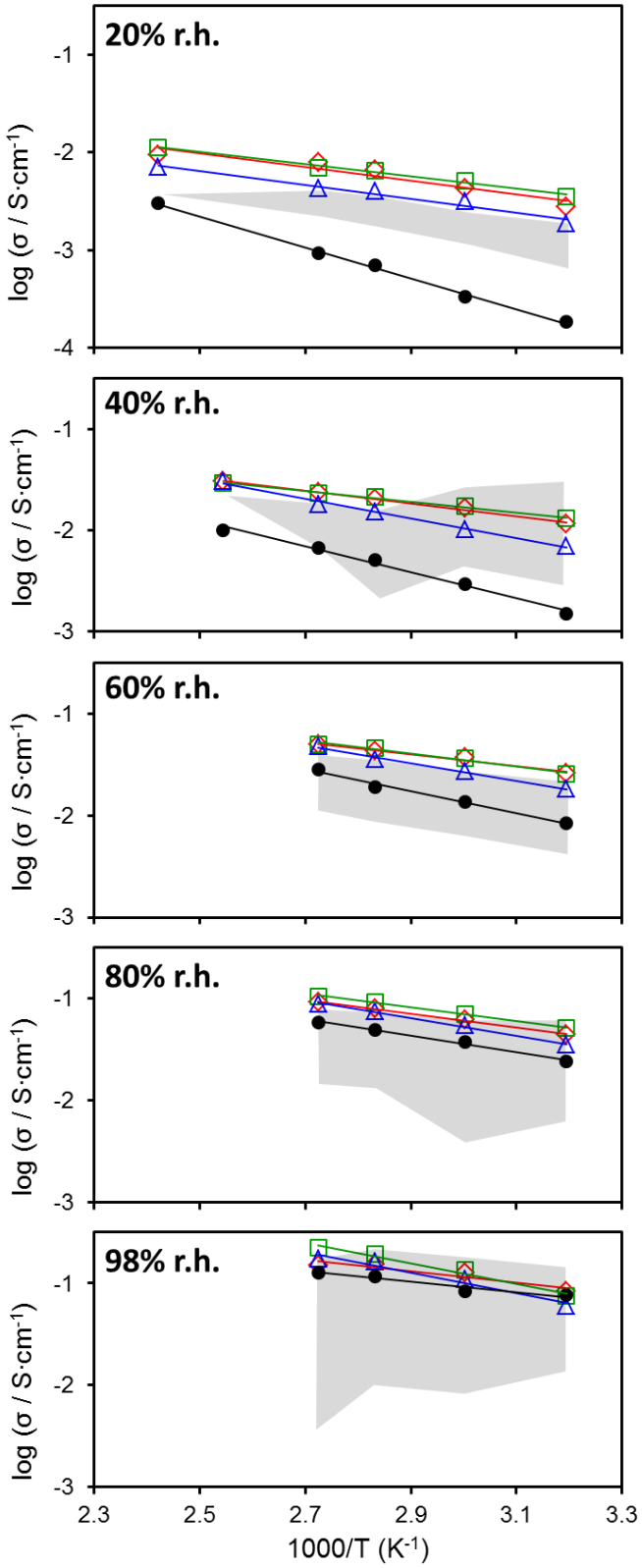

Figure 3.47. Arrhenius plots of Nafion® and Nafion®/S-Ph-PMO composite membranes measured under variable r.h. ●) Nafion® ◇) S-C24M3-5%; □) S-C24M3-10% and △) S-C24M3-20%. The grey areas represent several conductivity values for pure Nafion® based in literature data, for the same conditions.[228,258,271,276,279,280,287-296]

Table 3.7. E_a for the protonic conductivity under variable r.h. for the membranes with different filler content.

Sample	E_a (kJ·mol^{-1})				
	20% r.h.	40% r.h.	60% r.h.	80% r.h.	98% r.h.
Nafion®	33	27	23	18	13
S-C24M3-5%	17	16	14	16	17
S-C24M3-10%	15	13	15	16	17
S-C24M3-20%	17	21	16	19	16

The E_a values for Nafion® decrease from 33 to 13 kJ·mol^{-1} with increasing r.h. This is a common observation due to the lower activation enthalpy for proton mobility in the bulk of the larger aqueous domains of highly hydrated Nafion®. The pores are compressed for low r.h. due the elastic behaviour of the hydrophobic backbone,[33] and the protons are thus confined to the pore surface, where they are more attracted by the SO_3^- groups.[38,52] On the contrary, there is no obvious influence of the r.h. on the E_a of the composite membranes, all within the interval between 13 and 21 kJ·mol^{-1}. These figures are lower than for Nafion® at low r.h., but comparable at higher humidity.

The effect of the r.h. on the E_a of the composites can be rationalized in terms of parallel contributions of Nafion® and of the S-Ph-PMO phase, which has a much lower, r.h. independent E_a of ~6 kJ·mol^{-1} (see table 3.5). The low E_a of the powder sample S-C24M3 can be explained by the rigid porous structure that allows the protons to diffuse along the bulk of pores, thus minimizing the proton confinement admitted to occur in the dynamic Nafion® structure. In other words, the separation of the hydrophilic/hydrophobic domains in the S-Ph-PMO should not depend on the λ. In addition, as found for highly ordered mesoporous silica films,[213] the open and rigid structure of S-Ph-PMO may allow the capillary water condensation in the mesopores at relatively low r.h., yielding hydration numbers higher than for Nafion®, for comparable intermediate r.h. conditions.

The potentially higher hydration combined with the higher mobility of protons should yield high values of protonic conductivity of the pure S-Ph-PMO under low r.h. conditions. However, while still rather high, the conductivity of the S-C24M3 powder compacts at 20% r.h. (Fig. 3.23) is lower than that of a pure Nafion® membrane. The

differences may be much smaller because the S-Ph-PMO values are certainly underestimated due to the sample macroporosity, as discussed at the end of sub-section 3.3. Nevertheless, one would expect a progressive increase in the membranes conductivity with increasing filler content, which is contradicted by the data for the 20 wt.% composite (Fig 3.47). The same reasoning applies to the E_a, which should progressively decrease with increasing S-Ph-PMO content, at least for low r.h. In fact, the data in Table 3.7 suggests that from the view point of the conduction mechanism, there are no significant differences between membranes with 5, 10 or 20 wt.% filler. The reason for the important conductivity enhancement induced by the fillers is indeed quite complex and cannot be interpreted assuming simple bulk phenomena. The usually invoked arguments of higher W and the closely related higher $[H^+]$ (e.g.[222] and references therein) are not valid in the present case. The formation of ionic cross-links between the Nafion® SO_3H groups and the fillers, promoting long–range proton transport,[297] is also unlikely because the S-Ph-PMO are not chemically bonded to Nafion®, and the particle size is well above the nano-range.

The underlining advantage of the large S-Ph-PMO particles must be related to their percolating mesopore structure. The main reasons for the use the S-Ph-PMO fillers were the minimization of protonic confinement and the resulting higher mobility along the stable filler mesopores, mainly in dryer conditions. This can indeed provide a possible explanation for the effect of the r.h. on the conductivity of the composites. However, it cannot explain the weak dependence of the conductivity on the filler content, which in turn suggests that the membrane surface plays a restrictive role on the conductivity.

One possible explanation is related to the already mentioned anisotropic dry surface of the Nafion® membrane, where the water diffusion and protonic conductivity should be strongly reduced compared to the membrane bulk.[33] The formation of this poorly conductive film-like layer, consisting of packed polymer structures aligned along the membrane surfaces, is induced by the increase in internal pressure associated to the elastic contribution of the membrane swelling. The addition of S-Ph-PMO particles to Nafion® can lower the internal pressure by facilitating the access of the hydration water across the membrane surface, hence disrupting the poorly conductive "dry skin" structure, and locally reducing the swelling (due to the rigid mesostructure). Moreover,

the internal pressure is estimated to increase with decreasing temperature for a fixed r.h. due to the more rigid polymer structure,[33] which agrees with the observation of a stronger filler effect at low temperature. The modification of the surface morphology can indeed explain the higher conductivity of the composite membranes as a surface effect compatible with nominally low bulk filler concentrations (10 wt.% or less). Much higher filler volumes may disturb also the bulk of the membrane (typically above the percolation threshold), with bulk effects expected to show up if the conductivity of the filler is different from the Nafion® matrix. Indeed, the somewhat lower conductivity of the powder S-C24M3 (Fig. 3.23) in comparison to Nafion® may explain the slight decrease of the conductivity when the filler content is increased from 10 wt.% to 20 wt.%. As said before, the latter corresponds to about 36 vol.%, very likely above the percolation threshold, as suggested by the DMA (Fig.3.46) and SEM (Fig 3.44 C) data.

4 CONCLUSION AND OUTLOOK

This last chapter summarizes the principal outcomes and observations made throughout the PhD thesis. There is also a focus on the expectable and desirable future work to further deepen the knowledge and applicability of the materials studied in this thesis.

One of the main research focus in PEMFC development is to obtain a PEM with increased conductivity (0.1 $S \cdot cm^{-1}$) at higher temperature (T>120 °C) and lower r.h. (< 50%), to avoid several drawbacks brought by the use of low working temperatures of the state-of-the-art PEM material. With this in mind, the strategy used in this thesis was of incorporating hygroscopic phases inside a Nafion® matrix, in the form of acid-functionalised mesoporous organosilicas, with benzene as bridging moiety. These materials are optimal candidates to be used as fillers because they offer a stable rigid structure for the conduction of proton which is independent of r.h. and should not suffer from the confinement effect caused by the shrinkage of the pores, as it happens in Nafion®. Moreover, the structure of the acid functionalized PMO makes a good model of the structure of Nafion® pores in its hydrated form, with similar pore width and distance between acid sites.

For this work we prepared several mesoporous organosilica materials containing sulfonic or phosphonic acid functionalities.

Preliminary EIS studies show that the P-Ph-PMO samples do not show sufficient conductivity to be used as fillers in a composite Nafion® membrane. For this reason, only the S-Ph-PMO materials were used for this purpose.

The S-Ph-PMO samples were synthesised using conventional and MW heating sources in the several steps of the synthesis. By varying the time of self-assembly and hydrothermal steps and the type of heat source it was possible to obtain a set of materials with a great variety of values in several structural and microstructural characteristics, namely acid load, surface area, pore volume, pore order and molecular scale order. This enabled the study of the influence of such characteristics upon the protonic conductivity. The use of MW heating source instead of the conventional allowed the reduction of synthesis time in ~80% for sample with similar $[H^+]$, S_{BET} and structural order. However, an excess of MW energy in the hydrothermal step (> 3 h) leads to a dramatic decrease of structural order. There is a tendency for the decrease of the (100) peak intensity with increasing $[H^+]$, which can be related to the progressive diminution of the coherent diffraction volume. This is translated as an overall decrease of the pore order factor (χ) with increasing $[H^+]$.

The influence of the use of MW in the synthesis of S-Ph-PMO was evaluated by a multivariate analysis of the reaction kinetics. A model that predicts the acid load, pore order and molecular scale order, using the self-assembly and hydrothermal treatment time constant and type of heating as variables, was thus elaborated, based on experimental data. The $[H^+]$ values simulated by the model are in good agreement with the experimentally observed values while the predicted values for χ and $I_{(001)}$ show substantially higher errors. Remarkably, these errors are quite smaller for the samples synthesised using MW in both steps. Further analysis shows that the MW self-assembly step is responsible for the quickest increase of $[H^+]$ in all the synthesis process.

The S-Ph-PMO materials were analysed by EIS, in the form of powder pellets, as a function of temperature and r.h. The samples with the lowest $[H^+]$ tend to deviate from the Arrhenius behaviour at low r.h. This may be due to a fraction of physisorbed water molecules higher than the fraction of solvated water molecules around SO_3H groups. At low r.h., the driving force for the physisorption must be surpassed by the evaporation rate as the temperature increases, ultimately lowering the conductivity. However, as the r.h. increases, the driving force for the physisorption also increases, taking the conductivity upwards. This explains the observed trend of the samples with the lowest $[H^+]$ where the slope of the Arrhenius-type plots goes progressively from

positive to negative as r.h. increases. Samples with high [H^+] show Arrhenius-type behaviour starting even at low values of r.h. as the fraction of chemisorbed water molecules (solvated around the SO_3H) is always high enough. The condensation of water inside the pores may thus occur for lower r.h., hence contributing for the increased conductivity and observable Arrhenius behaviour across the entire r.h. range.

For samples with [H^+] lower than 1 mmol·g^{-1} and S_{BET} higher than 600 $m^2 \cdot g^{-1}$ the conductivity increases sharply with increasing r.h. up to ~60%, and more moderately thereafter. This effect is more pronounced for samples with low [H^+] and tends to fade away with increasing [H^+], being completely undetectable for samples with [H^+] above 1 mmol·g^{-1}. According to the literature,[213] the sharp increase in conductivity is related to the adsorption and clustering of water molecules around the acid sites, which eventually tends to condensate, driven by capillarity. By increasing the [H^+] and according to Kelvin's equation (eq. 2.3) the humidity threshold leading to condensation is shifted to lower r.h. values, explaining why the sharp increase tends to fade away with increasing [H^+] in our case, since there are no conductivity values under 20% r.h.

One of the major topics of this thesis is the study of the correlations between intrinsic factors and the protonic conductivity of the mesoporous materials. The conductivity values were analysed as an ensemble instead of individually for each sample, to minimize the impact of the apparent scatter of the data.

Data clearly show that the conductivity is increased for samples with increasing [H^+], demonstrating that higher charge carrier concentration, associated to the higher number of solvated and percolated SO_3H groups, leads to an increased conductivity. On the other hand, it was observed that the hierarchical order (typical of Ph-PMO materials) which is defined by the hexagonal order of the nano-scale pores and the molecular scale periodicity along the pore wall, have little or no influence on the protonic conductivity of S-Ph-PMOs.

When comparing the values of E_a at 98% r.h., an increase of E_a with increasing [H^+] and ASC is observed. This happens probably because the concentration of protons in the bulk is also increased, leading to a higher fraction of structurally diffusing protons, which typically shows E_a values up to 40 kJ·mol^{-1}.

The S-Ph-PMO materials obtained by co-condensation show conductivity values four orders of magnitude higher than the reported for materials made by grafting.[97] This should be related to a more homogeneous distribution of acid sites allowing better diffusion of proton through the pore channels.

The highest conductivity value obtained was of 0.11 $S \cdot cm^{-1}$ for the sample S-C48C24 at 80 ºC and 98% r.h., which is comparable to Nafion® in similar conditions.

The composite Nafion®/S-Ph-PMO membranes were analysed by EIS as a function of r.h. and temperature. By comparing a set of composite membranes with 10 wt.% of fillers, the Arrhenius-type plots show that for all the conditions of temperature and r.h. up to 80%, all the composite membranes show an enhanced conductivity compared to Nafion®. At 20% r.h. and 40 ºC the conductivity of the composite membrane S-C24M3-10% shows a value 19 times higher than the Nafion® reference. With increasing temperature the difference of conductivity between composite and reference membranes is smaller but still almost 4 times higher at 140 ºC. As the r.h. increases, and particularly at 98%, the data tend to converge. Nevertheless, almost all the composite membranes display a slightly better conductivity values than pure Nafion®.

Upon water uptake, one can observe a decrease of the membrane swelling with increasing fraction of the filler that can be explained by the presence of the rigid mesoporous structure of the S-Ph-PMO, which provides a certain free volume to accommodate water molecules without expanding, as it happens for the Nafion® matrix.

The EDS mapping of the cross-section of the membrane with less fillers (5 and 10 wt.%) show that the microstructure consists of particles dispersed in a polymer matrix whereas the microstructure of the 20 wt.% membrane can be defined by a network of interconnecting submicrometric particles with the spaces filled by the polymer.

There is a progressive positive impact of the increase in filler content on the storage modulus (*E*'), mainly above 120 ºC. The 20 wt.% composite membrane shows an *E*' of 0.05 GPa at 140 °C, which is one order of magnitude higher than Nafion®, suggesting enhanced mechanical performance. The existence of a percolating network of rigid mesoporous structures could neutralize the destabilization of the electrostatic network responsible for the degradation of the visco-elastic behaviour of Nafion® when temperature rises. The mesoporous structures, operating as permanently open

channels, can perturb the dry and compact anisotropic "skin" that is formed at the surface of Nafion® when the r.h. is increased,[33] ensuring a direct access of the surface water to the bulk of the membrane. For the low filler contents, because the percolation is either deficient (sample with 10 wt.%) or inexistent (5 wt.%), most of the water is absorbed by the Nafion® matrix. On the other hand, the highest filler content ensures the percolation and offers a large mesoporous volume that can accommodate the additional hydration water, minimizing the impact of the adsorption on the visco-elastic behaviour of the matrix.

The composite membranes with increasing S-C24M3 filler content show conductivity values higher than Nafion® with a maximum for the sample with 10 wt.%. The low dependence of the composites E_a on the r.h. can be understood as a sum of the contributions of Nafion® and the S-C24M3. The mesoporous material shows an E_a independent of the r.h. due to the rigid pore structure that allows the protons to diffuse along the bulk of pores with minimized confinement. The disruption of the dry surface "skin" can explain the increase in conductivity up to a filler content of 10 wt.% as it reduces the internal pressure when the r.h. increases and allows the hydration water to enter the bulk of the membrane. However, when the filler content is augmented to 20 wt.%, the bulk effect of the percolated S-Ph-PMO powders may disturb the bulk of the membrane and the lower conductivity of the hybrid particles may start to show on the overall conductivity.

In terms of future work, it would be interesting to return to the lab and perform some more adjustments to the synthesis of P-Ph-PMO, namely by modifying the acid precursor used, in order to obtain P-Ph-PMO with greater $[H^+]$ (closer to 1 $mmol \cdot g^{-1}$), while maintaining a high S_{BET}.

It is known that the capillarity threshold is affected by the pore size, according to Kelvin's equation (eq. 2.3) so the synthesis of new S-Ph-PMO materials with decreasing pore size (using surfactants C16 or C14 for example) could be interesting to assess the influence of this parameter on the conductivity of S-Ph-PMO and probably further improve the performance of these materials at low r.h.

The complexity of interfaces inside the measured pellets, with low densities, the presence of macroporosity, water and the actual bulk of the material is certainly high and hardly accountable. For this reason, one could easily state that the measured

conductivities are certainly under estimated. The synthesis of these materials in the form of thin films, much like the recent work done by Fujita *et al.*,[213] would allow a much more organized microstructure, with regular interfaces and higher densities, leading certainly to higher values of conductivity.

It could also be interesting to identify intermediary compositions for composite membranes (between 10 and 20 wt.%) that could be more conductive than the membrane with 10 wt.% of S-C24M3.

Naturally, the next logical step, which is already ongoing, is the characterization of the composite membranes in a fuel cell station test, where the membranes performance as a proton exchange membrane will be characterized as a function of temperature, r.h. and gas composition, using H_2 as fuel and O_2 of air as oxidant.

The international target of 0.1 $S \cdot cm^{-1}$ at 120 ºC and r.h.< 50% was not achieved yet, but the result of 0.03 $S \cdot cm^{-1}$ at 120 ºC and 40 % r.h. is quite promising. Moreover the reduced swelling and the enhanced storage modulus may be crucial to improve the thermo-mechanical stability of the membrane and of the electrode/electrolyte interface in a fuel cell environment.

5 REFERENCES

1. Union, E., *Energy 2020 - A strategy for competitive, sustainable and secure energy*, 2011, Publication of the Office of the European Union: Luxembourg.
2. *http://epp.eurostat.ec.europa.eu/portal/page/portal/eurostat/home/*. 7 March 2014.
3. *http://www.new-ig.eu/uploads/pdf/111026FCHtechnologiesinEurope-Financialandtechnologyoutlook2014-2020_000.pdf*. 9 January 2013.
4. *http://www.fch-ju.eu/sites/default/files/188213_2012_2640_FUEL_CELLS_AND_HYDROGEN1.pdf*. 9 January 2013.
5. *http://www.hydrogen.energy.gov/fuel_cells.html*. 9 January 2013.
6. Houchins, C., G. Kleen, J. Spendelow, J. Kopasz, D. Peterson, N. Garland, D. Ho, J. Marcinkoski, K. Martin, R. Tyler and D. Papageorgopoulos, *U.S. DOE Progress Towards Developing Low-Cost, High Performance, Durable Polymer Electrolyte Membranes for Fuel Cell Applications.* Membranes, 2012. 2(4). p. 855-878.
7. Schœnbein, C.F., *On the voltaic polarization of certain solid and fluid substances.* Philosophical Magazine Series 3, 1839. 14(85). p. 43-45.
8. Chen, E., *History*, in *Fuel Cell Technology Handbook*, G. Hoogers, Editor 2003, CRC Press: Boca Raton.
9. Grove, W.R., *On voltaic series and the combination of gases by platinum.* Philosophical Magazine Series 3, 1839. 14(86). p. 127-130.
10. Grove, W.R., *On a Gaseous Voltaic Battery.* Philosophical Magazine and Journal of Science, 1843. 21. p. 417-420.
11. Barbir, F., *PEM Fuel Cells - Theory and practice*. Academic Press Sustainable World, ed. R.C. Dorf 2005, Elsevier Academic Press, Burlington.
12. Baur, E. and H. Preis, *Über Brennstoff-Ketten mit Festleitern.* Zeitschrift für Elektrochemie und angewandte physikalische Chemie, 1937. 43(9). p. 727-732.
13. Devanathan, R., *Recent developments in proton exchange membranes for fuel cells.* Energy & Environmental Science, 2008. 1(1). p. 101-119.

14. Zhang, H.W. and P.K. Shen, *Recent Development of Polymer Electrolyte Membranes for Fuel Cells.* Chemical Reviews, 2012. 112(5). p. 2780-2832.
15. Litster, S. and G. McLean, *PEM fuel cell electrodes.* Journal of Power Sources, 2004. 130(1–2). p. 61-76.
16. EG&G Technical Services, I.U.S., *Fuel Cell Handbook* 2004, US Deparment of Energy, Morgantown, West Virginia.
17. Barbir, F. and S. Yazici, *Status and development of PEM fuel cell technology.* International Journal of Energy Research, 2008. 32(5). p. 369-378.
18. Smitha, B., S. Sridhar and A.A. Khan, *Solid polymer electrolyte membranes for fuel cell applications - a review.* Journal of Membrane Science, 2005. 259(1-2). p. 10-26.
19. Dupuis, A.C., *Proton exchange membranes for fuel cells operated at medium temperatures: Materials and experimental techniques.* Progress in Materials Science, 2011. 56(3). p. 289-327.
20. Mauritz, K.A. and R.B. Moore, *State of understanding of Nafion.* Chemical Reviews, 2004. 104(10). p. 4535-4585.
21. Shao, Y.Y., G.P. Yin, Z.B. Wang and Y.Z. Gao, *Proton exchange membrane fuel cell from low temperature to high temperature: Material challenges.* Journal of Power Sources, 2007. 167(2). p. 235-242.
22. Hickner, M.A., H. Ghassemi, Y.S. Kim, B.R. Einsla and J.E. McGrath, *Alternative polymer systems for proton exchange membranes (PEMs).* Chemical Reviews, 2004. 104(10). p. 4587-4611.
23. Gierke, T.D. and W.Y. Hsu, *The Cluster-network model of ion clustering in perfluorosulfonated membranes.* Acs Symposium Series, 1982. 180. p. 283-307.
24. Okada, T., G. Xie, O. Gorseth, S. Kjelstrup, N. Nakamura and T. Arimura, *Ion and water transport characteristics of Nafion membranes as electrolytes.* Electrochimica Acta, 1998. 43(24). p. 3741-3747.
25. Litt, M., *A reevaluation of Nafion(R) morphology.* Abstracts of Papers of the American Chemical Society, 1997. 213. p. 33-POLY.
26. Haubold, H.G., T. Vad, H. Jungbluth and P. Hiller, *Nano structure of Nafion: a SAXS study.* Electrochimica Acta, 2001. 46(10-11). p. 1559-1563.
27. Gebel, G. and O. Diat, *Neutron and x-ray scattering: Suitable tools for studying ionomer membranes.* Fuel Cells, 2005. 5(2). p. 261-276.
28. Kreuer, K.D., *On the development of proton conducting polymer membranes for hydrogen and methanol fuel cells.* Journal of Membrane Science, 2001. 185(1). p. 29-39.
29. Schmidt-Rohr, K. and Q. Chen, *Parallel cylindrical water nanochannels in Nafion fuel-cell membranes.* Nature Materials, 2008. 7(1). p. 75-83.
30. Rubatat, L., A.L. Rollet, G. Gebel and O. Diat, *Evidence of elongated polymeric aggregates in Nafion.* Macromolecules, 2002. 35(10). p. 4050-4055.
31. Diat, O. and G. Gebel, *Proton channels.* Nat Mater, 2008. 7(1). p. 13-4.
32. Kreuer, K.-D. and G. Portale, *A Critical Revision of the Nano-Morphology of Proton Conducting Ionomers and Polyelectrolytes for Fuel Cell Applications.* Advanced Functional Materials, 2013. p. n/a-n/a.
33. Kreuer, K.-D., *The role of internal pressure for the hydration and transport properties of ionomers and polyelectrolytes.* Solid State Ionics, 2013(0).

34. Schroder, P., *Über Erstarrungs–und Quellungserscheinungen von Gelatine.* Zeitschrift für Physikalische Chemie, 1903. 45. p. 75-117.
35. Eikerling, M., Y.I. Kharkats, A.A. Kornyshev and Y.M. Volfkovich, *Phenomenological theory of electro-osmotic effect and water management in polymer electrolyte proton-conducting membranes.* Journal of the Electrochemical Society, 1998. 145(8). p. 2684-2699.
36. Eikerling, M., A.A. Kornyshev, A.M. Kuznetsov, J. Ulstrup and S. Walbran, *Mechanisms of proton conductance in polymer electrolyte membranes.* Journal of Physical Chemistry B, 2001. 105(17). p. 3646-3662.
37. Jiao, K. and X.G. Li, *Water transport in polymer electrolyte membrane fuel cells.* Progress in Energy and Combustion Science, 2011. 37(3). p. 221-291.
38. Kreuer, K.D., S.J. Paddison, E. Spohr and M. Schuster, *Transport in proton conductors for fuel-cell applications: Simulations, elementary reactions, and phenomenology.* Chemical Reviews, 2004. 104(10). p. 4637-4678.
39. Tuckerman, M., K. Laasonen, M. Sprik and M. Parrinello, *Ab-initio molecular-dynamics simulation of the solvation and transport of hydronium and hydroxyl ion in water.* Journal of Chemical Physics, 1995. 103(1). p. 150-161.
40. Tuckerman, M.E., D. Marx, M.L. Klein and M. Parrinello, *On the quantum nature of the shared proton in hydrogen bonds.* Science, 1997. 275(5301). p. 817-820.
41. Agmon, N., *The Grotthuss mechanism.* Chemical Physics Letters, 1995. 244(5-6). p. 456-462.
42. Marx, D., M.E. Tuckerman, J. Hutter and M. Parrinello, *The nature of the hydrated excess proton in water.* Nature, 1999. 397(6720). p. 601-604.
43. Cohen, B. and D. Huppert, *Connection between proton abnormal conductivity in water and dielectric relaxation time.* Journal of Physical Chemistry A, 2003. 107(19). p. 3598-3605.
44. Kreuer, K.D., A. Rabenau and W. Weppner, *Vehicle mecahnism, a new model for the interpretation of the conductivity of fast proton conductors.* Angewandte Chemie-International Edition in English, 1982. 21(3). p. 208-209.
45. Agmon, N., *Hydrogen bonds, water rotation and proton mobility.* Journal De Chimie Physique Et De Physico-Chimie Biologique, 1996. 93(10). p. 1714-1736.
46. Laporta, M., M. Pegoraro and L. Zanderighi, *Perfluorosulfonated membrane (Nafion): FT-IR study of the state of water with increasing humidity.* Physical Chemistry Chemical Physics, 1999. 1(19). p. 4619-4628.
47. Lu, Z., G. Polizos, D.D. Macdonald and E. Manias, *State of water in perfluorosulfonic ionomer (Nafion 117) proton exchange membranes.* Journal of the Electrochemical Society, 2008. 155(2). p. B163-B171.
48. Pivovar, A.A. and B.S. Pivovar, *Dynamic behavior of water within a polymer electrolyte fuel cell membrane at low hydration levels.* Journal of Physical Chemistry B, 2005. 109(2). p. 785-793.
49. Zawodzinski, T.A., M. Neeman, L.O. Sillerud and S. Gottesfeld, *Determination of water diffusion coeficients in perfluorosulfonate ionomeric membranes.* Journal of Physical Chemistry, 1991. 95(15). p. 6040-6044.
50. Paciaroni, A., M. Casciola, E. Cornicchi, M. Marconi, G. Onori, M. Pica and R. Narducci, *Temperature-dependent dynamics of water confined in Nafion membranes.* Journal of Physical Chemistry B, 2006. 110(28). p. 13769-13776.

51. Perrin, J.-C., S. Lyonnard and F. Volino, *Quasielastic neutron scattering study of water dynamics in hydrated nafion membranes.* Journal of Physical Chemistry C, 2007. 111(8). p. 3393-3404.
52. Eikerling, M. and A.A. Kornyshev, *Proton transfer in a single pore of a polymer electrolyte membrane.* Journal of Electroanalytical Chemistry, 2001. 502(1-2). p. 1-14.
53. Paddison, S.J. and R. Paul, *The nature of proton transport in fully hydrated Nafion (R).* Physical Chemistry Chemical Physics, 2002. 4(7). p. 1158-1163.
54. Paddison, S.J., *The modeling of molecular structure and ion transport in sulfonic acid based ionomer membranes.* Journal of New Materials for Electrochemical Systems, 2001. 4(4). p. 197-207.
55. Paddison, S.J., *Proton conduction mechanisms at low degrees of hydration in sulfonic acid-based polymer electrolyte membranes.* Annual Review of Materials Research, 2003. 33. p. 289-319.
56. Dippel, T. and K.D. Kreuer, *Proton transport mechanism in concentrated aqueous solutions and solid hydrates of acids.* Solid State Ionics, 1991. 46(1-2). p. 3-9.
57. Kreuer, K.D., M. Schuster, B. Obliers, O. Diat, U. Traub, A. Fuchs, U. Klock, S.J. Paddison and J. Maier, *Short-side-chain proton conducting perfluorosulfonic acid ionomers: Why they perform better in PEM fuel cells.* Journal of Power Sources, 2008. 178(2). p. 499-509.
58. Du, X.Z., J.R. Yu, B.L. Yi, M. Han and K.W. Bi, *Performances of proton exchange membrane fuel cells with alternate membranes.* Physical Chemistry Chemical Physics, 2001. 3(15). p. 3175-3179.
59. Merlo, L., A. Ghielmi, L. Cirillo, M. Gebert and V. Arcella, *Membrane electrode assemblies based on HYFLON (R) ion for an evolving fuel cell technology.* Separation Science and Technology, 2007. 42(13). p. 2891-2908.
60. Arico, A.S., A. Di Blasi, G. Brunaccini, F. Sergi, G. Dispenza, L. Andaloro, M. Ferraro, V. Antonucci, P. Asher, S. Buche, D. Fongalland, G.A. Hards, J.D.B. Sharman, A. Bayer, G. Heinz, N. Zandona, R. Zuber, M. Gebert, M. Corasaniti, A. Ghielmi and D.J. Jones, *High Temperature Operation of a Solid Polymer Electrolyte Fuel Cell Stack Based on a New Ionomer Membrane.* Fuel Cells, 2010. 10(6). p. 1013-1023.
61. Elabd, Y.A. and M.A. Hickner, *Block Copolymers for Fuel Cells.* Macromolecules, 2010. 44(1). p. 1-11.
62. Einsla, M.L., Y.S. Kim, M. Hawley, H.S. Lee, J.E. McGrath, B.J. Liu, M.D. Guiver and B.S. Pivovar, *Toward improved conductivity of sulfonated aromatic proton exchange membranes at low relative humidity.* Chemistry of Materials, 2008. 20(17). p. 5636-5642.
63. Titvinidze, G., K.-D. Kreuer, M. Schuster, C.C. de Araujo, J.P. Melchior and W.H. Meyer, *Proton Conducting Phase-Separated Multiblock Copolymers with Sulfonated Poly(phenylene sulfone) Blocks for Electrochemical Applications: Preparation, Morphology, Hydration Behavior, and Transport.* Advanced Functional Materials, 2012. 22(21). p. 4456-4470.
64. Bouchet, R. and E. Siebert, *Proton conduction in acid doped polybenzimidazole.* Solid State Ionics, 1999. 118(3-4). p. 287-299.
65. Li, Q., J.O. Jensen, R.F. Savinell and N.J. Bjerrum, *High temperature proton exchange membranes based on polybenzimidazoles for fuel cells.* Progress in Polymer Science, 2009. 34(5). p. 449-477.

66. Ünsal, O. and J. Kiefer, *Polymer electrolyte membrane, method for the production thereof, and application thereof in fuel cells*, (Celanese Ventures GmbH), Patent WO03096465, 2003
67. Gubler, L., D. Kramer, J. Belack, O. Ünsal, T.J. Schmidt and G.G. Scherer, *Celtec-V - A polybenzimidazole-based membrane for the direct methanol fuel cell.* Journal of the Electrochemical Society, 2007. 154(9). p. B981-B987.
68. Boaventura, M. and A. Mendes, *Activation procedures characterization of MEA based on phosphoric acid doped PBI membranes.* International Journal of Hydrogen Energy, 2010. 35(20). p. 11649-11660.
69. Pefkianakis, E.K., V. Deimede, M.K. Daletou, N. Gourdoupi and J.K. Kallitsis, *Novel Polymer Electrolyte Membrane, Based on Pyridine Containing Poly(ether sulfone), for Application in High-Temperature Fuel Cells.* Macromolecular Rapid Communications, 2005. 26(21). p. 1724-1728.
70. Weber, J., K.D. Kreuer, J. Maier and A. Thomas, *Proton conductivity enhancement by nanostructural control of poly(benzimidazole)-phosphoric acid adducts.* Advanced Materials, 2008. 20(13). p. 2595-2598.
71. Weber, J., M. Antonietti and A. Thomas, *Mesoporous poly(benzimidazole) networks via solvent mediated templating of hard spheres.* Macromolecules, 2007. 40(4). p. 1299-1304.
72. Greaves, T.L. and C.J. Drummond, *Protic ionic liquids: Properties and applications.* Chemical Reviews, 2008. 108(1). p. 206-237.
73. Lee, S.-Y., T. Yasuda and M. Watanabe, *Fabrication of protic ionic liquid/sulfonated polyimide composite membranes for non-humidified fuel cells.* Journal of Power Sources, 2010. 195(18). p. 5909-5914.
74. Haile, S.M., D.A. Boysen, C.R.I. Chisholm and R.B. Merle, *Solid acids as fuel cell electrolytes.* Nature, 2001. 410(6831). p. 910-913.
75. Boysen, D.A., S.M. Haile, H.J. Liu and R.A. Secco, *High-temperature behavior of CsH2PO4 under both ambient and high pressure conditions.* Chemistry of Materials, 2003. 15(3). p. 727-736.
76. Haile, S.M., C.R.I. Chisholm, K. Sasaki, D.A. Boysen and T. Uda, *Solid acid proton conductors: from laboratory curiosities to fuel cell electrolytes.* Faraday Discussions, 2007. 134. p. 17-39.
77. Rouquerol, J., D. Avnir, F.C. W., D.H. Everett, J.H. Haynes, N. Pernicope, J.D.F. Ramsay, K.S.W. Sing and K.K. Unger, *Recommendations for the characterization of porous solids (technical report).* Pure & Applied Chemistry, 1994. 66(8). p. 1739-1758.
78. Hoffmann, F., M. Cornelius, J. Morell and M. Froba, *Silica-based mesoporous organic-inorganic hybrid materials.* Angewandte Chemie-International Edition, 2006. 45(20). p. 3216-3251.
79. Hoffmann, F. and M. Froba, *Vitalising porous inorganic silica networks with organic functions-PMOs and related hybrid materials.* Chemical Society Reviews, 2011. 40(2). p. 608-620.
80. Kresge, C.T., M.E. Leonowicz, W.J. Roth, J.C. Vartuli and J.S. Beck, *Ordered mesoporous molecular sieves synthesized by a liquid-crystal template mechanism.* Nature, 1992. 359(6397). p. 710-712.
81. Beck, J.S., J.C. Vartuli, W.J. Roth, M.E. Leonowicz, C.T. Kresge, K.D. Schmitt, C.T.W. Chu, D.H. Olson, E.W. Sheppard, S.B. McCullen, J.B. Higgins and J.L. Schlenker, *A new family of mesoporous molecular sieves prepared*

with liquid-crystal templates. Journal of the American Chemical Society, 1992. 114(27). p. 10834-10843.
82. Zhao, D.Y., J.L. Feng, Q.S. Huo, N. Melosh, G.H. Fredrickson, B.F. Chmelka and G.D. Stucky, *Triblock copolymer syntheses of mesoporous silica with periodic 50 to 300 angstrom pores.* Science, 1998. 279(5350). p. 548-552.
83. Zhao, D.Y., Q.S. Huo, J.L. Feng, B.F. Chmelka and G.D. Stucky, *Nonionic triblock and star diblock copolymer and oligomeric surfactant syntheses of highly ordered, hydrothermally stable, mesoporous silica structures.* Journal of the American Chemical Society, 1998. 120(24). p. 6024-6036.
84. Asefa, T., M.J. MacLachan, N. Coombs and G.A. Ozin, *Periodic mesoporous organosilicas with organic groups inside the channel walls.* Nature, 1999. 402(6764). p. 867-871.
85. Melde, B.J., B.T. Holland, C.F. Blanford and A. Stein, *Mesoporous sieves with unified hybrid inorganic/organic frameworks.* Chemistry of Materials, 1999. 11(11). p. 3302-3308.
86. Inagaki, S., S. Guan, Y. Fukushima, T. Ohsuna and O. Terasaki, *Novel mesoporous materials with a uniform distribution of organic groups and inorganic oxide in their frameworks.* Journal of the American Chemical Society, 1999. 121(41). p. 9611-9614.
87. Hatton, B., K. Landskron, W. Whitnall, D. Perovic and G.A. Ozin, *Past, present, and future of periodic mesoporous organosilicas - The PMOs.* Accounts of Chemical Research, 2005. 38(4). p. 305-312.
88. Mizoshita, N., T. Tani and S. Inagaki, *Syntheses, properties and applications of periodic mesoporous organosilicas prepared from bridged organosilane precursors.* Chemical Society Reviews, 2011. 40(2). p. 789-800.
89. Inagaki, S., S. Guan, T. Ohsuna and O. Terasaki, *An ordered mesoporous organosilica hybrid material with a crystal-like wall structure.* Nature, 2002. 416(6878). p. 304-307.
90. Bion, N., P. Ferreira, A. Valente, I.S. Goncalves and J. Rocha, *Ordered benzene-silica hybrids with molecular-scale periodicity in the walls and different mesopore sizes.* Journal of Materials Chemistry, 2003. 13(8). p. 1910-1913.
91. Das, D., J.F. Lee and S.F. Cheng, *Sulfonic acid functionalized mesoporous MCM-41 silica as a convenient catalyst for Bisphenol-A synthesis.* Chemical Communications, 2001(21). p. 2178-2179.
92. Das, D., J.F. Lee and S.F. Cheng, *Selective synthesis of Bisphenol-A over mesoporous MCM silica catalysts functionalized with sulfonic acid groups.* Journal of Catalysis, 2004. 223(1). p. 152-160.
93. Sow, B., S. Hamoudi, M.H. Zahedi-Niaki and S. Kaliaguine, *1-Butanol etherification over sulfonated mesostructured silica and organo-silica.* Microporous and Mesoporous Materials, 2005. 79(1-3). p. 129-136.
94. Rac, B., P. Hegyes, P. Forgo and A. Molnar, *Sulfonic acid-functionalized phenylene-bridged periodic mesoporous organosilicas as catalyst materials.* Applied Catalysis a-General, 2006. 299. p. 193-201.
95. Marschall, R., I. Bannat, J. Caro and M. Wark, *Proton conductivity of sulfonic acid functionalised mesoporous materials.* Microporous and Mesoporous Materials, 2007. 99(1-2). p. 190-196.
96. Wilhelm, M., M. Jeske, R. Marschall, W.L. Cavalcanti, P. Tolle, C. Kohler, D. Koch, T. Frauenheim, G. Grathwohl, J. Caro and M. Wark, *New proton*

conducting hybrid membranes for HT-PEMFC systems based on polysiloxanes and SO3H-functionalized mesoporous Si-MCM-41 particles. Journal of Membrane Science, 2008. 316(1-2). p. 164-175.
97. Sharifi, M., C. Kohler, P. Tolle, T. Frauenheim and M. Wark, *Proton Conductivity of SO3H-Functionalized Benzene-Periodic Mesoporous Organosilica.* Small, 2011. 7(8). p. 1086-1097.
98. Ho, K.Y., G. McKay and K.L. Yeung, *Selective adsorbents from ordered mesoporous silica.* Langmuir, 2003. 19(7). p. 3019-3024.
99. Lei, C.H., Y.S. Shin, J. Liu and E.J. Ackerman, *Entrapping enzyme in a functionalized nanoporous support.* Journal of the American Chemical Society, 2002. 124(38). p. 11242-11243.
100. Alvaro, M., A. Corma, D. Das, V. Fornes and H. Garcia, *Single-step preparation and catalytic activity of mesoporous MCM-41 and SBA-15 silicas functionalized with perfluoroalkylsulfonic acid groups analogous to Nafion (R).* Chemical Communications, 2004(8). p. 956-957.
101. Khatri, R.A., S.S.C. Chuang, Y. Soong and M. Gray, *Carbon dioxide capture by diamine-grafted SBA-15: A combined Fourier transform infrared and mass spectrometry study.* Industrial & Engineering Chemistry Research, 2005. 44(10). p. 3702-3708.
102. Yokoi, T., H. Yoshitake and T. Tatsumi, *Synthesis of amino-functionalized MCM-41 via direct co-condensation and post-synthesis grafting methods using mono-, di- and tri-amino-organoalkoxysilanes.* Journal of Materials Chemistry, 2004. 14(6). p. 951-957.
103. Kang, T., Y. Park, K. Choi, J.S. Lee and J. Yi, *Ordered mesoporous silica (SBA-15) derivatized with imidazole-containing functionalities as a selective adsorbent of precious metal ions.* Journal of Materials Chemistry, 2004. 14(6). p. 1043-1049.
104. Armatas, G.S., C.E. Salmas, M. Louloudi, G.P. Androutsopoulos and P.J. Pomonis, *Relationships among pore size, connectivity, dimensionality of capillary condensation, and pore structure tortuosity of functionalized mesoporous silica.* Langmuir, 2003. 19(8). p. 3128-3136.
105. Liang, Y., E.S. Erichsen, C. Song and R. Anwander, *Organozinc- and Imidazole-Modified Periodic Mesoporous Organosilicas by Means of Molecular Grafting.* European Journal of Inorganic Chemistry, 2012(34). p. 5741-5751.
106. Ohashi, M., M.P. Kapoor and S. Inagaki, *Chemical modification of crystal-like mesoporous phenylene-silica with amino group.* Chemical Communications, 2008(7). p. 841-843.
107. Cavalcanti, W.L., R. Marschall, P. Tolle, C. Kohler, M. Wark and T. Frauenheim, *Insight into proton conduction of immobilised imidazole systems via simulations and impedance spectroscopy.* Fuel Cells, 2008. 8(3-4). p. 244-253.
108. Marschall, R., M. Sharifi and M. Wark, *Proton conductivity of imidazole functionalized ordered mesoporous silica: Influence of type of anchorage, chain length and humidity.* Microporous and Mesoporous Materials, 2009. 123(1-3). p. 21-29.
109. Nishiwaki, S., K. Tadanaga, M. Tatsumisago and T. Minami, *Preparation and proton conductivity of surfactant-templated mesoporous silica gels impregnated with protonic acids.* Journal of the American Ceramic Society, 2000. 83(12). p. 3004-3008.

110. Matsuda, A., Y. Nono, T. Kanzaki, K. Tadanaga, M. Tatsumisago and T. Minami, *Proton conductivity of acid-impregnated mesoporous silica gels prepared using surfactants as a template.* Solid State Ionics, 2001. 145(1-4). p. 135-140.
111. Matsuda, A., T. Kanzaki, K. Tadanaga, T. Kogure, M. Tatsumisago and T. Minami, *Sol-gel derived porous silica gels impregnated with sulfuric acid - Pore structure and proton conductivities at medium temperatures.* Journal of the Electrochemical Society, 2002. 149(8). p. E292-E297.
112. Armento, P., M. Casciola, M. Pica, F. Marmottini, R. Palombari and F. Ziarelli, *Silica-zirconium phosphate-phosphoric acid composites: preparation, proton conductivity and use in gas sensors.* Solid State Ionics, 2004. 166(1-2). p. 19-25.
113. Jin, H.X., Q.Y. Wu and W.Q. Pang, *Preparation and conductivity of tungstovanadogermanic heteropoly acid supported on mesoporous silicate SBA-15.* Materials Letters, 2004. 58(29). p. 3657-3660.
114. Lu, S., D. Wang, S.P. Jiang, Y. Xiang, J. Lu and J. Zeng, *HPW/MCM-41 Phosphotungstic Acid/Mesoporous Silica Composites as Novel Proton-Exchange Membranes for Elevated-Temperature Fuel Cells.* Advanced Materials, 2010. 22(9). p. 971-+.
115. Lu, J., H. Tang, S. Lu, H. Wu and S.P. Jiang, *A novel inorganic proton exchange membrane based on self-assembled HPW-meso-silica for direct methanol fuel cells.* Journal of Materials Chemistry, 2011. 21(18). p. 6668-6676.
116. Zeng, J., Y. Zhou, L. Li and S.P. Jiang, *Phosphotungstic acid functionalized silica nanocomposites with tunable bicontinuous mesoporous structure and superior proton conductivity and stability for fuel cells.* Physical Chemistry Chemical Physics, 2011. 13(21). p. 10249-10257.
117. Zeng, J., P.K. Shen, S. Lu, Y. Xiang, L. Li, R. De Marco and S.P. Jiang, *Correlation between proton conductivity, thermal stability and structural symmetries in novel HPW-meso-silica nanocomposite membranes and their performance in direct methanol fuel cells.* Journal of Membrane Science, 2012. 397. p. 92-101.
118. Bruhwiler, D., *Postsynthetic functionalization of mesoporous silica.* Nanoscale, 2010. 2(6). p. 887-892.
119. Burkett, S.L., S.D. Sims and S. Mann, *Synthesis of hybrid inorganic-organic mesoporous silica by co-condensation of siloxane and organosiloxane precursors.* Chemical Communications, 1996(11). p. 1367-1368.
120. Mercier, L. and T.J. Pinnavaia, *Direct synthesis of hybrid organic-inorganic nanoporous silica by a neutral amine assembly route: Structure-function control by stoichiometric incorporation of organosiloxane molecules.* Chemistry of Materials, 2000. 12(1). p. 188-196.
121. Wan, Y., D.Q. Zhang, N. Hao and D.Y. Zhao, *Organic groups functionalised mesoporous silicates.* International Journal of Nanotechnology, 2007. 4(1-2). p. 66-99.
122. Wang, X.M., X.Z. Du, C.L. Li and X. Cao, *Preparation and characterization of different alkyl-modified SBA-15 by a single-step synthesis.* Materials Letters, 2008. 62(17-18). p. 3232-3235.
123. Chong, A.S.M. and X.S. Zhao, *Functionalization of SBA-15 with APTES and characterization of functionalized materials.* Journal of Physical Chemistry B, 2003. 107(46). p. 12650-12657.

124. Yokoi, T., H. Yoshitake and T. Tatsumi, *Synthesis of anionic-surfactant-templated mesoporous silica using organoalkoxysilane-containing amino groups.* Chemistry of Materials, 2003. 15(24). p. 4536-4538.
125. Che, S., A.E. Garcia-Bennett, T. Yokoi, K. Sakamoto, H. Kunieda, O. Terasaki and T. Tatsumi, *A novel anionic surfactant templating route for synthesizing mesoporous silica with unique structure.* Nature Materials, 2003. 2(12). p. 801-805.
126. Wang, X., J.C.C. Chan, Y.-H. Tseng and S. Cheng, *Synthesis, characterization and catalytic activity of ordered SBA-15 materials containing high loading of diamine functional groups.* Microporous and Mesoporous Materials, 2006. 95(1-3). p. 57-65.
127. Lim, M.H., C.F. Blanford and A. Stein, *Synthesis of ordered microporous silicates with organosulfur surface groups and their applications as solid acid catalysts.* Chemistry of Materials, 1998. 10(2). p. 467-+.
128. Margolese, D., J.A. Melero, S.C. Christiansen, B.F. Chmelka and G.D. Stucky, *Direct syntheses of ordered SBA-15 mesoporous silica containing sulfonic acid groups.* Chemistry of Materials, 2000. 12(8). p. 2448-2459.
129. Mikhailenko, S., D. Desplantier-Giscard, C. Danumah and S. Kaliaguine, *Solid electrolyte properties of sulfonic acid functionalized mesostructured porous silica.* Microporous and Mesoporous Materials, 2002. 52(1). p. 29-37.
130. Yang, Q.H., M.P. Kapoor and S. Inagaki, *Sulfuric acid-functionalized mesoporous benzene-silica with a molecular-scale periodicity in the walls.* Journal of the American Chemical Society, 2002. 124(33). p. 9694-9695.
131. Feng, Y.F., X.Y. Yang, Y. Di, Y.C. Du, Y.L. Zhang and F.S. Xiao, *Mesoporous silica materials with an extremely high content of organic sulfonic groups and their comparable activities with that of concentrated sulfuric acid in catalytic esterification.* Journal of Physical Chemistry B, 2006. 110(29). p. 14142-14147.
132. Rac, B., A. Molnar, P. Forgo, M. Mohai and I. Bertoti, *A comparative study of solid sulfonic acid catalysts based on various ordered mesoporous silica materials.* Journal of Molecular Catalysis a-Chemical, 2006. 244(1-2). p. 46-57.
133. Shylesh, S., P.P. Samuel, C. Srilakshmi, R. Parischa and A.P. Singh, *Sulfonic acid functionalized mesoporous silicas and organosilicas: Synthesis, characterization and catalytic applications.* Journal of Molecular Catalysis a-Chemical, 2007. 274(1-2). p. 153-158.
134. Cho, E.B. and D. Kim, *Direct synthesis of sulfonic acid-functionalized periodic mesoporous benzene-silicas with large pores.* Journal of Physics and Chemistry of Solids, 2008. 69(5-6). p. 1142-1146.
135. Marschall, R., I. Bannat, A. Feldhoff, L.Z. Wang, G.Q. Lu and M. Wark, *Nanoparticles of Mesoporous SO3H-Functionalized Si-MCM-41 with Superior Proton Conductivity.* Small, 2009. 5(7). p. 854-859.
136. Corriu, R.J.P., L. Datas, Y. Guari, A. Mehdi, C. Reye and C. Thieuleux, *Ordered SBA-15 mesoporous silica containing phosphonic acid groups prepared by a direct synthetic approach.* Chemical Communications, 2001(8). p. 763-764.
137. Jin, Y.G., S.Z. Qiao, Z.P. Xu, J.C.D. da Costa and G.Q. Lu, *Porous Silica Nanospheres Functionalized with Phosphonic Acid as Intermediate-Temperature Proton Conductors.* Journal of Physical Chemistry C, 2009. 113(8). p. 3157-3163.
138. Jin, Y.G., S.Z. Qiao, Z.P. Xu, Z.M. Yan, Y.N. Huang, J.C.D. da Costa and G.Q. Lu, *Phosphonic acid functionalized silicas for intermediate temperature proton conduction.* Journal of Materials Chemistry, 2009. 19(16). p. 2363-2372.

139. Wang, P.Y., L. Zhao, R. Wu, H. Zhong, H.F. Zou, J. Yang and Q.H. Yang, *Phosphonic Acid Functionalized Periodic Mesoporous Organosilicas and Their Potential Applications in Selective Enrichment of Phosphopeptides.* Journal of Physical Chemistry C, 2009. 113(4). p. 1359-1366.
140. Kapoor, M.P. and S. Inagaki, *Highly ordered mesoporous organosilica hybrid materials.* Bulletin of the Chemical Society of Japan, 2006. 79(10). p. 1463-1475.
141. Marschall, R., P. Tolle, W.L. Cavalcanti, M. Wilhelm, C. Kohler, T. Frauenheim and M. Wark, *Detailed Simulation and Characterization of Highly Proton Conducting Sulfonic Acid Functionalized Mesoporous Materials under Dry and Humidified Conditions.* Journal of Physical Chemistry C, 2009. 113(44). p. 19218-19227.
142. Sharifi, M., R. Marschall, M. Wilhelm, D. Wallacher and M. Wark, *Detection of Homogeneous Distribution of Functional Groups in Mesoporous Silica by Small Angle Neutron Scattering and in Situ Adsorption of Nitrogen or Water.* Langmuir, 2011. 27(9). p. 5516-5522.
143. Gedye, R., F. Smith, K. Westaway, H. Ali, L. Baldisera, L. Laberge and J. Rousell, *The use microwave ovens for rapid organic synthesis.* Tetrahedron Letters, 1986. 27(3). p. 279-282.
144. Galema, S.A., *Microwave chemistry.* Chemical Society Reviews, 1997. 26(3). p. 233-238.
145. Kappe, C.O., *Controlled microwave heating in modern organic synthesis.* Angewandte Chemie-International Edition, 2004. 43(46). p. 6250-6284.
146. Tompsett, G.A., W.C. Conner and K.S. Yngvesson, *Microwave synthesis of nanoporous materials.* Chemphyschem, 2006. 7(2). p. 296-319.
147. Bilecka, I. and M. Niederberger, *Microwave chemistry for inorganic nanomaterials synthesis.* Nanoscale, 2010. 2(8). p. 1358-1374.
148. Wu, C.G. and T. Bein, *Microwave synthesis of molecular sieve MCM-41.* Chemical Communications, 1996(8). p. 925-926.
149. Park, S.E., D.S. Kim, J.S. Chang and W.Y. Kim. *Synthesis of MCM-41 using microwave heating with ethylene glycol*. in *1st Asia-Pacific Catalysis Congress*. 1997. Kyongju, South Korea: Elsevier Science Bv.
150. Newalkar, B.L., S. Komarneni and H. Katsuki, *Rapid synthesis of mesoporous SBA-15 molecular sieve by a microwave-hydrothermal process.* Chemical Communications, 2000(23). p. 2389-2390.
151. Tian, B.Z., X.Y. Liu, C.Z. Yu, F. Gao, Q. Luo, S.H. Xie, B. Tu and D.Y. Zhao, *Microwave assisted template removal of siliceous porous materials.* Chemical Communications, 2002(11). p. 1186-1187.
152. Kim, D.J., J.S. Chung, W.S. Ahn, G.W. Kam and W.J. Cheong, *Morphology control of organic-inorganic hybrid mesoporous silica by microwave heating.* Chemistry Letters, 2004. 33(4). p. 422-423.
153. Newalkar, B.L., H. Katsuki and S. Komarneni, *Microwave-hydrothermal synthesis and characterization of microporous-mesoporous disordered silica using mixed-micellar-templating approach.* Microporous and Mesoporous Materials, 2004. 73(3). p. 161-170.
154. Park, S.E., J.S. Chang, Y.K. Hwang, D.S. Kim, S.H. Jhung and J.S. Hwang, *Supramolecular interactions and morphology control in microwave synthesis of nanoporous materials.* Catalysis Surveys from Asia, 2004. 8(2). p. 91-110.

155. Bandyopadhyay, A. and H. Gies, *Synthesis of MCM-48 by microwave-hydrothermal process.* Comptes Rendus Chimie, 2005. 8(3-4). p. 621-626.
156. Marschall, R., J. Rathousky and M. Wark, *Ordered functionalized silica materials with high proton conductivity.* Chemistry of Materials, 2007. 19(26). p. 6401-6407.
157. Yoon, S.S., W.J. Son, K. Biswas and W.S. Ahn, *Synthesis of periodic mesoporous organosilica by microwave heating.* Bulletin of the Korean Chemical Society, 2008. 29(3). p. 609-614.
158. Grabicka, B.E. and M. Jaroniec, *Microwave-assisted synthesis of periodic mesoporous organosilicas with ethane and disulfide groups.* Microporous and Mesoporous Materials, 2009. 119(1-3). p. 144-149.
159. Yu, H. and Q.Z. Zhai, *Microwave-Assisted Hydrothermal Synthesis of SBA-15 Molecular Sieve.* Asian Journal of Chemistry, 2009. 21(4). p. 2745-2754.
160. Procopio, A., G. De Luca, M. Nardi, M. Oliverio and R. Paonessa, *General MW-assisted grafting of MCM-41: Study of the dependence on time dielectric heating and solvent.* Green Chemistry, 2009. 11(6). p. 770-773.
161. Smeulders, G., V. Meynen, G. Van Baelen, M. Mertens, O.I. Lebedev, G. Van Tendeloo, B.U.W. Maes and P. Cool, *Rapid microwave-assisted synthesis of benzene bridged periodic mesoporous organosilicas.* Journal of Materials Chemistry, 2009. 19(19). p. 3042-3048.
162. Smeulders, G., C.J. Van Oers, K. Van Havenbergh, K. Houthoofd, M. Mertens, J.A. Martens, S. Bals, B.U.W. Maes, V. Meynen and P. Cool, *Smart heating profiles for the synthesis of benzene bridged periodic mesoporous organosilicas.* Chemical Engineering Journal, 2011. 175. p. 585-591.
163. Alberti, G., M. Casciola, S. Cavalaglio and R. Vivani, *Proton conductivity of mesoporous zirconium phosphate pyrophosphate.* Solid State Ionics, 1999. 125(1-4). p. 91-97.
164. Rodriguez-Castellon, E., J. Jimenez-Jimenez, A. Jimenez-Lopez, P. Maireles-Torres, J.R. Ramos-Barrado, D.J. Jones and J. Roziere, *Proton conductivity of mesoporous MCM type of zirconium and titanium phosphates.* Solid State Ionics, 1999. 125(1-4). p. 407-410.
165. Hogarth, W.H.J., J.C.D. da Costa, J. Drennan and G.Q. Lu, *Proton conductivity of mesoporous sol-gel zirconium phosphates for fuel cell applications.* Journal of Materials Chemistry, 2005. 15(7). p. 754-758.
166. Mal, N.K., A. Bhaumik, M. Matsukata and M. Fujiwara, *Syntheses of mesoporous hybrid iron oxophenyl phosphate, iron oxophosphate, and sulfonated oxophenyl phosphate.* Industrial & Engineering Chemistry Research, 2006. 45(23). p. 7748-7751.
167. Nishiyama, Y., S. Tanaka, H.W. Hillhouse, N. Nishiyama, Y. Egashira and K. Ueyama, *Synthesis of ordered mesoporous zirconium phosphate films by spin coating and vapor treatments.* Langmuir, 2006. 22(23). p. 9469-9472.
168. Mal, N.K., M. Fujiwara and A. Bhaumik, *New organic-inorganic hybrid mesoporous tantalum oxophosphate and sulfonated tantalum oxophenylphosphate.* Journal of Non-Crystalline Solids, 2007. 353(44-46). p. 4116-4120.
169. Chai, Z., D. Dong, C. Wang, H. Zhang, P.A. Webley, D. Zhao and H. Wang, *Nanoporous niobium phosphate electrolyte membrane for low temperature fuel cell.* Journal of Membrane Science, 2010. 356(1-2). p. 147-153.

170. Vichi, F.M., M.I. Tejedor-Tejedor and M.A. Anderson, *Effect of pore-wall chemistry on proton conductivity in mesoporous titanium dioxide.* Chemistry of Materials, 2000. 12(6). p. 1762-1770.
171. Garcia-Belmonte, G., V. Kytin, T. Dittrich and J. Bisquert, *Effect of humidity on the ac conductivity of nanoporous TiO2.* Journal of Applied Physics, 2003. 94(8). p. 5261-5264.
172. Yamada, M., D.L. Li, I. Honma and H.S. Zhou, *A self-ordered, crystalline glass, mesoporous nanocomposite with high proton conductivity of 2 x 10(-2) S cm(-1) at intermediate temperature.* Journal of the American Chemical Society, 2005. 127(38). p. 13092-13093.
173. Colomer, M.T., *Proton conductivity of nanoporous anatase xerogels prepared by a particulate sol-gel method.* Journal of Solid State Electrochemistry, 2006. 10(1). p. 54-59.
174. Colomer, M.T., *Nanoporous anatase ceramic membranes as fast-proton-conducting materials.* Journal of the European Ceramic Society, 2006. 26(7). p. 1231-1236.
175. Jun, Y., H. Zarrin, M. Fowler and Z. Chen, *Functionalized titania nanotube composite membranes for high temperature proton exchange membrane fuel cells.* International Journal of Hydrogen Energy, 2011. 36(10). p. 6073-6081.
176. Shen, H.Y., H. Maekawa, Y. Fujimaki, K. Kawada and T. Yamamura, *High proton conductivity of mesoporous Al2O3*. Solid State Ionics: The Science and Technology of Ions in Motion, ed. B.V.R. Chowdari, H.L. Yoo, G.M. Choi, and J.H. Lee 2004: 187-193.
177. Shen, H., H. Maekawa, J. Kawamura and T. Yamamura, *Development of high protonic conductors based on amorphous mesoporous alumina.* Solid State Ionics, 2006. 177(26-32). p. 2403-2406.
178. Shen, H., B. Guo, H. Maekawa, J. Guo and K. Shu, *Effect of chloride doping concentration on enhancement of protonic conductivity of mesoporous Al2O3.* Solid State Ionics, 2011. 192(1). p. 105-107.
179. Nogami, M., R. Nagao and C. Wong, *Proton conduction in porous silica glasses with high water content.* Journal of Physical Chemistry B, 1998. 102(30). p. 5772-5775.
180. Nogami, M. and Y. Abe, *Evidence of water-cooperative proton conduction in silica glasses.* Physical Review B, 1997. 55(18). p. 12108-12112.
181. Vichi, F.M., M.T. Colomer and M.A. Anderson, *Nanopore ceramic membranes as novel electrolytes for proton exchange membranes.* Electrochemical and Solid State Letters, 1999. 2(7). p. 313-316.
182. Colomer, M.T. and M.A. Anderson, *High porosity silica xerogels prepared by a particulate sol-gel route: pore structure and proton conductivity.* Journal of Non-Crystalline Solids, 2001. 290(2-3). p. 93-104.
183. Daiko, Y., T. Kasuga and M. Nogami, *Pore size effect on proton transfer in sol-gel porous silica glasses.* Microporous and Mesoporous Materials, 2004. 69(3). p. 149-155.
184. Li, H. and T. Kunitake, *Efficient proton conduction of nanometer-thick film of porous silica as prepared by oxygen plasma treatment.* Microporous and Mesoporous Materials, 2006. 97(1-3). p. 42-48.
185. Xiong, L. and M. Nogami, *Proton-conducting ordered mesostructured silica monoliths.* Chemistry Letters, 2006. 35(8). p. 972-973.

186. Colomer, M.T., F. Rubio and J.R. Jurado, *Transport properties of fast proton conducting mesoporous silica xerogels.* Journal of Power Sources, 2007. 167(1). p. 53-57.
187. Bering, B.P., M.M. Dubinin and Serpinsk.Vv, *Theory of volume fillng for vapor adsorption.* Journal of Colloid and Interface Science, 1966. 21(4). p. 378-393.
188. Colomban, P. and A. Novak, *Hydrogen bond and protonic species*, in *Proton Conductors*, P. Colomban, Editor 1992, Cambridge University Press: Cambridge.
189. Nogami, M., H.B. Li, Y. Daiko and T. Mitsuoka, *Proton-conducting phosphosilicate films prepared using template for pore structure.* Journal of Sol-Gel Science and Technology, 2004. 32(1-3). p. 185-188.
190. Wang, S.Q., J. Otomo, M. Ogura, C. Wen, H. Nagamoto and H. Takahashi, *Preparation and characterization of proton-conducting CsHSO4-SiO2 nanocomposite electrolyte membranes.* Solid State Ionics, 2005. 176(7-8). p. 755-760.
191. Otomo, J., H. Shigeoka, H. Nagamoto and H. Takahashi, *Phase transition behavior and proton conduction mechanism in cesium hydrogen sulfate/silica composite.* Journal of Physics and Chemistry of Solids, 2005. 66(1). p. 21-30.
192. Nishiyama, N., J. Kaihara, Y. Nishiyama, Y. Egashira and K. Ueyama, *Vapor-phase synthesis of mesoporous SiO2-P2O5 thin films.* Langmuir, 2007. 23(9). p. 4746-4748.
193. Nishiyama, Y., K. Ochi, N. Nishiyama, Y. Egashira and K. Ueyama, *Proton-conducting mesoporous Silica/Phosphate composite films prepared by vapor phase method.* Electrochemical and Solid State Letters, 2008. 11(1). p. B6-B9.
194. Tang, H. and S.P. Jiang, *Inorganic Electrolyte Membrane for High-temperature PEM fuel cell: Conception, Preparation and Performance*, in *Proton Exchange Membrane Fuel Cells 8, Pts 1 and 2*, T. Fuller, K. Shinohara, V. Ramani, P. Shirvanian, H. Uchida, S. Cleghorn, M. Inaba, S. Mitsushima, P. Strasser, H. Nakagawa, H.A. Gasteiger, T. Zawodzinski, and C. Lamy, Editors. 2008. p. 719-728.
195. Sharifi, M., R. Marschall, M. Wilkening and M. Wark, *Proton conductivity of ordered mesoporous materials containing aluminium.* Journal of Power Sources, 2010. 195(23). p. 7781-7786.
196. Tang, H., M. Pan, S. Lu, J. Lu and S.P. Jiang, *One-step synthesized HPW/meso-silica inorganic proton exchange membranes for fuel cells.* Chemical Communications, 2010. 46(24). p. 4351-4353.
197. Tang, H., M. Pan and S.P. Jiang, *Self assembled 12-tungstophosphoric acid-silica mesoporous nanocomposites as proton exchange membranes for direct alcohol fuel cells.* Dalton Transactions, 2011. 40(19). p. 5220-5227.
198. Zeng, J. and S.P. Jiang, *Characterization of High-Temperature Proton-Exchange Membranes Based on Phosphotungstic Acid Functionalized Mesoporous Silica Nanocomposites for Fuel Cells.* Journal of Physical Chemistry C, 2011. 115(23). p. 11854-11863.
199. Yue, W., X. Xu, Z. Su, J.T.S. Irvine, Y. Zou, Y. Liu and W. Zhou, *Syntheses and proton conductivity of mesoporous Nd2O3-SiO2 and NdOCl-SiO2 composites.* Journal of Materials Science, 2012. 47(5). p. 2146-2154.
200. Kreuer, K.D., *Proton conductivity: Materials and applications.* Chemistry of Materials, 1996. 8(3). p. 610-641.
201. Wu, Q.Y. and G.Y. Meng, *Preparation and conductivity of vanadotungstogermanic heteropoly acid.* Solid State Ionics, 2000. 136. p. 273-277.

202. Halla, J.D., M. Mamak, D.E. Williams and G.A. Ozin, *Meso-SiO(2)-C(12)EO(10)OH-CF(3)SO(3)H - A novel proton-conducting solid electrolyte.* Advanced Functional Materials, 2003. 13(2). p. 133-138.
203. Coutinho, D., Z.W. Yang, J.P. Ferraris and K.J. Balkus, *Proton conducting polyaniline molecular sieve composites.* Microporous and Mesoporous Materials, 2005. 81(1-3). p. 321-332.
204. Athens, G.L., Y. Ein-Eli and B.F. Chmelka, *Acid-functionalized mesostructured aluminosilica for hydrophilic proton conduction membranes.* Advanced Materials, 2007. 19(18). p. 2580-+.
205. Daiko, Y., K. Katagiri, K. Ogura, M. Sakai and A. Matsuda, *Preparation and characterization of surface-sulfonated phenylsilsesquioxane-methylsilsesquioxane particles.* Solid State Ionics, 2007. 178(7-10). p. 601-605.
206. McKeen, J.C., Y.S. Yan and M.E. Davis, *Proton Conductivity of Acid-Functionalized Zeolite Beta, MCM-41, and MCM-48: Effect of Acid Strength.* Chemistry of Materials, 2008. 20(16). p. 5122-5124.
207. Wang, C.M., E. Chalkova, C.D. Lute, M.V. Fedkin, S. Komarneni, T.C.M. Chung and S.N. Lvov, *Proton Conductive Inorganic Materials for Temperatures Up to 120 degrees C and Relative Humidity Down to 5%.* Journal of the Electrochemical Society, 2010. 157(11). p. B1634-B1642.
208. Thanganathan, U., *Structural study on inorganic/organic hybrid composite membranes.* Journal of Materials Chemistry, 2011. 21(2). p. 456-465.
209. Jiang, B., H. Tang and M. Pan, *Well-ordered sulfonated silica electrolyte with high proton conductivity and enhanced selectivity at elevated temperature for DMFC.* International Journal of Hydrogen Energy, 2012. 37(5). p. 4612-4618.
210. Sharifi, M., J. Schneider and M. Wark, *Investigation on the optimal oxidation agent for a maximum yield of sulfonic acid groups in MCM-41.* Microporous and Mesoporous Materials, 2012. 151. p. 506-510.
211. Sharifi, M., M. Wark, D. Freude and J. Haase, *Highly proton conducting sulfonic acid functionalized mesoporous materials studied by impedance spectroscopy, MAS NMR spectroscopy and MAS PFG NMR diffusometry.* Microporous and Mesoporous Materials, 2012. 156. p. 80-89.
212. Hamoudi, S., S. Royer and S. Kaliaguine, *Propyl- and arene-sulfonic acid functionalized periodic mesoporous organosilicas.* Microporous and Mesoporous Materials, 2004. 71(1-3). p. 17-25.
213. Fujita, S., A. Koiwai, M. Kawasumi and S. Inagaki, *Enhancement of Proton Transport by High Densification of Sulfonic Acid Groups in Highly Ordered Mesoporous Silica.* Chemistry of Materials, 2013. 25(9). p. 1584-1591.
214. Schuster, M., T. Rager, A. Noda, K.D. Kreuer and J. Maier, *About the choice of the protogenic group in PEM separator materials for intermediate temperature, low humidity operation: A critical comparison of sulfonic acid, phosphonic acid and imidazole functionalized model compounds.* Fuel Cells, 2005. 5(3). p. 355-365.
215. Laberty-Robert, C., K. Valle, F. Pereira and C. Sanchez, *Design and properties of functional hybrid organic-inorganic membranes for fuel cells.* Chemical Society Reviews, 2011. 40(2). p. 961-1005.
216. Antonucci, P.L., A.S. Arico, P. Creti, E. Ramunni and V. Antonucci, *Investigation of a direct methanol fuel cell based on a composite Nafion (R)-silica electrolyte for high temperature operation.* Solid State Ionics, 1999. 125(1-4). p. 431-437.

217. Adjemian, K.T., S.J. Lee, S. Srinivasan, J. Benziger and A.B. Bocarsly, *Silicon oxide Nafion composite membranes for proton-exchange membrane fuel cell operation at 80-140 degrees C.* Journal of the Electrochemical Society, 2002. 149(3). p. A256-A261.
218. Lin, Y.F., C.Y. Yen, C.C.M. Ma, S.H. Liao, C.H. Lee, Y.H. Hsiao and H.P. Lin, *High proton-conducting Nafion (R)/-SO_3H functionalized mesoporous silica composite membranes.* Journal of Power Sources, 2007. 171. p. 388-395.
219. Tominaga, Y., I.C. Hong, S. Asai and M. Sumita, *Proton conduction in Nafion composite membranes filled with mesoporous silica.* Journal of Power Sources, 2007. 171(2). p. 530-534.
220. Jin, Y.G., S.Z. Qiao, L. Zhang, Z.P. Xu, S. Smart, J.C.D. da Costa and G.Q. Lu, *Novel Nafion composite membranes with mesoporous silica nanospheres as inorganic fillers.* Journal of Power Sources, 2008. 185(2). p. 664-669.
221. Tay, S.W., X. Zhang, Z. Liu, L. Hong and S.H. Chan, *Composite Nafion (R) membrane embedded with hybrid nanofillers for promoting direct methanol fuel cell performance.* Journal of Membrane Science, 2008. 321(2). p. 139-145.
222. Pereira, F., K. Valle, P. Belleville, A. Morin, S. Lambert and C. Sanchez, *Advanced mesostructured hybrid silica-nafion membranes for high-performance PEM fuel cell.* Chemistry of Materials, 2008. 20(5). p. 1710-1718.
223. Tang, H.L. and M. Pan, *Synthesis and characterization of a self-assembled nafion/silica nanocomposite membrane for polymer electrolyte membrane fuel cells.* Journal of Physical Chemistry C, 2008. 112(30). p. 11556-11568.
224. Wang, K.P., S. McDermid, J. Li, N. Kremliakova, P. Kozak, C.J. Song, Y.H. Tang, J.L. Zhang and J.J. Zhang, *Preparation and performance of nano silica/Nafion composite membrane for proton exchange membrane fuel cells.* Journal of Power Sources, 2008. 184(1). p. 99-103.
225. Ojeda, M.C., C. del Rio, P.G. Escribano, F. Sanchez and J.L. Acosta, *Study of Hybrid Membranes with Sulfonated-organomodified Fillers. Systems Based on Sulfonated-phenyl SBA-15.* Journal of New Materials for Electrochemical Systems, 2009. 12(2-3). p. 127-131.
226. Sahu, A.K., S.D. Bhat, S. Pitchumani, P. Sridhar, V. Vimalan, C. George, N. Chandrakumar and A.K. Shukla, *Novel organic-inorganic composite polymer-electrolyte membranes for DMFCs.* Journal of Membrane Science, 2009. 345(1-2). p. 305-314.
227. Xu, K., C. Chanthad, M.R. Gadinski, M.A. Hickner and Q. Wang, *Acid-Functionalized Polysilsesquioxane-Nafion Composite Membranes with High Proton Conductivity and Enhanced Selectivity.* Acs Applied Materials & Interfaces, 2009. 1(11). p. 2573-2579.
228. Hong, L.-Y., S.-Y. Oh, A. Matsuda, C.-S. Lee and D.-P. Kim, *Hydrophilic and mesoporous SiO2-TiO2-SO3H system for fuel cell membrane applications.* Electrochimica Acta, 2011. 56(9). p. 3108-3114.
229. Tsai, C.-H., H.-J. Lin, H.-M. Tsai, J.-T. Hwang, S.-M. Chang and Y.-W. Chen-Yang, *Characterization and PEMFC application of a mesoporous sulfonated silica prepared from two precursors, tetraethoxysilane and phenyltriethoxysilane.* International Journal of Hydrogen Energy, 2011. 36(16). p. 9831-9841.
230. Shea, K.J., D.A. Loy and O. Webster, *Arylsilsesquioxane gels and related materials - new hybrids of organic and inorganic networks.* Journal of the American Chemical Society, 1992. 114(17). p. 6700-6710.

231. Bohmer, V., W. Vogt, S. Chafaa, J. Meullemeestre, M.J. Schwing and F. Vierling, *(O-hydroxyphenyl)methylphosphonic acids - Synthesis and potentiometric determinations of their pKa values.* Helvetica Chimica Acta, 1993. 76(1). p. 139-149.
232. Toney, M.F., *X-ray Diffraction*, in *Encyclopedia of Materials Characterization*, C.R. Brundle, C.A. Evans, and S. Wilson, Editors. 1992, Butterworth-Heinemann: Boston.
233. Gregg, S.J. and K.S.W. Sing, *Adsorption, Surface Area and Porosity*. 2nd ed 1982, Academic Press, London.
234. Mitropoulos, A.C., *The Kelvin equation.* Journal of Colloid and Interface Science, 2008. 317(2). p. 643-648.
235. Brunauer, S., P.H. Emmett and E. Teller, *Adsorption of gases in multimolecular layers.* Journal of the American Chemical Society, 1938. 60. p. 309-319.
236. Kruk, M., M. Jaroniec and A. Sayari, *Application of large pore MCM-41 molecular sieves to improve pore size analysis using nitrogen adsorption measurements.* Langmuir, 1997. 13(23). p. 6267-6273.
237. Jaroniec, M. and L.A. Solovyov, *Improvement of the Kruk-Jaroniec-Sayari method for pore size analysis of ordered silicas with cylindrical mesopores.* Langmuir, 2006. 22(16). p. 6757-6760.
238. Williams, D.B. and C.B. Carter, *Transmission Electron Microscopy, A Textbook for Materials Science*. 2nd ed 2009, Springer, New York.
239. Geiss, R.H., *Energy-Dispersive X-ray Spectroscopy*, in *Encyclopedia of Materials Characterization*, C.R. Brundle, C.A. Evans, and S. Wilson, Editors. 1992, Butterworth-Heinemann: Boston.
240. Rasband, W.S., *Image J. v.1.45s*, U.S. National Institutes of Health, Bethesda, Maryland, USA, 1997-2004.
241. Grimmer, A.-R. and B. Blümich, *Introduction to Solid-State NMR*, in *Solid-State NMR I Methods*, B. Blümich, Editor 1994, Springer Berlin Heidelberg. p. 1-62.
242. Engelhardt, G. and D. Michel, *High-esolution Solid-State NMR of Silicates and Zeolites* 1987, John Wiley & Sons, New York.
243. Sel, O., T. Azais, M. Marechal, G. Gebel, C. Laberty-Robert and C. Sanchez, *Sulfonic and Phosphonic Acid and Bifunctional Organic-Inorganic Hybrid Membranes and Their Proton Conduction Properties.* Chemistry-an Asian Journal, 2011. 6(11). p. 2992-3000.
244. Aliev, A., D.L. Ou, B. Ormsby and A.C. Sullivan, *Porous silica and polysilsesquioxane with covalently linked phosphonates and phosphonic acids.* Journal of Materials Chemistry, 2000. 10(12). p. 2758-2764.
245. Pan, Y.-C., H.-H.G. Tsai, J.-C. Jiang, C.-C. Kao, T.-L. Sung, P.-J. Chiu, D. Saikia, J.-H. Chang and H.-M. Kao, *Probing the Nature and Local Structure of Phosphonic Acid Groups Functionalized in Mesoporous Silica SBA-15.* Journal of Physical Chemistry C, 2012. 116(2). p. 1658-1669.
246. Yang, Q.H., J. Yang, J. Liu, Y. Li and C. Li, *Synthesis and characterization of phosphonic acid functionalized organosilicas with bimodal nanostructure.* Chemistry of Materials, 2005. 17(11). p. 3019-3024.
247. Menard, K.P., *Dynamic Mechanical Analysis - A Practical Introduction*. 2 nd ed 1999, CRC Press, Boca Raton.

248. Kyu, T., M. Hashiyama and A. Eisenberg, *Dynamic mechanical studies of partially ionized and neutralized Nafion polymers.* Canadian Journal of Chemistry, 1983. 61. p. 680-687.
249. Yeo, S.C. and A. Eisenberg, *Physical properties and supramolecular structure of perfluorinated ion-containing (nafion) polymers.* Journal of Applied Polymer Science, 1977. 21. p. 875-898.
250. Page, K.A., K.M. Cable and R.B. Moore, *Molecular Origins of the Thermal Transitions and Dynamic Mechanical Relaxations in Perfluorosulfonate Ionomers.* Macromolecules, 2005. 38. p. 6472-6484.
251. Cox, J.N., *Fourier Transform Infrared Spectroscopy*, in *Encyclopedia of Materials Characterization*, C.R. Brundle, C.A. Evans, and S. Wilson, Editors. 1992, Butterworth-Heinemann: Boston.
252. Hatakeyama, T. and Z. Liu, *Handbook of thermal analysis* 1998, Wiley, Chichester.
253. Greenspan, L., *Humidity fixed points of binary saturated aqueous solutions.* Journal of Research of the National Bureau of Standards Section a-Physics and Chemistry, 1977. 81(1). p. 89-96.
254. Berne, B.J. and R. Pecora, *Dynamic Light Scattering* 1976, Jonh Wiley & Sons, New York.
255. Barsoukov, E. and J.R. Macdonald, *Impedance Spectroscopy: Theory, Experiment, and Applications*. 2 ed 2005, Wiley, Hoboken.
256. Yuan, X., C. Song, H. Wang and J. Zhang, *Electrochemical impedance spectroscopy in PEM fuel cells: Fundamentals and applications* 2010, Springer, New York.
257. Macdonald, J.R., *Impedance Spectroscopy: Emphasizing Solid Materials and Systems* 1987, Wiley, New York.
258. Yadav, R. and P.S. Fedkiw, *Analysis of EIS Technique and Nafion 117 Conductivity as a Function of Temperature and Relative Humidity.* Journal of the Electrochemical Society, 2012. 159(3). p. B340-B346.
259. Buck, A.L., *New equations for computing vapor-pressure and enhancement factor.* Journal of Applied Meteorology, 1981. 20(12). p. 1527-1532.
260. Goto, Y. and S. Inagaki, *Synthesis of large-pore phenylene-bridged mesoporous organosilica using triblock copolymer surfactant.* Chemical Communications, 2002(20). p. 2410-2411.
261. Marler, B., U. Oberhagemann, S. Vortmann and H. Gies, *Influence of the sorbate type on the XRD peak intensities of loaded MCM-41.* Microporous Materials, 1996. 6(5-6). p. 375-383.
262. Hamoudi, S. and S. Kaliaguine, *Sulfonic acid-functionalized periodic mesoporous organosilicas.* Nanotechnology in Mesostructured Materials, 2003. 146. p. 473-476.
263. Nakamura, T., Y. Yamada and K. Yano, *Direct synthesis of monodispersed thiol-functionalized nanoporous silica spheres and their application to a colloidal crystal embedded with gold nanoparticles.* Journal of Materials Chemistry, 2007. 17(35). p. 3726-3732.
264. Yang, Q.H., M.P. Kapoor, N. Shirokura, M. Ohashi, S. Inagaki, J.N. Kondo and K. Domen, *Ethane-bridged hybrid mesoporous functionalized organosilicas with terminal sulfonic groups and their catalytic applications.* Journal of Materials Chemistry, 2005. 15(6). p. 666-673.

265. Lourenco, M.A.O., R. Siegel, L. Mafra and P. Ferreira, *Microwave assisted N-alkylation of amine functionalized crystal-like mesoporous phenylene-silica.* Dalton Transactions, 2013. 42(16). p. 5631-5634.
266. Blinka, T.A., B.J. Helmer and R. West, *Polarization Transfer NMR Spectroscopy for Silicon-29: The INEPT and DEPT Techniques*, in *Advances in Organometallic Chemistry*, F.G.A. Stone and W. Robert, Editors. 1984, Academic Press. p. 193-218.
267. Silverstein, R.M., F.X. Webster and D.J. Kiemle, *Spectrometric identification of organic compounds*. 7th ed 2005, Jonh Wiley & Sons, New York.
268. Domingues, E.M., N. Bion, P. Ferreira and F.M. Figueiredo, *Synthesis of sulfonic acid-functionalized mesoporous benzene-silica hybrids assisted with microwave radiation.* Ciência e Tecnologia dos Materiais, 2011. 23(1-2). p. 20-24.
269. Onida, B., L. Borello, C. Busco, P. Ugliengo, Y. Goto, S. Inagaki and E. Garrone, *The surface of ordered mesoporous benzene-silica hybrid material: An infrared and ab initio molecular modeling study.* Journal of Physical Chemistry B, 2005. 109(24). p. 11961-11966.
270. Sasidharan, M., K. Nakashima, N. Gunawardhana, T. Yokoi, M. Ito, M. Inoue, S.-i. Yusa, M. Yoshio and T. Tatsumi, *Periodic organosilica hollow nanospheres as anode materials for lithium ion rechargeable batteries.* Nanoscale, 2011. 3(11). p. 4768-4773.
271. Lu, J., H. Tang, C. Xu and S.P. Jiang, *Nafion membranes with ordered mesoporous structure and high water retention properties for fuel cell applications.* Journal of Materials Chemistry, 2012. 22(12). p. 5810-5819.
272. Hudson, S., D.A. Tanner, W. Redington, E. Magner, K. Hodnett and S. Nakahara, *Quantitative TEM analysis of a hexagonal mesoporous silicate structure.* Physical Chemistry Chemical Physics, 2006. 8. p. 3467-3474.
273. Siegel, R., E. Domingues, R. De Sousa, F. Jerome, C.M. Morais, N. Bion, P. Ferreira and L. Mafra, *Understanding the high catalytic activity of propylsulfonic acid-functionalized periodic mesoporous benzenesilicas by high-resolution (1)H solid-state NMR spectroscopy.* Journal of Materials Chemistry, 2012. 22(15). p. 7412-7419.
274. Yang, Q.H., J. Liu, J. Yang, M.P. Kapoor, S. Inagaki and C. Li, *Synthesis, characterization, and catalytic activity of sulfonic acid-functionalized periodic mesoporous organosilicas.* Journal of Catalysis, 2004. 228(2). p. 265-272.
275. Lu, Q.Y., B. Yang, L. Zhuang and J.T. Lu, *Pattern recognition on the structure-activity relationship of nano Pt-Ru catalysts: Methodology and preliminary demonstration.* Journal of Physical Chemistry B, 2005. 109(18). p. 8873-8879.
276. Marechal, M., J.L. Souquet, J. Guindet and J.Y. Sanchez, *Solvation of sulphonic acid groups in Nafion (R) membranes from accurate conductivity measurements.* Electrochemistry Communications, 2007. 9(5). p. 1023-1028.
277. Li, T., A. Wlaschin and P.B. Balbuena, *Theoretical studies of proton transfer in water and model polymer electrolyte systems.* Industrial & Engineering Chemistry Research, 2001. 40(22). p. 4789-4800.
278. Toelle, P., C. Koehler, R. Marschall, M. Sharifi, M. Wark and T. Frauenheim, *Proton transport in functionalised additives for PEM fuel cells: contributions from atomistic simulations.* Chemical Society Reviews, 2012. 41(15). p. 5143-5159.
279. Matos, B.R., E.I. Santiago, J.F.Q. Rey, A.S. Ferlauto, E. Traversa, M. Linardi and F.C. Fonseca, *Nafion-based composite electrolytes for proton exchange membrane*

fuel cells operating above 120 degrees C with titania nanoparticles and nanotubes as fillers. Journal of Power Sources, 2011. 196(3). p. 1061-1068.
280. Blumenthal, G., M. Cappadonia and M. Lehmann, *Investigation of the Proton Transport in Nafion (R) Membranes as a Function of Direction, Temperature and Relative Humidity.* Ionics, 1996. 2(2). p. 102-106.
281. Lim, M.H. and A. Stein, *Comparative studies of grafting and direct syntheses of inorganic-organic hybrid mesoporous materials.* Chemistry of Materials, 1999. 11(11). p. 3285-3295.
282. Mondal, J., M. Nandi, A. Modak and A. Bhaumik, *Functionalized mesoporous materials as efficient organocatalysts for the syntheses of xanthenes.* Journal of Molecular Catalysis a-Chemical, 2012. 363. p. 254-264.
283. Domingues, E.M., M.A. Salvador, P. Ferreira and F.M. Figueiredo, *Proton conductivity of acid-functionalised periodic mesoporous organosilicas.* Ciência e Tecnologia dos Materiais, 2012. 24(3/4). p. 180-183.
284. Lamb, S.H., *Hydrodynamics 6th Ed.* 1945, Dover, New York.
285. Nemours, D.P.d., *DuPont Fuel Cells - DuPont Nafion PFSA membranes*, 2009.
286. Domingues, E.M., M.A. Salvador, P. Ferreira and F.M. Figueiredo, *Acid-functionalised periodic mesoporous benzenosilica proton conductors.* Solid State Ionics, 2012. 225(0). p. 308-311.
287. Baradie, B., C. Poinsignon, J.Y. Sanchez, Y. Piffard, G. Vitter, N. Bestaoui, D. Foscallo, A. Denoyelle, D. Delabouglise and M. Vaujany, *Thermostable ionomeric filled membrane for H-2/O-2 fuel cell.* Journal of Power Sources, 1998. 74(1). p. 8-16.
288. Bauer, B., D.J. Jones, J. Roziere, L. Tchicaya, G. Alberti, M. Casciola, L. Massinelli, A. Peraio, S. Besse and E. Ramunni, *Electrochemical characterisation of sulfonated polyetherketone membranes.* Journal of New Materials for Electrochemical Systems, 2000. 3(2). p. 93-98.
289. Lufrano, F., I. Gatto, P. Staiti, V. Antonucci and E. Passalacqua, *Sulfonated polysulfone ionomer membranes for fuel cells.* Solid State Ionics, 2001. 145(1-4). p. 47-51.
290. Bae, J.M., I. Honma, M. Murata, T. Yamamoto, M. Rikukawa and N. Ogata, *Properties of selected sulfonated polymers as proton-conducting electrolytes for polymer electrolyte fuel cells.* Solid State Ionics, 2002. 147(1-2). p. 189-194.
291. Jung, D.H., S.Y. Cho, D.H. Peck, D.R. Shin and J.S. Kim, *Preparation and performance of a Nafion (R)/montmorillonite nanocomposite membrane for direct methanol fuel cell.* Journal of Power Sources, 2003. 118(1-2). p. 205-211.
292. He, R.H., Q.F. Li, G. Xiao and N.J. Bjerrum, *Proton conductivity of phosphoric acid doped polybenzimidazole and its composites with inorganic proton conductors.* Journal of Membrane Science, 2003. 226(1-2). p. 169-184.
293. Kim, Y.S., F. Wang, M. Hickner, T.A. Zawodzinski and J.E. McGrath, *Fabrication and characterization of heteropolyacid (H3PW12O40)/directly polymerized sulfonated poly(arylene ether sulfone) copolymer composite membranes for higher temperature fuel cell applications.* Journal of Membrane Science, 2003. 212(1-2). p. 263-282.
294. Yang, C., S. Srinivasan, A.B. Bocarsly, S. Tulyani and J.B. Benziger, *A comparison of physical properties and fuel cell performance of Nafion and zirconium phosphate/Nafion composite membranes.* Journal of Membrane Science, 2004. 237(1-2). p. 145-161.

295. Xie, L., E.-B. Cho and D. Kim, *Sulfonated PEEK/cubic (Im3m) mesoporous benzene-silica composite membranes operable at low humidity.* Solid State Ionics, 2011. 203(1). p. 1-8.
296. Li, J.R., H.L. Tang, L.T. Chen, R. Chen, M. Pan and S.P. Jiang, *Highly ordered and periodic mesoporous Nafion membranes via colloidal silica mediated self-assembly for fuel cells.* Chemical Communications, 2013. 49(58). p. 6537-6539.
297. Di Noto, V., M. Piga, G.A. Giffin, K. Vezzù and T.A. Zawodzinski, *Interplay between mechanical, electrical and thermal relaxations in naocomposite proton conducting membranes based on nafion and a [(ZrO2)-(Ta2O5)0.119] core-shell nanofiller.* Journal of the American Chemical Society, 2012. 134. p. 19099-19107.